Normal fault interaction and relay ramp development on the Volcanic Tableland, E. California.

Peter James McFadzean

Thesis submitted for the degree of
Doctor of Philosophy

University of Edinburgh
2002

Acknowledgements

I would firstly like to thank my principal supervisors, Patience Cowie and Nancye Dawers, who have provided enthusiastic help throughout the duration of my PhD. I would further like to thank my principal sponsors Statoil R&D, Norway, for their generous support and also the White Mountain Research Station, University of California, for financial assistance.

I am lucky enough to be the proud owner of more friends than I would ever dare have hoped for. They are my raison d'être, the source of hope when it feels frail to be human.

The PhD is dedicated to my parents, for unwavering support from the very beginning.

ABSTRACT

With increasing extension, normal faults initially growing in isolation will grow into proximal configurations with other faults and undergo interaction prior to fault linkage. The transition from a fault growing in isolation to a fault undergoing interaction and the controlling parameters in this transition are poorly defined at present. Further to this, the control exerted by the spatial geometry of neighbouring faults on the degree of fault interactions experienced is poorly understood, as are the mechanisms that allow fault interactions to take place over multiple earthquake cycles.

Fault arrays and relay ramps on the Volcanic Tableland, E California, USA, are surveyed with a view to assessing the manifestation of fault interactions on fault displacement profiles and the controls on varying strengths of interaction. Surveyed faults are several hundred metres to several kilometres in length with up to tens of metres of displacement. The maximum displacement (D_{max}): length (L) ratio of a fault segment, extracted from survey data, is used as a guide to a faults interaction state. Rock mass heterogeneities, fault linkage, and fault interaction at both tips are shown to obscure evidence of profile asymmetry, a previously commonly used interaction indicator. Fault growth in isolation is quantitatively re-defined in this study as those faults separated from their nearest neighbour by greater than $0.1*L_t$, where L_t refers to the combined length of the two faults under consideration. This is evidenced by an increase in fault D_{max}:L ratios with decreasing separation distances below $0.1*L_t$, and an independence of D_{max}:L ratios on separation distances above this threshold. D_{max}:L ratios show a broad positive correlation with overlap (O):separation (S) ratio, indicative of increasing fault interaction with increasing overlap. A length normalised O:S plot reveals a wedge-shaped area along the overlap axis devoid of data points. This suggests O:S ratios are restricted such that faults are only capable of attaining increasing overlap by increasing the separation distance between a fault pair. This in turn implies the existence of stress shadows that scale with the final fault dimensions. Stress perturbations created in the crust from individual slip events may thus be able to accumulate to some degree over multiple slip cycles.

Rock mass heterogeneity is shown capable of seriously affecting fault growth. Faults growing into or along joints develop anomalously low tip gradients and D_{max}:L ratios. Faults growing into fumaroles develop anomalously high tip gradients and D_{max}:L ratios. These phenomenon can in turn significantly alter fault interaction signatures. Joints and fumaroles thus appear to act predictably as zones of low and high shear strength respectively within the rock mass.

Relay ramps and their bounding fault tips are seldom well preserved at the earth's surface and so their evolution as a combined system remains poorly understood. Relay ramps surveys are undertaken to assess the critical controls on their geometrical evolution, including the role of bounding fault displacement gradients, fault propagation folding and fault linkage. Separation distance is shown to exert a critical control on ramp dip direction with ramps separated by less than 70m dipping toward the collective hangingwall and unlinked ramps separated by greater than this distance dipping toward the collective footwall. Fault propagation folding is shown capable of significantly affecting ramp dip and creating localised zones of anomalously high strain. It is demonstrated that in order to create a ramp dipping toward the collective hangingwall, one does not have to invoke secondary ramp altering processes such as erosion or fault propagation folding as previous authors have suggested. Relay ramp strain is shown to control the likelihood of fault linkage with high strain ramps more likely to be linked than their low strain equivalents. The strain within a ramp is controlled by the cutoff gradients of the bounding faults, which in turn are controlled by the manner in which a fault partitions growth into footwall uplift and hangingwall subsidence. This growth partitioning appears independent of the fault interaction phenomena that produces elevated tip gradients and profile asymmetry.

This thesis makes significant contributions to our understanding of fault interactions prior to linkage, their manifestations in fault displacement profiles and their controlling parameters. The demonstrated role of rock mass heterogeneity in predictably affecting fault growth and interaction signals represents one of the few studies of its kind in the literature. Significant improvements are also made to our understanding of the critical parameters controlling the geometrical evolution of relay ramps and fault linkage. Together, the results from this study provide the details of a more complete picture of the evolution of extensional settings.

Table of Contents

Chapter 1 – Introduction

Chapter 2 - Geological Setting

Chapter 3 – Surveying methodologies and fault survey data

Chapter 4 – Defining fault growth in isolation and assessing controls on fault profile shape

Chapter 5 - The relationship between fault dimensions and fault array geometries as controlled by fault interactions

Chapter 6 – Relay ramp evolution

Chapter 7 – Conclusions and future work

Chapter 1 – Introduction

1.1 Rationale

Extending terranes accommodate strain by the growth, interaction, and linkage of normal fault segments (e.g. Walsh and Watterson, 1989; Peacock and Sanderson, 1991; Anders and Schlische, 1994; Trudgill and Cartwright, 1994; Childs et al., 1995; Dawers and Anders, 1995; Huggins et al., 1995; Nicol et al., 1996; Schlische et al. 1996, Willemse et al., 1996, Moore and Schultz, 1999). Initially diffusely distributed faults growing in relative isolation at low strains will propagate and interact with neighbouring structures with further strain (e.g. Walsh and Watterson, 1989; Peacock and Sanderson, 1991; Childs et al., 1995; Nicol et al., 1996; Gupta and Scholz, 2000b; Poulimenos, 2000). Proximal faults in overlapping configurations preserve distinctly different displacement profile shapes and dimensions from faults that have grown in relative isolation as a result of fault interactions (e.g. Walsh and Watterson, 1989; Peacock and Sanderson, 1991; Dawers and Anders, 1995; Nicol et al., 1996; Willemse et al., 1996; Cartwright and Mansfield, 1998; Gupta and Scholz, 2000a). This change in displacement profile shape has been reproduced in mechanical models of fault interaction in an elastic material (e.g. Segall and Pollard, 1980; Burgmann et al., 1994; Willemse et al. 1996, Crider and Pollard, 1998).

Although a range of fault interaction signatures have been recognised in field data, e.g. displacement profile asymmetry and elevated maximum displacement to length ratios, little has been done to examine and quantify the controls on differing degrees of fault interaction and their manifestation in fault displacement profiles. Gupta and Scholz (2000a) undertake the most rigorous study of this kind in the literature but for minor faults of centimetre scale. This project attempts to identify different degrees of fault interaction, via displacement profile analysis of major, multiple earthquake rupture faults with 10's of metres of displacement and up to several kilometres in length, and relate the strength of this interaction signal to the spatial geometry of the faults in question. In tandem with this analysis, the role of rock mass heterogeneity is examined in terms of its ability to alter fault growth and obscure a fault interaction signal. Such problems have seldom been studied for faults of this scale and a quantitative analysis of the role of heterogeneities in affecting fault growth provides an important new contribution to the literature. Much remains to be understood on the manner in which faults grow through multiple slip cycles. By examining faults of this scale this project aims to help fill this gap in understanding. In doing so, it will also test the validity of using simple mechanical models (e.g. Willemse et al. 1996) to approximate the behaviour of interacting faults on geological time-scales.

Relay ramps represent the material link between overlapping, interacting fault pairs and allow for displacement transfer between two faults (e.g. Larsen, 1988; Morley et al., 1990; Peacock and Sanderson, 1991; Trudgill and Cartwright, 1994; Childs et al., 1995; Dawers and Anders, 1995; Huggins et al., 1995; Mack and Seager, 1995; Schlische et al., 1996; Crider and Pollard, 1998; Walsh et al., 1999; Ferrill et al., 2000). The mechanisms of relay ramp development are intrinsically linked to the development of their bounding, interacting faults (e.g. Peacock and Sanderson, 1991; Huggins et al., 1995; Ferril and Morris, 2001) and attempts at ramp breaching (e.g. Peacock and Sanderson, 1991; Trudgill and Cartwright, 1994, Walsh et al., 1999). Crider and Pollard (1998) present a mechanical model for relay ramp evolution although they have been unable to successfully reproduce ramp dip directions commonly encountered in the field, i.e. toward the collective hangingwall of an interacting fault pair. A lack of studies of fault pairs and their associated ramps in the literature motivates a detailed analysis of relay ramp geometries in the field. Two aspects of relay ramp development receive special attention, specifically the potential factors controlling ramp dip direction and controls on fault linkage. As relay ramps often control sediment dispersal in evolving extensional terranes (e.g. Gawthorpe and Hurst, 1993) and can act as sites of fluid migration in hydrocarbon reservoirs it is crucial to understand the controls on their geometrical evolution.

1.1.1 Aims

The principle aim of this thesis is to improve on the current understanding of mechanisms of fault interaction prior to and in the lead up to fault linkage. This aim is approached via analysis of normal fault arrays on the Volcanic Tableland, eastern California, USA. The Volcanic Tableland is a low strain setting of less than a few percent (Dawers et al., in review), with a large population of superbly preserved normal faults (e.g. Dawers et al., 1993). High-resolution surveys of fault scarp displacement profiles, fault array geometries and relay ramps are employed here to gain insight into processes of fault interaction. Fault displacement profiles are analysed, potential evidence for fault interactions are identified and quantitatively analysed in the spatial context of the array. Fundamental controls on relay ramp geometries are examined via analysis of the displacement gradients on ramp bounding faults, spatial fault array geometries, internal ramp strain and the presence or absence of ramp breaching structures. The excellent quality of fault and ramp exposure on the Tableland, including fault tips, makes it unique for a survey of this kind and allows results to be quantitatively analysed in more detail than most surveys allow. Furthering our understanding of fault interactions has many applications, including improving models of basin subsidence, risk estimates in seismic hazard assessment studies and improving models of sub-surface structure based on seismic data of inherently limited resolution.

The role of rock mass heterogeneity in affecting fault growth and fault interactions is simultaneously analysed. The Volcanic Tableland is affected by a pervasive set of tectonic conjugate joints and numerous dome-like volcanic vents, both of which form significant strength heterogeneities in the rock mass. Fault parameters, where a fault appears to interact with a heterogeneity, are quantitatively compared with those of faults growing in relatively homogenous rock, and in so doing the ability of heterogeneities to obscure a fault interaction signal is considered. This component of the project aims to improve our understanding of the variation in fault profile shapes which can result from changes in the rock mass shear strength alone.

1.1.2 Structure of the thesis

This chapter introduces the ideas and aims behind this study, provides a summary of fault terminology used throughout the thesis and a summary of the current understanding of earthquake and fault interactions from field and mechanical modelling data, highlighting the gaps in knowledge which this project aims to fill. Chapter 2 introduces the principal field area of this study, the Volcanic Tableland, with emphasis on the structural features present and the seismic history of the region. Chapter 3 describes the surveying techniques used to record topographic information in the field and presents the raw fault survey data. Chapters 4 and 5 analyse this data, reassessing the definition of fault growth in isolation, analysing evidence for fault interactions, assessing spatial controls on the strength of these interactions and on fault array geometries, and analysing the role of rock mass heterogeneity in affecting fault growth. Chapter 6 presents relay ramp survey data and analyses ramp topography with respect to the displacement gradients on bounding faults, spatial fault pair geometries, ramp breaching faults, and erosion. Conclusions from this work and recommendations for future work are made in Chapter 7.

1.2 Fault terminology and fault growth models

This section will provide some of the basic nomenclature used throughout this thesis to describe faults, fault arrays and relay ramps, put in context by simultaneously discussing observation driven models for fault growth.

1.2.1 Basic fault terminology

Normal faults are 3 dimensional features that offset crustal material primarily in a vertical sense (e.g. Twiss and Moores, 1992). The simplest case to be considered is that of an isolated single normal fault that has grown wholly contained within the rock volume and has not interacted with other faults (Walsh and

Watterson, 1987). This kind of fault will approach an elliptical displacement profile, with displacement (D) increasing steadily from zero at the outer tip line toward a maximum displacement (D_{max}) at the centre of the fault (Rippon 1985, Barnett et al., 1987, Walsh and Watterson, 1987) (Figure 1.1). The length of the fault (L) is at a maximum at the centre of the ellipse and the maximum height (H) forms the other major axis of the ellipse. The ratio of these two parameters, i.e. L/H, has been referred to as the fault surface ellipticity (Walsh and Watterson, 1989) or fault aspect ratio (Nicol et al., 1996; Willemse et al., 1996) and can be used to describe the shape of a fault plane. Nicol et al. (1996) find an average aspect ratio for blind isolated faults of 2.15. A 2D section through a displacement ellipse at the ground surface, such as labelled in Figure 1.1, defines the fault trace on the ground and has its own characteristic L and $D_{max.}$ Walsh and Watterson (1987) show that for elliptical displacement profiles, normalised D vs normalised L plots taken through any random section of the ellipse will have approximately similar forms.

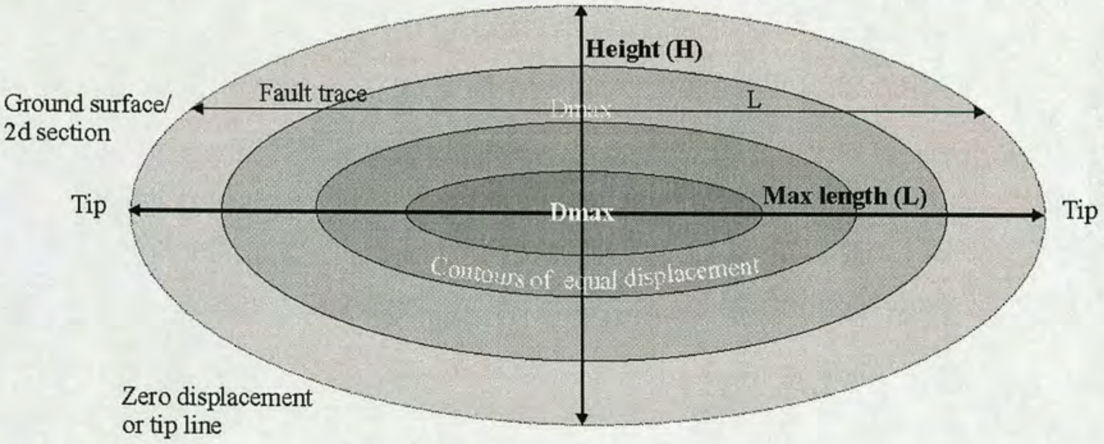

Figure 1.1. Three dimensional elliptical fault plane for an ideal single fault (Walsh and Watterson, 1987) with a maximum displacement at the centre (D_{max}) tapering to zero displacement at the outer tip line. The major axes of the ellipse represent the maximum fault length (L) and height (H), both bisecting the D_{max}.

1.2.2 Observation driven fault growth models

Conceptual and numerical models of fault growth have arisen based in large part on the data obtained from fault scarps over a variety of scales and in a variety of tectonic settings. It has long been understood that faults have varying amounts of displacement along strike, from a maximum offset at some point along strike to zero offset at the fault tips (e.g. Muraoka and Kamata, 1983; Rippon, 1985; Watterson, 1986; Walsh and Watterson, 1987; Peacock and Sanderson, 1991; Cowie and Scholz, 1992a; Dawers et al., 1993). Muraoka and Kamata (1983) find a positive linear correlation between the D_{max} and L of their surveyed faults, the gradient of which is dependent on the competency of the rock unit being faulted. This phenomenon is commonly recounted in subsequent papers on the topic of fault growth. Schlische et al. (1996) go on to perform a simple analysis of the ratio of D_{max} on a fault with respect to L for multiple published fault data sets from different tectonic settings (Figure 1.2). This plot reveals a positive correlation between D_{max} and L over more than 8 orders of magnitude in length. This provides strong evidence to suggest faults grow in a predictable self-similar manner, irrespective of tectonic setting or scale. The correlation is, however, not a simple one as it has an order of magnitude scatter in both D_{max} and L.

Isolated fault growth by radial propagation

Single, isolated faults are reasoned to grow by a process of radial propagation whereby fault length increases with increasing fault displacement or vice-versa (e.g. Barnett et al., 1987; Walsh and Watterson, 1987; Cowie and Scholz, 1992a) (Figure 1.3). Such a growth process is necessary to explain the positive correlation observed between D_{max} and L for faults of all kinds in the field as observed in Figure 1.2 and discussed by Cowie and Scholz (1992a). Indeed, Cowie and Scholz (1992a) point out that such a correlation is intuitive as the accumulation of displacement on a fault will by default raise the stress concentration at fault tips thus causing the fault to propagate in length.

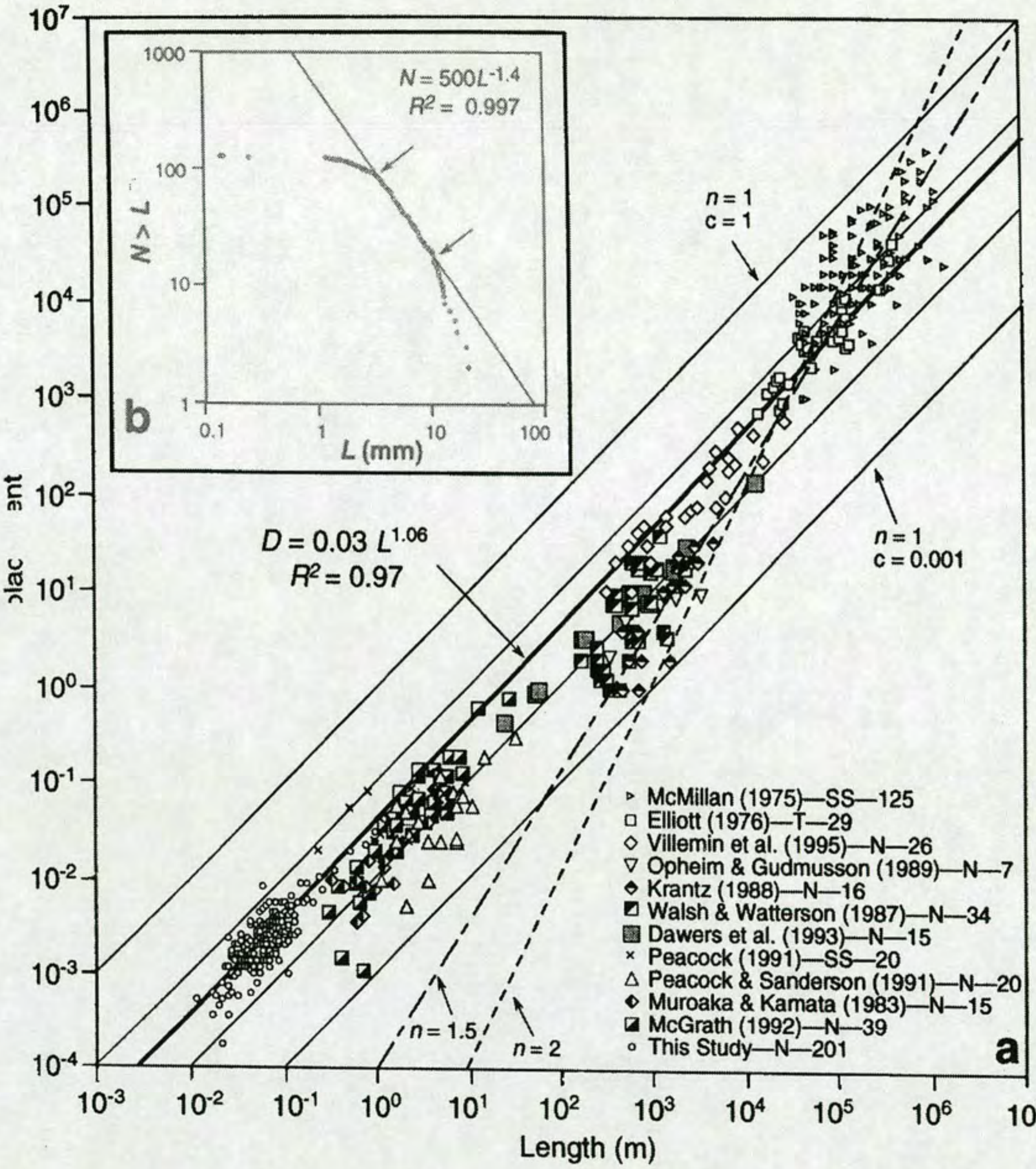

Figure 1.2. Figure 5 from Schlische et al. (1996) showing the positive correlation between fault displacement (D) and length (L) over 8 orders of magnitude although with a significant degree of scatter in both parameters. A best-fit line through the data is shown with the format $D = cL^n$, i.e. $D = 0.03L^{1.06}$. Several other lines are shown that would be produced by varying the c and n parameters in this equation.

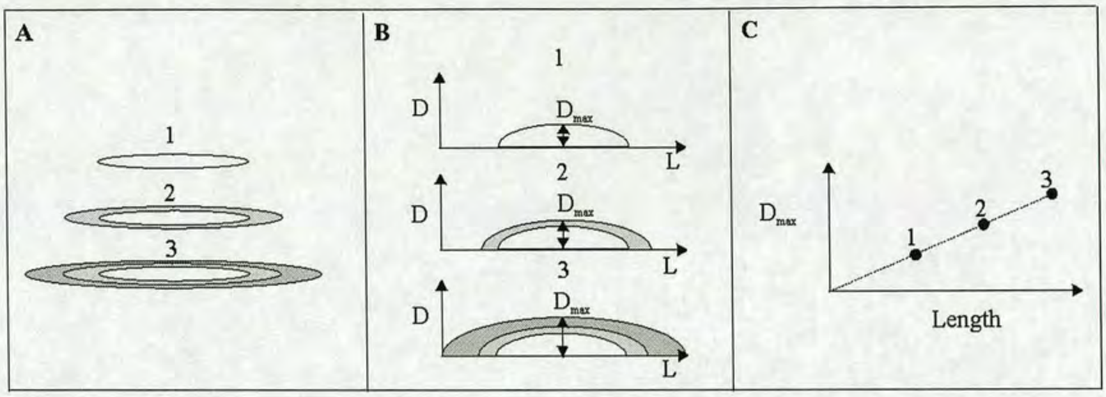

Figure 1.3. Isolated fault growth by radial propagation. 'A' shows the evolution of an idealised single elliptical fault plane in space from stage 1 to stage 3. Each new superimposed ellipse represents a new increment of growth. 'B' shows the evolution of the same fault plane shown in the form of a D vs distance plot, including the consistent location of the D_{max} in the centre of the fault. 'C' shows the evolution of the D_{max}:L ratio of this fault plane through time, displaying a positive linear correlation.

Various authors suggest that faults growing in relative isolation have an approximately linear relationship between D_{max} and L, as shown in Figure 1.3C, the gradient of which is dependent on rock type (e.g. Muraoka and Kamata, 1983; Cowie and Scholz, 1992a; Dawers et al., 1993). This observation highlights the importance of rock properties such as shear strength and Poisson's ratio in controlling fault growth (Cowie and Scholz, 1992a).

Fault growth by linkage

In an extending setting, with increasing strain, initially isolated fault structures will undergo radial propagation as described in the previous section and come into the vicinity of neighbouring fault structures (e.g. Walsh and Watterson, 1989; Peacock and Sanderson, 1991; Childs et al., 1995; Nicol et al., 1996; Gupta and Scholz, 2000b; Poulimenos, 2000). Proximal faults that grow into overlapping configurations are described as having an en echelon geometry and have a characteristic overlap (O) and separation (S) distance at any stage in their growth history. The region separating the 2 faults, accommodating displacement transfer between the 2 structures, is known as a relay ramp (Figure 1.4).

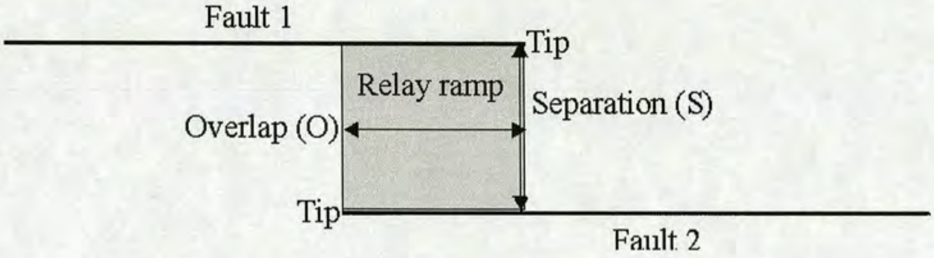

Figure 1.4. An en echelon fault pair with a characteristic overlap (O) and separation distance (S) bounding a relay ramp that accommodates displacement transfer between the two faults.

At this stage in the fault growth process, the faults shown in Figure 1.4 are interacting although unlinked. Understanding the manifestation of this 'pre-linkage' fault interaction in fault displacement profiles and the controls on its strength are fundamental goals of this project and so the issue is considered separately and discussed in detail in section 1.3 of this chapter.

It has been extensively documented in the field and in seismic data that faults are often composed of several linked segments via the breaching of relay ramps such as that shown in Figure 1.4 (e.g. Peacock and Sanderson, 1991; Anders and Schlische, 1994; Trudgill and Cartwright, 1994; Cartwright et al., 1995; Childs et al., 1995, Dawers and Anders, 1995; Huggins et al., 1995, Cartwright and Mansfield, 1998, Ferril et al., 1999; Walsh et al., 1999; Dawers and Underhill, 2000; Macleod et al., 2000; Kattenhorn and Pollard, 2001) (Figure 1.5). The phenomenon of fault growth by linkage has also been monitored in analogue models of evolving fault arrays (e.g. Mansfield and Cartwright, 2001). Fault linkage has a major effect on the temporal evolution of fault displacement profiles. Immediately following fault linkage the displacement profile of a newly linked fault has a displacement deficit at the site of linkage (e.g. Anders and Schlische, 1994; Cartwright et al., 1995). This in turn lowers the D_{max}:L ratio of the newly established fault and explains some of the scatter in Figure 1.2 (Cartwright et al., 1995). In time it is thought that the new fault can re-equilibrate to the displacement profile expected for a single fault of its length (e.g. Anders and Schlische, 1994; Cartwright et al., 1995, Dawers and Anders, 1995).

The process of fault growth by a combination of initial radial propagation and subsequent linkage is sketched in Figure 1.6.

Despite the wealth of qualitative observational data available on fault linkage, the principle controls on fault linkage remain poorly understood. Theoretically, it is clear that with increasing displacement gradients in the ramp region, and thus increasing relay ramp strain, fault linkage should become increasingly likely (e.g. Larsen, 1988; Cartwright et al., 1995). Little observational data has been presented in the literature to back up this premise as relay ramps are rarely preserved at the earth's surface, or are significantly eroded. The role of fault propagation folding beneath a ramp in terms of its ability to alter ramp topography has also seldom been discussed using real examples.

Numerical modelling of relay ramp development by Crider and Pollard (1998) has been unable to successfully replicate the topography, specifically the dip direction, of relay ramps commonly encountered in the field, which is often toward the collective hangingwall of an interacting fault pair. Predicting the dip direction of a ramp is clearly very important to the sedimentation history of an extending region. This observation motivates an analysis here of the principal controls on ramp dip direction in the field.

The issues discussed above will be directly addressed in this project via a combined analysis of high resolution relay ramp and fault survey data. To re-iterate, this analysis will focus on understanding the principle controls on relay ramp topography, specifically the ramp dip direction, and the role of relay ramp strain in controlling fault linkage. This study represents a new contribution to the literature, using real examples of high quality field data, on the fundamental controls on relay ramp development.

Figure 1.5. Figure 3 from Dawers and Anders (1995) showing an en echelon array containing faults in varying stages of linkage, from unlinked to displaying a fully breached relay ramp as is the case for the ramp containing the arrows.

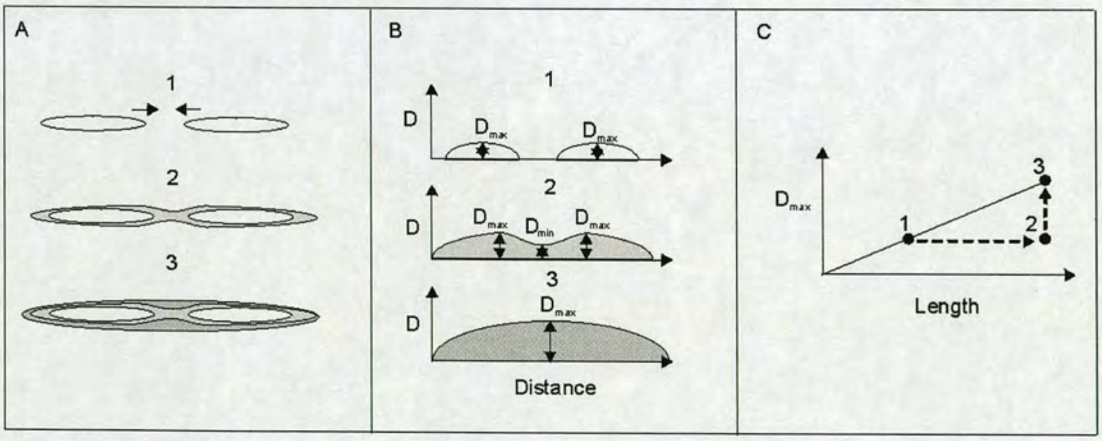

Figure 1.6. Fault growth by radial propagation and linkage. 'A' shows the evolution of 2 idealised elliptical fault planes through time from radial propagation in stage 1, to linkage in stage 2 and further growth in stage 3. 'B' shows the evolution of the same fault planes shown in the form of a D vs distance plot, including the location of the D_{max} and D_{min} through time. 'C' shows the evolution of the fault plane D_{max}:L ratios through time, from an isolated ratio for both faults in stage 1, to a significant

drop in the ratio immediately following linkage in stage 2, and a re-equilibration toward the anticipated ratio for a single fault of its length in stage 3 (modified from Cartwright et al., 1995).

1.3 Fault interactions prior to linkage

The largest component of the data acquisition and analysis in this project is designed to improve our understanding of fault interactions prior to and in the lead up to fault linkage. Fault interactions prior to linkage refer to the period when two faults become aware of each other and start to affect each others growth (e.g. Peacock and Sanderson, 1991; Childs et al., 1995; Dawers and Anders, 1995; Huggins et al., 1995; Nicol et al., 1996; Willemse et al., 1996; Ackermann and Schlische, 1997; Cartwright and Mansfield, 1998, Gupta and Scholz, 2000a). Fault interactions, by default, involve the development of a relay ramp accommodating displacement transfer between the 2 structures involved (e.g. Peacock and Sanderson, 1991; Childs et al., 1995). A discussion of the current understanding of fault interactions will be undertaken in this section, highlighting the gaps in knowledge that this project aims to fill.

1.3.1 Earthquake interactions

To commence this discussion, it is necessary to take a step back and study the building blocks of faults, i.e. earthquakes (e.g. King et al., 1988; Stein et al., 1988), in particular the ability of one earthquake to trigger, advance or retard another earthquake event (e.g. Harris and Simpson, 1992; King et al., 1994; Hodgkinson et al., 1996; Stein et al., 1997; Harris, 1998, Hubert-Ferrari et al., 2000, Kilb et al., 2000). This is an essential component of any discussion of fault interactions as the interaction between earthquakes is ultimately responsible for shaping the final appearance and geometry of any fault population. The scale of the faults under consideration in this study, with up to 90 metres of displacement, makes them indisputably the product of multiple earthquake ruptures and thus multiple earthquake interactions. This is clear as even very large magnitude normal fault earthquakes seldom have displacements of more than a few metres in one event (e.g. Lee et al., 2001a).

Following an earthquake of known slip distribution, it is possible to model the static stress changes in the adjacent rock mass caused by this event using Couloumb failure stress calculations (Harris, 1998) (Equation 1.1). These stress changes can then be resolved into changes in normal and shear stress (Harris, 1998) (Figure 1.7), on a particular fault plane.

Equation 1.1.

$$\Delta CFS = \Delta\tau_{slip} + \mu(\Delta\sigma_n + \Delta P) \cong \Delta\tau_{slip} + \mu'\Delta\sigma_n$$

where ΔCFS refers to the change in Coulomb failure stress brought about by an earthquake. If ΔCFS on the fault is > 0 then the first earthquake advanced the second earthquake toward failure. If ΔCFS is < 0 then the first earthquake delayed the occurrence of the second earthquake. $\Delta\tau_{slip}$ is the change in shear stress due to the first earthquake resolved in the slip direction of the second earthquake. $\Delta\sigma_n$ is the change in normal stress due to the first earthquake, resolved in the direction orthogonal to the second fault plane, μ is the coefficient of friction and ΔP is the change in pore pressure. Using μ' is a simplification of the first equation, i.e. $\Delta\tau_{slip} + \mu(\Delta\sigma n + \Delta P)$, meaning the apparent coefficient of friction accounting for pore pressure (after Harris, 1998).

If a neighbouring fault plane is sited in such a region of stress change, the normal and shear stress components on that fault plane can be altered accordingly. In this way, earthquakes can advance or delay rupture on a neighbouring fault plane.

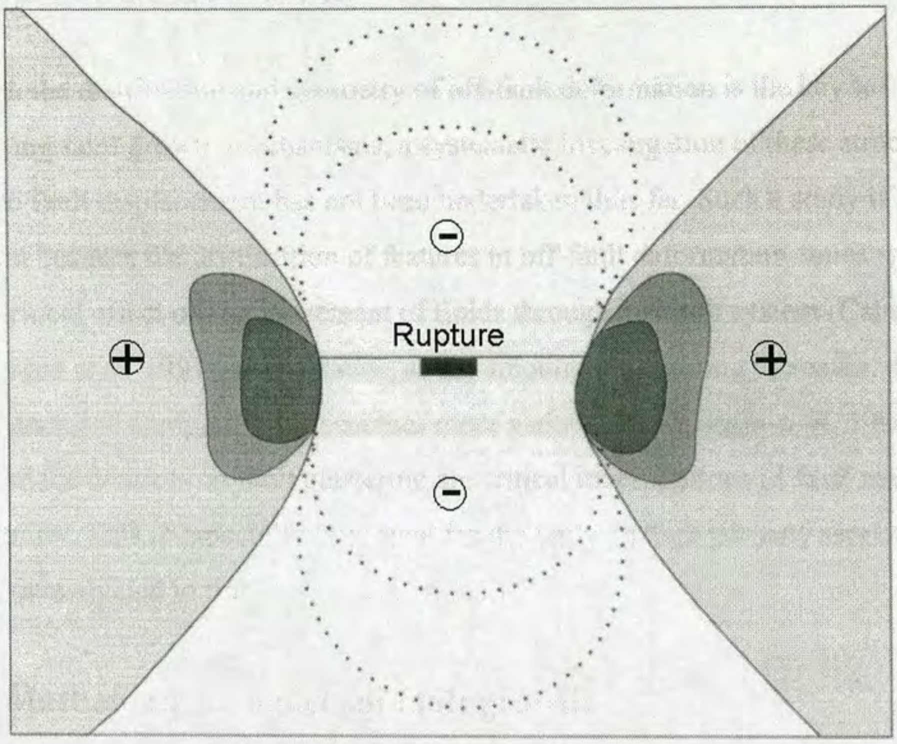

Figure 1.7. General patterns of Coulomb failure stress change following an earthquake rupture with a normal sense of displacement on a 60° dipping fault plane (after Hodgkinson et al., 1996). Areas of increased stress are sited around the fault tips while stress around the body of the fault is reduced and the rock effectively relaxed.

Advancing a fault plane toward failure is sometimes referred to as static stress triggering (Harris, 1998). Stein et al. (1997) show that the North Anatolian earthquake cascade consisted of a series of earthquakes occurring in regions of static stress increase created by previous ruptures. They suggest there is a 10-year average period between triggering and rupturing in this particular case. A similar phenomenon of static stress triggering is shown for the 1954 Rainbow Mountain – Fairview Peak – Dixie Valley, Nevada sequence by Hodgkinson et al. (1996). Harris and Simpson (1992) calculate that the 1992 Landers earthquake of magnitude 7.3 should hasten the next earthquake on the San Andreas fault by one to two decades. By contrast, Simpson and Reasenberg (1994) show that the 1906 rupture on the San Andreas fault relaxed many nearby faults by putting them into a stress shadow, or area of reduced shear stress. This is the opposite effect to static stress triggering and involves delaying subsequent ruptures on a fault plane. Interestingly, subsequent ruptures on the relaxed faults in question occurred at a time consistent with the time required for long term tectonic loading to remove the effect of the stress shadow and bring the faults back to a near failure state (Simpson and Reasenberg, 1994). This result in particular suggests that long term earthquake interactions can occur despite the very small static stress changes involved, i.e. on the order of 1-10 bars, equivalent to several years or decades of tectonic loading (Stein et al., 1997).

Dynamic earthquake interactions, from the transient passage of seismic waves in the rock, can lead to one earthquake triggering another within seconds (e.g. Harris and Day, 1993; Kilb et al., 2000). The passage of such seismic waves from one fault to another does not change the permanent load on a fault and thus induced seismicity on a long timescale has to result from a forced change in the properties of the fault, such as a dynamic weakening of the fault zone itself (Kilb et al, 2000). Understanding in this field is still basic and it is unclear whether dynamic interactions play a lesser or greater role than static stress interactions in affecting fault array evolution (Harris, 1998).

It is clear, however, that static stress changes can advance or delay faults toward or from failure although the time-scales remain unclear, particularly for near-field effects, beyond using the change in Couloumb failure stress (ΔCFS) divided by the tectonic loading rate as a rule of thumb (Harris, 1998). The role of static stress changes over multiple earthquake cycles has received limited attention in the literature (e.g. Gupta et al., 1998; Cowie and Roberts, 2001), partly due to the long timescales involved and thus the lack of historical evidence. This thesis intends to make a contribution to this problem by analysing evidence for and controls on fault interactions over geological time scales. In so doing, it will be possible to infer the manner in which static stress changes from individual earthquakes can affect fault growth over multiple earthquake cycles, with implications for the persistence of such stress changes in the crust.

1.3.2 Fault interactions

Walsh and Watterson (1989) initially recognised that normal faults growing in overlapping arrays typically possess higher tip gradients in the zones of overlap than isolated faults. They also show that the summation of displacements from each structure in the array forms a profile of similar shape to that anticipated for an isolated fault with the same length as the whole array. The observation that overlapping faults develop anomalously high tip gradients was also found by Peacock and Sanderson (1991) and assigned to the role of fault interactions in modifying fault growth. Peacock and Sanderson (1991) break down fault array evolution into 4 stages: 1) isolated fault growth by radial propagation, 2) fault overlap, interaction and the formation of a relay ramp, 3) partial relay ramp breakdown by linking faults, 4) complete fault linkage and the abandonment of old fault tips. These stages of fault array evolution are shown in Figure 1.8. The stage with which much of this project is concerned is stage 2 in the growth cycle. The development of high tip gradients in zones of fault overlap and the associated development of displacement profile asymmetry has been observed for normal fault arrays in numerous settings and on numerous scales over the last decade (e.g. Peacock and Sanderson, 1991; Childs et al., 1995; Dawers and Anders, 1995; Huggins et al., 1995; Nicol et al., 1996; Willemse et al., 1996; Cartwright and Mansfield, 1998; Walsh et al., 1999; Gupta and Scholz, 2000a). Associated with this development of profile asymmetry, an overlapping fault is often shown to have a D_{max}:L ratio above that expected for an isolated fault segment (e.g. Dawers and Anders, 1995; Peacock and Sanderson, 1996; Nicol et al., 1996, Willemse et al., 1996; McFadzean et al., 1999; Gupta and Scholz, 2000a; Poulimenos, 2000). It is thus clear that normal faults growing in close proximity are capable of mutually enhancing their accrued displacement in the region of fault overlap (Figure 1.9).

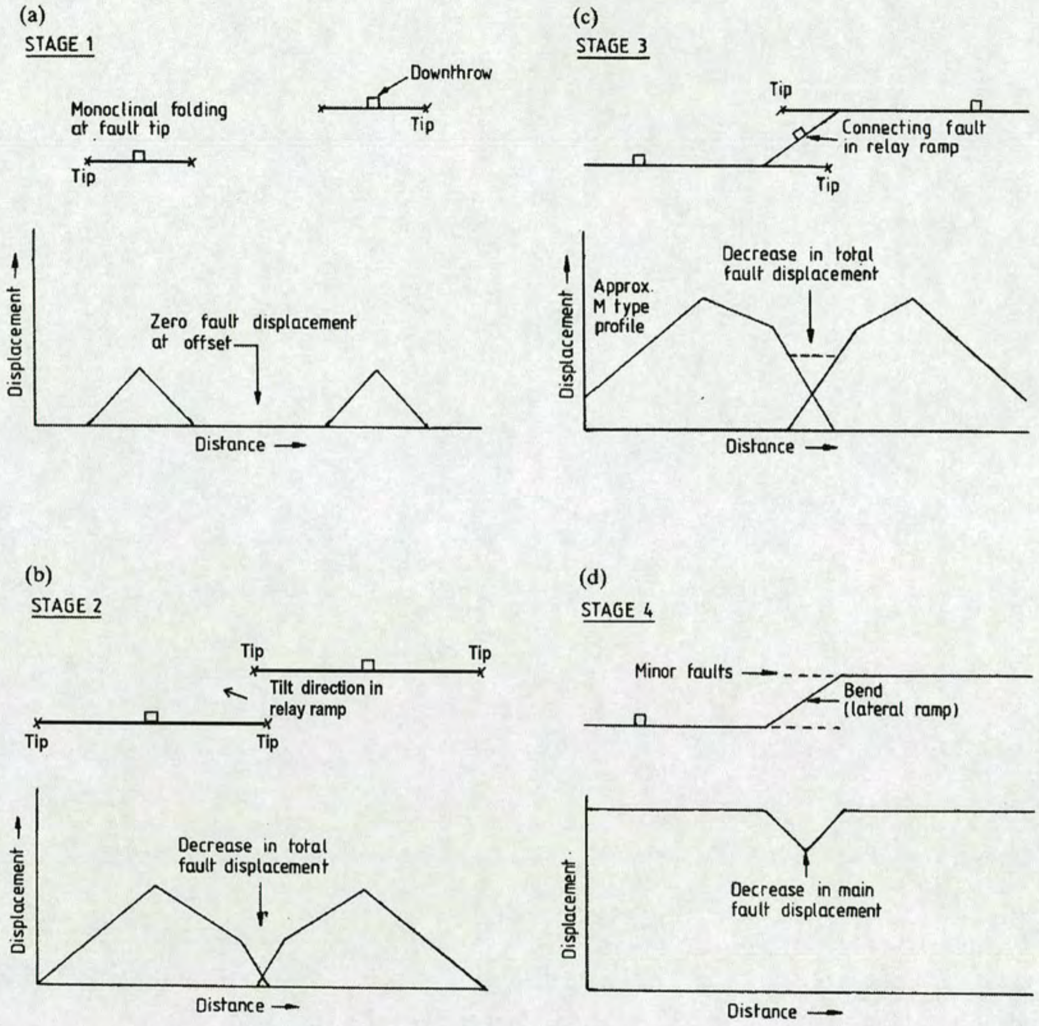

Figure 1.8. Figure 12 from Peacock and Sanderson (1991) showing 4 stages in the fault evolution cycle from isolated radial propagation to fault pair overlap, relay ramp development and fault linkage. Much of this thesis is concerned with stage 2 in this growth cycle when faults begin to overlap and a ramp develops prior to fault linkage.

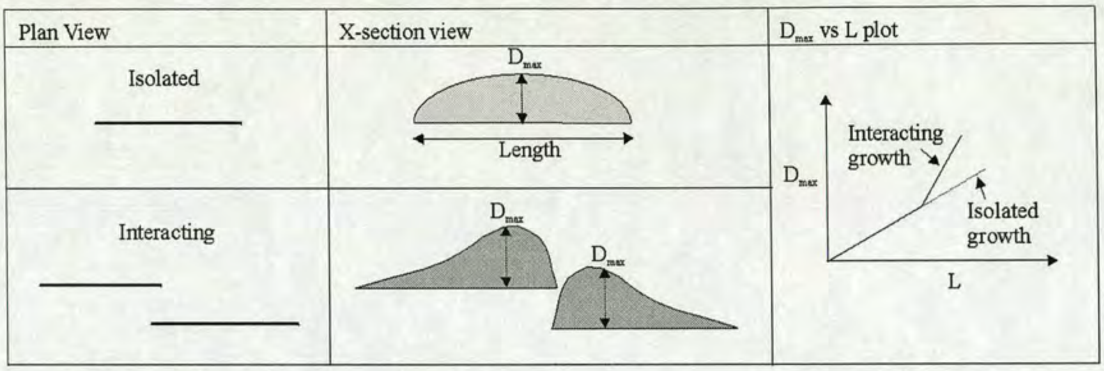

Figure 1.9. Sketch highlighting the difference between the displacement profiles and D_{max}:L ratios of isolated and overlapping, interacting faults. Isolated faults show symmetrical displacement profiles while interacting faults develop asymmetric profiles and elevated D_{max}:L ratios.

What remains unclear in previous studies of fault interaction is what are the principal controls on both the development of displacement profile asymmetry and the degree to which D_{max}:L ratios are elevated? The vast majority of fault interaction studies make qualitative observations on changes in displacement profile shapes and dimensions for overlapping faults but do not attempt to assess the controls on these changes. Such studies are often limited by the nature of the data from which the fault data is extracted, i.e. seismic or mine plan data, mediums in which it is impossible to know exactly what the structural and lithological situation is owing to resolution limits or data density. In such studies it is not possible to categorically assign changes in fault profile shape to interactions with a specific fault, as there may be unresolved faults or heterogeneities otherwise affecting the profile. Lithological heterogeneities in particular have been shown capable of having a pronounced effect on fault displacement profiles (e.g. Muraoka and Kamata, 1983; Nicol et al., 1996; Gross et al., 1997).

The field studies that provide an exception to this rule are those undertaken by Ackermann and Schlische (1997) and Gupta and Scholz (2000a) on a population of centimetre scale normal faults from the Solite quarry. The study by Ackermann and Schlische (1997) provides the first direct field evidence in the literature for faults interacting via their stress fields. These authors examine the spatial distribution of normal fault segments along bedding planes and find that there is a distinct pattern whereby small faults are anticlustered around larger faults (Figure 1.10). This leaves a deformation free zone around the larger faults, referred to as a 'crack shield' by Ackermann and Schlische (1997) and likened to a stress reduction shadow into which the later formed smaller faults will not propagate.

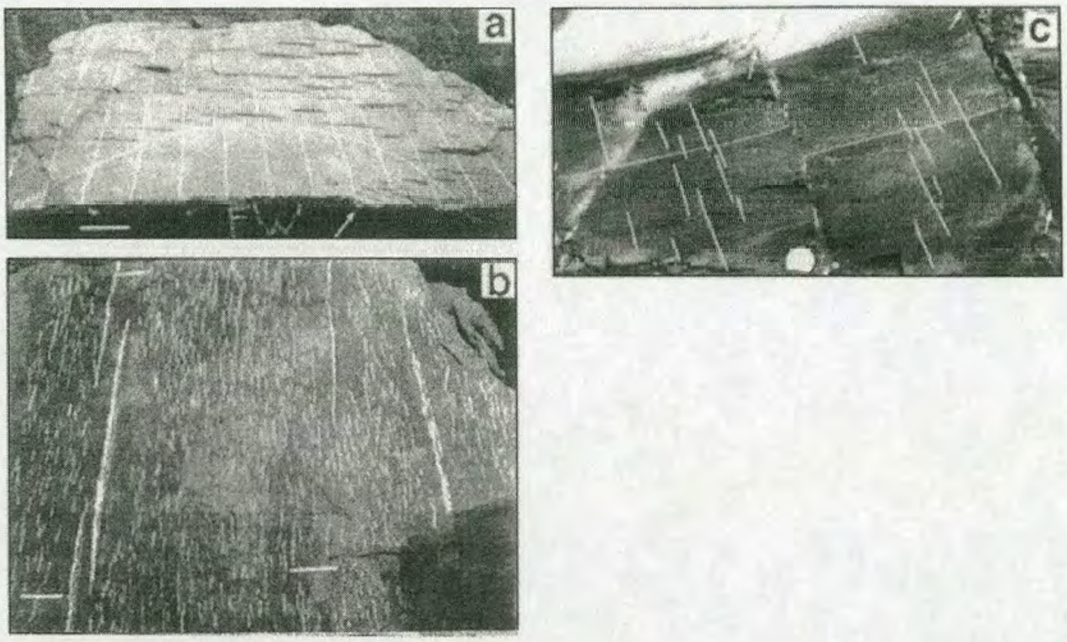

Figure 1.10. Figure 1 from Ackermann and Schlische (1997) showing the anticlustering of small faults around larger structures, both in plan view (b) and cross-section view (c).

Gupta and Scholz (2000a) go on to analyse the displacement distributions of the same fault population in considerable detail and make comparisons with an elastic model of fault interactions. The model shall be considered separately in section 1.4 of this chapter on the mechanical modelling of fault interactions. Gupta and Scholz (2000a) undertake the analysis of displacement profiles by firstly preparing an average isolated displacement profile for comparison with overlapping fault profiles. The preparation of this average isolated profile, specifically in terms of the faults selected, is clearly crucial to the study as it forms the benchmark against which all other faults are compared. Gupta and Scholz (2000a) rely jointly on the definition of fault growth in isolation defined for strike-slip fault data by An (1997) and that produced from modelling data by Willemse (1997). An (1997) finds that strike-slip faults will not link at distances of > 10% of their total combined length and Willemse

(1997) finds that cracks are unlikely to influence each other at separations of greater than 12.5% of their length. With these results in mind, Gupta and Scholz (2000a) raise their threshold for fault interactions to separation distances of < 15% of the total combined fault length. Faults with separations of greater than this are considered isolated assuming they do not show profile asymmetry in which case they are not included. Given that the definition of fault growth in isolation is so important to any fault interaction study, this thesis completely reassesses the definition of isolation based on real field data, making no assumptions on the distances over which faults may be able to interact.

After construction of an average isolated profile, Gupta and Scholz (2000a) go on to define the variation in interacting fault displacement profiles from the average isolated profile in terms of standard deviations away from the mean profile. These authors find that with increasing proximity to the 'crack shield', as defined by Ackermann and Schlische (1997), faults show increasing amounts of deviation away from an average isolated displacement profile (Figure 1.11).

The combined spatial arrangement and displacement patterns of this fault population are taken to imply that these faults are interacting via their stress fields, with varying strength depending on the relative proximity of fault segments (Gupta and Scholz, 2000a). The study by Gupta and Scholz (2000a) is the only example of an attempt to rigorously quantify the controls on differing degrees of normal fault interactions prior to fault linkage. Crucially, this has been undertaken for centimetre scale faults, the mechanics of whose growth are perhaps fundamentally different from the kilometre scale features examined in this project. The importance of the scale of the faults under study cannot be underestimated if one is interested in understanding mechanisms of fault growth over multiple earthquake cycles. Although the Solite quarry faults scale as multi-rupture earthquake faults, i.e. with D_{max}:L ratios of > 0.01 rather than 0.00001 as would be expected of an average single earthquake rupture (Scholz, 1982), their absolute size dictates that they cannot have grown in as many events as the faults on the Volcanic Tableland.

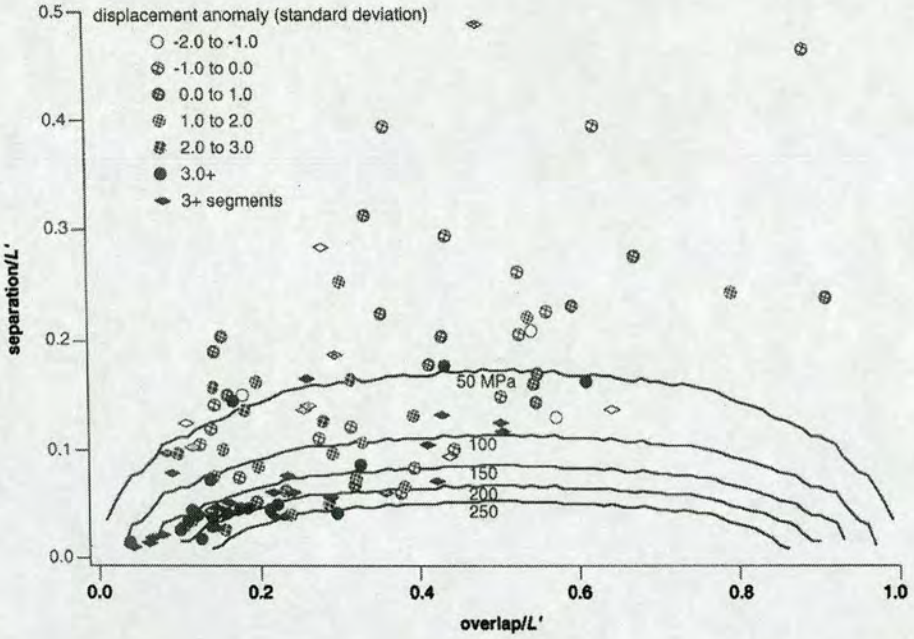

Figure 1.11. Figure 8 from Gupta and Scholz (2000a) showing the increase in fault displacement anomaly, i.e. increased profile asymmetry and elevation in D_{max}:L ratios, with increasing stress shadow as a fault attempts to attain increasing overlap for a given separation distance.

In the course of this project, several publications have emerged documenting large-scale faults whose dimensions are suggested to be controlled by elastic interactions. Gupta & Scholz (2000b) propose that a stress shadowing effect, such as that described above, is responsible for controlling the D_{max}:L ratios of evolving continental rift faults in the Afar region. These faults are one to two orders of magnitude larger than the faults considered in this project, attaining up to 80 kilometres in length. Gupta and Scholz (2000b) find an increase in D_{max}:L ratios with increasing strain, believed to be a manifestation of the "pinning of fault growth by stress interaction with other faults". Contreras et al. (2000) suggest a similar story for the evolution of major faults in the Lake Malawi rift, part of the East African rift system. Importantly, in this case, fault growth histories are temporally constrained using sediment infill patterns with depth from high-resolution seismic data. This information allows the timing of overlap, cessation of fault growth and displacement rates to be constrained. Macleod et al. (2000) examine the temporal and spatial evolution of faults in the Strathspey-Brent-Statfjord array of the northern North sea using high resolution 3D seismic data. These authors find convincing evidence for faults becoming inactive as a result of being sited in areas of reduced stress adjacent to major growing segments. Poulimenos (2000) describes fault scaling parameters from active normal faults in the western Corinth Graben, central Greece. This author finds that upon a domain attaining 'fracture saturation', equivalent to a critical amount of extension or strain, faults start to grow mostly by accumulating displacement, as evidenced by a rise in D_{max}:L ratios compared with faults in an adjacent lower strain domain. It is suggested that this shift in growth style may result from the mechanical interaction of fault segments as described above.

Although these publications discuss larger faults, as stated earlier in this section the controls on differing degrees of fault interaction are seldom discussed in the literature on a fault by fault basis, and indeed for faults of the scale examined in this project, a rigorous quantitative analysis has never taken place. This is undoubtedly an area of fault study with significant inherent difficulties, as the dimensions of fault scarps we observe today, in field or seismic data, provide a snapshot of a cumulative growth history that may have spanned thousands or millions of years. The Volcanic Tableland, however, provides a unique opportunity to undertake a study of this kind as it offers both a low strain setting (< a few percent, Dawers et al., in revision) and superbly preserved examples of relatively young faults in varying stages of underlap and overlap prior to linkage. With increasing strain or poorer preservation, as encountered in most extensional settings, a study of this kind becomes impossible as most faults are linked or the original fault dimensions are massively altered via erosion and sedimentation.

Fault interactions on the Volcanic Tableland

Previous field studies on the structure of the Volcanic Tableland have been undertaken by Dawers et al. (1993), Dawers and Anders (1995), Pinter et al. (1994), Pinter and Keller (1995), Pinter (1995), Willemse et al. (1996), Ferril et al. (1999) and Ferril et al. (2000). Of these studies, Dawers et al. (1993), Dawers and Anders (1995) and Willemse (1996) present fault survey data and in the latter 2 cases consider the role of fault interactions in altering displacement profiles, although only considering a small number of examples.

Dawers et al. (1993) study the dimensions and shapes of individual fault displacement profiles at different scales. Their data support a linear relationship between D_{max} and L. These authors also identify a potential layer thickness control on fault displacement profile shapes as they find that those faults with lengths of greater than 700m start to develop flat-topped profiles. One explanation proposed for this is a change in fault growth style upon faults breaking through the ca. 150m thick welded tuff sheet. Dawers and Anders (1995) look at the displacement profiles and linkage features on a major 7 kilometre long en echelon array. They find that individual overlapping fault segments have displacement profiles significantly removed from that expected of an isolated segment in this setting. However, the summation of displacement from each segment, and continuous deformation between segments, forms a profile more like that expected of a single segment fault with length equivalent to the total length of this array (Figures 1.12 and 1.13).

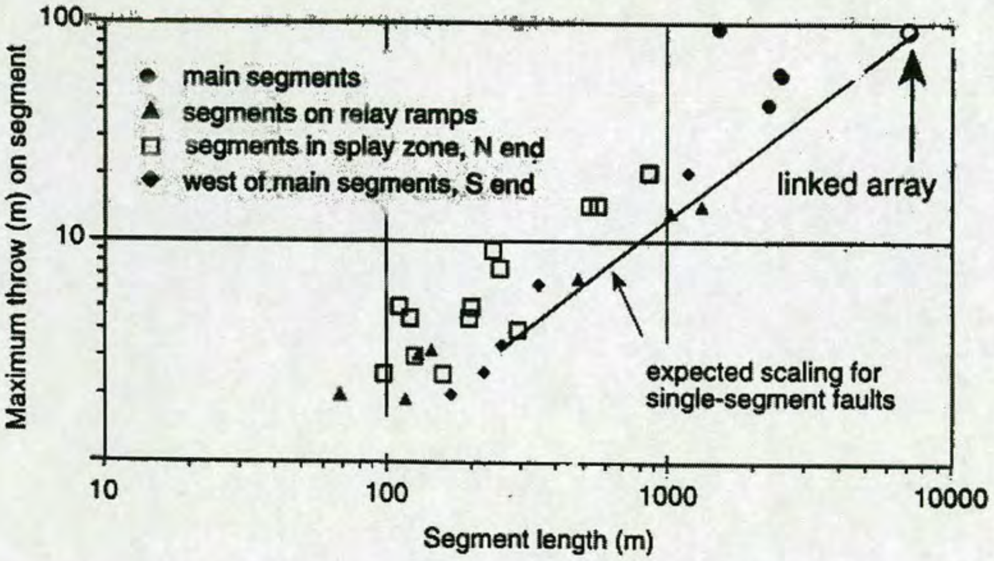

Figure 1.12. Figure 6 from Dawers and Anders (1995) showing the increase in D_{max}:L ratios for interacting fault segments in comparison to those expected for more isolated single-segment faults.

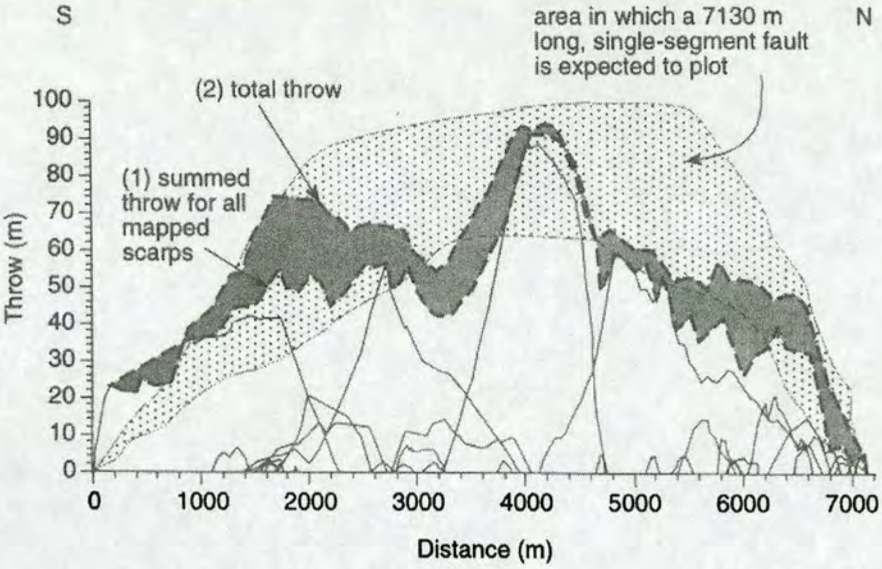

Figure 1.13. Figure 5 from Dawers and Anders (1995) showing displacement profile asymmetry and elevated D_{max}:L ratios for interacting faults. A cumulative displacement profile for the entire array has dimensions and shape more similar to that expected of an isolated, single segment profile shape.

The predictable difference between the dimensions of single faults surveyed by Dawers et al. (1993) and the significantly overlapping faults surveyed by Dawers and Anders (1995) is assigned to the role of pre-linkage fault interactions although the controls on the degree of interaction for each segment are not analysed further. Willemse et al. (1996) survey an en echelon fault array on the Volcanic Tableland for quantitative comparison with the output from a numerical model of fault interactions. The model shall be discussed in section 1.4. The field results from their study show the existence of significant profile asymmetry for overlapping faults, elevated D_{max}:L ratios, displacement gradients steepening on approach to overlap zones and shallowing within them.

This thesis expands significantly from these papers by rigorously quantifying differing degrees of fault interaction for a wide range of spatial fault array geometries, including a detailed analysis of the role of heterogeneities in altering fault growth and interaction. A study of this detail and for faults of this scale has not been undertaken on the Volcanic Tableland or indeed in other extensional settings.

1.4 Mechanical models of fault interactions

Numerous authors have approached aspects of fault interactions via numerical modelling including Segall and Pollard (1980), Aydin and Schultz (1990), Cowie and Scholz (1992b), Burgmann et al. (1994), Willemse et al. (1996), Willemse (1997), Cowie and Shipton (1998), Cowie (1998), Crider and Pollard (1998), Gupta and Scholz (1998) and Gupta and Scholz (2000a). Most of the potential controls on fault interactions are covered in these papers including spatial fault array geometries, 3 dimensional fault plane shape and host rock properties. In particular, Willemse et al. (1996), Willemse (1997) and Gupta and Scholz (2000a) present fault interaction models whose results can be directly compared with the field data analysis being undertaken for this thesis. For this reason, this section will focus on a discussion of the basic principles and results of these studies as well as their limitations for application to real faults.

Willemse et al. (1996) and Willemse (1997) use a 3D boundary element program to numerically model the interaction between angular dislocations buried in a linear-elastic whole-space. These angular dislocations achieve all their displacement in one event as the model does not include fault propagation. The size of the stress perturbations created by dislocations in this model, which ultimately control fault interactions, depend on the slip magnitude on the fault, which in turn is proportional to the elastic shear modulus, the fault aspect ratio (i.e. L/H) and Poisson's ratio. The redistribution of stress around such a dislocation is qualitatively similar to the pattern of redistribution of Coulomb failure stress around a rupture as shown previously in Figure 1.7, although derived from a different solution (Figure 1.14). Willemse et al. (1996) model fault or dislocation interactions at a range of overlap and separation distances in order to assess the role of spatial fault array geometries in controlling degrees of fault interaction. They also model the effects of varying 3D fault plane shape by varying the fault height parameter and thus the fault aspect ratio. Their results show that fault interactions will strengthen with increasing fault pair overlap, decreasing fault pair separation, and increasing fault height (or reduced aspect ratio). Strengthening fault interactions are defined as degrees of increase in the D_{max}:L ratios of overlapping faults and degree of profile asymmetry.

Willemse et al. (1996) claim to successfully model the broad displacement characteristics of an en echelon fault array on the Volcanic Tableland although they do not go into a rigorous test of their model results with field data. In this thesis I survey fault pairs and arrays over a wide spectrum of O:S ratios and thus am able to provide a proper quantitative test of the results of this model.

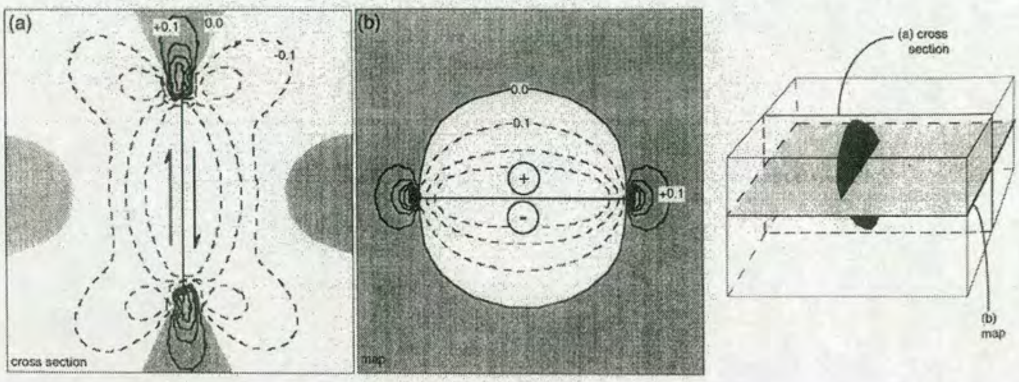

Figure 1.14. Figure 4 from Willemse et al. (1996) showing the redistribution of stress around a vertical circular crack in an elastic material in: a) cross section view, b) plan view and c) showing the 3 dimensional geometry of the crack.

Several features of this model are unrealistic with respect to real fault growth and are acknowledged by Willemse et al. (1996). These are, principally, the attainment of all fault displacement in one event and the lack of friction on fault surfaces. Discrepancies in results between field data analysis from this thesis and the model of Willemse et al. (1996) can thus be analysed with a view to these major differences and the theoretical problems they could generate in a model of fault interactions. For example, stress shadows in the rock mass generated by increments of fault propagation are likely to diminish in magnitude throughout the earthquake cycle, via the erosive effects of tectonic loading. Thus, by the time a fault has achieved its final dimensions, it is unlikely to have created stress perturbations in the rock mass that would be generated by a fault of its total size growing in one event. Given that faults on the Tableland have not grown in one event, the role of fault height may also play a very different role from that projected in the model of Willemse et al. (1996). For example, if the slipping patch on a fault is very small with respect to the total fault dimensions during incremental fault growth (Cowie and Shipton, 1998), the size of this patch will control the size of the stress perturbations generated during propagation, not the total fault height. This would mean, by default, that the range of fault interactions is significantly smaller (Cowie and Shipton, 1998) than were the whole fault slipping in one event. Modelling faults without friction is also clearly unrealistic, although the exact consequences of this are less clear as the issue of fault zone healing and the timescales involved remain areas of active research (e.g. Marone, 1998).

Gupta and Scholz (2000a) calculate stress drops generated around dislocations in an elastic medium and go on to predict interactions between dislocations with varying spatial geometries. The solution for stress drop used by Gupta and Scholz (2000a) is different from that used by Willemse et al. (1996) as they believe the 3D elastic crack model is inadequate at describing the tip region of a single fault. Gupta and Scholz (2000a) thus modify a 2D solution for the deflection of a horizontal surface for use in 3 dimensions. These authors find that as a dislocation or fault grows into an overlapping configuration, the stress reduction zone present around the body of the neighbouring structure will retard its growth. This results in fault propagation in length becoming increasingly retarded with increasing overlap whilst displacement can still accrue, thus generating profile asymmetry and elevated D_{max}:L ratios for overlapping faults. Gupta and Scholz (2000a) suggest there is a critical stress threshold, modelled at 200-300 MPa, beyond which overlapping faults will not propagate. This, they suggest, is equivalent to the crack shield seen for real faults in the Solite quarry by Ackermann and Schlische (1997).

Similar problems exist with this model as exist in the model of Willemse et al. (1996), i.e. the growth of faults in one event and the lack of fault zone friction. The former problem is particularly highlighted in the fact that this model produces stress drops of several hundred MPa as the stress drop scales with the total displacement on the fault, not a single growth increment. The stress changes actually generated in individual earthquakes are on the order of 0.1 MPa in nature (Scholz, 1982) and so it is unlikely that stress drops in the crust of several hundred MPa could ever be generated. Nonetheless, the broad results of this model are directly compared with field data from this project as, much like the model of Willemse et al. (1996), it provides a very useful end member scenario for fault interactions against which to compare real field data.

1.5 Summary

This thesis intends to focus on the following issues with a view to significantly improving our understanding of fault interactions and relay ramp development in an extensional setting.

- Quantitatively re-assessing the definition of an isolated normal fault using field data.

- Identifying fault interaction signals for multi-rupture faults with 10's of metres of displacement.

- Examining the role of spatial fault array geometries in controlling the strength of fault interactions.

- Examining the role of rock strength heterogeneity in affecting fault growth and obscuring a fault interaction signal.

- Comparing the results of static-elastic fault interaction models with real fault data and discussing implications for fault interactions over multiple earthquake cycles.

- Examining the fundamental controls on the geometrical evolution of relay ramps, in particular ramp dip direction, and assessing the controls on fault linkage.

Chapter 2 - Geological Setting

2.1 Introduction

This chapter introduces the principal field area of this study, the Volcanic Tableland, Eastern California, USA. The regional and local geology of the area are discussed together with the regional and local seismicity. Structural features affecting the Tableland, including normal faults, tectonic joints and volcanic fumaroles are then discussed in more detail.

2.2 Geological Setting

The Volcanic Tableland is the name given to a relatively flat area of welded ignimbrite and interbedded hybrid fall deposits (Wilson and Hildreth, 1998) occupying a section of northern Owens Valley in Eastern California, immediately north of the town of Bishop (Figure 2.1). The material, known collectively in the literature as the Bishop tuff (Gilbert, 1938), erupted from Long Valley caldera in a massive unroofing event approximately 762,200 years ago (+/- 4.7ka) (Sarna-Wojcicki et al., 2000). Ash from this event has been found in numerous localities across North America and in Pacific deep sediment core, covering an incredible area of approximately 2,000,000 km^2 (Sarna-Wojcicki et al., 2000). Owens Valley, forming the topographic depression into which much of the tuff settled, represents the westernmost downthrown block of the Basin and Range province. The valley is flanked on both sides by massive uplifted mountain ranges, the Sierra Nevada mountains to the west and the White-Inyo mountains to the east (Figure 2.2 and Figure 2.3). This fault-bounded valley structure is typical of the Basin and Range province that has formed by active extension and volcanism since at least mid-Miocene times.

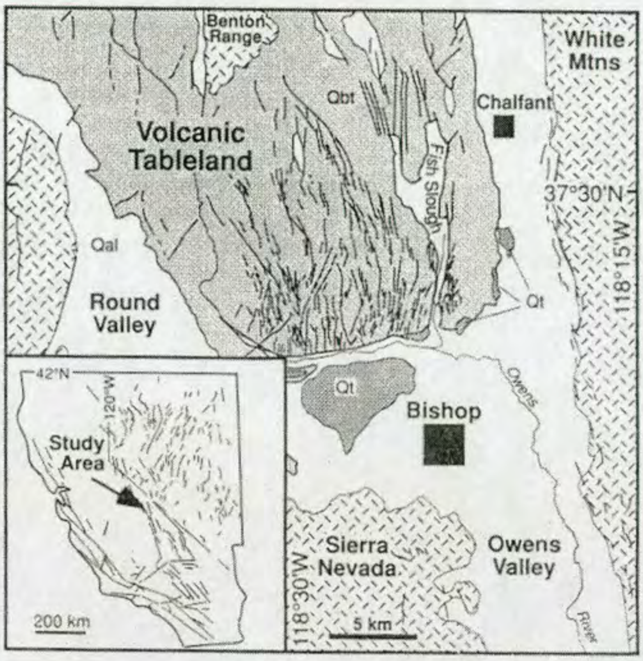

Figure 2.1. Location map of the Volcanic Tableland, north of the town of Bishop, in Eastern California, USA (after Dawers et al., 1993).

The cause of general Basin and Range extension is ambiguous although it may be partially in response to active mantle upwelling (Liu and Shen, 1998) as evidenced in the significant volcanism of this region. Other suggestions include a change in plate tectonic regime, specifically via a drop in compressive stress, as Farallon plate subduction beneath North America has been replaced with strike slip motion on the San Andreas fault (Zoback et al., 1981).

Owens Valley is generally believed to have formed by active Basin and Range style tectonics largely in the last 2-4 million years (e.g. Bateman, 1965; Bachman, 1978; Lueddecke et al., 1998). Bounding the west side of the valley lie the Mesozoic granitic plutons (Bateman, 1965) of the 4,000 metre high Sierra Nevada mountains, a by-product of the subduction of the Pacific plate beneath the North American continent. Immediately to the East lie the deformed Paleozoic meta-sedimentary sequences of the 4000 metre high White-Inyo Mountains.

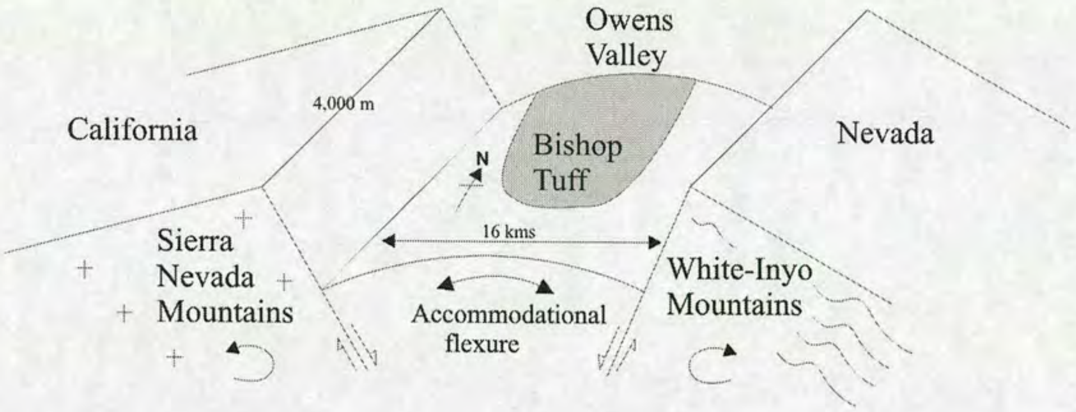

Figure 2.2. The regional geology of northern Owens Valley in the vicinity of the Volcanic Tableland showing the sense of motion on the bounding fault blocks.

Lueddecke et al. (1998) use changes in sedimentation style at the White-Inyo mountain range front in combination with $^{40}Ar/^{39}Ar$ dating techniques to infer the start of uplift of this range at around 3Ma. However, Stockli et al. (2000) date the start of the uplift of the White Mountains at 12 Ma, using (U-Th)/He thermochronometry. The steep footwall escarpments of the Sierra Nevada and White Mountain chains meet the valley floor at around 1500m and their continuing uplift and erosion is manifested in massive alluvial fans spilling into the valley.

The neotectonics of Owens Valley, part of the Eastern California shear zone (Figure 2.4, after Dixon et al., 1995), has been intensively studied as a result of several significant earthquakes in the last 2 centuries, i.e. the 1872 Lone Pine earthquake and the 1986 Chalfant Valley sequence (e.g. Lee et al., 2001b). Modern GPS techniques have been employed to monitor the current plate kinematics of the region and relate this to historical and ongoing seismicity and visible surface rupturing. Considered in its entirety, Dixon et al. (1995) show that the Eastern California shear zone accommodates 10.7 +/- 1.6mm/yr of right lateral strike slip motion and a minor component of extension oriented W-SW/E-NE at a rate of around 1mm/yr. Their results come from analysis of space geodetic data and late Quaternary geological data. Miller et al. (2001) use GPS data from 1993-1998 to constrain plate kinematics in this area and suggest the Eastern California shear zone is currently accommodating 13-14 mm/yr of dextral shear.

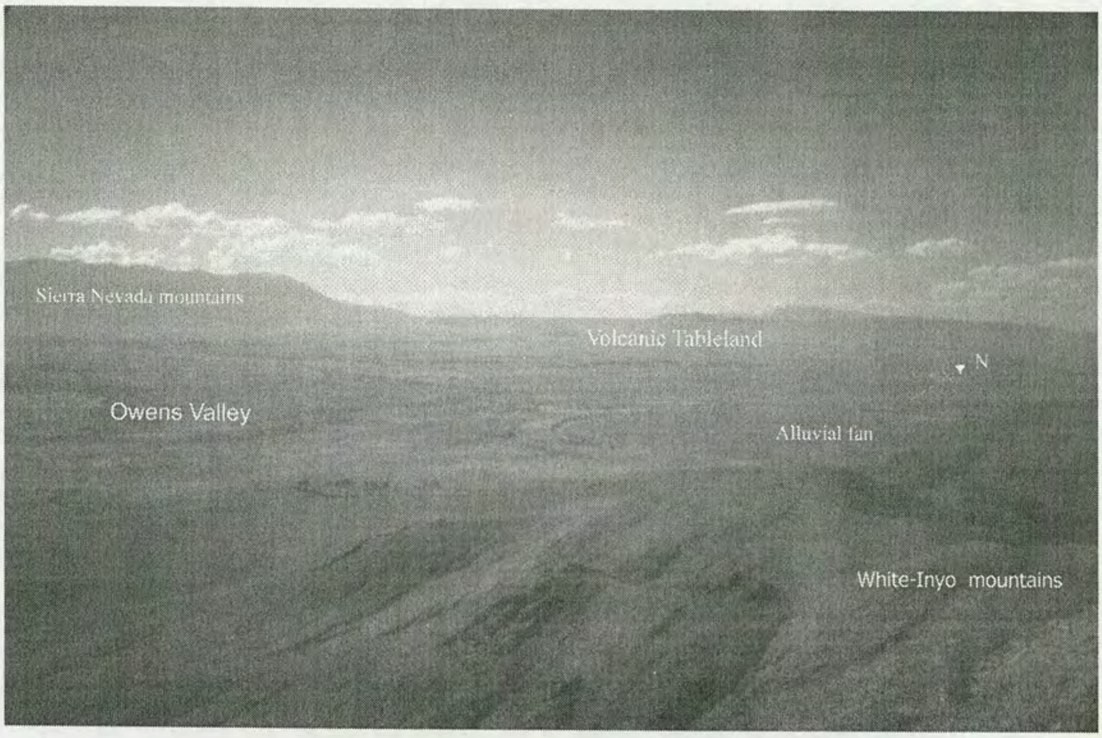

Figure 2.3. Photo of Owens Valley taken from the foothills of the White-Inyo mountains looking north-west across the valley toward the Volcanic Tableland and the Sierra Nevada mountains. The dark lineations visible on the Volcanic Tableland are normal fault scarps. An alluvial fan is also indicated at the base of the White-Inyo mountains.

The Owens Valley fault zone (OVFZ) and White Mountain fault zone (WMFZ) of Northern Owens Valley adjacent to the Tableland comprise two of the major strike slip faults making up this shear zone (Dixon et al., 1995).

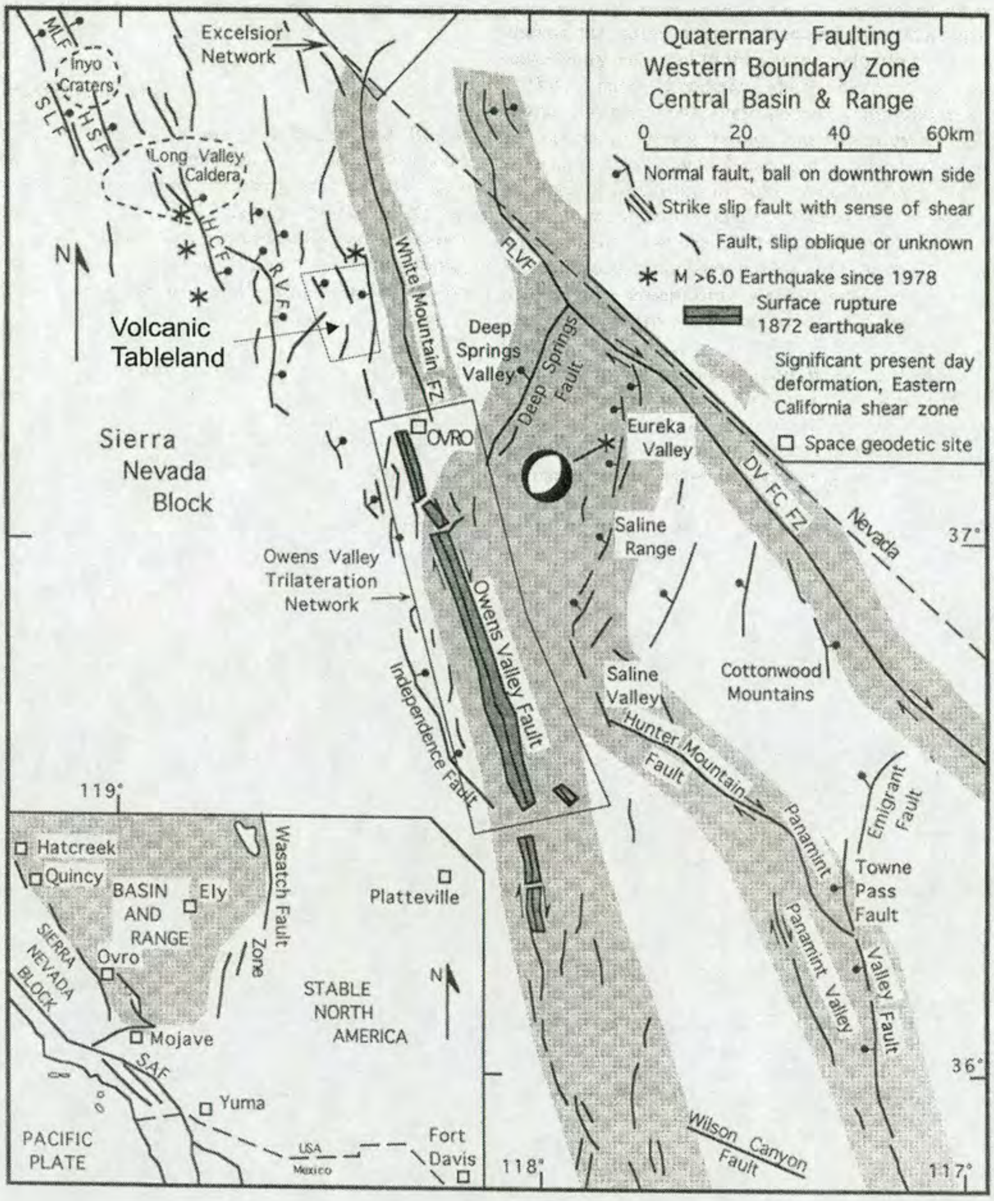

Figure 2.4. The Eastern California shear zone after Dixon et al. (1995). Major Quaternary faults and the extent of surface rupture from the 1872 Owens Valley earthquake are highlighted. An inset box shows the approximate location of the Volcanic Tableland.

In 1872, the Owens Valley earthquake of M7.5-7.7 created a surface rupture over 100km long (Beanland and Clark, 1994), through the towns of Big Pine and Lone Pine, south of Bishop. The ratio of vertical to horizontal offset along this structure is 1:6 with a right lateral sense of horizontal motion (Beanland and Clark, 1994). The Owens Valley earthquake was thus predominantly a strike slip event with a small dip slip component. In 1986, the Chalfant Valley earthquake of maximum magnitude M6.3 (Smith and Priestley, 2000) occurred in northern Owens Valley adjacent to the White-Inyo mountains and directly beneath the northern section of the Volcanic Tableland (e.g. Pachoco and Nabalek, 1988; Smith and Priestley, 2000). This event had no major ground breaking rupture associated with it although Lienkaemper et al. (1987) mapped numerous minor surface breaks in the weeks immediately following the earthquake. Their mapping showed abundant fracturing at the base of the White Mountains (WMFZ) with small right lateral displacements of 10's of centimetres. Vertical displacements in these examples were not clearly evident. In the northern Volcanic Tableland they found numerous examples of left stepping en-echelon crack arrays with up to 5cm of opening but no measurable oblique or vertical slip. They acknowledge that owing to the nature of the unconsolidated sands in which the fractures formed such offsets may not be preserved. Smith and Priestley (2000) analyse the focal mechanism solutions for 3 main shocks of the Chalfant Valley earthquake and resolve motion on conjugate strike-slip faults. The first event, M5.7, involves left-lateral motion on a NE trending fault from a depth of 7 km. The second, and largest, event (M6.3) involves right lateral motion on a NW trending fault dipping to the south-west, initiating at 10.5 km depth. The motion on the third event (M5.5), ten days after the largest shock, is not defined beyond being classified as a strike slip event. Both of the results for the first two events are in agreement with the motions previously proposed for the same events by Pacheco and Nabalek (1988). Dixon et al. (1995) conclude that both the Owens Valley and White Mountain fault zones currently record predominantly right lateral shear at rates of between 3 and 4mm/yr. Evidently the WMFZ has undergone a shift in tectonic style as it must have accommodated more dip slip motion in its earlier history in order to create the 3000m of relief currently seen on the White Mountains range front.

Extension within the northern Owens Valley, such as recorded in the normal faults of the Tableland, has been related to accomodational flexure of the valley between the actively rotating fault blocks of the Sierra Nevada and White-Inyo mountains (Pinter, 1995). Understanding the cause of extension in this area is clearly fundamental to any further studies of the character of the extensional faults. It is clear from the discussion of seismicity in northern Owens Valley that there is an anomaly between the predominantly strike-slip seismicity recorded beneath and adjacent to the Tableland and the extensional features on the Tableland surface.

Pinter (1995) notes that the modal trend of fault scarps on the Tableland is N10 to N20°W. He goes on to highlight that this is co-incident with the average trend of the 1872 OVFZ rupture at N17°W. The major ambiguity is obviously that the OVFZ is a mostly right lateral strike slip feature while the Tableland faults record no evidence for oblique motion other than the en-echelon arrangement of normal fault scarps. It is unclear whether right lateral strike slip motion at depth in a zone trending N10-20°W could create a population of en echelon normal faults at the surface trending approximately north south, though Bateman (1965) discusses this possibility. One possibility is that the extensional faults on the Tableland may not be responding to the tectonic regime at depth, merely recording the surface flexure of the Owens Valley between rotating fault blocks (Pinter, 1995).

Geological and geodetic evidence for the rotation of fault blocks bounding the Owens Valley shall be considered here in order to assess the flexural mechanism as a cause for normal fault development. Westward rotation of the Sierra Nevada block is demonstrated by Unruh (1991) based on field studies in the eastern Great Valley. Unruh (1991) finds late Neogene angular unconformities which vary in magnitude with time, correlable to progressive tilting of the Sierra Nevada block since approximately 5Ma at a rate of 0.28°/Ma. Unruh (1991) suggests the post Miocene rotation or tilting of the Sierra Nevada block is part of the general late Cenozoic uplift of the northern Basin and Range. Bounding the eastern margin of the Owens Valley, the White Mountains are by contrast suggested to be tilting to the east by at least 0.47°/Ma (Pinter, 1995 after Marchand, 1971). Pinter and Keller (1995) use a variety of field techniques to show that the Owens Valley itself is tilting to the east at between 3.5 and 6.1°/Ma. These techniques include analysis of paleo-drainage channel trends on the Tableland, uplift of dated river terraces to the south of the Tableland and the tilt of alluvial fan deposits at the base of the White mountains. Recent studies by Dixon et al. (2000) and Hearn and Humphreys (1998) suggest that the Sierra Nevada block is not only moving northwest at around 13-14mm/yr but also has associated minor counterclockwise rotation. Bennet et al. (1999) suggest significant counter-clockwise rotation may be occurring on the Sierra Nevada block from their velocity field study of the Western US. They acknowledge, however, that there are discrepancies between this conclusion and the conclusions drawn from the kinematics of active faulting in this region. Assuming some degree of counter clockwise rotation for the Sierra Nevada block and the opposite sense of rotation for the White-Inyo block, Figure 2.2 shows arrows indicating the general sense of motion on the ranges bounding Owens Valley.

In summary, current earthquake activity in the northern Owens Valley suggests deformation on conjugate strike slip faults trending obliquely to the normal faults at the base of the White Mountains and Sierra Nevada range (e.g. Smith and Priestley, 2000). This being the case, structures on the Volcanic Tableland must either be accommodating this motion via their en echelon arrangements, or are responding to a different stress regime than that dominating at depth. The flexural mechanism for extensional fault growth on the Tableland is the most convincing with the knowledge available at this time.

Geology of the Bishop tuff

The Bishop Tuff, in the vicinity of the Volcanic Tableland, consists specifically of reworked ash-fall deposits and partly welded ignimbrite (Wilson and Hildreth, 1997). Wilson and Hildreth (1997) split the basal fall deposits into 9 units with up to 5 metres of total thickness. These are particularly well exposed on Chalk Bluff road at the southern extremity of the Tableland. At this locality the fall deposits show minor extensional faulting although unfortunately the faults cannot be traced upward into the overlying ignimbrite owing to erosion. The overlying pyroxene bearing ignimbrites are around 100 metres thick in this location and unwelded for the most part becoming poorly to moderately welded in the top 10-15 metres (Wilson and Hildreth, 1997) In Owens gorge, on the western side of the Volcanic Tableland, the Bishop tuff can be seen to overlie poorly consolidated coarse granite conglomerates from the unroofing of the adjacent Sierra Nevada mountains. Beneath this level the stratigraphy cannot be directly observed. A basic log through the generalised observed stratigraphy of the southern Volcanic Tableland is shown in Figure 2.5. It is not possible to trace faults from the tuff into the underlying rock units although it is clear that the vastly different mechanical properties of a comparatively strong tuff unit and weak poorly consolidated sediments will have a significant affect on fault growth. The anticipated affect may be for displacement on a single fault within the tuff to be diffusely distributed on numerous minor structures within the underlying sediments although this cannot be directly demonstrated.

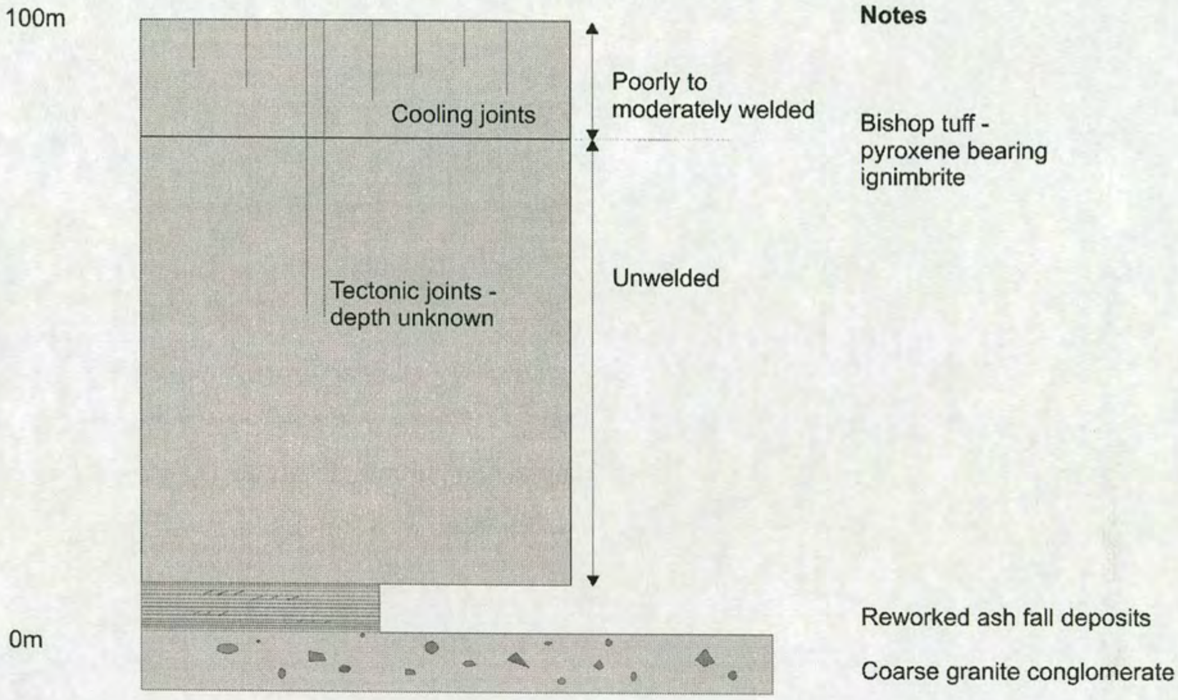

Figure 2.5. Generalised observed stratigraphic log through the geology of the Volcanic Tableland.

2.3 Structural features of the Volcanic Tableland

The Bishop tuff, immediately north of the town of Bishop, forms a broad table-like sheet across much of the Owens Valley, known as the Volcanic Tableland. The Tableland is a misleading name as its upper surface displays a variety of geomorphological features that render its surface far from smooth. These include a large population of normal faults, a set of conjugate tectonic joints, ubiquitous cooling joints, volcanic fumarole mounds and ancient drainage channels. The aridity of the Owens Valley, lying in the rain shadow of the Sierra Nevada, means that such structural features are particularly well preserved. Several of the structural features affecting the Tableland are now discussed in detail.

2.3.1 Faults and fractures

The Tableland surface is known to be cut by over 200 normal fault scarps (Bateman, 1965; Scholz et al., 1993; Pinter, 1995). These faults obviously post-date the deposition of the Bishop tuff although further age constraints are not currently available. Seismicity beneath the Tableland is ongoing and evidence can be found for very recent surface faulting in 2 different localities. In the Owens Gorge at the western edge of the Tableland, lineations in the tuff created by blasting during recent road construction are offset in an extensional fashion along listric normal fault zones (Figure 2.6). It could be argued that this offset may have been induced by blasting although the manner in which the failure has occurred still implies a release of local stress in an E-W extensional direction. Also at this locality, numerous mineralised veins, potentially hydrofractures, are exposed on cliff faces lining the gorge walls. The typical appearance and orientation of these features, as recorded with a compass clinometer, are shown in Figures 2.7 and 2.8. The steep, near vertical dip, and N-S strike of the majority of these tensile cracks is in keeping with the stress regime required to produce the faulting on the upper Tableland surface. Pinter (1995) also finds evidence for recent faulting on the Tableland in the form of a fresh, undegraded fault scarp with the pre-rupture soil profile preserved and up to 2-3 metres of displacement (Figure 2.9). Other localities with similarly preserved displaced soil profiles have also been identified elsewhere on the Tableland (N. Dawers, Pers.Comm., 2001).

Faults trend north-south to northwest-southeast and are typically arcuate in form, although occasionally linear. Arcuate faults are mostly convex to the East. Ferrill et al. (1999) suggest that the eastward convexity of many fault segments relates to the rollover of the tuff into the Fish Slough fault and the resultant accommodational extension of the crest of the rollover. Fault lengths range from several metres to several kilometres and have displacements of less than a metre to over 150 m, as is the case for the Fish Slough fault (Bateman, 1965; Ferrill et al., 1999). Linked fault arrays can attain over 10 kilometres in length.

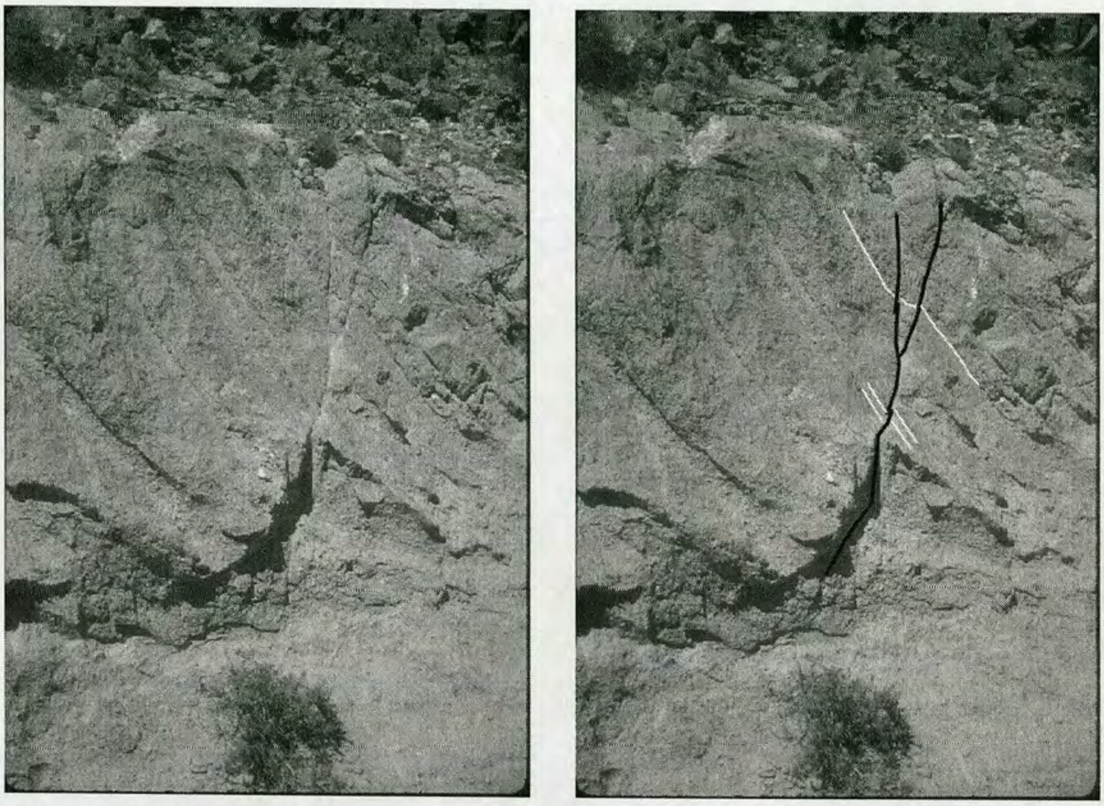

Figure 2.6. Scanned photo of recent normal fault offset in the Owens river gorge on the western side of the Tableland. The cliff face shown is approximately 3 m high and the fault trends approximately north south.

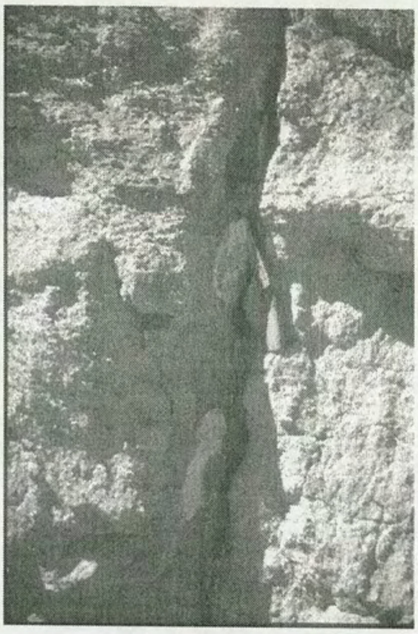

Figure 2.7. Example of a fracture in the Owens river gorge with white mineralised vein fill. The fractures trend approximately north south and are mostly sub-vertical. The knife shown is 20 cm long for scale.

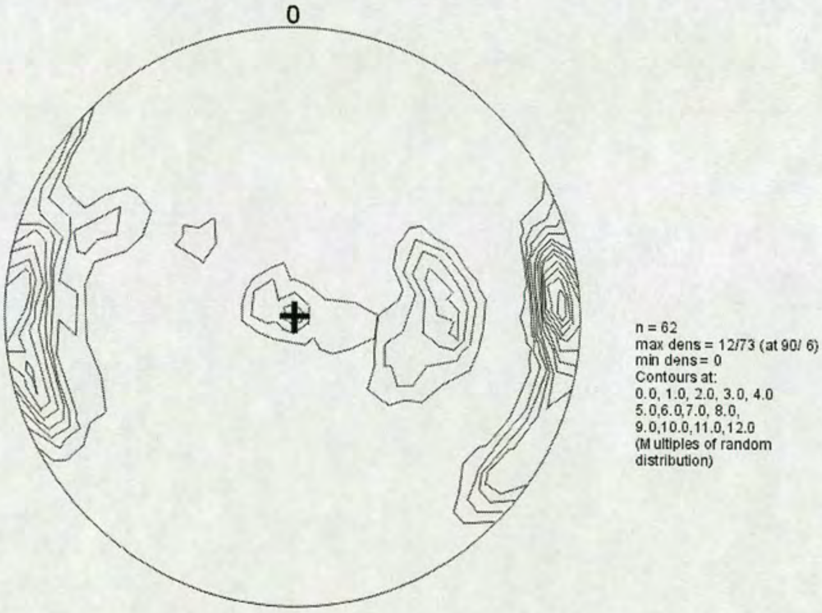

Figure 2.8. Stereoplot showing the orientations of mineralised veins in Owens river gorge as recorded with a compass clinometer.

Figure 2.9. Recent normal fault rupture on the Volcanic Tableland from Pinter (1995) with the pre-rupture soil profile clearly visible above the current ground surface.

All spatial configurations of faults are preserved on the Tableland, from isolated segments, to overlapping pairs separated by unbreached relay ramps, to fully linked fault pairs with breached relay ramps. The low strain setting of the Tableland of less than a few percent (Dawers et al., in revision) means that unlinked fault pairs predominate at this early stage of extension.

Fault scarp morphology varies from vertical cooling joint faces, exposed by collapse of the original scarp as tectonic slickensides are seldom seen, to rubbly talus slopes with large sand aprons where significant erosion has removed most or all of the original scarp (Figure 2.10). The volume of blocky material at the scarp base, or in adjacent hangingwall depocentres, can be used to estimate the degree of degradation of individual scarps. Paleo-drainage channels provide clear evidence of mass transport of erosional material away from fault scarps to basin lows. A lack of sediment beneath an individual scarp is therefore not a guarantee of minimal erosion *per se*. Scarps must be examined on a case by case basis in conjunction with analysis of the relevant drainage system to allow qualitative estimates of varying degrees of erosion. Further to this, holes can be dug in the sand depocentres to estimate minimum sediment thicknesses.

2.3.2 Joints

Analysis of aerial photos shows a pervasive set of conjugate joints affecting the upper tuff surface, most clearly seen west of the major en echelon array surveyed by Dawers and Anders (1995) (Figure 2.11). This joint set appears to affect much of the Tableland although becomes less evident in eastern areas. Joints strike approximately NNW and NNE. In many cases the joints are clearly oblique to the trend of major faults and faults can be seen to divert into joints. In other cases joint and fault trends appear to be almost co-incident. On the ground surface, away from major faults, the manifestation of these joints are rows of enhanced vegetation growth. These appear on aerial photos as dark, structural lineations. Proximal to major faults, typically on the footwall adjacent to the scarp, open fissures are sometimes present with opening displacements of between 20 cm and 4 metres. In cases where no surface opening is seen, owing to sedimentary cover, the joints are at least acting as fluid conduits from the depth of the water table in order to fuel extra vegetation growth. Joints typically have no discernible vertical offset apart from where subsequently utilised by faults.

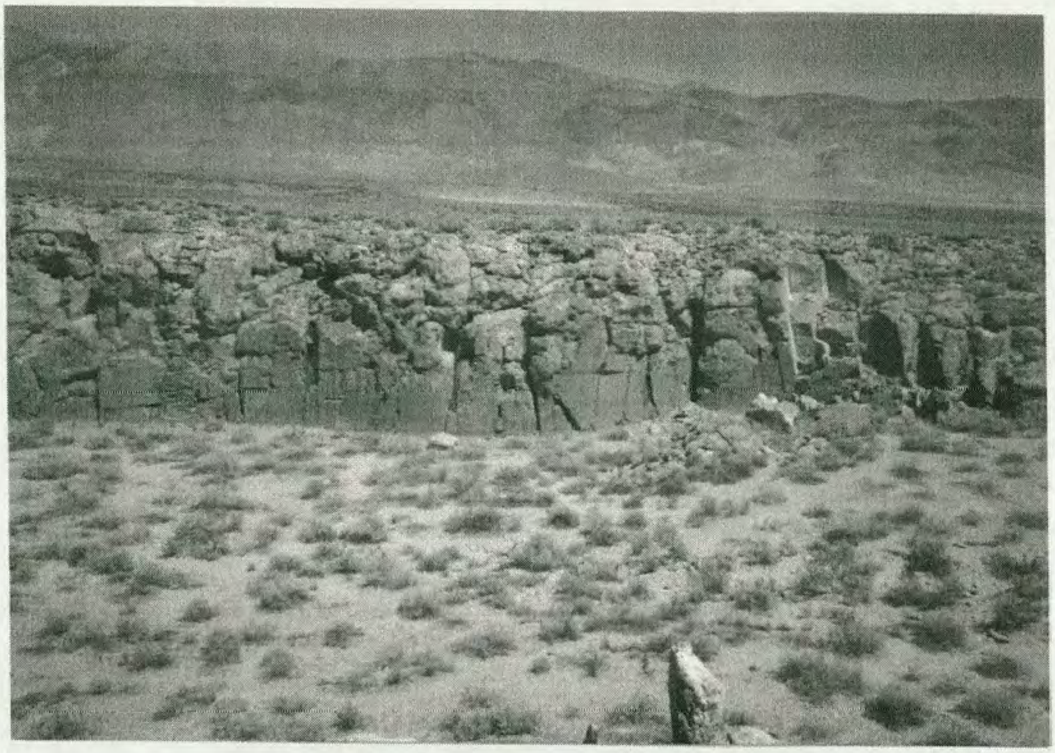

Figure 2.10. Examples of fault scarps on the Tableland with varying degrees of degradation, from vertical cooling joint faces in the upper image to rubbly talus slopes in the lower image.

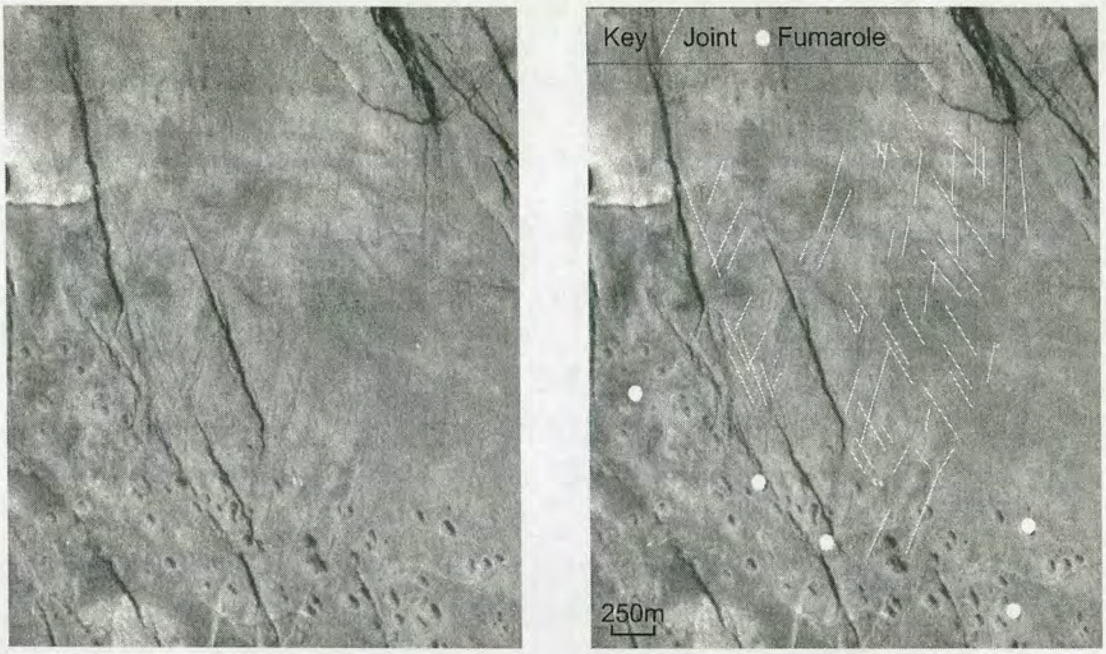

Figure 2.11. Aerial photo, with and without annotation, showing examples of joints and fumarole mounds on the upper surface of the Tableland. Fault tips can be clearly seen to deflect into joints in several cases.

The tectonic origin of this joint set is unclear. The deflection of normal faults into and along joints dates them as at least syn or pre-major extensional faulting. Peacock (2001) lays down numbered guidelines for determining the relative timing of joints and faults. These guidelines are applied to this setting in the order in which they appear in his paper and conclusions drawn from each: 1) The NNW conjugate joint trend is often co-incident or sub-parallel to major fault trends. This is particularly clear in the west-central region of the Tableland. The NNE conjugate joint trend is co-incident with several major fault trends in the south-west corner of the Tableland and with many jogs or deflections in major fault traces elsewhere. Faults trending N-S, specifically in southern and central regions of the Tableland are oblique to both of these joint trends. From this geometrical information it is not possible to say if the 2 sets of fractures, joints and faults, were formed in the same stress regime. However, it is possible to say that the theoretical stress regime one would infer to create conjugate jointing of this nature in plan view is not in keeping with the classic stress regime associated with extensional faulting (Figure 2.12). 2) Joints often show dilation around the fault zone as shown in Figure 2.13. These are probably tectonic joints utilising cooling joints on a small scale. This is most commonly found adjacent to the scarp on the footwall high of major faults. 3) Joints do not appear to cross-cut faults although in places do terminate against them. This termination is not taken to indicate that all joints post-date faults as suggested by Peacock (2001), since some faults clearly deflect into joints thus eliminating this possibility as an acceptable explanation. It is possible, however, that *some* joints post-date *some* of the faults. 4) Joints do not curve to abut faults in this setting. 5) Different frequencies of joints do appear to exist on either side of major faults, specifically a complete absence of joints in elliptical areas behind the footwall of several major fault segments. This may be interpreted as faults acting as a stress barrier to joint formation during or after fault growth as suggested by Peacock (2001). It may also be interpreted as faults closing pre-existing open joints via footwall uplift and localised compression. This closure would prevent joints from acting as fluid conduits from depth and they would not appear on aerial photos as linear zones of enhanced vegetation, albeit that they still existed, merely in a closed fashion. This is discussed further in Chapter 5. 6) Joint frequency does not increase toward a fault zone, and indeed joints are common in areas of no surface faulting. It has been suggested that joints in areas of no surface faulting may represent the surface manifestation of buried faults. It seems unlikely that the surface manifestation of a buried normal fault would take the form of a conjugate joint set with no displacement. Joints also show no evidence of strike-slip displacement despite the focal mechanisms of earthquakes beneath the Tableland showing strike-slip motion on conjugate NW-NE striking planes. The conclusions drawn from the above guidelines leave significant ambiguity in determining the relative timing of jointing and faulting in this setting.

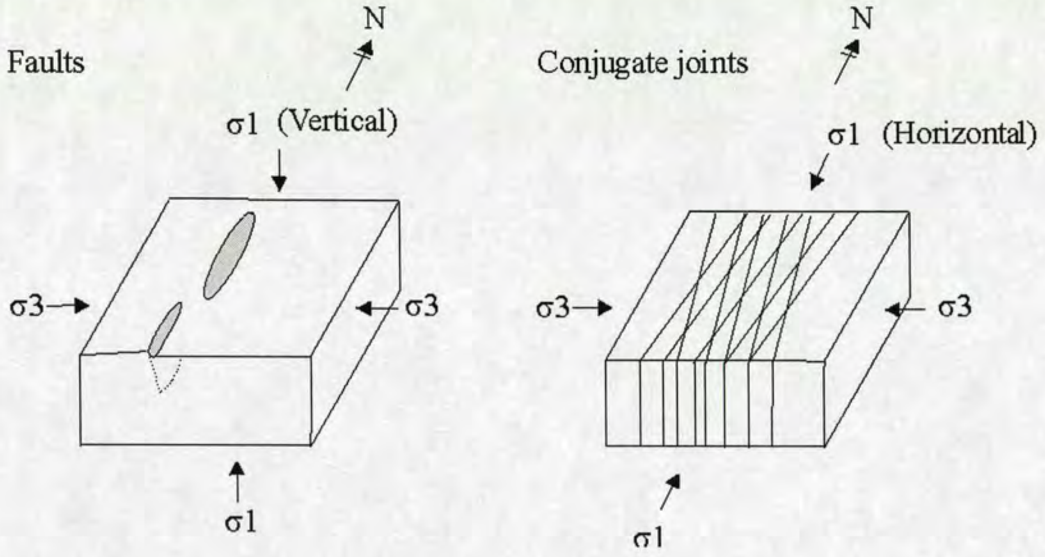

Figure 2.12. Classical orientation of stress regimes anticipated for extensional faulting and conjugate fracturing, both of which appear on the upper surface of the Tableland. The principal stress vector is vertical for extensional faulting and horizontal for conjugate fractures.

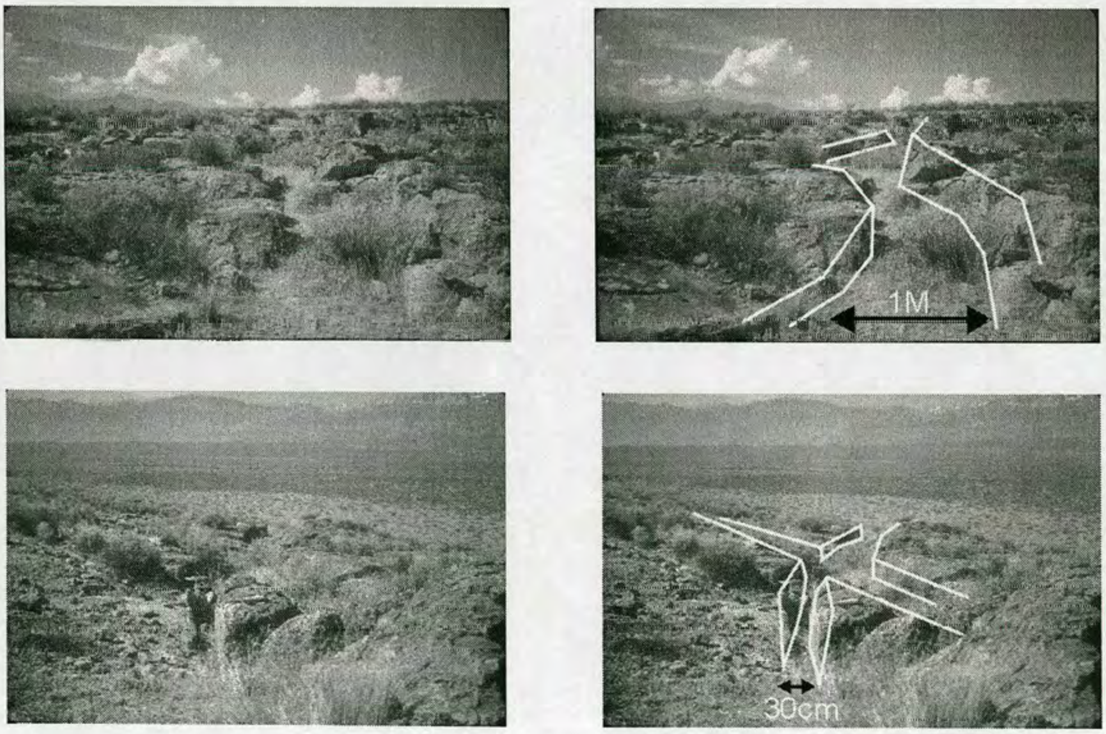

Figure 2.13. Scan of dilated conjugate joints behind the footwall scarp of a major fault segment.

As discussed in section 2.2, focal mechanisms for earthquakes beneath the Tableland suggest motion on NW trending right lateral strike slip faults and NE trending left lateral features (Pacheco and Nabalek, 1988; Smith and Priestley, 2000). It could be speculated that such a regime could shear and extend the Tableland simultaneously such that a riedel-shear type set of conjugate fractures, with varying amounts of opening displacement, could form prior to pure extensional slip taking over strain accommodation. This explanation requires the growth of joints to pre-date faulting, followed by a shift in the controlling stress regime and a move to pure extensional faulting. If this were the explanation it is not clear why some faults would grow obliquely to joint trends when joints provided zones of significantly low shear strength and thus an easy route for fault propagation (J. Crider, Pers.Comm., 2000). If joints pre-dated faulting this would also require the apparent absence of joints in footwall high regions to be explained by the closure of joints during footwall uplift. Alternatively, folding of the Tableland due to flexure (Pinter, 1995) or rollover (Ferrill et al., 1999), albeit relatively minor, could be responsible for fold inducing fracturing. Twiss and Moores (1992) show how 3 orientations of fractures can form on the crest of a fold, in a similar manner to the orientations of the conjugate joint set and major fault trend seen on the Tableland (Figure 2.14). The only other example of similar structural relationships in an extending setting, to the best of this author's knowledge, is from the Tanganyika rift, East Africa (Morley et al., 1990). An annotated fault map shows conjugate lineations on the footwall high of a major normal fault whose trend bisects the acute angle between the lineations. The tectonic explanation for these features is not discussed.

The phenomenon of faults growing along joints has been observed before. Trudgill and Cartwright (1994) discuss how normal faults in the Canyonlands area of southeast Utah reactivate an extremely pervasive joint set in extension. In this case, one of the conjugate joint trends matches the trend of the normal faults and so most faults have probably utilised joints during growth. In this setting joints also play a major role in fault linkage by providing pre-existing flaws for internal ramp deformation. The other interesting phenomenon in terms of the distribution of jointing on the Tableland, as mentioned previously, is the marked absence of such features in the footwall high regions of several major faults.

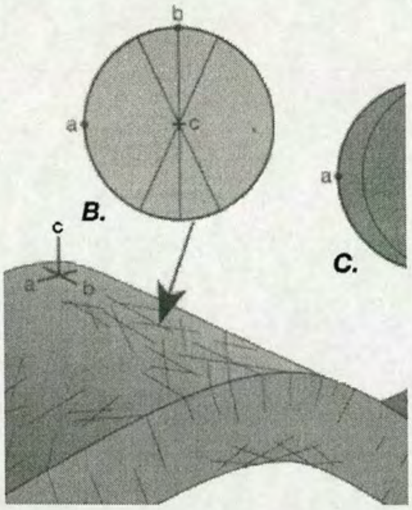

Figure 2.14. A potential fracture pattern on the hinge of a folded surface after Twiss and Moores (1992). Three orientations of fractures form simultaneously due to accommodational flexure of the surface on the outer arc of the fold hinge.

This can be most clearly seen on aerial photos to the west of the major linked array surveyed by Dawers and Anders (1995). This phenomenon shall be discussed in detail in chapter 5. Moore and Schultz (1999) document the closure of joints in areas of footwall uplift in the Canyonlands graben areas of SE Utah. The Canyonlands setting has the advantage of joint surfaces being highly visible on the ground, even when closed.

2.3.3 Fumarole mounds

The upper surface of the Tableland preserves a large number of dome-shaped mounds with up to 10 metres of positive relief from the local surface elevation (Figure 2.11). Bateman (1965) and Sheridan (1970) document these features and describe them as fumaroles, sites of degassing during the settling of the tuff sheet. Holt and Taylor (1998) conducted an isotopic analysis of the tuff in the vicinity of these features, as exposed in gorge walls, and found an enrichment in ^{16}O that could only be explained by the interaction of the tuff with meteoric water at high temperatures and over a short duration on the order of 10 years. This led to Holt and Taylor (1998) redefining these features as sites of intense and short-lived high temperature meteoric-hydrothermal events, equivalent to jets of steam escaping from the tuff sheet shortly after eruption. Some of this meteoric water would have come from the ancestral Owens Valley drainage network upon which the tuff was deposited. The fumarole mounds are well indurated and thus well preserved, particularly on the western side of the Tableland and will subsequently be shown capable of significantly affecting fault growth.

Chapter 3 – Surveying methodologies and fault survey data

3.1 Rationale

This chapter describes the general nature of faulting present on the Volcanic Tableland and introduces the surveying techniques utilised for the collection of structural data for this project. The faults selected for high-resolution surveys are identified on aerial photos and the survey data is subsequently presented. Fault data is shown in the form of displacement (D) versus along-strike distance profiles for en echelon arrays.

3.2 Overview of fault geometries on the Volcanic Tableland

The Volcanic Tableland preserves hundreds of normal fault scarps in a wide range of spatial configurations from relatively isolated segments to significantly overlapping fault pairs and multi-segment arrays. Faults generally trend north-south, often in left-stepping en-echelon arrays, and have segment lengths of 10's of metres to several kilometres with displacements of up to 100 metres (Dawers et al. 1993). Linked arrays can attain over 15 kilometres in length and 150 metres in displacement as is the case for the Fish Slough fault bounding the eastern margin of the Tableland (Ferrill et al., 1999). Much of the deformation is accommodated on 2 major left stepping arrays either side of the Casa Diablo road in the centre of the Tableland. Both arrays trend NNW but have opposite senses of throw and therefore form a graben, though the bounding arrays differ in length and location of D_{max}. Dawers & Anders (1995) surveyed the major linked array west of Casa Diablo road while part of the eastern array is surveyed in this project.

For this study, fault pairs and arrays were short-listed for surveying depending on their O:S ratios measured from aerial photos. In order to test the importance of fault proximity in influencing fault interactions it is necessary to choose fault pairs that display a wide range of spatial geometries. Imposing this stipulation is pre-requisite to asking one of the fundamental questions of this project: do closely spaced, or proximal, fault segments grow in a predictably different manner from isolated, or distal, ones? Fault scarp preservation was subsequently assessed during field reconnaissance and the best-preserved examples chosen for surveying.

Figure 3.1 shows an annotated version of a 1:25000 NAPP (No. 482-116, 7/5/87) aerial photo of the Volcanic Tableland. This figure shows faults surveyed in this study and faults surveyed in previously published work on the Tableland, specifically those faults surveyed by Dawers et al. (1993) and Dawers & Anders (1995). Some of the remaining faults are either too poorly preserved for high resolution surveying, or are affected by topographic complexities such as fumaroles which disguise the true fault profile shape and are thus discarded as surveying candidates.

3.3 Surveying methodologies

Two techniques have been employed for the high-resolution surveying of fault and relay ramp structures on the Volcanic Tableland owing to logistical reasons and equipment availability. These are use of a total station laser theodolite surveying instrument and use of differential GPS surveying. The two techniques are outlined in turn below and their relative merits discussed briefly.

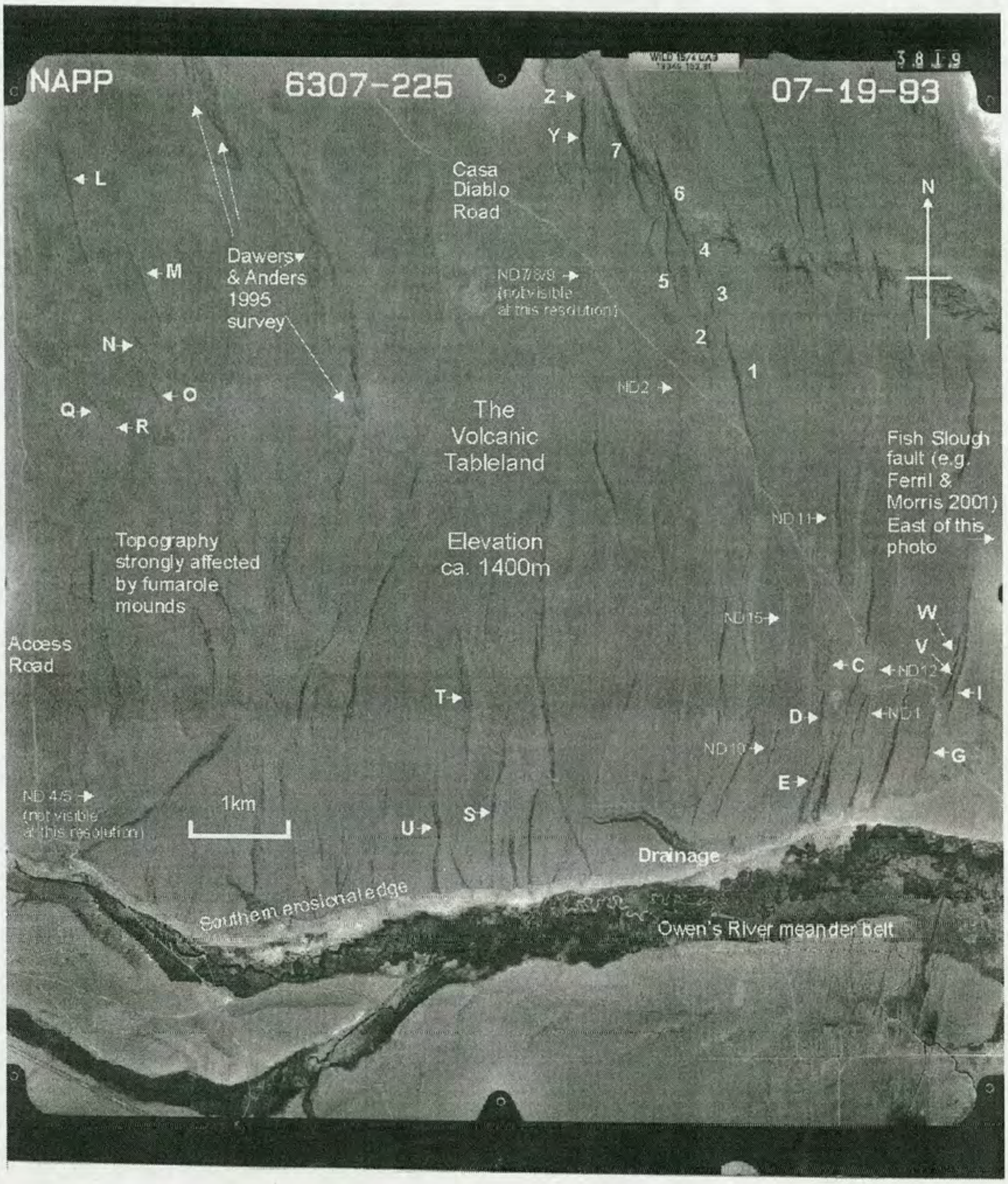

Figure 3.1. Annotated NAPP aerial photo of the Volcanic Tableland showing faults surveyed in this study and faults present in Dawers et al. (1993) (faults with ND label) and Dawers & Anders (1995). Note that several of the faults present in Dawers et al. (1993) are too small to be easily resolved on this scanned aerial photo. The Fish Slough fault (e.g. Ferrill and Morris, 2001) is to the east of this photo.

3.3.1 Total Station surveying

Total station surveying equipment is typically utilised in engineering projects owing to its mm scale accuracy, but for this project it has been employed for the high-resolution surveying of fault scarps and relay ramps. The equipment consists of a theodolite that sends a laser signal to a hand-held reflector, a telescope for focusing on the reflector and an electronic distance metre (EDM) to measure the distance travelled by the signal. The base station, incorporating the theodolite, telescope and EDM, is mounted on a tripod and the telescope is designed to rotate through 360 degrees in the vertical and horizontal plane (Figure 3.2).

In this manner it is possible to survey any remote point which is within line of sight of the base station within a distance of up to1-2 km. The surveying itself requires 2 people, one to hold a pole-mounted corner cube reflector at survey points, and the other to focus the theodolite on this reflector, send a signal and record the distance travelled by the signal. The design of the reflector is such that an incoming signal will be returned along its outward path irrespective of the angle of incidence. The location of a survey point is attained via the equipment calculating the horizontal and vertical angles through which the theodolite must be rotated to focus on the survey point and by sending a signal to the reflector to gauge its relative distance from the base station (Figure 3.3). The equipment internally transforms these values into a 3 co-ordinate location, stating the distance of the point from the base station in northing and easting co-ordinates and relative height. The total station set-up used is capable of attaining an accuracy of plus or minus 5 mm over a distance of 2 kilometres. This level of accuracy is more than adequate for a survey of this nature. Significantly greater components of error are introduced by the role of erosion, small scale (i.e. 10-20cm) roughness of the Tableland surface and scarp degradation that cannot be accurately quantified.

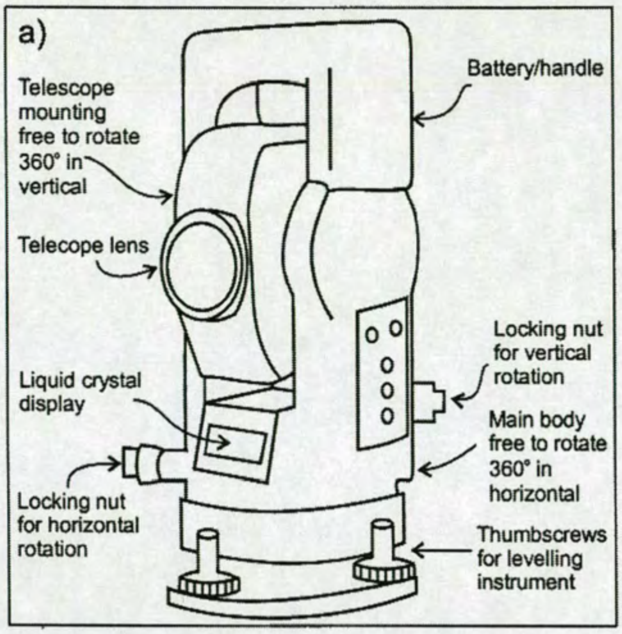

Figure 3.2. Topcon GTS-3B total station base station (after Shipton 1999, unpublished PhD thesis).

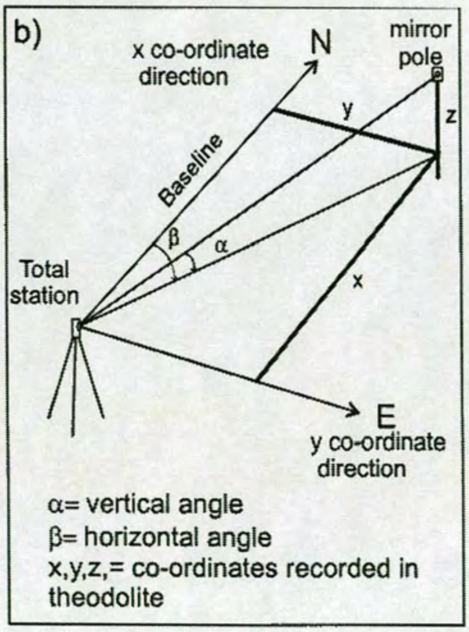

Figure 3.3. Angles and distances utilised by the base station to produce the co-ordinates of a survey point (after Shipton 1999, unpublished PhD thesis).

A survey of this nature requires the total station to be mounted on a tripod at a point within line of sight of some or all of the survey target. The tripod is carefully levelled using 3 thumb-screws and a bubble level on the instrument. The telescope must then be rotated through 360 degrees in the vertical plane to define up and down directions. The surveyors then choose a survey point that is directly north of the base station using a compass and survey in this point to define the northing axis. The instrument is then automatically capable of defining the easting axis. Relative height values must be corrected for the difference in height between the centre of the theodolite, as mounted on the tripod, and the height of the reflector pole. The height of the theodolite clearly varies with each movement of the base station owing to it being mounted on a tripod which needs levelled. The height of the reflector pole does not change throughout the field season for ease of subsequent data adjustments.

Fault scarps were surveyed for this project by walking along the top and bottom edge of the scarp, i.e. the footwall and hangingwall cutoffs, and stopping with the reflector approximately every 20 paces to record a data point (Figure 3.4).

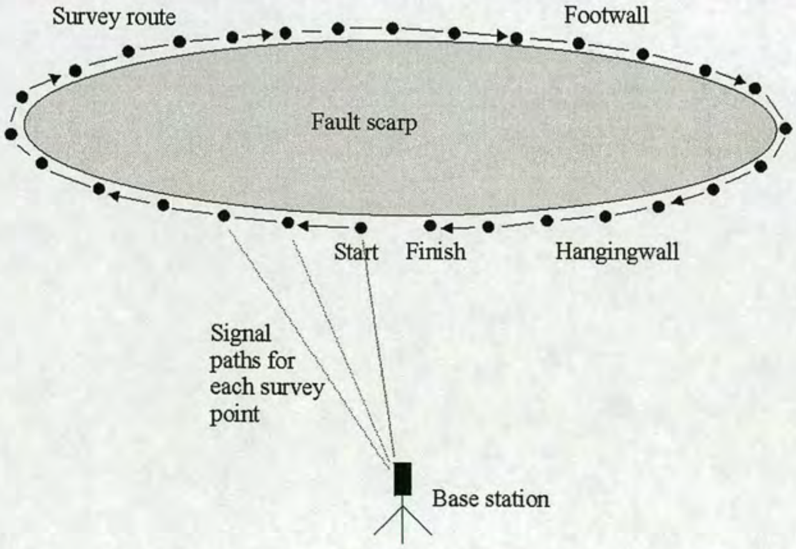

Figure 3.4. Surveying a fault scarp using total station equipment. The surveyor walks out a route around the footwall and hangingwall of the fault scarp, stopping at regular intervals to direct the reflector at the base station and record a location point.

Such is the length of many faults on the Tableland that one base station site is often insufficient to get line of site coverage of the entire fault. In this scenario the base station must be moved one or more times to cover the whole structure. In order to subsequently combine these data sets shot from different locations, it is necessary to survey 2 or more common points from each base station. This gives the relative distance of one base station from the other. When subsequently amalgamating datasets it is necessary to apply matrix rotations to the datasets so that the common points line up as inevitably there will be a degree of error introduced in defining the northing directions of different surveys with a compass. In this manner whole fault and fault array surveys can be built up into one dataset from multiple base station locations. The procedure for amalgamating multiple datasets from different base station locations is outlined in Appendix 1.

3.3.2 Differential GPS surveying

Global Positioning System (GPS) surveying is also carried out for this thesis. Differential GPS data collection and processing refers to the simultaneous collection of GPS data on 2 receivers whilst surveying, one completely stationary and one mobile, with subsequent processing of one data set against the other. This technique has a major benefit over total station surveys of requiring only one surveyor who is completely mobile and not restricted to a limited survey area.

The first stage in using this technique is setting up a secure base station at a location of very well known geographical co-ordinates and elevation. The base station site must have predictably high quality satellite coverage and be sited away from aerial obstructions. The receiver mounted on a tripod at this station acts as a stationary unit for receiving GPS data when the surveyor is in the field. This unit can be remote from the survey area by distances of up to several hundred miles although in this case was set up approximately 15 kilometres from the survey area. The satellite coverage in central California is generally superb. A minimum of 8-10 satellites were typically in appropriate orbital space to provide data during surveying for this project. This is significantly more than is necessary to ensure the minimum resolution of the equipment is achieved. The surveyor provides input to the stationary receiver detailing its exact co-ordinates and elevation, as discerned from an accurate map. The receiver can then internally calibrate itself from the position it believes it occupies via incoming satellite data, to its actual position as input by the surveyor. This calibration is ongoing as satellite orbits are eccentric around the earth, following a crude sinuous path, and thus the distance covered by incoming data from the satellite is constantly changing. As such, corrections made for atmospheric effects must change accordingly. Prior to a day of surveying, the base station receiver is told to record data between set times, co-incident with the minimum anticipated time for surveying that day. The mobile receiver needs only to be assigned its approximate co-ordinates at the start of a surveying session. Following this, a data recording speed is selected and surveying can commence. Data collection speeds must be equal for the base station and mobile receivers. The surveyor then walks out the structure of interest, stopping where necessary to make effective bookmarks in the data file at points of interest, or sub-divisions of the file, such as when mapping out a ramp-breaching splay. The main source of error at this stage is keeping the survey antenna at a constant distance from the ground surface during mobile surveying. Errors introduced by the surveyor at this stage seldom exceed 10 cm in height and are thus considered negligible for surveying of this nature.

Following surveying, data files are downloaded from the mobile and stationary receivers to a personal computer. Magellan MCOMM software was used for this task in this project. The mobile file is then post-processed against the stationary file, in this case using MSTAR software. This post-processing phase constitutes the 'differential' part of the process and provides the high-resolution data unattainable with a single receiver. The only input to the personal computer at this stage, other than the raw files, is the data collection speeds and an almanac file containing the known position of the base station. In processing the mobile file against the stationary file, highly accurate positional corrections made for fluctuations in satellite orbits and coverage, as executed by the stationary receiver, are applied to the mobile file, thus dramatically improving the resolution of the mobile data. In this way an accuracy in height of +/- 0.5m is generally achieved and plan view accuracy of 10's of centimetres.

This technique yields survey data in any number of global co-ordinate systems with corresponding heights either above sea level or at an arbitrary level as defined by the user. Plan view co-ordinates are recorded in UTM and heights relative to the base station for this study.

3.4 Fault survey sites and results

Survey data for faults labelled in Figure 3.1 are presented in this section. Each surveyed fault pair or array is shown in plan view in section 3.4.1 and in displacement vs distance format in section 3.4.2. Section 3.4.3 provides survey information relating to the dimensions and character of each fault in a tabular format.

3.4.1 Plan view survey sites

As stated in section 3.2, fault pairs and arrays were selected for surveying based upon displaying a wide range of O:S geometries and having well preserved scarps. Figures 3.5, 3.6 and 3.7 show enlarged sections of aerial photos containing the faults that met these requirements and were selected for surveying.

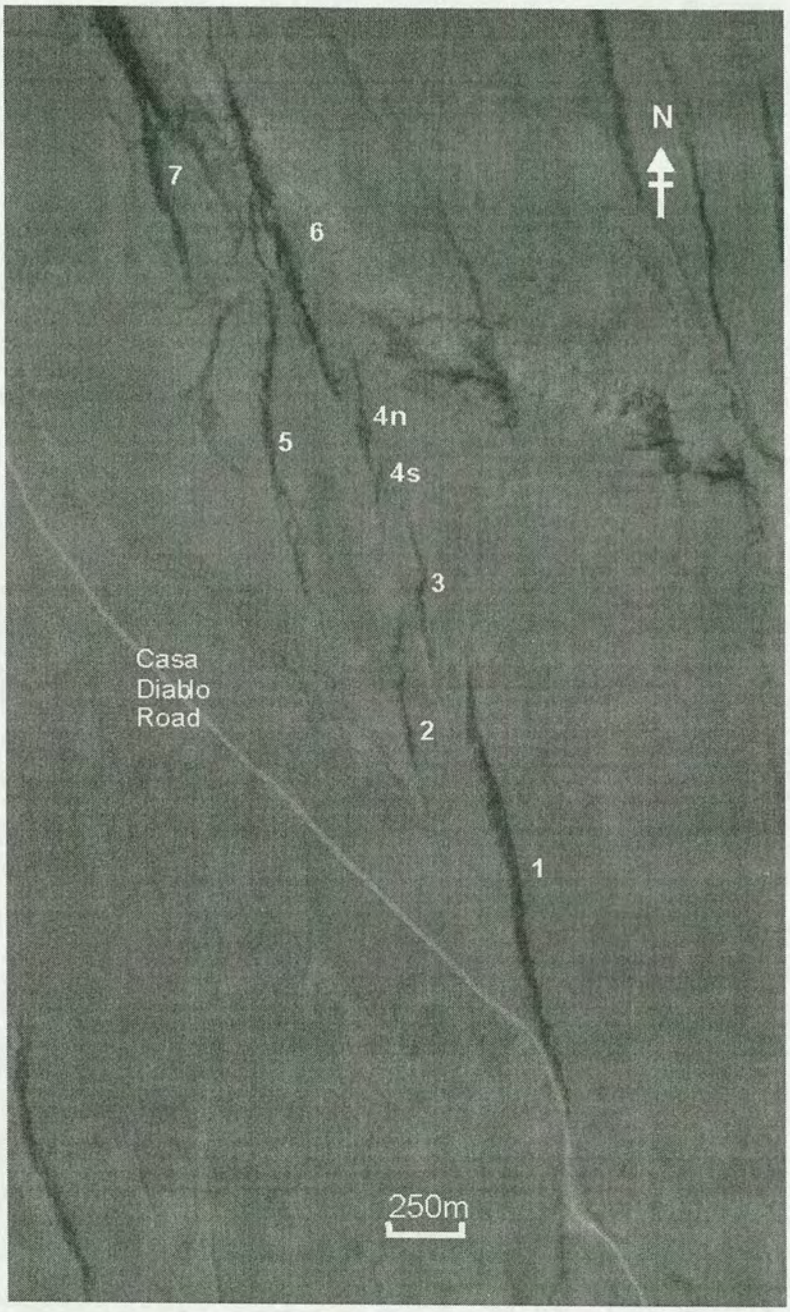

Figure 3.5. Enlarged section of Figure 3.1 showing faults 1-7 and the Casa Diablo access road that crosses the Tableland.

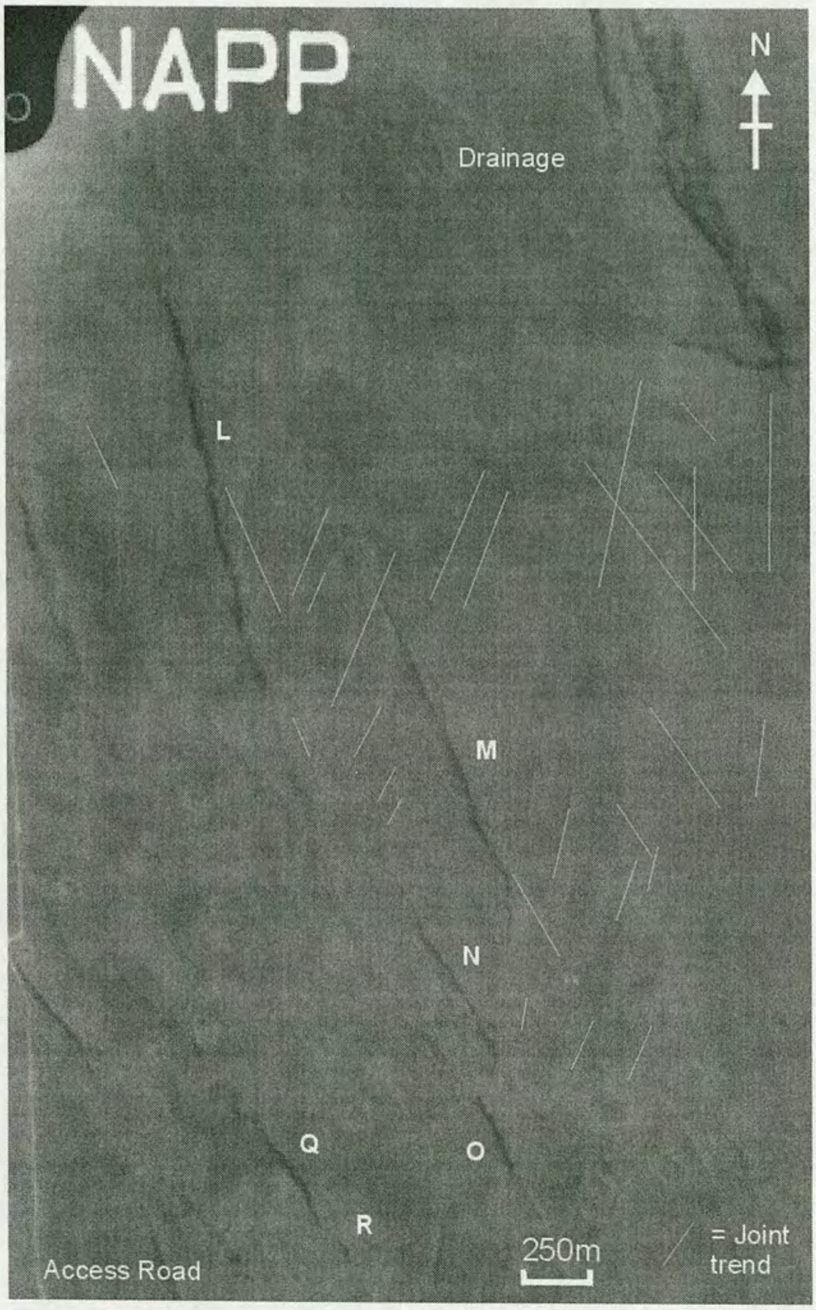

Figure 3.6. Enlarged section of Figure 3.1 showing faults L/M/N/O, Q/R and the trends of the conjugate joint set affecting much of the Tableland.

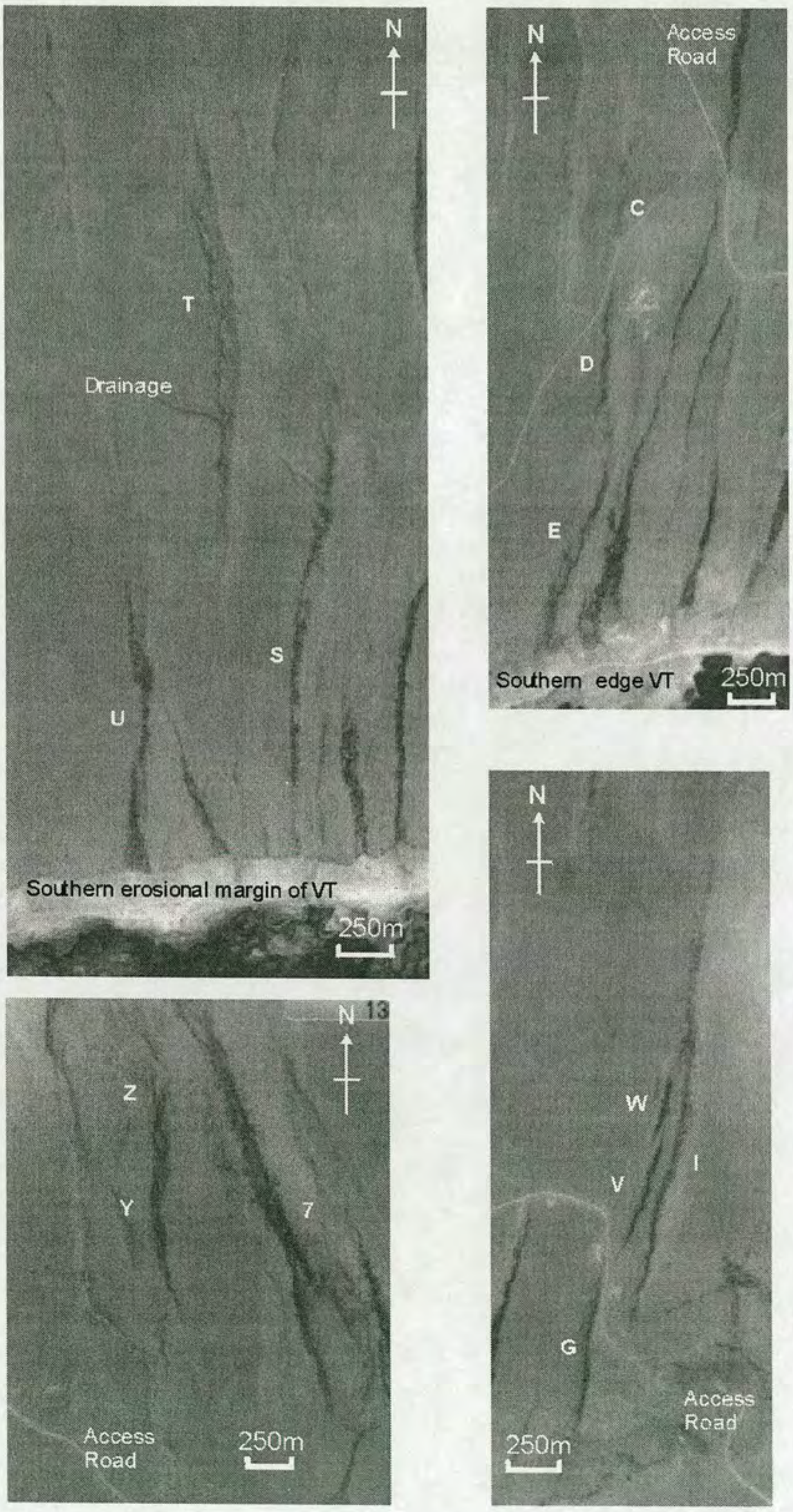

Figure 3.7. Enlarged section of Figure 3.1 showing faults C/D/E, G/I, S/T/U, V/W and Y/Z.

3.4.2 Displacement (D) vs distance data

Fault studies in recent literature typically include displacement vs distance along strike plots for the faults under study (e.g. Muraoka & Kamata, 1983; Walsh & Watterson, 1987; Peacock and Sanderson, 1991; Dawers et al., 1993; Cartwright et al., 1995; Bohnenstiehl & Kleinrock, 2000). These plots may be derived from 2 dimensional horizontal sections through a fault plane, as is typical in field data where a fault ruptures the ground surface, or be taken from a specific level on a fault plane resolved in 3 dimensions, such as from 3D seismic data. The value of such plots is in their depiction of how displacement is distributed along-strike of the fault. This, in turn, provides an important snapshot of the cumulative fault growth history to date. Knowledge of a fault's cumulative displacement pattern is the major tool available to geologists to imply the presence or absence of fault interactions during the growth cycle (e.g. Gupta & Scholz, 2000a). On the Volcanic Tableland, faults have ruptured the ground surface and so 2 dimensional displacement profiles can be constructed from high-resolution ground surveys. The rationale behind preparing displacement versus distance plots for all surveyed structures is to look at the variability in profile dimensions and shapes along fault pairs with different O:S ratios. This variability is analysed in detail in chapters 4 and 5. This type of study has seldom been undertaken, owing to the lack of field areas with sufficient quantity and quality of data.

Construction of displacement vs distance profiles

The construction of displacement versus distance profiles involves subtracting hangingwall survey points from their 'equivalent' footwall survey points at regular intervals along strike of the fault. In this way fault throw is being recorded as opposed to dip-slip displacement. Equivalent hanging-wall and footwall points sit on perpendicular sections across the strike of the fault (Figure 3.8). The difference in height between the 2 points represents the throw on the fault at any point on the trace. This value is then plotted against distance along the fault, measured from either tip. Figure 3.9 shows the displacement vs distance data obtained for all surveyed structures in this project, subdivided into their respective en echelon arrays.

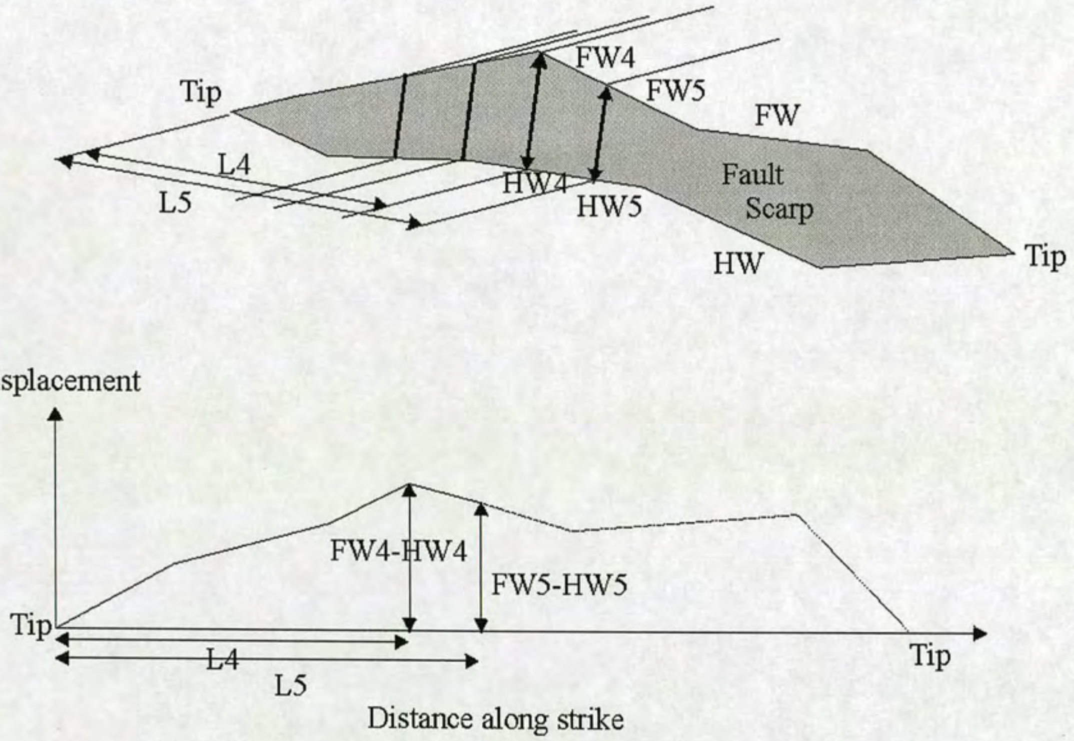

Figure 3.8. Sketch showing the methodology for the construction of displacement (D) versus distance plots. 'Equivalent' footwall and hangingwall points, e.g. FW4 and HW4, are subtracted along strike of the fault and plotted against their distance from the tip, e.g. L4. In this manner a complete displacement profile is constructed for the surveyed fault scarp.

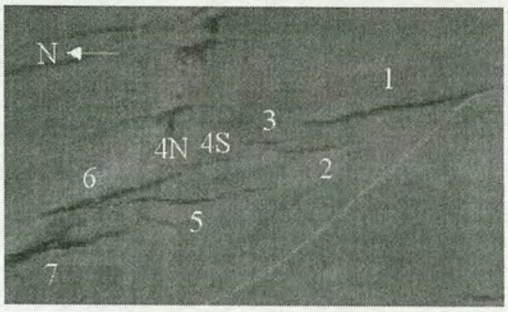

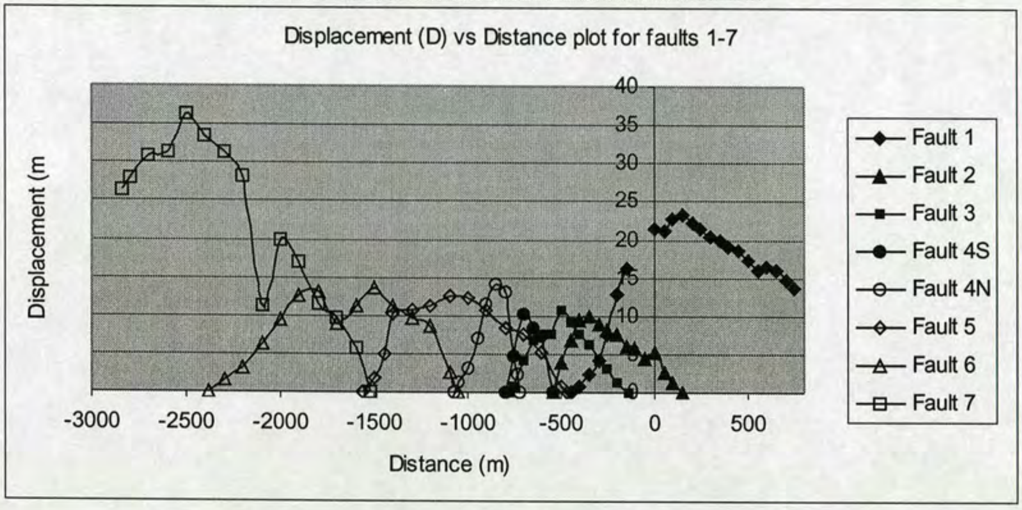
Displacement (D) vs Distance plot for faults 1-7

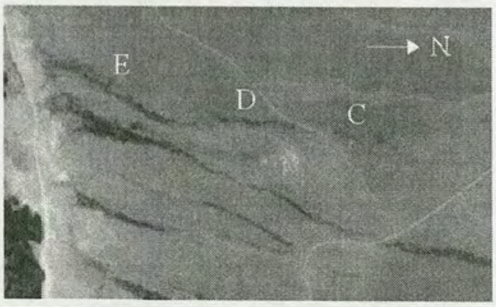

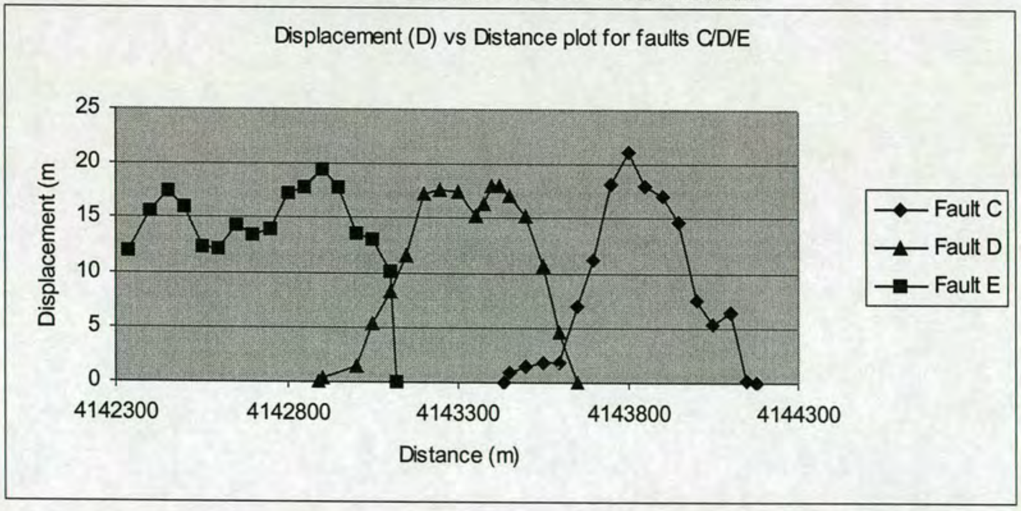
Displacement (D) vs Distance plot for faults C/D/E

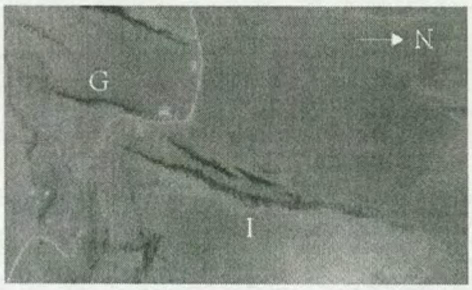
N
G
I

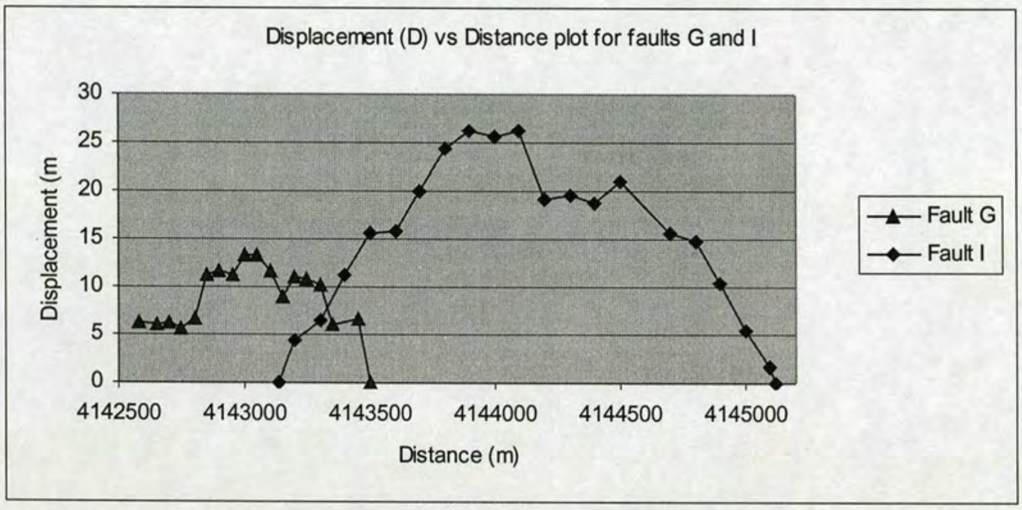
Displacement (D) vs Distance plot for faults G and I
Displacement (m
30
25
20
15
10
5
0
4142500
4143000
4143500
4144000
4144500
4145000
Distance (m)
Fault G
Fault I

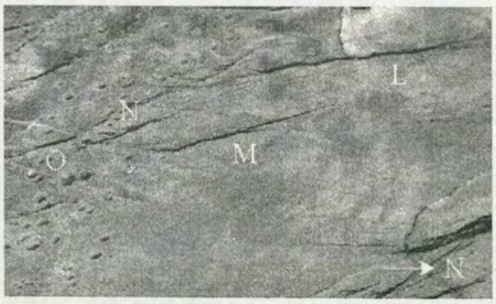
L
N
O
M
N

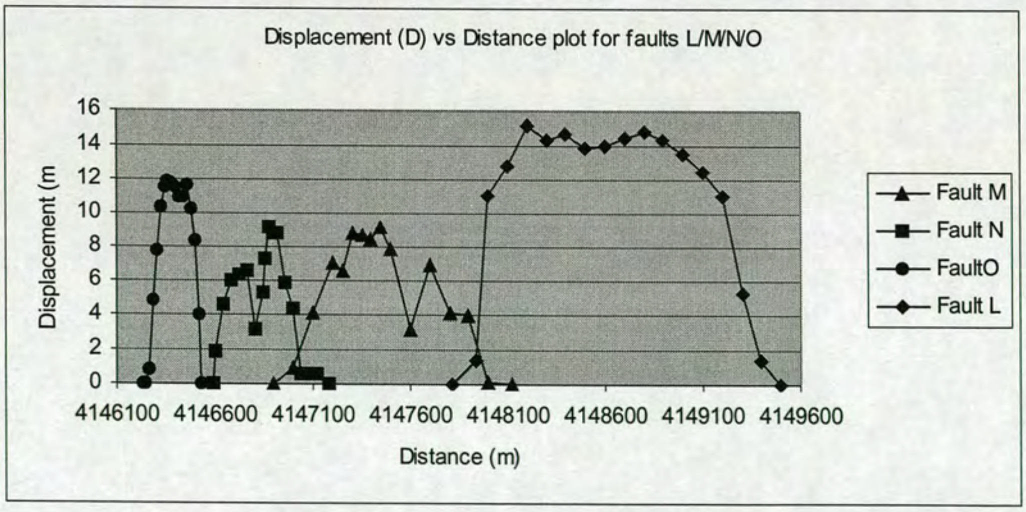
Displacement (D) vs Distance plot for faults L/M/N/O
Displacement (m
16
14
12
10
8
6
4
2
0
4146100
4146600
4147100
4147600
4148100
4148600
4149100
4149600
Distance (m)
Fault M
Fault N
FaultO
Fault L

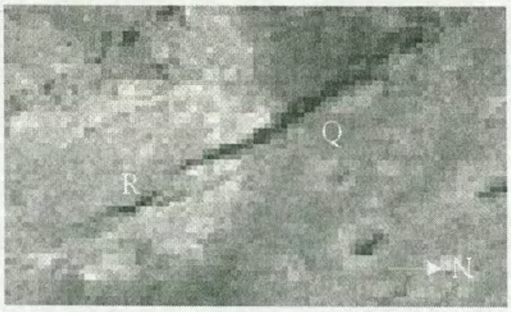
Q
R
N

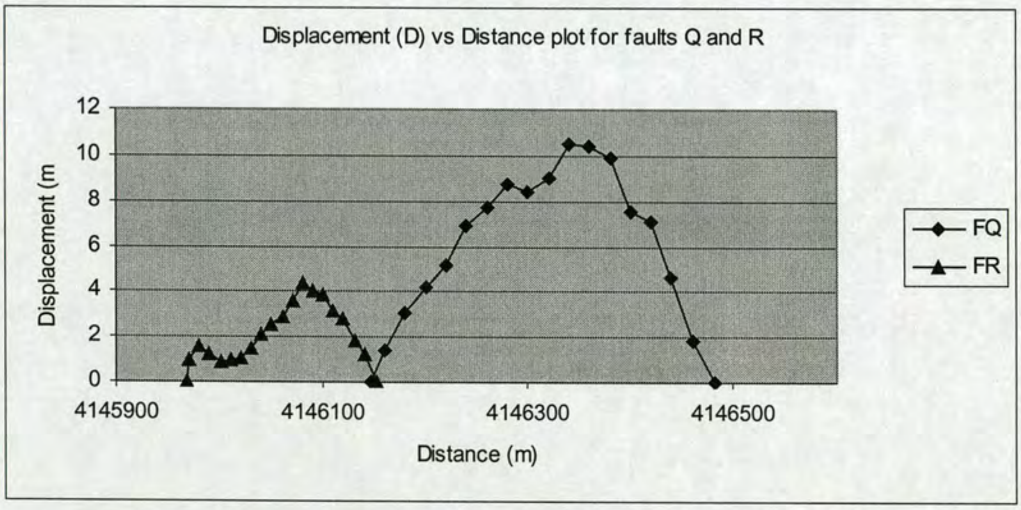
Displacement (D) vs Distance plot for faults Q and R
Displacement (m
0
2
4
6
8
10
12
Distance (m)
4145900
4146100
4146300
4146500
FQ
FR

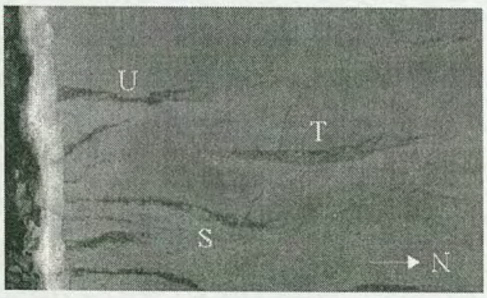
U
T
S
N

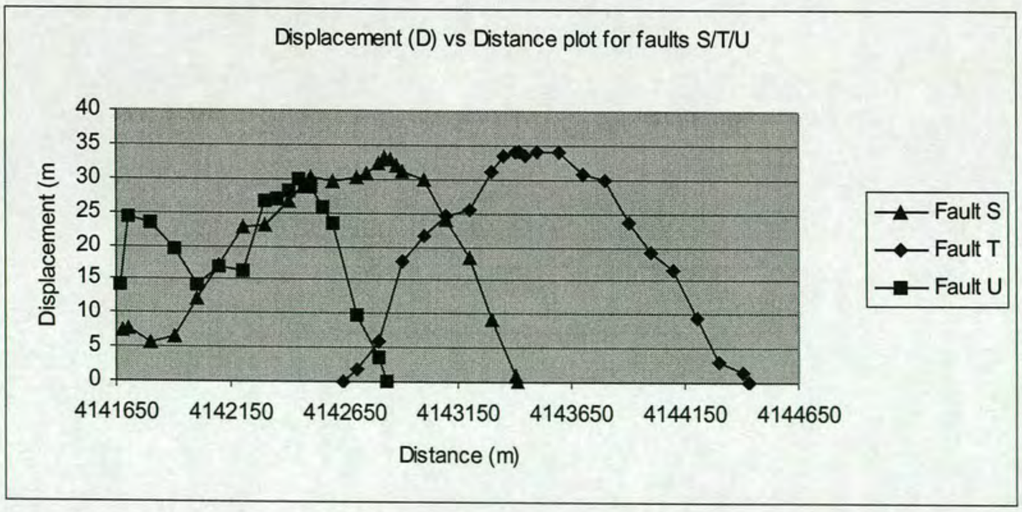
Displacement (D) vs Distance plot for faults S/T/U
Displacement (m
0
5
10
15
20
25
30
35
40
Distance (m)
4141650
4142150
4142650
4143150
4143650
4144150
4144650
Fault S
Fault T
Fault U

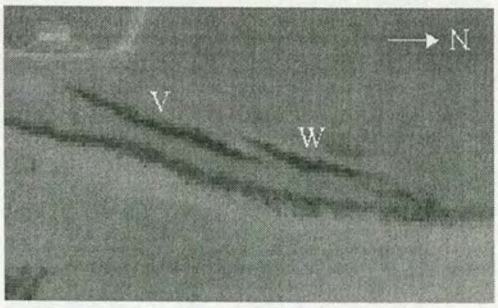

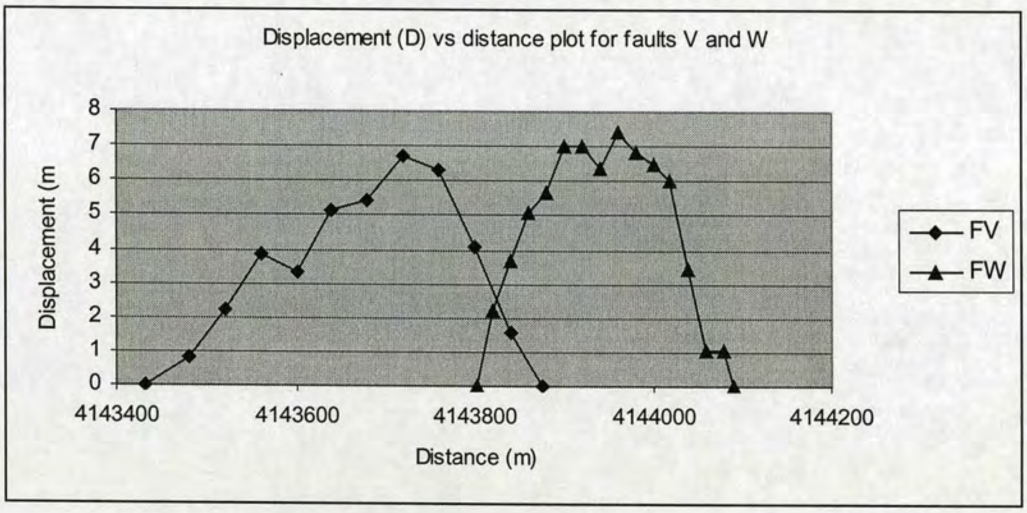
Displacement (D) vs distance plot for faults V and W

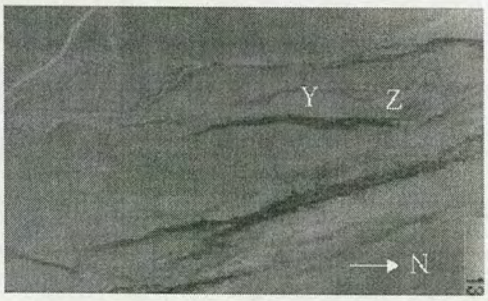

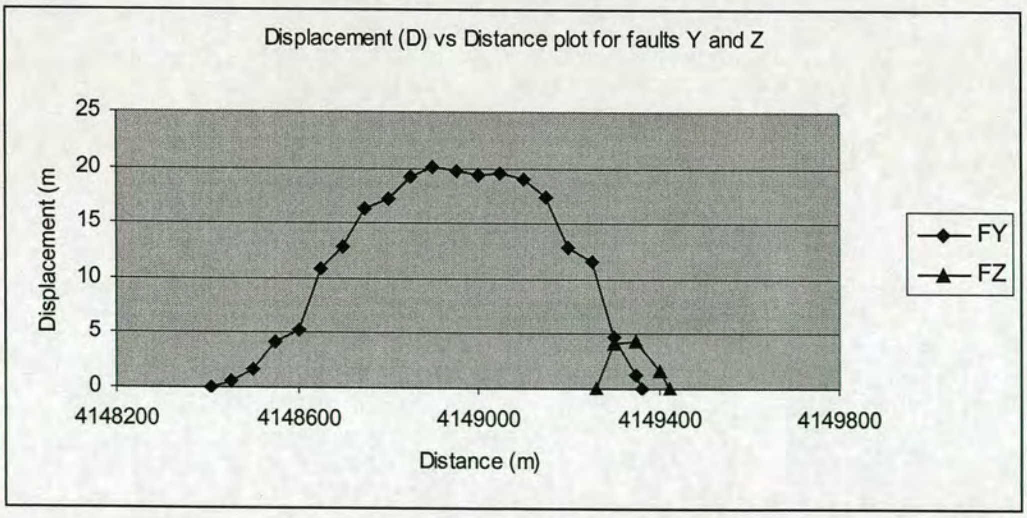
Displacement (D) vs Distance plot for faults Y and Z

Figure 3.9. Displacement (m) vs distance (m) plots for all surveyed faults. Annotated aerial photos are shown above each plot to show the surveyed faults and the plot orientation with respect to the ground.

3.4.3 Table of fault parameters

Fault*	Length	Dmax	Notes
F1	1254	23.2	Unlinked
F2	616	9.95	Unlinked
F3	537	10.1	Partially breached ramp between F3/F4
F4	441	7.8	Composed of 2 linked segments
F5	943	14.05	Partially breached ramp between F5/F6
F6	1068	12.1	Composed of 2 linked segments
F7	-	-	Partially breached ramp between F6/7
FC	725.9	21.1	Unlinked / Possible interaction with joint
FD	865.1	18.1	Unlinked / Interacts with joint
FE	-	-	Intersects southern erosional edge of VT
FG	-	-	Intersects southern erosional edge of VT
FI	2025	26.2	Unlinked
FL	1678	15.2	Unlinked / Interacts with joints
FM	1279.2	9.1	Unlinked / Interacts with joints
FN	644	9.2	Unlinked / Interacts with joints
FO	300.1	11.8	Unlinked / Interacts with fumarole
FQ	385.1	10.5	Unlinked / Interacts with fumarole
FR	205.5	4.4	Unlinked
FS	-	-	Intersects southern erosional edge of VT
FT	1795	34.2	Unlinked
FU	-	-	Intersects southern erosional edge of VT
FV	468.2	6.7	Partially breached ramp with FW

FW	303.6	7.4	Partially breached ramp with FV
FY	960	20.1	Linked with FZ
FZ	170	4.3	Linked with FY
ND10	696	8.4	Isolated (see discussion in Ch4)
ND15	866	8.3	Isolated (see discussion in Ch4)

* all faults surveyed for this project apart from ND10 and ND15 which were surveyed by Dawers et al. 1993.

Chapter 4 – Defining fault growth in isolation and assessing controls on fault profile shape

4.1 Rationale

In order to determine the role of fault interactions in modifying displacement profiles, this chapter begins by quantitatively re-assessing the definition of fault growth in 'isolation'. In this way, truly isolated fault structures on the Tableland are identified and their profile shapes can be compared with faults that are believed to be interacting. This comparison includes analysis of profile symmetry, tip gradient magnitudes and D_{max}:L ratios of individual structures. If faults grow differently when influenced by neighbouring structures this should become apparent. The role of rock strength heterogeneity in affecting fault growth is simultaneously analysed.

4.2 The definition of an isolated fault

High-resolution displacement profiles obtained from interacting fault pairs have the potential to be reliably compared with those of isolated faults from the same setting. Both sets of faults have grown under the same general set of rock mechanical and boundary conditions. In sub-surface studies this guarantee can often not be made as unresolved structures and lithological heterogeneities can cause unpredictable changes in fault profile shapes. Before commencing a comparison of potentially interacting profiles with isolated profiles it is necessary to strictly define what is meant by an isolated fault. Qualitatively, the term isolated is used to imply that a fault that has grown without the influence of any neighbouring structures. By inference, it must therefore be separated from neighbouring structures by sufficient distance that the structures are not aware of each other. Quantitatively, few studies have been undertaken to discover what this critical distance may be, or how it scales with fault size. Indeed, this fundamental gap in understanding provided part of the motivation for this thesis. It is obviously highly desirable to put constraints on the distances over which normal faults can communicate in order to improve our understanding of the evolution of extensional settings.

4.2.1 Previous work on the definition of fault growth in isolation

One study of this kind, containing the most data in the literature including natural fault data, was undertaken for strike slip faults by An (1997). This paper included data from laboratory derived strike slip faults (after An and Sammis, 1996b), natural faults from geological maps and earthquake data from Knuepfer (1989). An (1997) asserts that the state of stress in the overlap zone between 2 faults is related to the length of each fault, i.e. the dimensions of the zones of perturbed stress ahead of a growing fault scale with the fault length. This provides the justification for seeking a relationship between likelihood of fault linkage and the total fault pair length (L_t), i.e. the summed length of the individual faults. An (1997) concludes that the vast majority of faults will not link if the separation distance is greater than 0.1* L_t. The relationship is originally seen for lab data, where no linked faults have separations of $> 0.1\ L_t$. For natural faults, 98% of the data agree with this relationship, as do 93% of the earthquake rupture data. The author also notes that longer faults generally have longer link distances than small faults. This is used to confirm that the total length of the faults in question controls the state of stress in the overlap zone. Martel (1990) also notes that strike-slip faults in granite of the Sierra Nevada, California, link over greater distances with greater fault length and displacement. By inference, from the work of An (1997), a strike-slip fault separated from its nearest neighbour by $> 0.1\ L_t$ is implied to be growing in isolation.
Gupta and Scholz (2000a) compare isolated and interacting normal fault profiles from the Solite Quarry making partial use of An's (1997) definition of isolation in selecting their isolated faults. In their study, the critical threshold for fault interaction to occur is increased to separation distances of $<15\%\ L_t$. This is done to match the conclusions of Willemse (1997), who finds that faults in his elastic static-crack interaction model are unlikely to interact significantly at separations of $>12.5\%$ L_t for a given fault aspect ratio. Interaction is defined as an increase or decrease in propagation tendency as induced by a neighbouring fault. Gupta and Scholz (2000a)

not only impose a critical separation distance on their selection of isolated faults but also insist on the profiles being approximately symmetrical. This relates to the fact that profile asymmetry is assumed to be a classic indicator of fault interactions. Gupta and Scholz (2000) disregard profiles if they are asymmetrical, irrespective of their separation distance from a neighbouring fault. In this project, no *a priori* assumptions are made on the critical distance over which interactions may occur between neighbouring faults as determining this distance is one of the main goals of the study.

In order for 2 overlapping faults to interact one assumes that the zones of perturbed stress ahead of and around propagating fault tips must overlap. If one accepts the postulate that the perturbed stress field around a propagating fault tip is proportional to the length of the fault (An, 1997), one can assume that the state of stress in a region of fault overlap is proportional to the combined lengths of the overlapping faults. This is the assumption made and partially confirmed by An (1997).

4.2.2 Blind test on the role of separation distance in fault interactions

It is of interest to test, in an effectively 'blind' fashion, whether separation distance does indeed play any role in long term fault interactions as argued by An (1997) and Gupta and Scholz (2000a) and implied by the model of Willemse (1997). It should be remembered that the normal faults studied by Gupta and Scholz (2000a) are cm-scale features, very much smaller than the faults studied on the Tableland. The study by An (1997), meanwhile, was based solely on strike-slip faults. In order to assess the role of separation distance in fault interactions, a proxy for the 'interaction status' of a fault must be chosen. In this case D_{max}:L ratios are chosen as the proxy, as the complexity of displacement profiles on the Tableland often makes asymmetry an ambiguous parameter, as will be demonstrated later in this thesis. More specifically, profile shape fluctuations created by segment linkage, fault interaction at both tips and fault interaction with heterogeneities can make profile symmetry unpredictable.

It is insufficient to merely plot D_{max}:L against the separation distance between a fault pair as the separation distance must firstly be scaled relative to the length of the faults in question. For example, two 100m long faults may not be aware of each other over a separation distance of 100m, but two kilometre long faults may well be. For this reason, separation distance is normalised by the summed lengths of the two faults in question, i.e. L_t, and then plotted against D_{max}:L. Figure 4.1 shows D_{max}:L plotted against S/L_t for data from this project and data from Dawers et al. (1993).

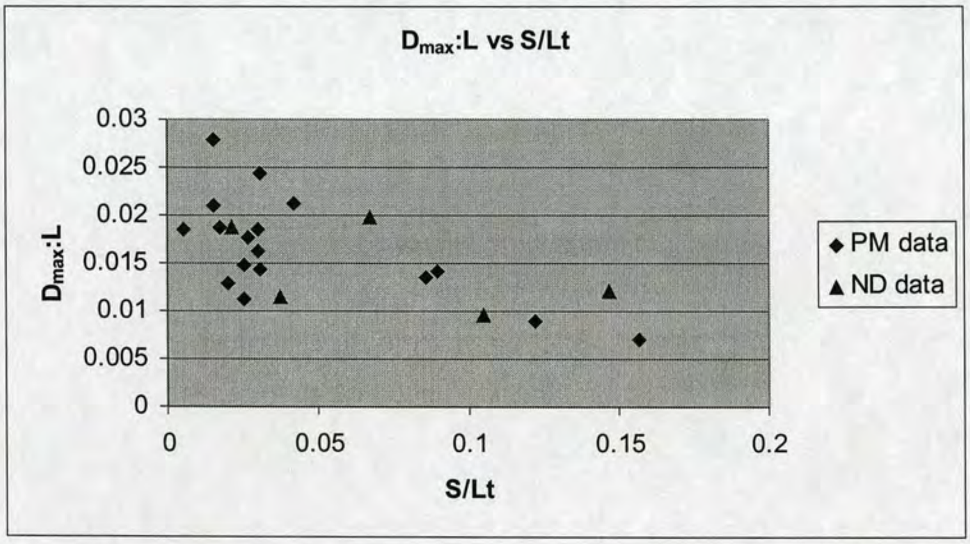

Figure 4.1. D_{max}:L plotted against S/ L_t for faults surveyed for this project (PM data) and faults from Dawers et al. (1993) (ND data).

Figure 4.1 suggests that a broad negative correlation may exist between D_{max}:L and S/L_t with considerable scatter in D_{max}:L at low values of S/L_t. Before analysing Figure 4.1 further, it is useful to consider how this plot would appear if separation distance and L_t completely controlled fault interactions and D_{max}:L was a perfect guide to a faults' interaction state. In a scenario whereby fault interaction increases linearly with reducing separation distance, for constant fault length, a perfect negative correlation is expected (Figure 4.2A). In a scenario whereby fault interaction starts below a critical separation threshold, this correlation should only be present beneath a critical value of S/L_t. Above this value of S/L_t, the D_{max}:L ratios of faults growing in isolation should be independent of S/L_t and have a best-fit line with no gradient (Figure 4.2B). In a scenario whereby fault interaction is independent of separation distance, no correlation should be seen on this plot (Figure 4.2C).

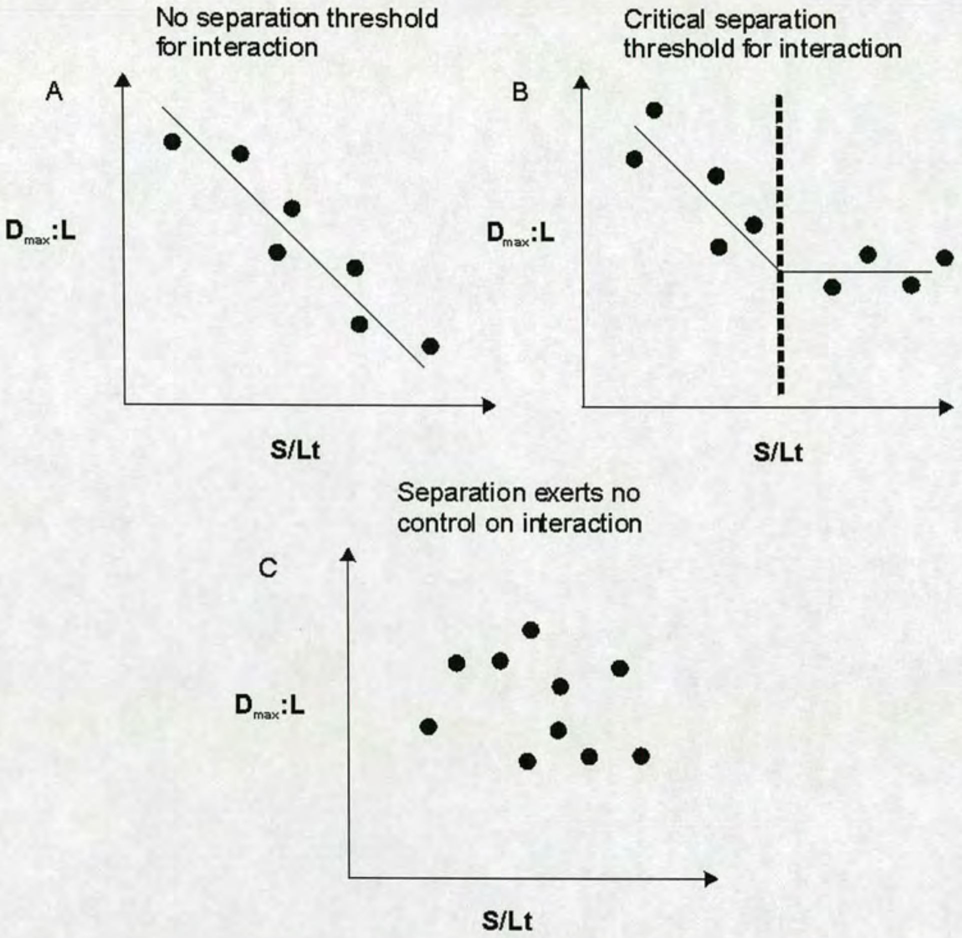

Figure 4.2. Hypothetical relationships between D_{max}:L and S/L_t assuming that the separation distance between faults entirely controls fault interactions and that D_{max}:L is a perfect guide to a faults interaction state. Figure 4.2A shows faults that interact increasingly with decreasing separation distance. Figure 4.2B shows faults that only interact within a minimum separation distance and then interact increasingly with decreasing separation distance. Figure 4.2C shows fault interaction that is independent of separation distance.

4.2.3 Interpretation of D_{max}:L versus S/ L_t

Of the scenarios presented in Figure 4.2, none fit the data ideally although option C is the least appropriate as there does appear to be a negative correlation on Figure 4.1. At low S/ L_t values, however, there is considerable scatter in D_{max}:L. In order to explore the causes of this scatter, Figure 4.3 splits the faults on Figure 4.1 into different categories dependent upon their state of linkage, overlap and whether or not they grow partially or wholly along joints. More reference will be made to this latter phenomenon, specifically highlighting the affected faults, later in section 4.3 of this chapter. Length is also a potential cause of data scatter on the Tableland as demonstrated by Dawers et al. (1993). These authors suggested that some of the longer flat-topped faults might be breaking through the tuff sheet into unconsolidated sediments, possibly explaining observed lower D/L ratios. Figure 4.4 shows the same plot as Figure 4.1 but with points split into 2 fault length categories.

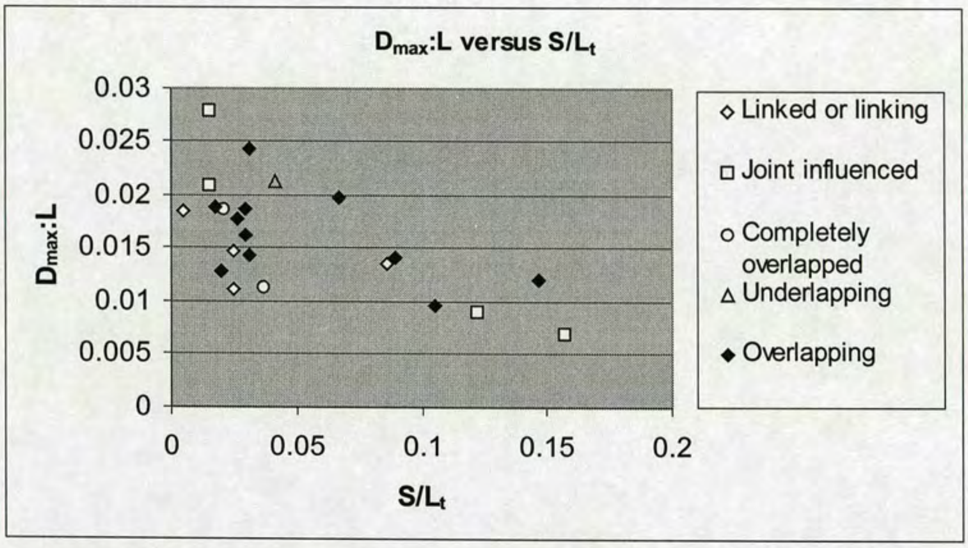

Figure 4.3. As Figure 4.1 with faults split up into the following categories: 1) obviously linked or linking with other faults, 2) growing partially or wholly along joints, 3) completely overlapped by neighbouring faults at low separation distances, 4) underlapping and 5) partially overlapping.

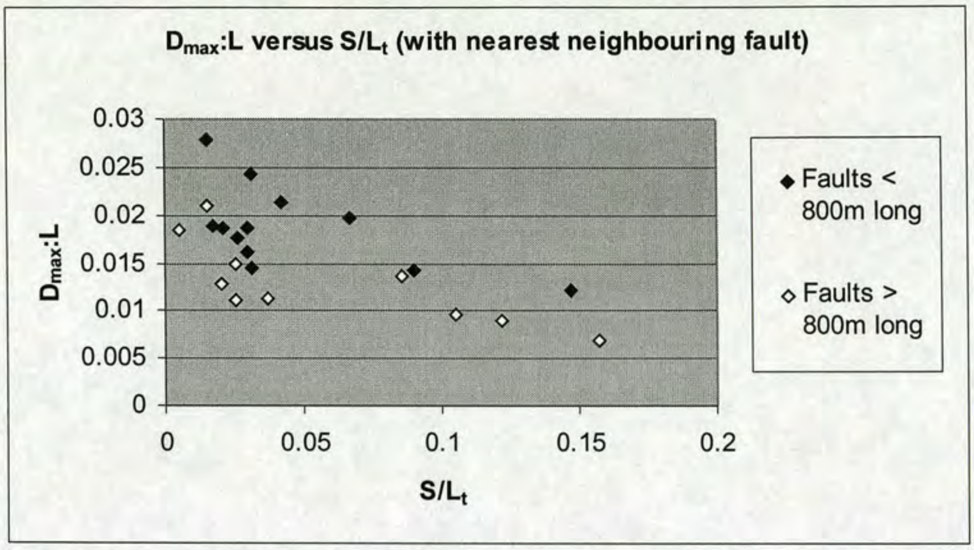

Figure 4.4. As for Figure 4.1 except with faults split into 2 fault length categories, greater than and less than 800 metres long. The threshold of 800 metres is chosen based on displacement profile observations presented later in this chapter in section 4.4.

As can be seen from Figure 4.3, a small component of the scatter in D_{max}:L at low values of S/ L_t can be assigned to the role of fault linkage and fault overlap. The two lowest D_{max}:L values at S/ L_t values of <0.05 are for a linked fault with a preserved displacement minimum and a completely overlapped fault. Fully linked faults may have low D_{max}:L ratios as they experience a rapid increase in fault length during linkage (e.g. Cartwright et al., 1996, Bohnenstiehl and Kleinrock, 2000). Linking faults with partially breached ramps have yet to undergo this major increase in length although are presumably slightly longer than they would otherwise be via the extension of the fault during this early stage of attempted linkage. Faults that are completely overlapped, i.e. entirely in the shadow of their nearest neighbour, at low separations, may be expected to suffer inhibited growth. It is notable on Figure 4.4 that longer faults have lower D_{max}:L ratios across the full range of S/L_t values. This also explains some of the scatter in D_{max}:L at low S/L_t values. It is possible, as mentioned earlier, that some of the long faults with low D_{max}:L ratios may have broken through the tuff sheet. One manifestation of a layer thickness control may be the inability of throughgoing faults to accumulate displacement in a similar manner to faults wholly contained within the tuff, irrespective of the proximity of a neighbouring fault. Fault displacement beneath the tuff could be diffusely distributed in the weak sediments rather than localised on one fault plane. This phenomenon is discussed further in section 4.4 on displacement profile shapes With increasing S/L_t, a broad negative correlation is shown with D_{max}:L ratios levelling off to some degree above S/L_t values of 0.1. There are insufficient D_{max}:L data for faults with S/L_t values of > 0.1 to determine the significance of this change in gradient. Two of the points that have S/L_t values of > 0.1 grow along joint trends as labelled on Figure 4.3. This chapter will go on to discuss that such faults, utilising joints for propagation, will often possess anomalously low D_{max}:L ratios. The two remaining points with S/L_t values of > 0.1 are faults 10 and 15 from the data set of Dawers et al. (1993). Both of these faults have approximately symmetrical profiles with D_{max}:L ratios of 0.0121 and 0.010 respectively (to 3 d.p.).

4.2.4 Conclusion comparisons – previous work vs blind test

An (1997) presented evidence for a critical S/L_t threshold for fault interaction of 0.1. Given the levelling off of D_{max}:L ratios at around this threshold on Figure 4.1 it is reasonable to explore the distribution around this value. If the threshold is applied to data from this project it can be seen that faults with S/L_t values of > 0.1 do have lower D_{max}:L ratios than those with S/L_t values of <0.1. Statistically, D_{max}:L ratios above and below this threshold have averages of 0.010 and 0.018 respectively with standard deviations of 0.005 and 0.002 (to 3 d.p.). As stated earlier, the faults growing along joints with high values of S/L_t are expected to have anomalously low D_{max}:L ratios. The 2 remaining faults with S/L_t ratios of >0.1 would be deemed to be good representations of isolated structures if applying the selection criteria of An (1997).

The analysis of D_{max}:L vs S/L_t for Tableland faults in Figures 4.1-4.4 represents a new quantitative approach for assessing the relative isolation of fault structures. It is undertaken independently of the results of previously published work and has the potential to be applied to other fault populations. A broad negative correlation between D_{max}:L and S/L_t is present in Figure 4.1. Some of the scatter at low S/L_t values is shown to come from linked, linking, completely overlapped and long faults. All of these fault types may be anomalously long for their given displacements, irrespective of their proximity to a neighbouring structure. A change in gradient of this broad negative correlation occurs at S/L_t values of 0.1, albeit derived from a limited number of data points. If the D_{max}:L ratio of a fault became independent of S/L_t at this value then this would confirm a critical separation distance threshold existed for fault interactions. From the data available, it is suggested that closely spaced faults are undergoing more interaction than widely spaced faults on the Tableland, with those faults separated by more than 0.1*Lt perhaps growing independently of each other.

4.2.5. Constructing an average isolated Tableland fault

Dawers et al. (1993) presented displacement profiles for a number of faults that they subjectively considered to be growing in isolation on the Tableland. The definition of fault growth in isolation in this area can now be quantitatively re-examined making use of their data (Dawers et al. 1993, Dawers, N., Pers.Comm., 2001). From this analysis, many of the faults from Dawers et al. (1993) are not considered here to be growing in isolation. Only two faults from Dawers et al. (1993) fitted the definition of isolation defined in the previous section by having S/L_t values of >0.1. This being the case, an 'average' isolated displacement profile on the Tableland was constructed from the 2 most appropriate faults, 10 and 15, as demonstrated in Appendix 2. The D_{max}:L ratio of this average fault construct equals 0.011 (to 3 d.p.) with a standard deviation of 0.002 (to 3 d.p.). This is the average value of 2 faults from Dawers et al. (1993) which were deemed to be truly isolated based on their separation distance from the nearest structure.

4.3 Displacement profile comparisons with an average isolated fault

Displacement profiles from Chapter 3, section 3.4 are compared here with the construct of an average isolated Tableland fault from Appendix 2. In order to facilitate a scale-independent comparison, displacement profiles are normalised by fault lengths. Shifts in profile symmetry, fluctuations in tip gradients and D_{max}:L ratios become clearly evident in these plots (Figure 4.5).

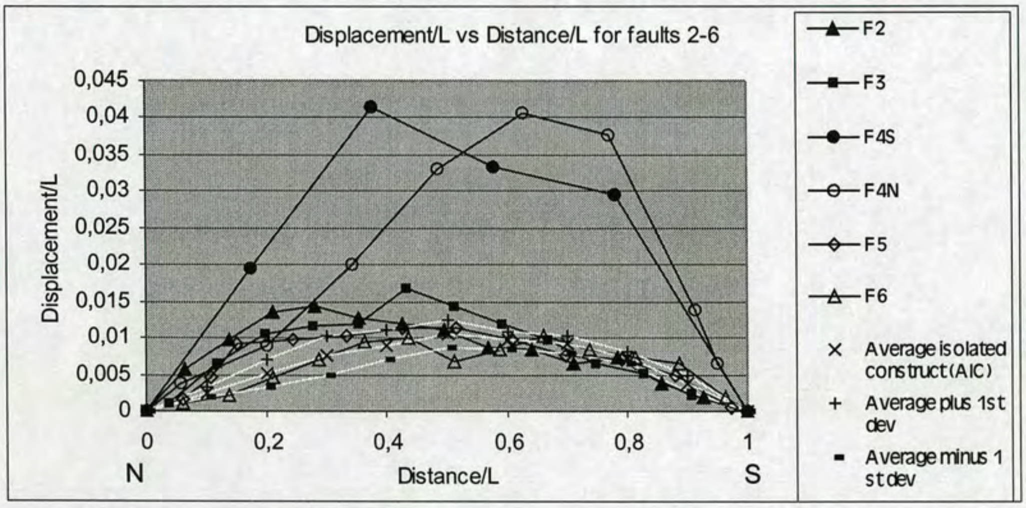

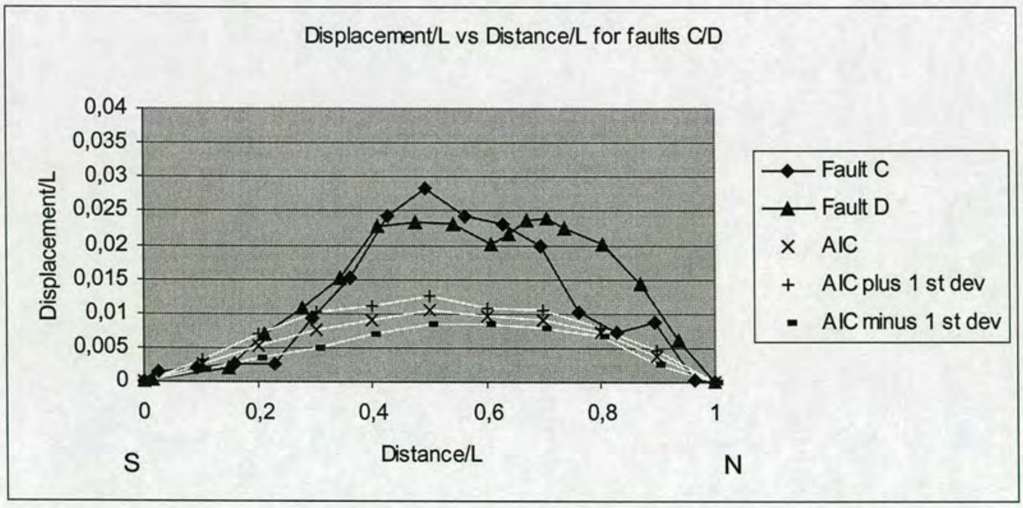

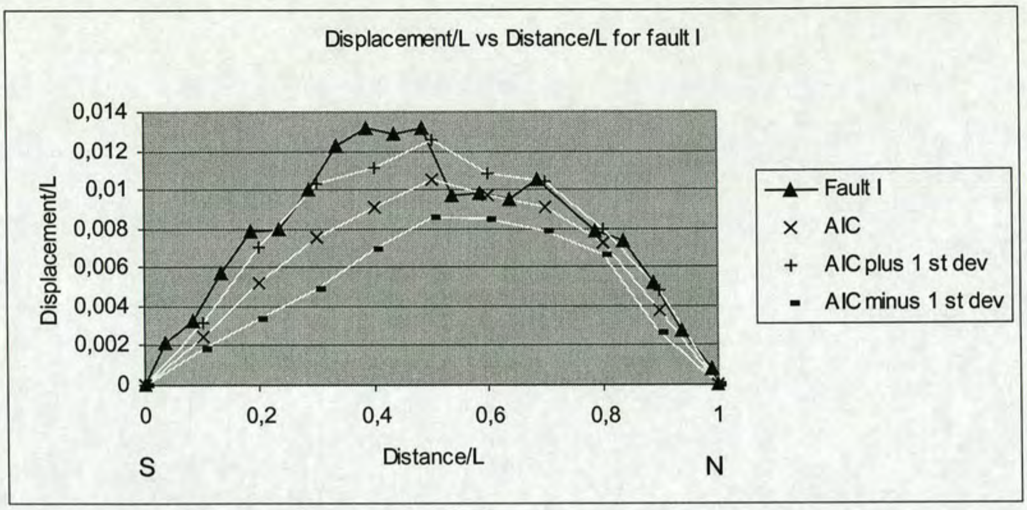
Displacement/L vs Distance/L for fault I
Displacement/L
0,014
0,012
0,01
0,008
0,006
0,004
0,002
0
0
0,2
0,4
0,6
0,8
1
S
Distance/L
N
Fault I
AIC
AIC plus 1 st dev
AIC minus 1 st dev

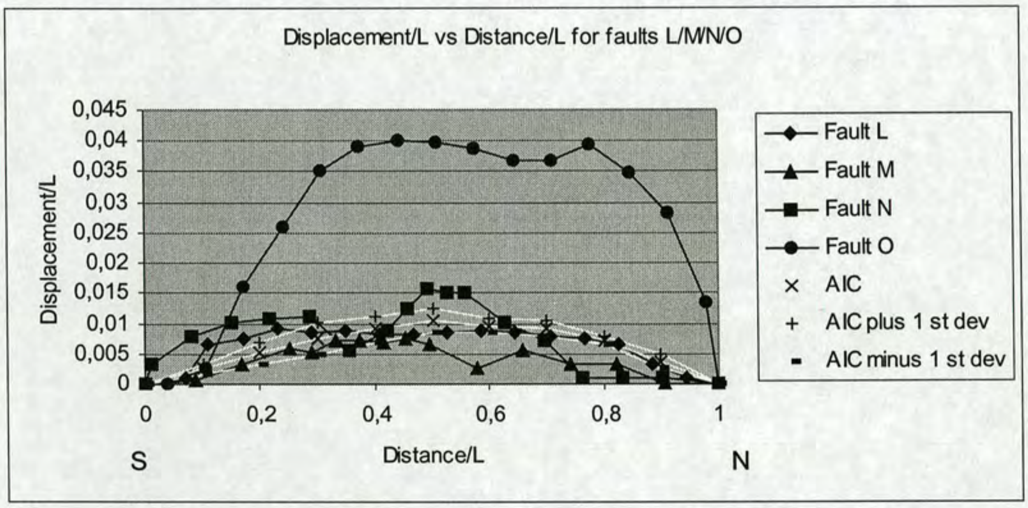
Displacement/L vs Distance/L for faults L/M/N/O
Displacement/L
0,045
0,04
0,035
0,03
0,025
0,02
0,015
0,01
0,005
0
0
0,2
0,4
0,6
0,8
1
S
Distance/L
N
Fault L
Fault M
Fault N
Fault O
AIC
AIC plus 1 st dev
AIC minus 1 st dev

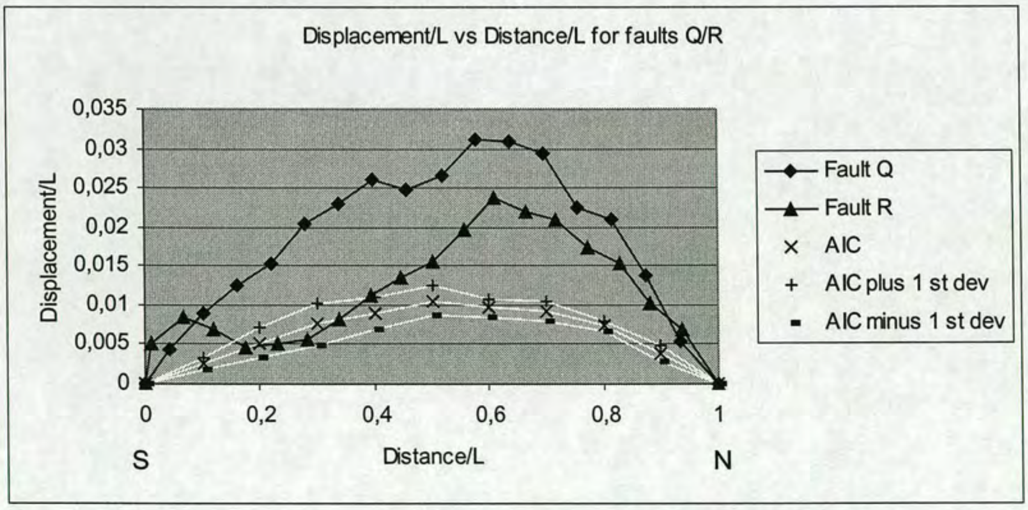
Displacement/L vs Distance/L for faults Q/R
Displacement/L
0,035
0,03
0,025
0,02
0,015
0,01
0,005
0
0
0,2
0,4
0,6
0,8
1
S
Distance/L
N
Fault Q
Fault R
AIC
AIC plus 1 st dev
AIC minus 1 st dev

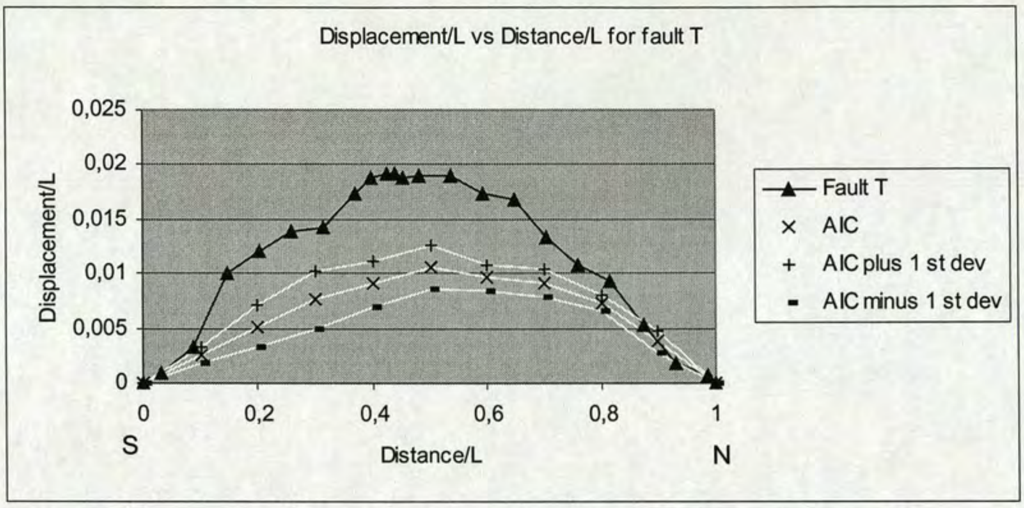

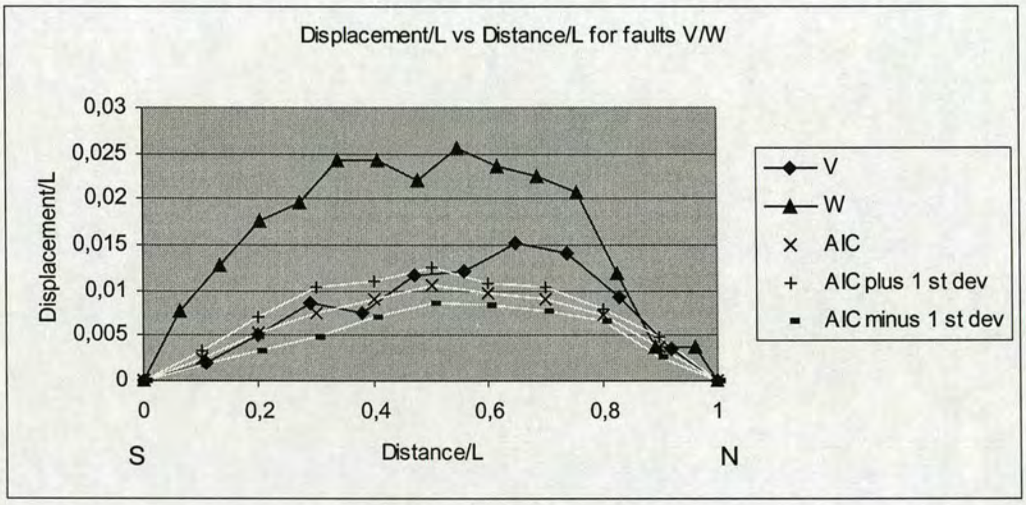

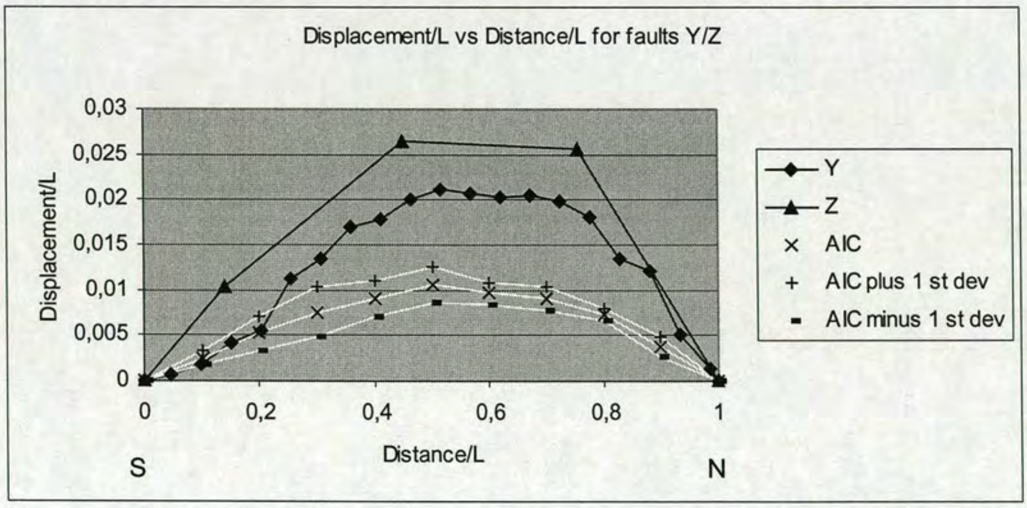

Figure 4.5. Normalised D vs distance plots for all complete faults (i.e. not intersecting the southern erosional edge of the Tableland) from section 3.4 with

faults shown in their respective en echelon arrays. Each plot includes a constructed profile of an average isolated Tableland fault (AIC) for comparative purposes, including one standard deviation above and below the average isolated profile (AIC plus 1 standard deviation and AIC minus 1 standard deviation respectively). The construction of this profile is shown in Appendix 2. North is to the right of the normalised distance axis on all plots with the exception of the first plot as labelled.

4.3.1 Interpretation

Faults C and D on Figure 4.5 show many of the salient features that distinguish between interacting and isolated faults. These faults overlap at low separation distances and so are ideal candidates for interaction. Three components of the displacement profiles are compared against the isolated fault, the D_{max}:L ratio, the tip gradients and the profile symmetry. Faults C and D both have D_{max}:L ratios significantly (>1 standard deviation) above those of the isolated fault. The northern tip gradients of each fault are significantly greater (>1 standard deviation) than that of the isolated fault. The southern tip gradients of faults C and D are very low, almost one standard deviation below that of the isolated fault. As can be seen on Figure 4.6, there is a clear change in fault strike evident at the southern tip of fault D. In the field this can be seen to reflect the diversion of the fault tip into an open joint. Discussion of faults L and M below will show that low tip gradients are typical of faults that have unambiguously diverted into joints. Fault C also tips out in an open joint at its southern tip.

Faults L, M, N and O grow in an intensely jointed region of the Tableland and clearly demonstrate the role of heterogeneities in altering displacement profiles. Faults L, M and N fall below the average isolated displacement profile for much of their lengths (Figure 4.5). The southern tip of faults L and M clearly deflect into joints. This can be seen unambiguously in the field and from aerial photos (Figure 4.7). The point at which faults L and M deflect into joints is co-incident with a significant inflexion point in the displacement profile. From this point to the tips, the tip gradients are approximately one standard deviation beneath that of an isolated fault. This provides unambiguous evidence of the role of jointing in affecting fault growth. The separation of faults L and M is sufficiently high ($>0.1L_t$) that one may not expect them to be interacting. It is probable that the asymmetry of fault L relates to its interaction with a fault to the southwest rather than fault M. The internal profile complexity of faults M and N make it difficult to make any analysis of the overall symmetry of these faults.

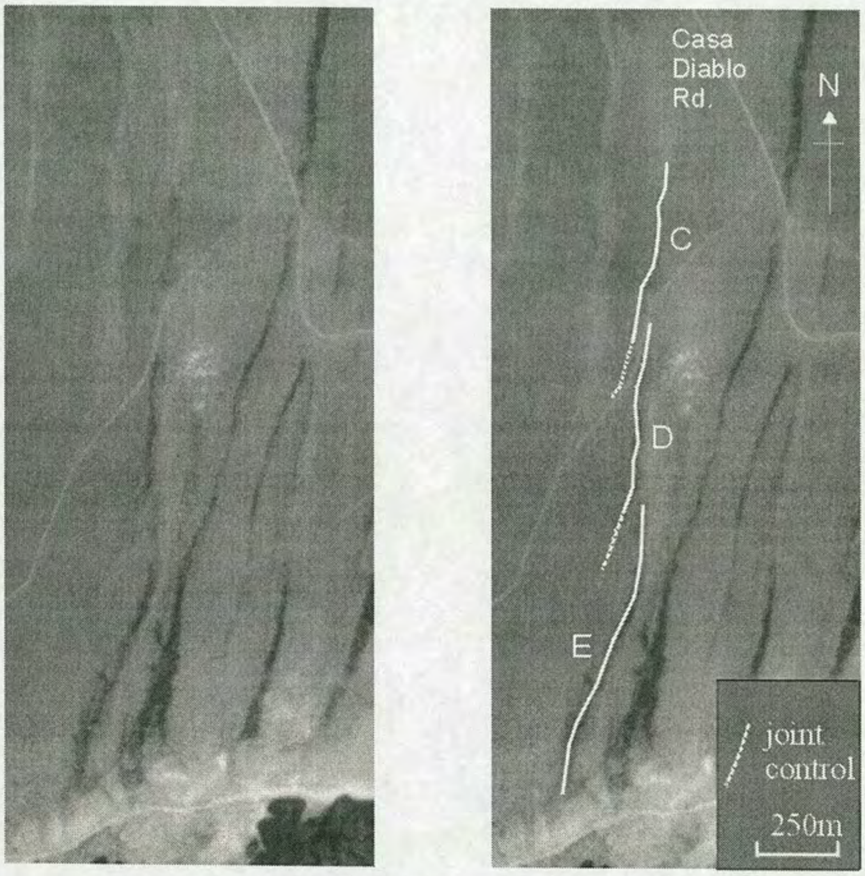

Figure 4.6. Annotated aerial photo showing the diversion of fault D into a joint at its southern tip. The change in fault trend is co-incident with a significant drop in the tip gradient. Fault C also tips out in an open joint at its southern tip.

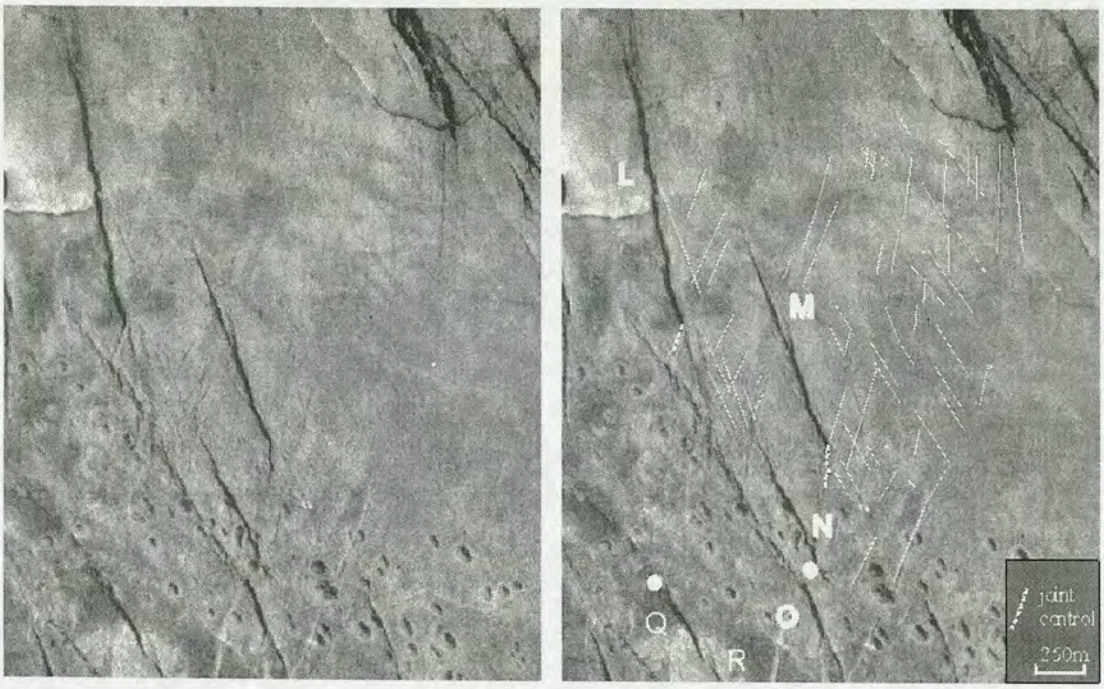

Figure 4.7. Annotated aerial photo showing the diversion of faults L and M into joints at their southern tips and the fumaroles sited between faults N and O and at the northern tip of fault Q.

Accounting for the role of jointing in altering fault displacement profiles

At this stage in the data analysis, a method is introduced for altering fault displacement profiles when it appears that a fault tip has grown into a joint. This process attempts to mimic how a fault might have looked had it not diverted into a joint. This is worth doing at this stage as all the fault parameters currently under consideration, namely D_{max}:L ratios, tip gradients and profile symmetry, are affected when a fault grows into a joint. The selection criterion for such faults are: 1) possessing tip gradients below that of an average isolated fault, and either 2) having a trend change co-incident with the point of reduction in tip gradient to match the trend of neighbouring joints or 3) running co-incident to the trend of neighbouring joints. In such cases the low gradient of the joint controlled tip can be effectively removed and replaced with a hypothetical tip as outlined in Appendix 3. In the case of faults which grow along joints for their entire length it is clearly not possible to extract the whole signature of jointing from the growth profile.

If this process is undertaken on fault C, the profile asymmetry becomes decidedly more pronounced on removal of the low gradient tip. In order to quantify profile asymmetry, an asymmetry index is defined in Figure 4.8.

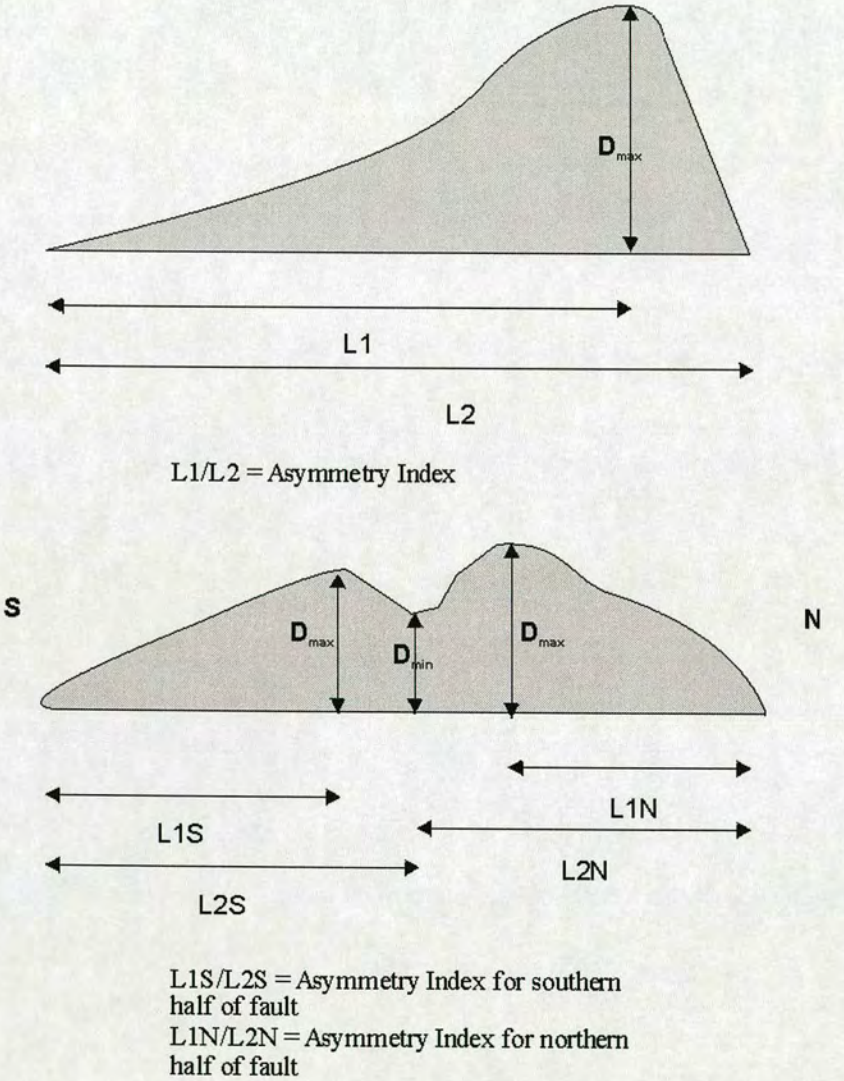

L1/L2 = Asymmetry Index

L1S/L2S = Asymmetry Index for southern half of fault
L1N/L2N = Asymmetry Index for northern half of fault

Figure 4.8. Methodology for calculating an asymmetry index from a displacement profile. In the top case, the length from one tip to the site of the D_{max} (L1), is divided by the total fault length (L2). In the bottom case, the fault is treated as 2 segments, south and north of the displacement minimum. The displacement minimum is effectively treated as a tip and asymmetry indexes are worked out as for the top example.

Fault C in its entirety has an asymmetry index of 0.505 to the south. Removing the joint controlled tip results in a shift in the asymmetry index from 0.505 to 0.626 to the south. This is shown in Figure 4.9. Fault D is asymmetric to the north and its overlapping tip with fault C. It also displays internal asymmetry toward an internal displacement minimum. Removal of the joint controlled southern tip makes the fault more symmetric overall, perhaps reflecting the dual interaction at both tips with fault E to the south and fault C to the north.

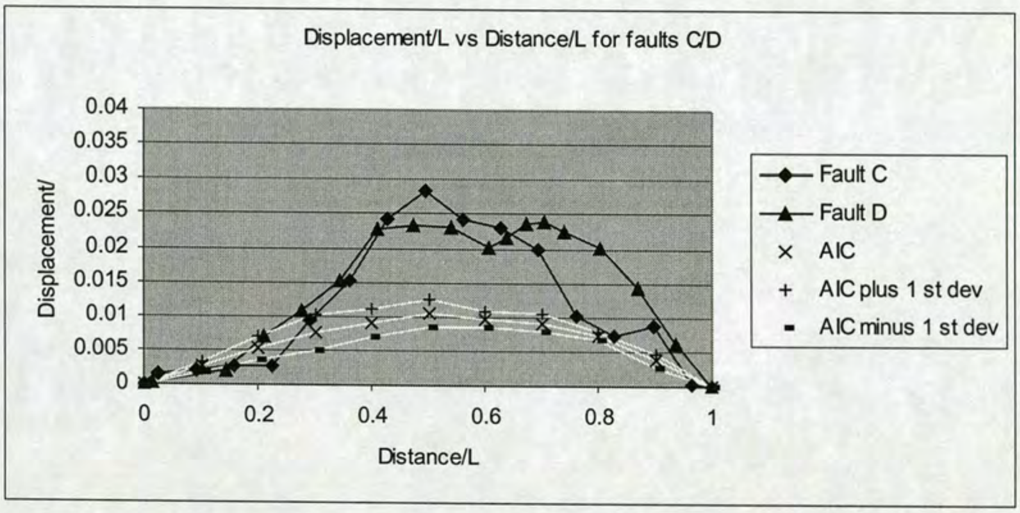

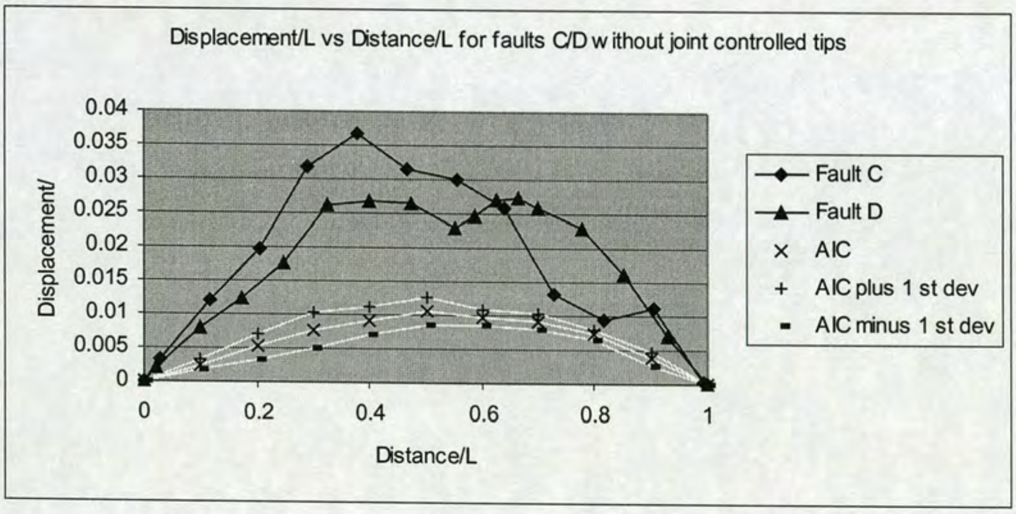

Figure 4.9. Normalised D:L plots for faults C and D with and without low gradient tips. Note how removal of the low gradient tip for fault C enhances the asymmetric skew of the profile toward fault D. For fault D the profile becomes more symmetric, potentially reflecting the interaction occurring at both tips with faults E and C. North is to the right on both plots as before.

Faults C and D thus highlight some of the salient features of interacting faults and introduce the role of jointing in altering displacement profiles and effectively disguising interaction signatures. The role of joints in affecting fault displacement profiles is confirmed by subsequent analysis of faults L and M, faults growing in a heavily jointed region of the Tableland.

The role of fumaroles in altering D profiles

The other heterogeneity prevalent across the Volcanic Tableland is fumarolic mounds, or volcanic vents (Holt and Taylor, 1998). One such feature is sited between the southern tip of fault N and the northern tip of fault O (see Figure 4.7). These 2 faults underlap by a short distance and the fumarole sits in this region of underlap. The D_{max}:L ratio of fault O is the highest of the surveyed faults on the Tableland. The southern tip gradient of fault N is significantly greater than that of an isolated fault and the northern tip gradient of fault O is the highest in the data set. From this evidence, it appears that the fumarole may be blocking the growth of faults N and O into overlapping configurations by limiting their propagation in length in this area. This impediment to fault propagation would create the extremely high D_{max}:L ratio of fault O and the significantly elevated tip gradients of southern fault N and northern fault O. In another surveyed case, a fumarole is sited near the northern tip of fault Q that in turn also preserves an anomalously high tip gradient. Further evidence for the role of fumaroles as strength heterogeneities can be seen elsewhere on the Tableland where faults bifurcate into 2 strands to bypass a fumarole mound. The implications of this shall be discussed further in Chapter 5.

Analysis of D profiles for the whole dataset

Considering the data-set as a whole, faults 1, 2, 3, 4, 7, C, D, E, G, I, N, O, Q, R, S, T, U, V,W,Y and Z all have D_{max}:L ratios above that of the average isolated fault. The significance of the elevation in D_{max}:L varies from less than one standard deviation to greater than 3 standard deviations. Faults L, M, 6 and 5 are the exceptions to the rule, two of which are potentially fully joint controlled and thus would be expected to have low D_{max}:L ratios. Profile asymmetry is common in faults with S/L_t ratios of <0.1. However, displacement profiles can also show significant complexity with displacement minima common at sites of remnant segment linkage and often more than one displacement maxima along strike, e.g. fault 6. Symmetrical profiles, such as fault D, may have proximal faults at both tips and thus overall asymmetry may be cancelled out. Heterogeneities, such as joints or fumaroles, have been shown capable of significantly altering displacement profiles and as such could disguise or remove profile asymmetry. Data from this project suggests such complexities make profile asymmetry a somewhat unreliable guide to the interaction status of a fault. This result is in contrast to work done on smaller faults in the Solite Quarry by Gupta and Scholz (2000a) where profiles are considerably less complex and profile asymmetry can reliably be used as an interaction indicator.

4.4 Displacement profile shape

Fault displacement profile shapes in section 3.4 clearly have a variety of forms from very peaked as in fault 4N to very flat-topped as in fault 5. It has been observed in various studies on fault sizes that parameters such as layer thickness (Dawers et al. 1993), crustal thickness (e.g. Bohnenstiehl and Kleinrock, 2000), and lithological heterogeneities (e.g. Muraoka and Kamata, 1983) can have significant and predictable effects on the shape of fault displacement profiles. In order to discern if there is a pattern to profile shapes, potentially other than that imparted by fault interactions, displacement profile shapes are analysed with respect solely to the length of individual fault structures. Profiles are put into descriptive categories depending on the relative flatness of their profile. A qualitative distinction is made between peaked and flat-topped profiles at this stage by analysing the magnitude of displacement gradients in the central portion of the fault. Consistently low gradients in the central portion of the fault define a flat-topped profile, although no profiles are perfectly flat, while steep gradients approaching a point define a peaked profile.

Using this system, faults 5, 6 and L are deemed to be very flat, faults 1, D, E and M are deemed flat or moderately flat, faults 2, 3, C, N, O, Q, R, T, I, V, W, and Z are deemed peaked or moderately peaked, and fault 4S and 4N are deemed very peaked.

4.4.1 Interpretation

Qualitative analysis of displacement profiles in section 3.4 suggests there is a threshold at fault lengths of approximately 800m above which displacement profiles typically flatten out. In order to test this, a null hypothesis is proposed that there will be no predictable difference in profile shapes above and below a threshold of 800m in length. Eighteen of the twenty faults considered, or 90% of the data, are suggested to disagree with this null hypothesis. This suggests the null hypothesis should be rejected and a relationship between fault length and profile shape exists. Varying the threshold around this value is not found to change this result. Figure 4.10 shows examples of length normalised displacement profiles split into 2 plots for faults with lengths less than and greater than 800m. These are suggested to correspond with peaked and flat-topped profiles respectively.

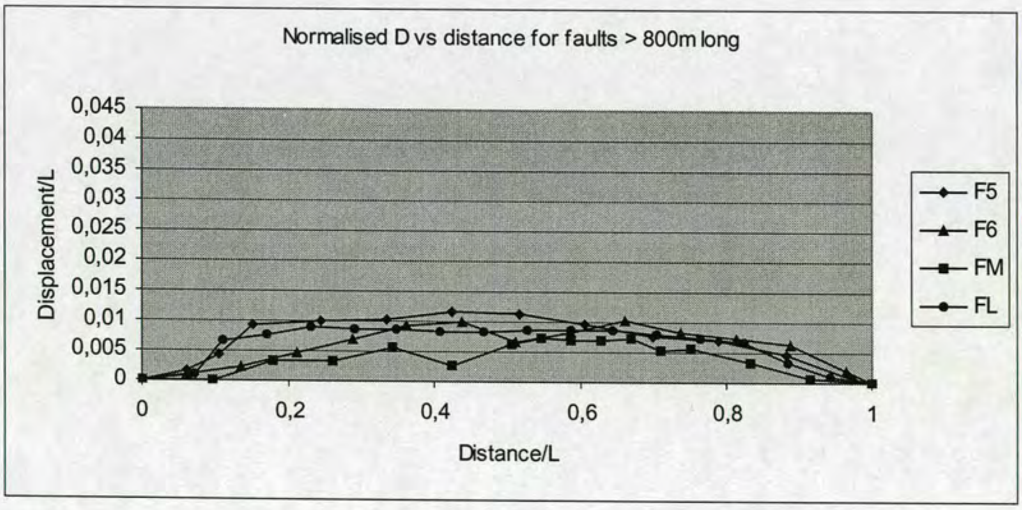

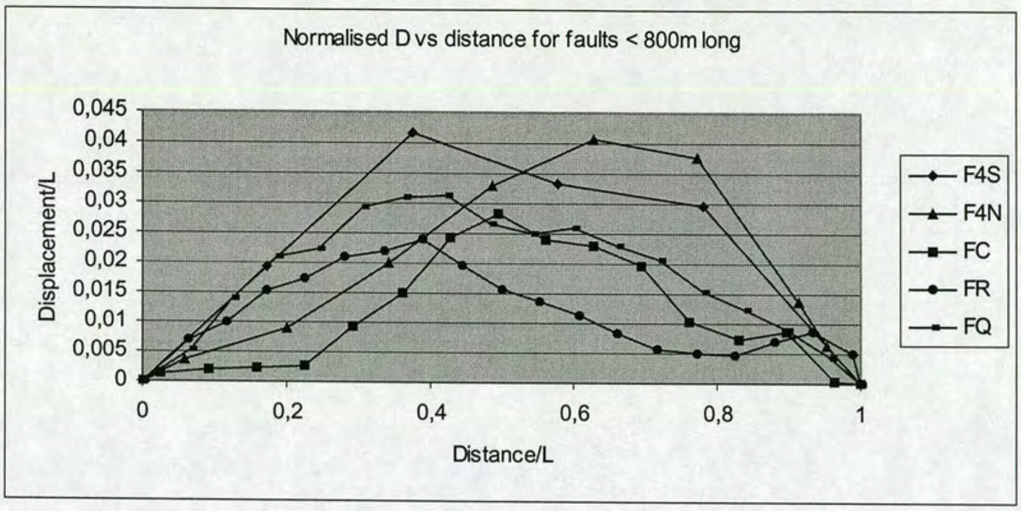

Figure 4.10. Examples of length-normalised displacement profiles split into 2 plots with faults greater than and less than 800 metres long respectively. It is suggested here that these plots correspond to faults with flat-topped and peaked profiles respectively. Note that the normalised displacement axes have the same scale in both plots.

Having quantitatively re-assessed the definition of fault growth in isolation in this chapter, and explored various controls on fault displacement profile shape, Chapter 5 will develop from these themes by further quantifying the controls on differing degrees of fault interaction and the restrictions such interactions can impose on attainable plan view fault geometries. The field results from Chapters 4 and 5 will be summarised together at the end of Chapter 5.

Chapter 5 – The relationship between fault dimensions and fault array geometries as controlled by fault interactions

5.1 Rationale

This chapter focuses on providing a quantitative assessment of the ability of one fault to affect the growth of another. This is primarily undertaken by statistical analysis and cross-plotting of those fault parameters that may reflect the interaction status of a fault segment. Firstly, D_{max}: L ratios and tip gradients of proximal faults are statistically compared with those that were determined in Chapter 4 to have grown in isolation from the data-set of Dawers et al. (1993). Subsequently, D_{max}:L ratios and tip gradients of individual faults are plotted against O:S ratios, a numerical proxy for their spatial proximity to neighbouring fault structures. If faults are able to interact during growth, and increasingly so with increasing proximity, this should be reflected in these comparative plots.

Further to this, it is postulated that plan view fault array geometries as observed today may not be a matter of co-incidence, rather a consequence of fault interactions. Aydin and Schultz (1990) suggested that fault interactions may explain the predominance of en echelon geometries seen in natural strike slip fault arrays. To examine this hypothesis, a scale independent examination of O:S ratios across the Tableland is undertaken. Results are compared with published data from Gupta & Scholz (2000a) on a smaller population of faults in the Solite Quarry, North Carolina, U.S. Throughout this quantitative assessment of fault interactions, the role of rock strength heterogeneity is considered in terms of its ability to dilute or enhance a potential fault interaction signature. Finally, it is recognised that elliptical areas in the footwall high region of linked and unlinked fault segments in this area remain clear of structural deformation. The implications of this are discussed in terms of the role of footwall uplift and stress shadowing in controlling fault and joint densities.

5.2 Maximum displacement vs length ratios

Two parameters that are commonly utilised to classify the dimensions of a fault are the D_{max} of the structure and the resolvable tip to tip length (L) (see Ch1). The relationship of D_{max} to L, if any, is integral to the mechanics of fault growth and has been the subject of considerable debate in recent years (e.g. Watterson, 1986; Walsh & Watterson, 1988; Marrett and Allmendinger, 1991; Cowie & Scholz, 1992b; Gillespie et al., 1992; Dawers et al., 1993). In field data, as discussed in section 3.4.2, D_{max} and L parameters are typically derived from a 2D section through some level of the fault plane. On the Volcanic Tableland, the section of the fault plane displayed at the ground surface may represent a section through the centre of the fault plane if faults have nucleated at the ground surface as suggested by Pinter (1995). For such a section, D_{max} and L values at the ground surface would represent the maximum D_{max} and L on the fault plane in 3 dimensions. After construction of displacement vs distance plots for surveyed faults in chapter 3, D_{max} and L are extracted for each example. Figure 5.1 shows D_{max} plotted against L for all faults surveyed for this project.

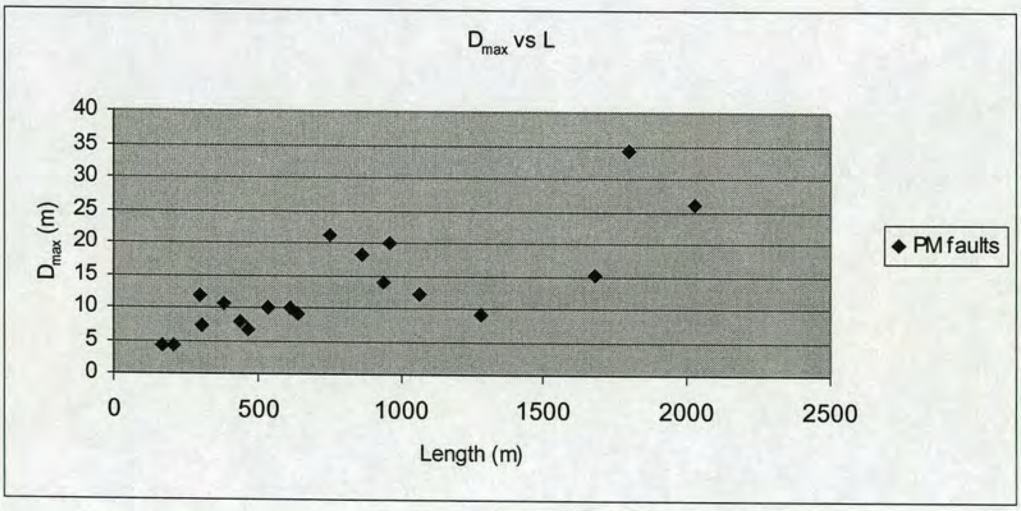

Figure 5.1. D_{max} plotted against L for faults surveyed for this project (PM faults). Note that faults that intersect the southern edge of the Tableland are not included in this plot due to censoring of L, i.e. the full fault length is not visible.

Chapter 4 highlighted the role of jointing and fumaroles in affecting fault displacement profiles and showed how D_{max}:L ratios were often predictably altered. A significant component of the data analysis in this thesis attempts to extract a signal for fault interactions and so it is extremely important to be able to account for the role of rock mass heterogeneities in altering this signal. For this reason, in analysis of D_{max}:L ratios, faults affected by jointing and fumaroles are considered separately from the rest of the population. Figure 5.2 shows a similar plot to Figure 5.1 but with the data separated into those faults that are known from field and displacement profile evidence to be affected by jointing and fumaroles and those that are not.

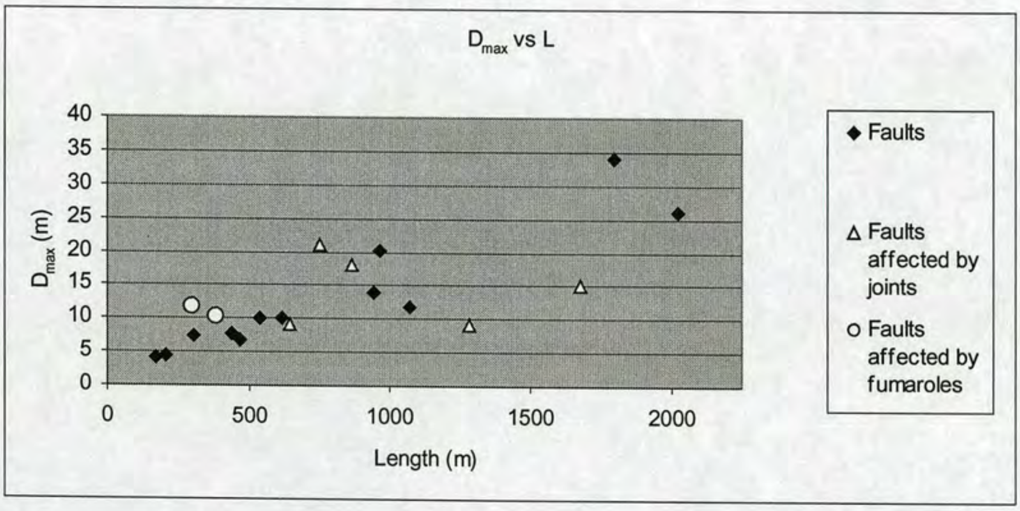

Figure 5.2. As for Figure 5.1 but with faults affected by jointing and fumaroles plotted as separate data series.

5.2.1 Interpretation of D_{max}:L ratios

Figure 5.1 clearly shows a broad positive correlation between D_{max} and L. Figure 5.2 shows that some of the scatter in this relationship is introduced by the effects of jointing and fumaroles on altering fault parameters. This is evidenced in particular by two data points that fall well below the rest of the data set. Figure 5.3 shows a least squares best-fit regression line through D_{max} vs L data for faults not obviously affected by heterogeneities. An R^2 coefficient of 0.835 (to 3 d.p.) indicates a strong linear relationship between D_{max} and L. In order to compare potentially interacting faults with isolated faults from the same tectonic setting, Figure 5.4 includes D_{max}:L data from the 2 faults defined as most likely to be growing in isolation from the data of Dawers et al. (1993) in Chapter 4, section 4.2.

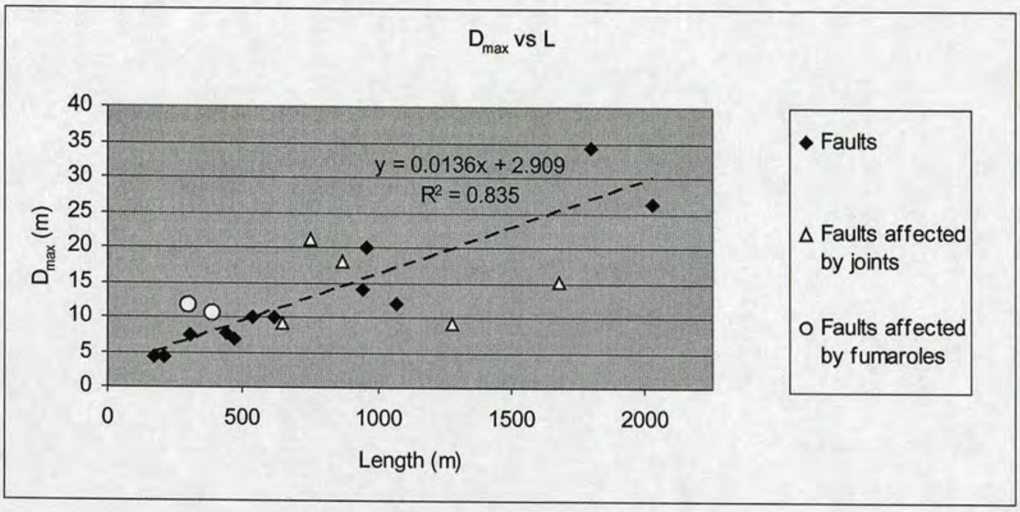

Figure 5.3. D_{max} plotted against L including a least squares regression best-fit calculation for faults not obviously affected by heterogeneities.

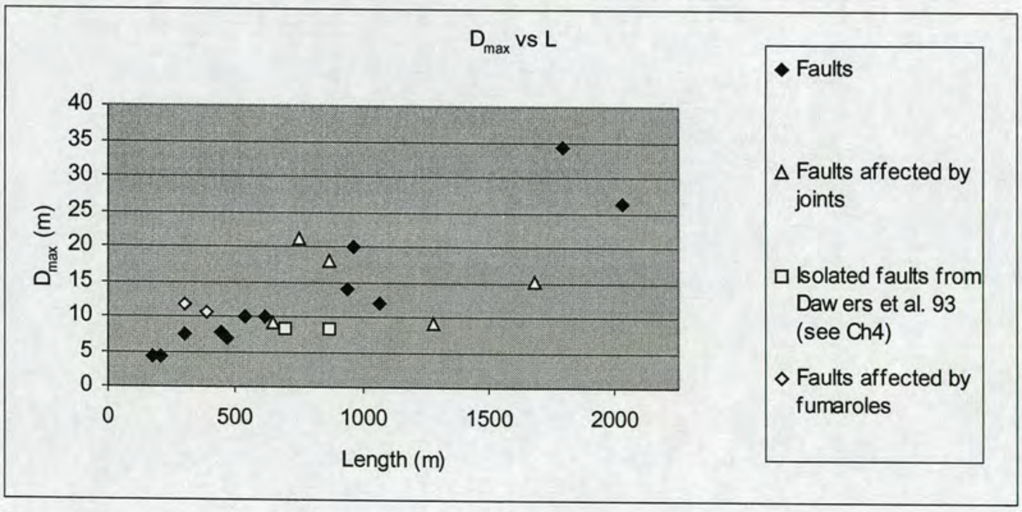

Figure 5.4. D_{max} plotted against L including 2 faults from the data of Dawers et al. (1993) which fit this projects definition of isolated structures, i.e. separated from their nearest neighbour by at least $0.1*L_t$ (see Ch4).

The 2 faults which fit this projects definition of isolated structures, from the data-set of Dawers et al. (1993), have D_{max}:L ratios that fall below those of the majority of faults not affected by heterogeneities. A statistical comparison of D_{max}:L ratios for potentially interacting and isolated faults, as determined by their S/L_t ratio, is summarised in Table 1 below. In addition, statistics for potentially interacting faults are recalculated after the exclusion of faults affected by heterogeneities in the form of tectonic joints or fumaroles.

	D_{max}:L Range	Average D_{max}:L	Standard Deviation
All potentially* interacting faults (* S/Lt < 0.1)	0.007 – 0.039	0.019	0.008
As above without faults affected by joints or fumaroles	0.011- 0.025	0.018	0.004
Isolated** faults from Dawers et al. 1993 (** S/Lt > 0.1)	0.01 - 0.012	0.011	0.002

Table 1. A statistical comparison of D_{max}:L ratios for potentially interacting faults, with and without those faults affected by joints or fumaroles, versus isolated faults selected from Dawers et al. (1993).

As shown in Table 1, the average D_{max}:L ratio for potentially interacting faults not affected by heterogeneities equals 0.018, with a standard deviation of 0.004 (to 3 d.p.), higher than the average ratio for isolated faults of 0.011, with a standard deviation of 0.002 (to 3 d.p.). The difference between the two means is statistically significantly to one standard deviation although the data-set for isolated faults is very small. It could be speculated that with more data from the same setting the statistical gap between average D_{max}:L values for isolated and interacting faults may widen. However, in a setting of this nature, despite the relatively low cumulative strain of less than a few percent (Dawers et al., in revision), the diffuse nature of deformation makes it difficult to find structures that fit the definition of growing in isolation. Aydin & Schulz (1990) discuss the tendency for underlapping faults to propagate towards each other so it is perhaps not a co-incidence that isolated faults are seldom seen. For this reason it is not possible to build up a large data-set of perfectly isolated faults, which by default will lessen the significance of the statistical tests. Earlier in the evolution of this setting, with cumulative strains of 0-2%, this may have been possible.

Using the information from Table 1, two new hypothetical trend-lines are constructed in the D_{max} vs L plot shown in Figure 5.5. These lines represent one standard deviation above and below the best-fit D_{max} vs L line in Figure 5.3 for potentially interacting faults not affected by heterogeneities.

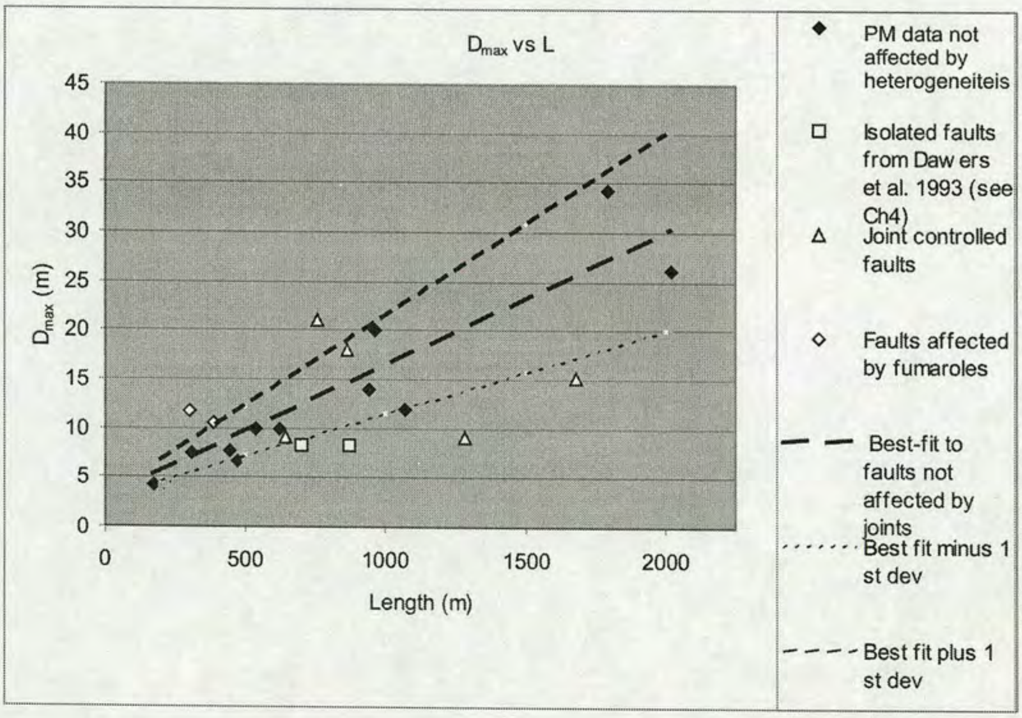

Figure 5.5. D_{max} plotted against L with new trend-lines inserted at one standard deviation above and below the best-fit line for potentially interacting faults surveyed for this project not affected by heterogeneities (i.e. PM data).

Two of the four points that fall below the minus one standard deviation trend-line are for faults L and M, both faults that grow along or subparallel to joints as shown in section 3.4. Faults C and D, only partially affected by jointing, fall well above the best-fit line. It is probable that faults C and D have undergone significant interaction owing to the very low separation distance (<10m) between faults in this array. Faults C and D have low tip gradients typical of faults deflecting into joints but the role of fault interactions in elevating D_{max}:L ratios appears to have significantly outweighed the partial role of joint control in moulding the final fault parameters. The remaining 2 faults sitting below the minus one standard deviation trend-line are those faults deemed to be isolated from the data-set of Dawers et al. (1993). This confirms that isolated faults and potentially fully joint controlled faults have lower D_{max}:L ratios than the rest of the population under consideration.

5.3 D_{max}:L versus Overlap:Separation ratios

Section 4.2 demonstrated that fault pairs that have grown within separation distances of < 0.1Lt tend to develop higher D_{max}:L ratios than faults that have grown in comparative isolation. This suggests that closely spaced faults are aware of each other during growth, manifested in their ability to enhance each others D_{max}:L ratios if sited within a given separation distance. This question was initially approached as a side affect of attempting to quantify the term 'isolated' when applied to fault growth. This was undertaken via plotting D_{max}:L against separation distance, normalised by the combined length of the fault pair (see Ch4). This plot showed that D_{max}:L ratios have a broad inverse relationship with separation distance below a certain threshold, for a given fault pair length. Separation distance, however, is only one of 2 potential spatial controls on fault interactions in plan view. The other potential controlling parameter is fault pair overlap (O). To introduce this parameter to the analysis, O:S ratios of individual fault pairs are used as a numerical proxy for the relative 2D spatial proximity of a fault pair. D_{max}:L ratios are plotted against O:S ratios in Figure 5.6. For an individual fault pair, the D_{max}:L ratio of each fault is plotted against the O:S ratio. For a multi-segment array the D_{max}:L ratio of a fault with neighbouring structures at either tip is plotted twice against the O:S ratio found at either tip respectively. Plotting D_{max}:L ratios against O:S ratios contributes to answering one of the fundamental questions of chapters 3 and 4: Does fault interaction increase with increasing fault proximity?

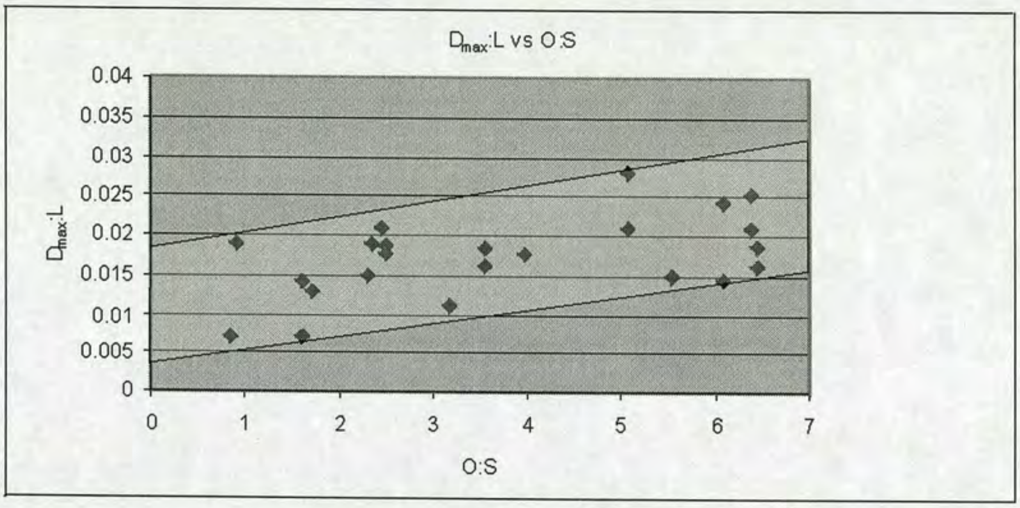

Figure 5.6. D_{max}:L ratios plotted against O:S ratios for potentially interacting fault pairs. For an individual fault pair, the D_{max}:L ratio of each fault is plotted against the O:S ratio. For a multi-segment array, the D_{max}:L ratio of a fault with neighbouring faults at either tip is plotted twice against the O:S ratio found at either tip respectively. The D_{max}:L ratio of faults intersecting the southern erosional edge of the Tableland are not included. The broad positive correlation band between D_{max}:L and O:S is annotated in light grey.

The affect of joints on fault displacement profiles, and specifically tip gradients, was clearly demonstrated in Chapter 4. A methodology for constructing fault displacement profiles with the effects of jointing at least partially removed, was outlined in Appendix 2 and discussed in Chapter 4. Concomitantly, this process hypothetically alters the plan view geometries of affected fault pairs, as fault lengths must change. In this section it is of interest to re-calculate both D_{max}:L ratios and O:S ratios for faults affected by jointing, after altering the displacement vs distance profiles in the manner outlined in Appendix 3. The data produced from this process are added to Figure 5.6 in Figure 5.7. The faults that were altered to produce this data were C, D, L, M and N. It is important to note that the process outlined in Appendix 3 at best removes part of the effect of jointing on displacement profiles. It is only possible to remove joint controlled tips where they clearly divert off the main body of the fault into a joint or are anomalously low on a fault clearly growing along a joint. This is well suited to faults C, D, L, M and N. It is not possible to alter entire fault displacement profiles where they may have grown wholly within a joint, e.g. possibly faults L, M, and N. Any effect revealed by this process is thus a diluted version of the total affect of jointing on controlling fault displacement profiles.

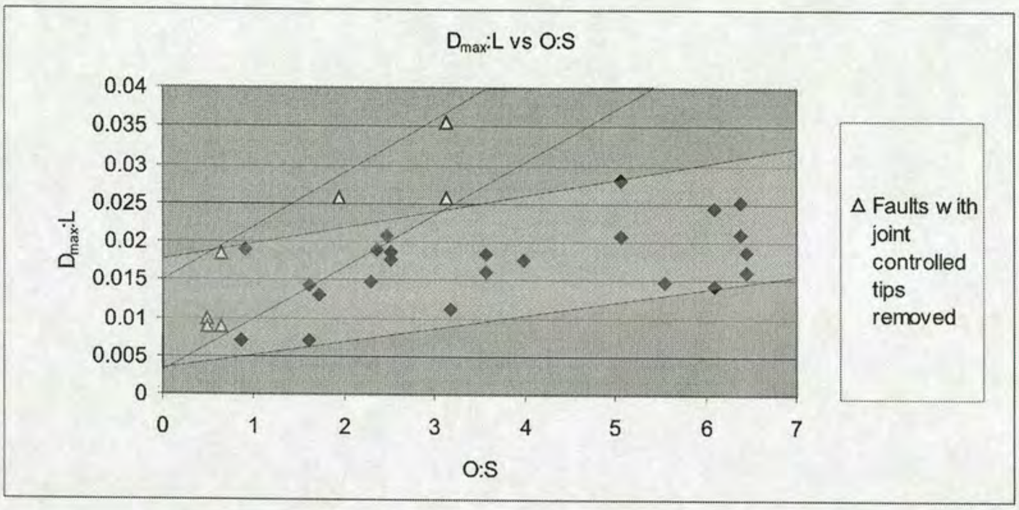

Figure 5.7. D_{max}:L ratios plotted against O:S ratios as in Figure 5.6, including re-calculated D_{max}:L and O:S ratios for faults and fault pairs affected by jointing after removal of joint controlled tips as outlined in Appendix 3.

5.3.1 Interpretation of D_{max}:L vs O:S plot

Figure 5.6 shows that there is a broad positive correlation between D_{max}:L and O:S ratios although with significant scatter. A light coloured annotated area superimposed on the plot contains all the data points and highlights this correlation band. The effect of removing joint controlled tips from fault displacement profiles and re-calculating O:S ratios using the new overlap distance between extrapolated tips is demonstrated graphically in Figure 5.7. Removing fault tips, where they have diverted into joints and assumed an anomalously low gradient, and replacing them with a steeper hypothetical tip acts both to increase the D_{max}:L ratios of the fault in question and lower the O:S ratio of the relevant fault pair. This is shown by the increase in gradient of a new annotated correlation band containing these data points in Figure 5.7. These results are intuitive if one accepts that joints lower D_{max}:L ratios by allowing anomalous accumulation of length for very little displacement. This extra length yields higher O:S ratios than if faults had grown in unjointed rock and had developed tip gradients as controlled by the shear strength of structurally intact tuff, with or without the additional affect of interactions. The significant change in gradient in the correlation band between Dm:L and O:S which results from the operation of removing joint controlled tips suggests that much of the fault population may be influenced by joints despite it not being obvious at the ground surface.

5.4 Tip gradients vs Overlap:Separation ratios

Tip gradients are directly related to the finite stress concentration imposed on a rock mass at the fault tips (Cowie & Scholz, 1992). For this reason, perfectly elliptical displacement profiles are unrealistic in nature, as they would require an infinite stress concentration at the tip that no real rock material can support. Gupta & Scholz (2000a) incorporate the fact that tip gradients control finite stress concentrations at fault tips into their model of fault interactions. Faults that interact in the model are produced in one 'fault-sized' rupture event. These faults rupture an elastic material thus producing significant stress shadows, or areas of relaxed rock, adjacent to the body of the fault. In order for faults to overlap, they must overcome the shear stress reduction felt behind the body of a neighbouring segment. This shear stress reduction will increase with increasing overlap until the overlapping fault is perpendicular to the maximum displacement on the neighbouring segment. Gupta and Scholz (2000a) thus suggest that in order for faults to attain increasing overlap, they require ever increasing tip gradients. This theoretical, highly idealised, concept motivates analysis of fault tip gradients on the Tableland with respect to the degree of overlap attained between fault pairs. Figure 5.8 shows tip gradients plotted against O:S ratios for the fault pair under consideration. Two sets of tip gradients are shown, calculated using the representative techniques discussed in Appendix 4. These graphs include faults that have diverted into or grown wholly within joints although not fault tips affected by fumaroles as these are anomalously high outliers. This data is shown subsequently in Table 2.

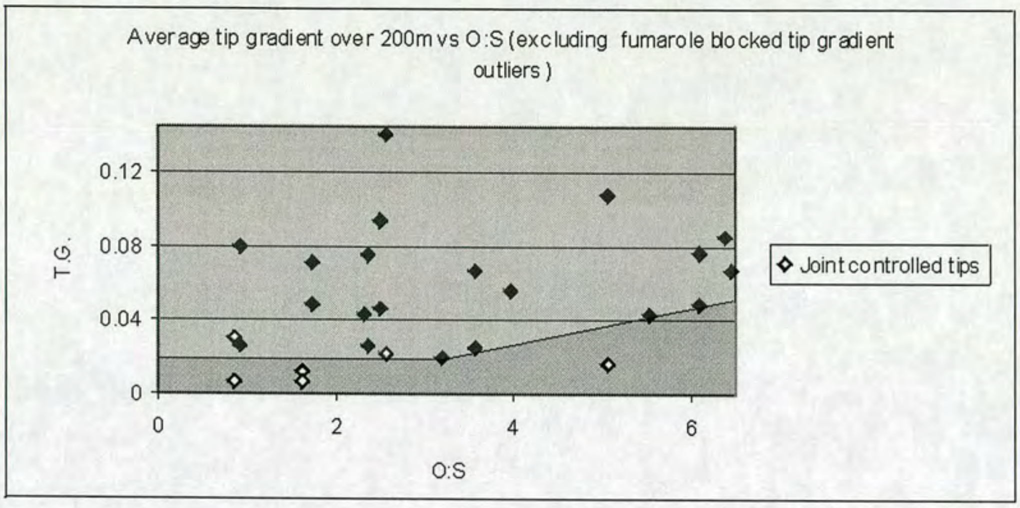

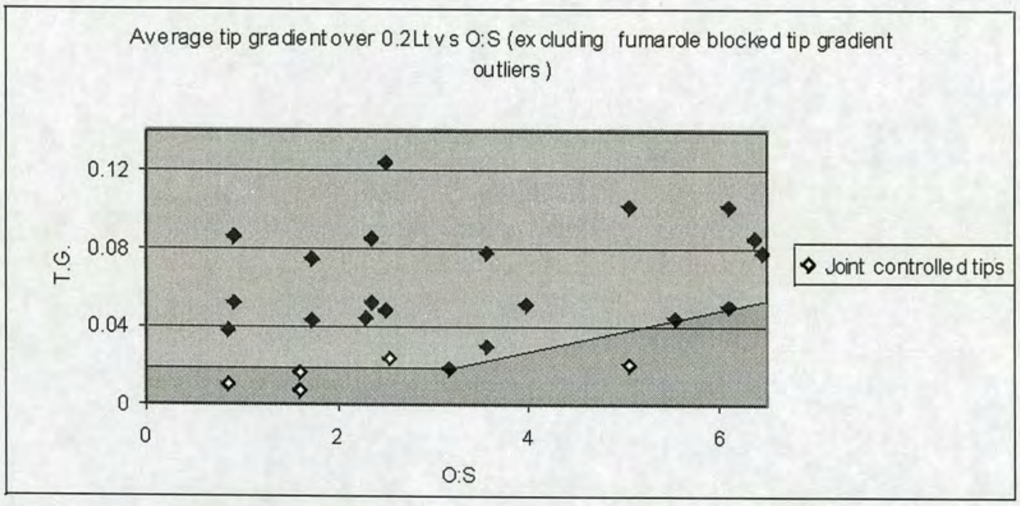

Figure 5.8. Tip gradients plotted against O:S ratios for surveyed fault pairs. Two averaging techniques are shown with the average gradient recorded at 200m from the fault tip and the average gradient at $0.2*L_t$ from the fault tip. The light grey area of both plots is annotated to show the rise in minimum non-joint controlled tip gradients above O:S ratios of ca 3.

5.4.1 Interpretation of tip gradients vs O:S ratios

The most striking feature of Figure 5.8 is the unique area occupied by fault tip gradients controlled by joints. These values, as discussed qualitatively in section

4.3, are generally significantly lower than those of potentially interacting faults, irrespective of their interaction status. A statistical analysis of tip gradients, using the 2 different averaging techniques selected in Appendix 4, is shown below in Table 2.

	Average tip gradient over 200m (to 3dp)	Standard Deviation (to 3dp)	Average tip gradient over 0.2Lt (to 3dp)	Standard Deviation (to 3dp)
Joint controlled (jc) tips	**0.016**	**0.008**	**0.020**	**0.010**
Overlapping non-jc fault tips	0.062	0.038	0.069	0.050
As above w/out tips blocked by fumaroles	**0.049**	**0.031**	**0.050**	**0.029**
Isolated sub-set of Dawers et al. (1993) data	**0.036**	**0.009**	**0.039**	**0.011**

Table 2. Statistical analysis of tip gradients using 2 different averaging techniques. Faults are split up into those with tips affected by joints or fumaroles and those that are not. Tip gradients are also shown for those faults that are deemed to have grown in isolation from the data set of Dawers et al. (1993).

There is a large difference between the average magnitude of joint controlled and non-joint controlled tip gradients, excluding faults affected by fumaroles as shown on Table 2. However, the high standard deviations for non-joint controlled tip gradients mean this cannot be classified as a statistically significant difference. It has been shown unambiguously in previous sections that faults utilising joints for propagation can accumulate length with anomalously low associated displacement. This is important as it provides direct evidence for predictable variation in the mechanics of fault growth when influenced by shear strength heterogeneities in the rock mass. Tip gradients for the isolated sub-set of faults selected from Dawers et al. (1993) are intermediate in magnitude between the tips of joint controlled and non-joint controlled potentially interacting faults. The standard deviations for isolated fault tip gradients are predictably small owing to the size of the data set although it may be expected that isolated faults have more constant tip gradients than those experiencing interaction.

The relationship between fault tip gradients and O:S ratios, if any, is ambiguous as there is much scatter in the cross-plots. The maximum range of tip gradients on Figure 5.8 occurs at an O:S value of approximately 2.55. The average O:S ratio for surveyed faults is 2.54 so the full range of tip gradients occurs at an average O:S value. The range of tip gradients narrows with increasing O:S ratio. When joint controlled faults are excluded however, a potentially important lower bounding positive correlation above O:S ratios of 3 is highlighted on Figure 5.8.

5.5 O:S plots normalised by fault length

After discovery of a broad positive correlation between D_{max}:L and O:S ratios in section 5.3, this section asks whether O:S ratios are controlled by fault interactions. In order to approach this issue directly, O:S ratios on the Tableland are studied in a scale independent fashion from aerial photo analysis. Rather than plotting overlap versus separation, both parameters are normalised by the length of each fault in an interacting pair respectively, and then plotted against each other. This is done in a similar manner to that described in Gupta & Scholz (2000a). Figure 5.9 thus shows a plot of $O/L_{(1/2)}$ vs $S/L_{(1/2)}$, where $L_{(1/2)}$ refers to the length of the two faults in the interacting pair respectively, i.e. O and S are plotted twice, once dividing both by L_1 and once dividing both by L_2. This yields a scale independent analysis of O:S ratios on the Tableland. Faults affected by joints are plotted as a separate data series.

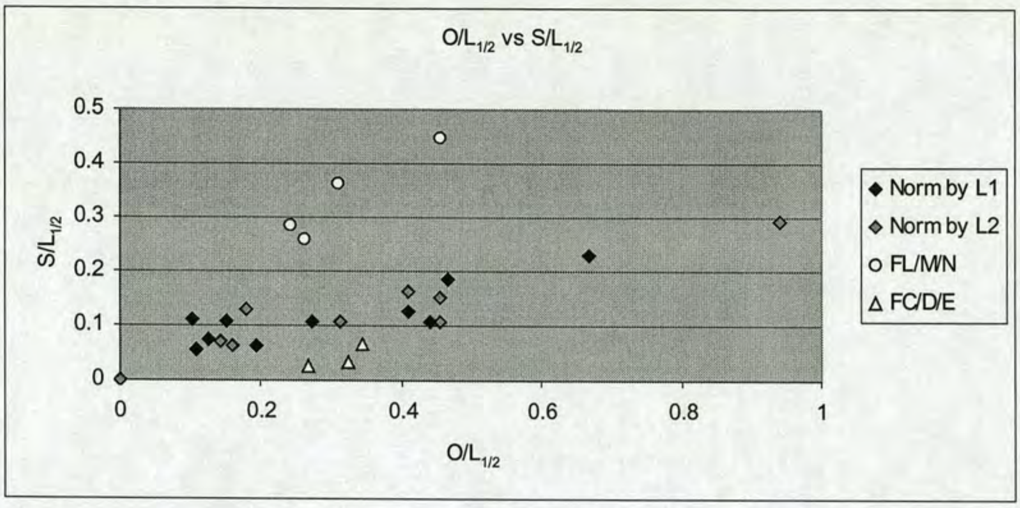

Figure 5.9. Overlap plotted against separation for fault pairs surveyed for this project, with both parameters normalised successively by the length of each fault in the pair (i.e. Norm by L_1 and Norm by L_2). Faults affected by joints are plotted separately and highlighted as the white data points (i.e. FL/M/N and FC/D/E).

5.5.1 Normalised O:S plot interpretation

Data points in Figure 5.9 show a wedge, devoid of data, of increasing width on moving away from the origin. A lower bounding positive correlation is thus present in the data set in a similar manner to that seen in Figure 5.6. Several of the lowest points that bound the data wedge are for partially joint controlled faults, specifically faults C, D and E. Gupta & Scholz (2000a), undertaking a similar analysis of O:S ratios for cm-scale faults in the Solite quarry, found a similar area devoid of data points. These authors suggested a theoretical basis for this phenomenon via the numerical modelling of fault interactions in an elastic material. They showed that an elliptical area devoid of data points could represent a generic area of sufficiently high stress reduction that faults could not propagate into this zone (Figure 5.10). The data of Gupta & Scholz (2000a) are added to Figure 5.9 for comparative purposes in Figure 5.11. The 2 data sets, from very different tectonic settings and covering 2 orders of magnitude of fault dimensions, span very similar ranges. The implications of this shall be considered in the synthesis of field results at the end of this chapter.

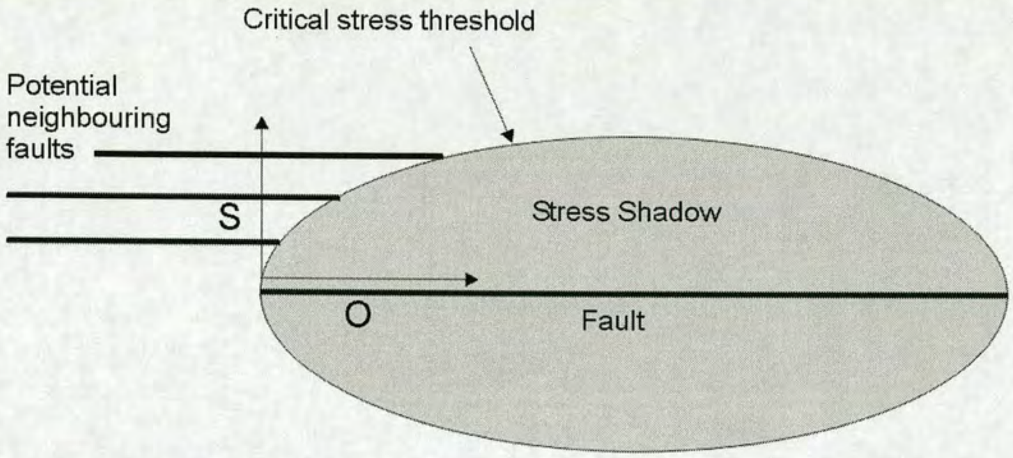

Figure 5.10. Cartoon of a stress shadowing effect on impeding fault pair overlap at varying separation distances. Increasing the separation distance between potential neighbouring faults in a pair allows for increasing fault overlap.

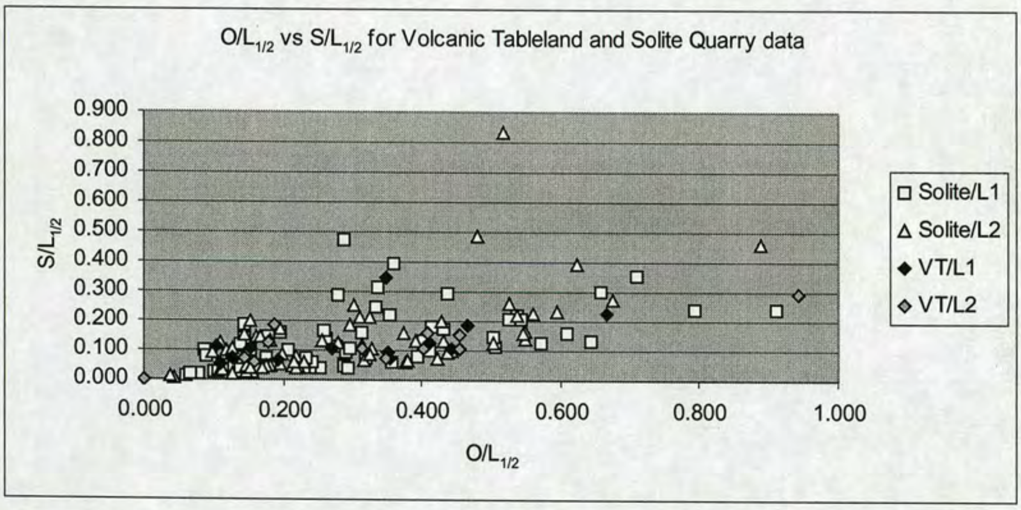

Figure 5.11. Length normalised O:S plot comparing data from Figure 5.9 with data from cm-scale faults from the Solite quarry, made available for use by Anupma Gupta.

5.6 Normalised O:S vs D_{max}:L

D_{max}:L ratios of individual faults are now plotted against length normalised O:S ratios (Figure 5.12) to look for any predictable changes in D_{max}:L ratios upon moving toward the threshold of the fault free area identified in Figure 5.9. Faults O and Q, which are affected by fumaroles and have anomalous D_{max}:L ratios as a result, are omitted from this discussion. Each normalised O:S ratio is plotted twice as it must be plotted against the D_{max}:L ratio of both faults making up the pair.

5.6.1 Interpretation of normalised O:S vs D_{max}:L

The 2 plots of Figure 5.12 show a general increase in D_{max}:L ratios toward the length normalised overlap axis and the origin. This suggests that fault interactions are increasing toward the threshold of the fault free area identified in Figure 5.9. In order to highlight and aid in identification of such existing trends, the data from Figure 5.12 are converted into pseudo-3D surfaces. Figure 5.13 shows these surface plots. The plan view surface is gridded in increments of O/L and S/L. The third dimension in height represents the D_{max}:L ratio of a fault with such a normalised O:S ratio. In order to build the surface a linear interpolation algorithm is applied to turn an irregular array of points into a gridded surface. This introduces some error in areas of sparse data coverage but these can easily be identified with reference to the original data plot. In sections 5.3 and 5.4 it was shown that D_{max}:L ratios and tip gradients increase with increasing O:S ratio, although with a significant degree of scatter in both cases. It is this degree of scatter that is responsible for introducing complexity to the plots in Figure 5.12.

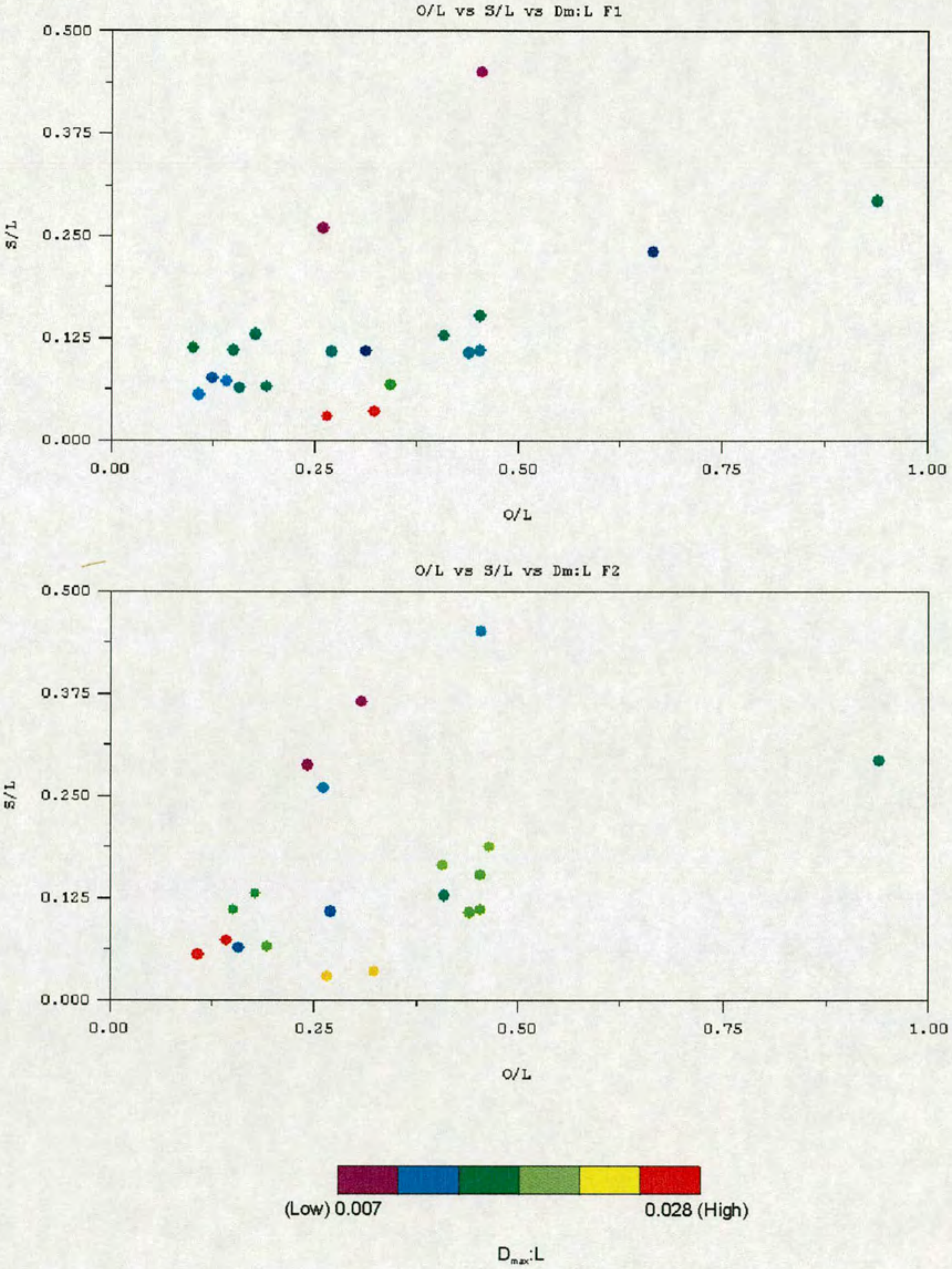

Figure 5.12. $O/L_{(F1/F2)}$ vs $S/L_{(F1/F2)}$ vs $D_{max}:L_{(F1/F2)}$ for surveyed fault pairs. D_{max}:L ratios are colour coded for magnitude as per the key beneath the plots.

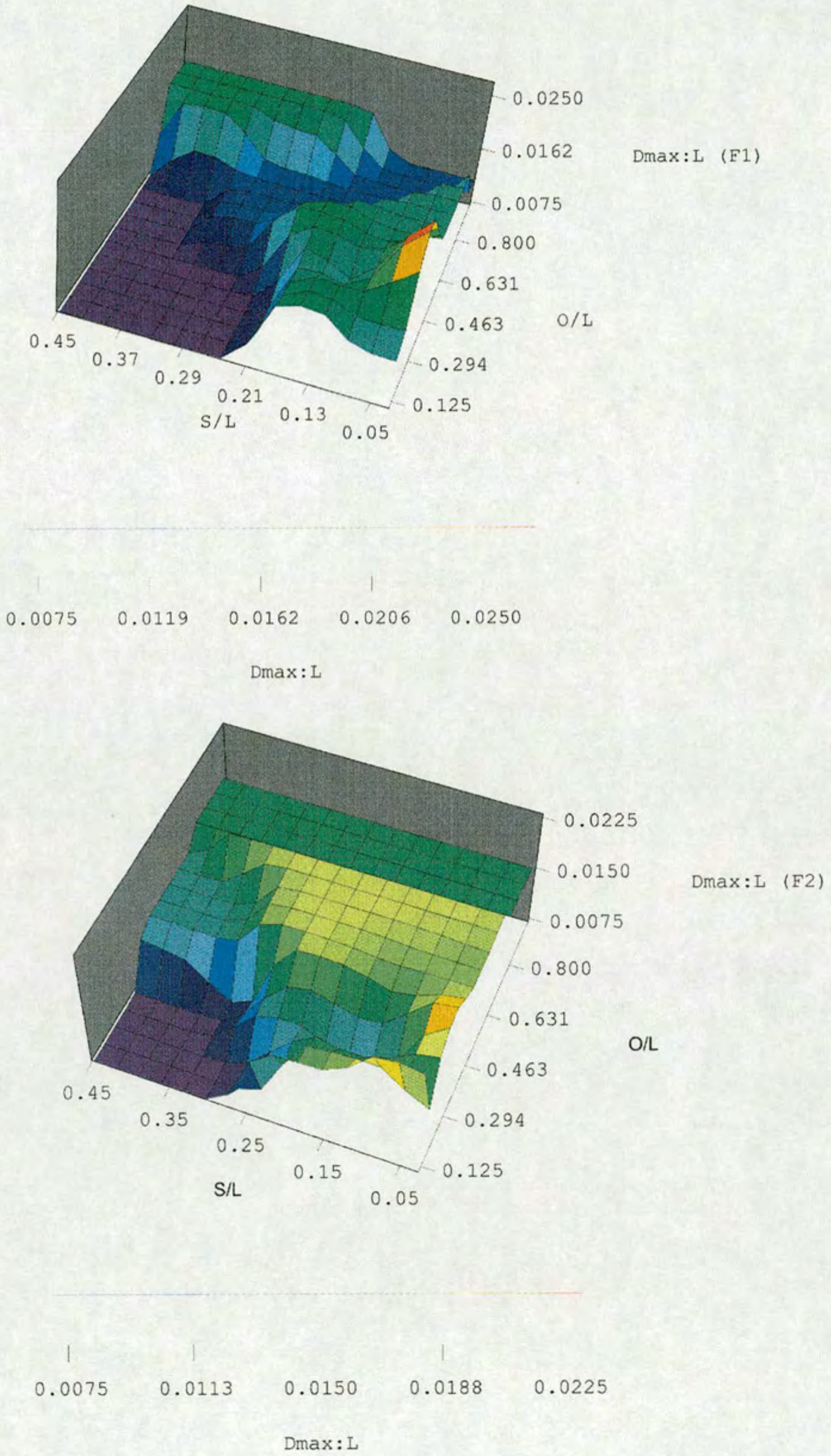

Figure 5.13. Pseudo-3D surfaces constructed from the data in Figure 5.12. The surface is gridded in increments of O/L and S/L and the third dimension is the D_{max}:L ratio of one fault in the pair (F1 then F2 respectively). In both plots, the highest topography, equivalent to the highest D_{max}:L ratios, can be found along the overlap

axis, especially toward the origin. This indicates strengthening fault interactions at low separations for a given overlap.

5.7 Deformation free zones adjacent to faults

Analysis of aerial photos clearly shows that semi-elliptical areas in the footwall high regions of several major fault structures are almost wholly free of deformation, be it in the form of joints or faults (Figure 5.14).

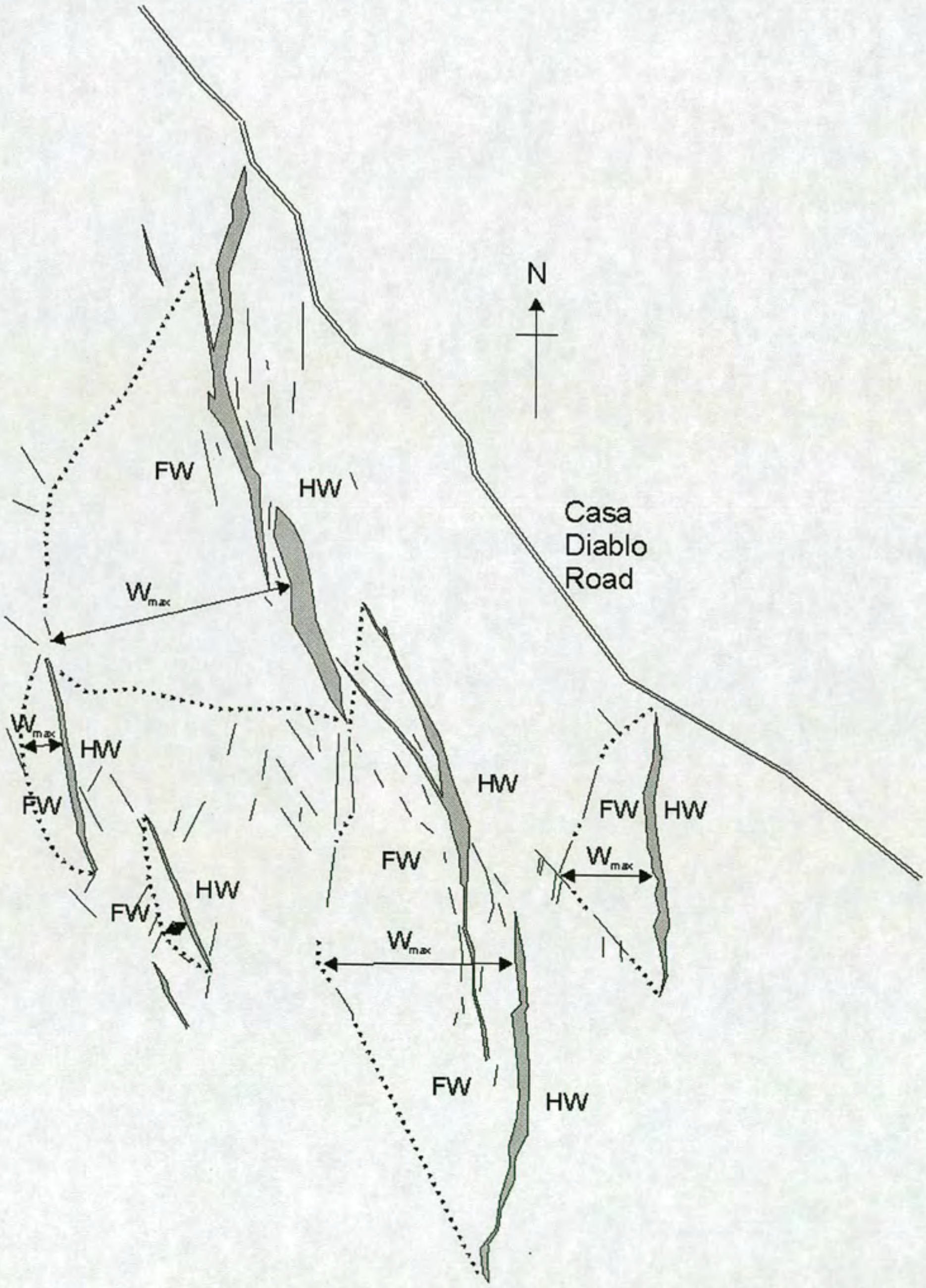

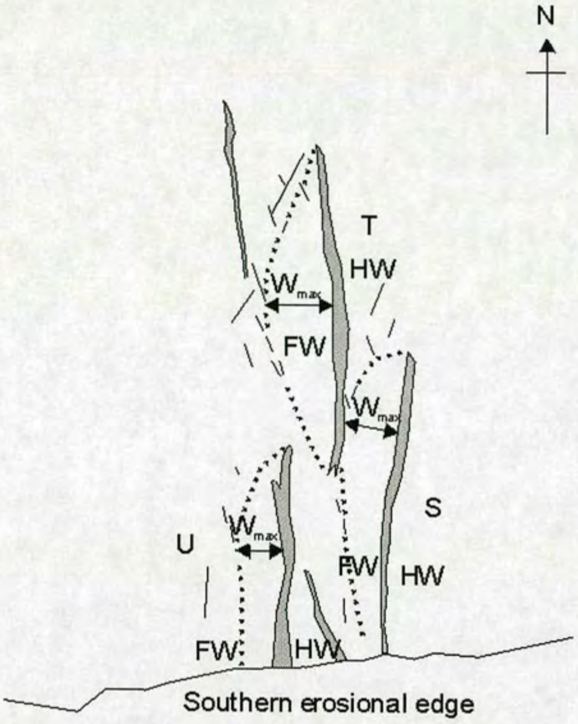

Figure 5.14. Annotated aerial photo tracings showing deformation free areas in the footwall of major faults. W_{max} refers to the maximum width of these deformation free zones and the dashed lines show the fault or linked fault arrays that the zones appear to scale with. The upper figure shows the fault array surveyed by Dawers and Anders (1995) while the lower figure shows faults S, T and U surveyed for this project.

Figure 5.14 suggests that all of the deformation free zones correspond in length with one fault segment or the combined length of an overlapping multi-segment structure. This observation implies that the dimensions of these deformation zones are related to their associated fault structures. Thus, the maximum width of these zones is plotted against the total arcuate fault length of the structure that they appear related to in Figure 5.15. Similar deformation free areas are not present in the hangingwall of the featured faults.

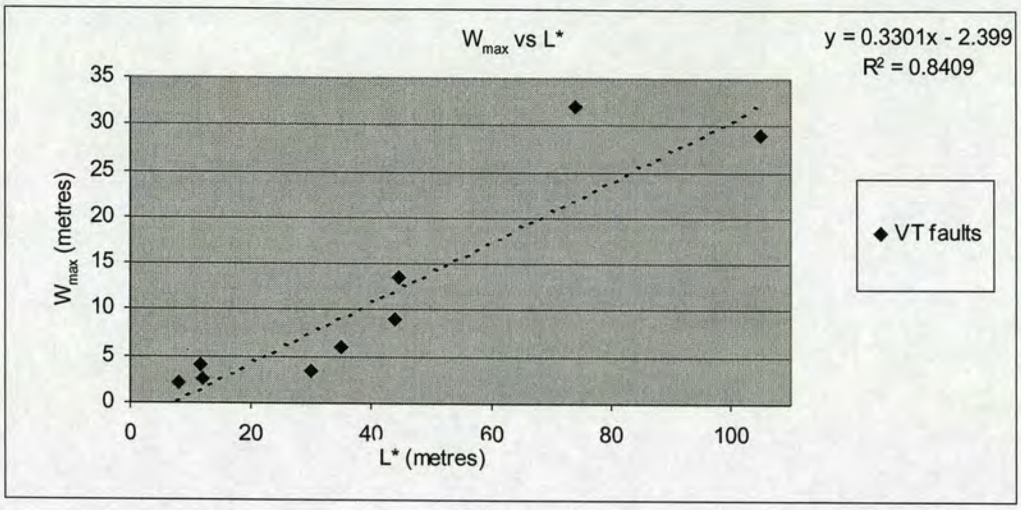

Figure 5.15. Maximum widths of deformation free zones (W_{max}) vs the total arcuate fault length of the structure they appear to scale with (L*). Both parameters are recorded in metres.

5.7.1 Interpretation of deformation free zones

A positive linear correlation exists between the width of deformation free zones and the total length of the related structure (Figure 5.15). An R^2 correlation co-efficient of 0.8409 is attained, suggesting a strong linear relationship exists between the 2 variables. It should be noted that only the clearest, most unambiguous examples of this phenomenon, as recognised in aerial photos, are used in Figure 5.15. Numerous other examples are recognised qualitatively, although the resolution of joint trends or fault lengths may be poor in these cases and so they are not included.

The gradient of the best-fit regression line shows that the width of the deformation free zones is proportional to 1/3rd of the total arcuate fault length to which the zone corresponds. This suggests that these faults may be controlling the development of adjacent deformation over a significant distance perpendicular to fault strike. If these deformation free zones are considered analogous to the crack shields found by Ackermann and Schlische (1997) (see Ch1), where the width of the crack shield (S) was equal to 3*d, which for a D_{max}:L ratio of 1:100 gives a crack shield width of 0.03L, the zones on the Tableland are 10 times as wide. Significant potential for future work exists in this area as the width of the deformation free zones may provide clues to the fault aspect ratio (N.Dawers, Pers.Comm., 2002), or indeed the width may scale with displacement variations and thus potentially with stress drop.

5.8 Synthesis of field evidence for fault interactions

The summary section at the end of Chapter 1 presented the fault interaction issues on which this thesis intended to focus. Chapters 3, 4 and 5 have presented and discussed data that advance the current state of understanding in these areas. The results obtained and their implications are summarised below in the order in which the major issues of interest were listed at the end of Chapter 1. Results from the analysis of the geometrical evolution of relay ramps will be discussed at the end of Chapter 6.

- Isolated faults on the Volcanic Tableland are quantitatively re-defined from the data available as those separated from their nearest neighbour by greater than $0.1*L_t$, where L_t is the summed length of the two faults in question. Fault pair separation distance exerts a control on the strength of fault interactions at separations of less than 0.1*Lt, specifically fault interactions strengthen with decreasing separation distance.

- D_{max}:L ratios are predictably higher for faults in overlapping pairs or multi-segment arrays than faults growing in comparative isolation in the same setting. This is assigned to the role of fault interactions and D_{max}:L ratios are used as a guide to a fault's interaction state. Profile asymmetry can be seen for many faults although is shown to be easily obscured for structures of this scale by fault interaction with rock mass heterogeneities, fault linkage or fault interaction at both tips. The D_{max} magnitude and location on a fault segment provides crucial information on the spatial history of fault growth along strike. Taken in tandem with the fault length, D_{max} can reveal if a fault has grown in a predictable manner with D_{max} increasing steadily with L, or if variations in this style of growth have occurred, e.g. have fault interactions caused the accumulation of displacement to increase at the expense of fault length.

- D_{max}:L ratios show a positive correlation with the O:S ratio of an interacting fault pair. This suggests that fault interactions strengthen with attainment of increasing overlap for a given separation distance. Fault pair O:S ratios are also restricted by fault interactions. Fault pairs are shown capable of attaining increasing overlap only by increasing the separation distance between faults. This suggests areas of stress reduction are present around the body of faults that scale with the total length of the fault, an area into which neighbouring faults will not propagate.

- Rock mass heterogeneity is shown to significantly affect fault growth. Faults growing into or along joints have anomalously low tip gradients and D_{max}:L ratios. Faults blocked by fumaroles have anomalously high tip gradients and D_{max}:L ratios. These heterogeneities thus act as zones of low and high shear strength respectively within the rock mass, and can significantly disguise a fault interaction signal.

- Fault interaction signals, in the form of elevated D_{max}:L ratios, have been identified for faults in this field area that have unambiguously grown through multiple earthquake cycles. The strength of fault interactions is shown to increase with increasing relative fault proximity. The range of overlap ratios attainable by fault pairs is restricted by fault interactions. These results show some concordance with the general results of static-elastic models for fault interaction where faults grow in one event, and stress changes in the surrounding rock mass scale with the final fault size. For field data to show some coherency with the results from these models suggests that stress changes, as induced by earthquakes, are capable of at least partially accumulating in the rock mass over multiple slip cycles. Were this not so, faults should not display the signs of fault interaction found here, the nature of which implies the existence of stress perturbations in the rock mass that scale with the final fault dimensions.

Chapter 6 – Relay ramp evolution

6.1 Rationale

During fault array evolution, the formation and breaching of relay ramps is an ongoing process as fault segments grow into overlapping configurations and link (e.g. Larsen, 1988; Morley et al., 1990; Peacock and Sanderson, 1991; Gawthorpe & Hurst, 1993; Anders & Schlische, 1994; Peacock & Sanderson, 1994; Trudgill & Cartwright, 1994; Childs et al., 1995; Dawers & Anders, 1995; Huggins et al., 1995; Mack & Seager, 1995; Cartwright et al., 1996; Crider & Pollard, 1998; McFadzean et al., 1999; Peacock et al., 2000; Ferrill & Morris, 2001). Mechanisms of relay ramp growth are intrinsically related to the development of their bounding faults into an overlapping geometry (e.g. Ch5) and the rheological behaviour of the ramp material. However, relay ramps and their bounding faults are seldom well preserved at the ground surface for study and so the fundamental controls on their geometrical evolution and on fault linkage remain poorly understood.

This chapter provides a detailed analysis of the relationship between fault and ramp evolution, incorporating high-resolution field survey data on both components. Of particular interest, with a view to understanding the mechanics of ramp evolution, is the relationship between present-day ramp topographies, including ramp dip directions and gradients, with the spatial proximity and cutoff gradients (see definition in section 6.2) of bounding faults, and the presence or absence of linking faults within the ramp. Is ramp strain controlled by the cutoff gradients of the ramp bounding faults? Can fault propagation folding beneath a ramp be identified by its affect on ramp strain? Can the spatial geometry of overlapping faults be used to imply a likely ramp dip direction? Can relay ramp strain be used to predict the likelihood of fault linkage? Does significant fault interaction necessarily imply significant ramp strain? Previous studies on relay ramp evolution have seldom included high resolution data on all these components, thus making a multi-component study, such as undertaken here, unfeasible.

Relay ramp evolution has also been simulated in the fault interaction model of Crider and Pollard (1998). Significantly, this model, with the same founding mechanical principles as the fault interaction model of Willemse (1996) and Willemse et al. (1997) discussed in earlier chapters, fails to correctly predict the ramp dip direction commonly encountered in the field, i.e. toward the collective hangingwall of an interacting fault pair. This major discrepancy between modelling results and field observations provides further motivation to undertake a study of this kind.

Given the tendency for relay ramps to act as zones of preferential fluid transfer in evolving extensional basins, both on the surface (e.g. Morley et al., 1990; Gawthorpe & Hurst, 1993) and in the subsurface, anticipating the state and orientation of ramp breaching with regard to the impedance or enhancement of fluid flow is of fundamental importance, particularly in the hydrocarbon industry. A predictive tool for fault linkage would also be very useful in the interpretation of seismic reflection data where faults affecting a ramp may be beneath the limits of seismic resolution. Relay ramps, if unbreached, may also act in some instances as barriers to earthquake propagation (dePolo et al., 1991) and are thus integral components of any assessment of seismic hazard. This study contributes to an area of field research that remains relatively undeveloped, yet is of critical importance to understanding fault interactions and the mechanics of fault growth (e.g. Schultz, 1999).

6.2 Relay ramp development

As two proximal normal faults grow into an overlapping situation (e.g. Ch5), the rock mass separating the faults in the region of overlap must deform to accommodate the distribution of displacement across this area. This area of deformed rock, between overlapping fault tips, has been referred to variously as a relay structure (Larsen, 1988), relay ramp (e.g. Peacock and Sanderson, 1994; Trudgill & Cartwright, 1994), relay zone (Crider & Pollard, 1998) and transfer zone

(Morley et al., 1990) amongst others (Figure 6.1). The term relay ramp is chosen for use in this project.

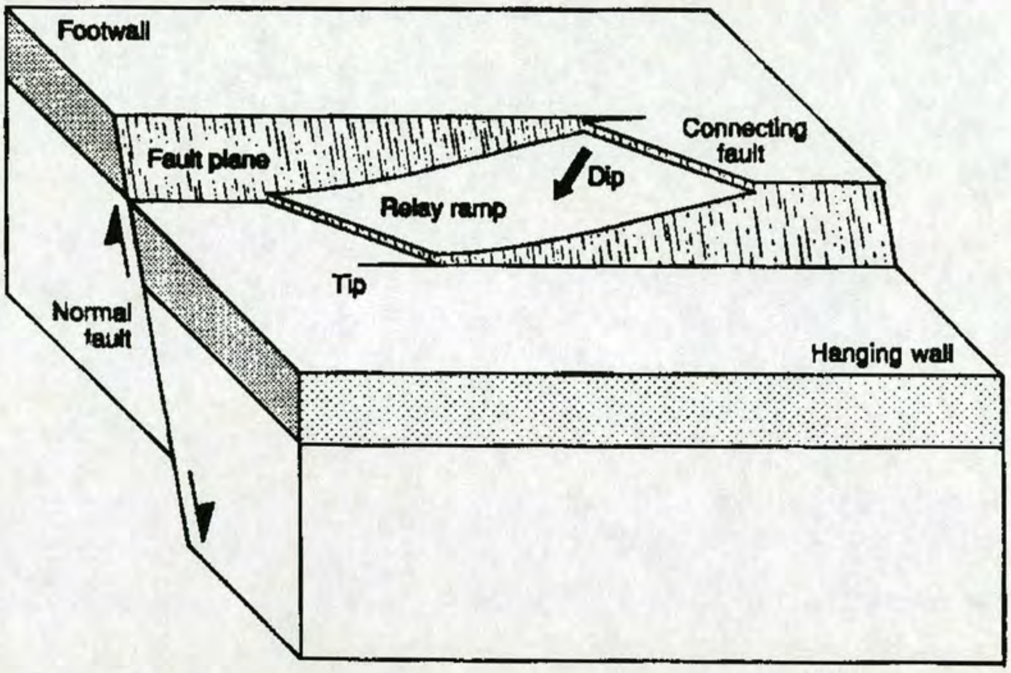

Figure 6.1. Figure 1 from Peacock and Sanderson (1994) showing the basic components of a linked relay ramp separating two overlapping normal faults.

Figure 6.2 shows in more detail the geometrical components of a relay ramp whose evolution will undergo analysis in this chapter. Of particular interest in this study are the cutoff gradients of the ramp bounding faults, defined as the topographic gradient encountered walking along the footwall of the front fault and hangingwall of the back fault in the region of fault overlap. Cutoff gradient magnitudes have previously not been incorporated into a survey based field study of relay ramp development.

Initial deformation of a relay ramp, assuming sufficient rock strength and a sufficiently low strain rate has been described as ductile on a large scale (Larsen, 1988; Walsh and Watterson, 1991; Peacock and Sanderson, 1994; Trudgill and Cartwright, 1994). This is proposed to explain the development of an approximately coherent ramp separating the footwall cutoff of one fault from the hangingwall cutoff of an overlapping fault.

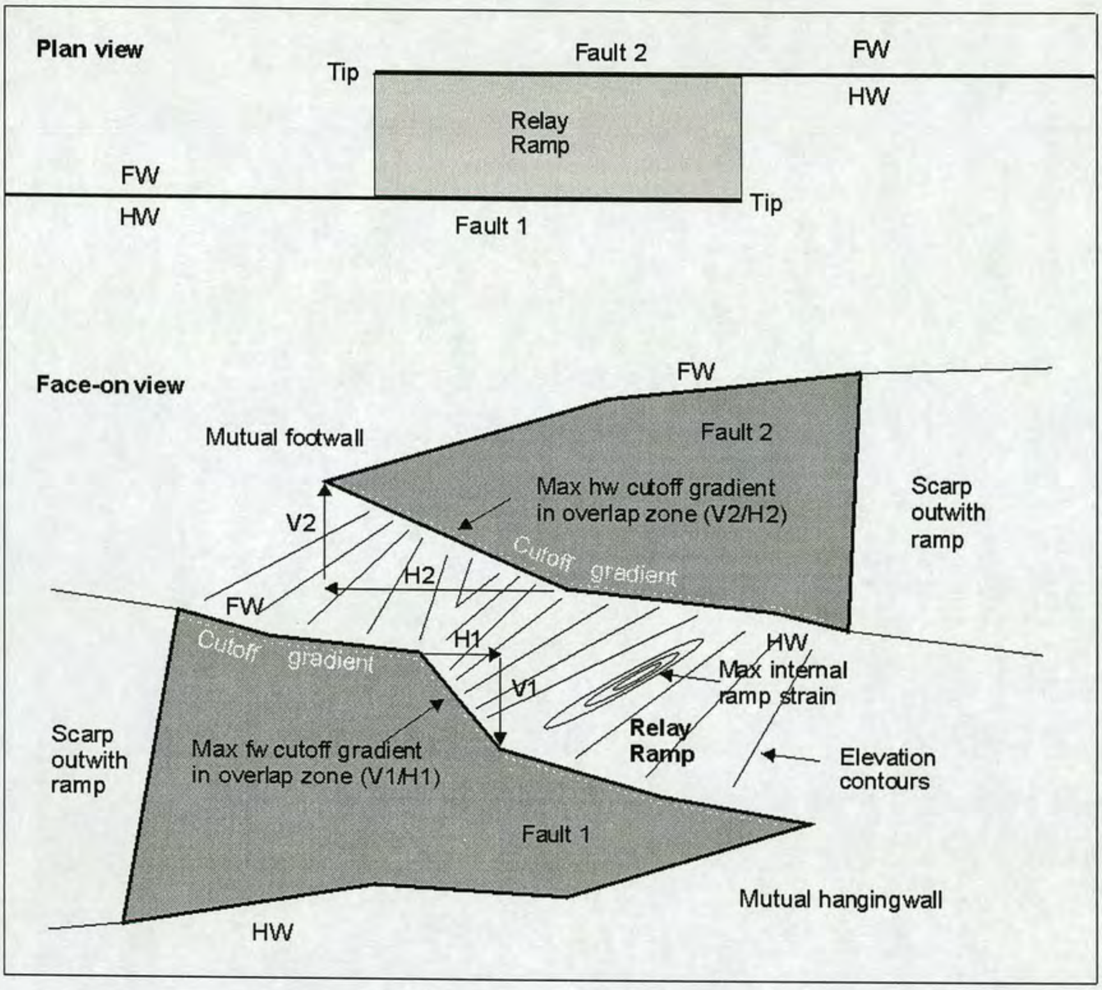

Figure 6.2. Fundamental geometrical components of a relay ramp in plan and face-on view, with sketched elevation contours, decreasing in height from left to right. Cutoff gradients are defined as the topographic gradient encountered walking along the top or bottom of a fault scarp within the ramp and as such are different from tip gradients that combine information from the high and low side of the fault. The maximum cutoff gradients are defined for the footwall of fault 1 and the hangingwall of fault 2 as V1/H1 and V2/H2 respectively. Ramp gradients are taken as a proxy for ramp strain and as such the maximum internal ramp strain is represented by an elliptical zone of anomalously tight contours that exceeds the adjacent cutoff gradients on the bounding faults.

With increasing strain and extension, brittle deformation commences with the formation of visible fractures in the ramp (e.g. Larsen, 1988; Walsh and Watterson, 1991; Peacock and Sanderson, 1994; Trudgill and Cartwright, 1994).

Ramp deformation prior to linkage is not described as elastic behaviour in the cited papers above, although many may implicitly assume a component of elastic strain. The relationship between ramp strain and brittle ramp failure depends on the rheological behaviour of the ramp material. Chapters 4 and 5 have presented evidence, in the form of stress shadows and fault array geometries amongst others, for elastic interactions between faults in this setting. The tuff is thus suggested to be capable of accumulating some degree of elastic strain over the geological time-scale. Considerable ambiguity exists in the literature over the use of the term "ductile" to describe deformation (Twiss and Moores, 1992) with some authors using the term in a qualitative fashion referring to ramp deformation on a mesoscopic scale. In order to maintain consistency with previous chapters, the preference here is to describe the formation and eventual failure of relay ramps as representing different stages in the evolution of a material under increasing strain in the elastic-brittle regime. Figure 6.3 shows a plot of displacement versus stress for a granite sample under axial loading in the laboratory (Figure 1 from Lockner et al. (1991)). Between stages 'a' and 'b' in this figure, near the top of the elastic deformation curve, a flattening of the stress-strain curve occurs as brittle failure commences on a microscopic scale prior to complete throughgoing failure of the sample. The period between stages 'a' and 'b' is thought equivalent to the stage of ramp development when sufficient elastic strain has accumulated and ramp failure has commenced on a small scale prior to major through-going breaching of the ramp.

As shown in Figure 6.1, relay ramps are often breached by linking or connecting faults. Partially linked or unlinked faults may be described as 'soft-linked' in the literature (Walsh & Watterson, 1991). If fractures traverse the entire ramp without a break, the faults become 'hard-linked' (Trudgill & Cartwright, 1994). The term 'abandoned' is sometimes used to describe these hard-linked ramps. Recognition of abandoned ramps in the field requires the identification of fully breached ramps, often difficult if erosion and sedimentation obscure evidence for linkage. In seismic reflection data, the recognition of distinct changes in fault strike with associated displacement minimum (Peacock & Sanderson, 1991) often suggest the presence of a breached ramp.

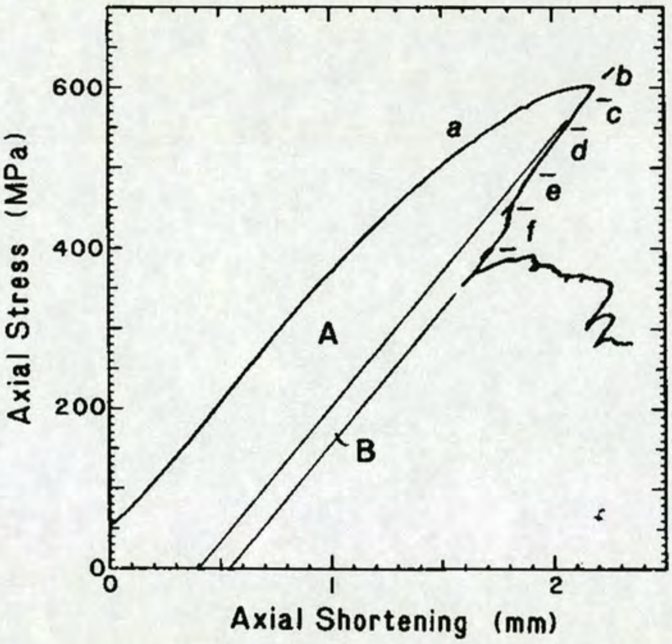

Figure 6.3. Figure 1 from Lockner et al. (1991) showing displacement vs stress for a sample of granite under axial loading in the laboratory. The initial linear gradient represents elastic or recoverable deformation. Between 'a' and 'b' there is a flattening of the stress-strain curve as brittle failure commences on a microscopic scale but overall sample strain is still increasing. At 'b' there is complete brittle failure of the sample and development of a through-going failure plane.

The nature of fault growth in 3 dimensions is such that a fault plane which anastamoses with depth may preserve a variety of unbreached and breached ramps in different 2d sections through the fault (Huggins et al., 1995).

6.3 Relay ramp survey sites

The Volcanic Tableland is a low strain setting of less than a few percent (Dawers et al., in revision) and so preserves a large number of unbreached or partially breached relay ramps between overlapping fault pairs. Relay ramps selected for this study display well preserved bounding fault tips and a wide range of overlap (O): separation (S) geometries. Both soft-linked and hard-linked examples are selected. Figures 6.4 and 6.5 show the ramps that are selected for surveying in this study on annotated aerial photos.

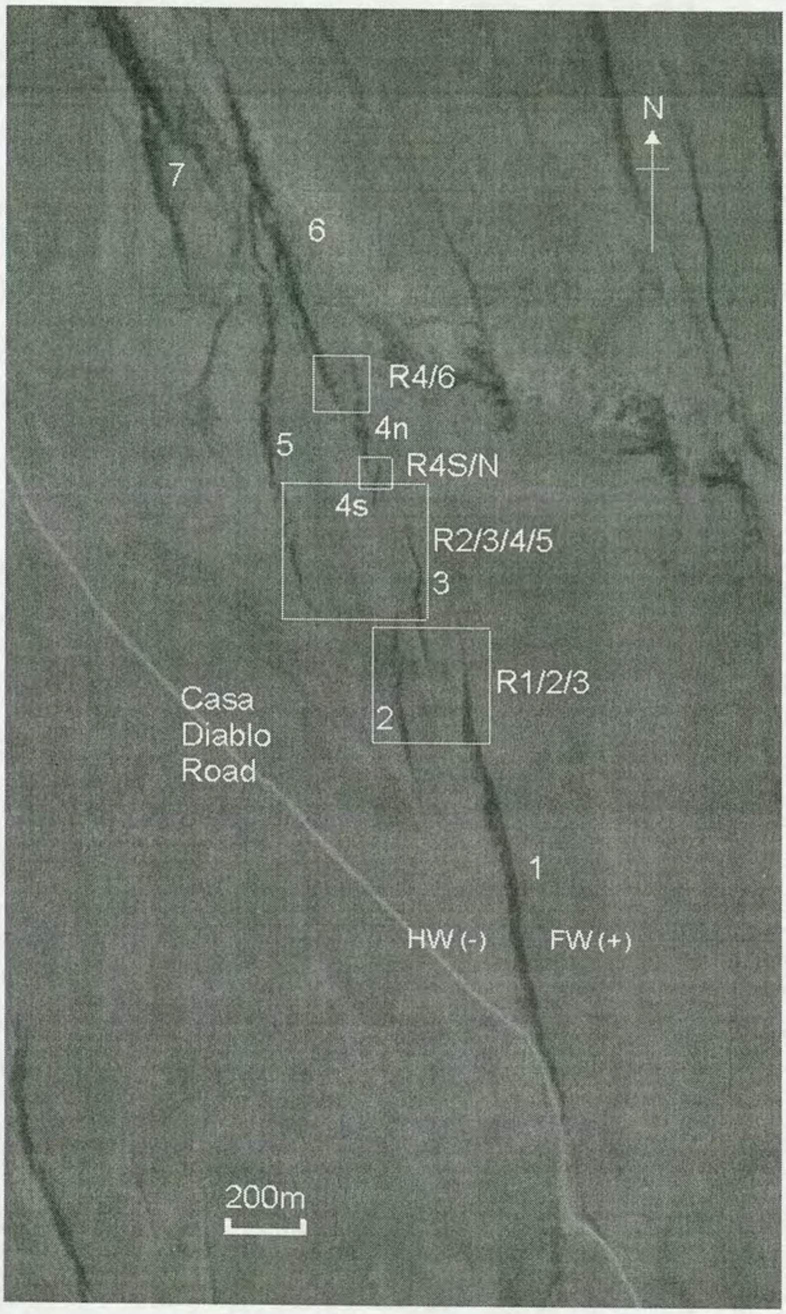

Figure 6.4. Annotated aerial photo showing approximate ramp survey areas from the fault array containing faults 1-7. Note that all faults in this array have the same sense of throw as that marked for fault 1.

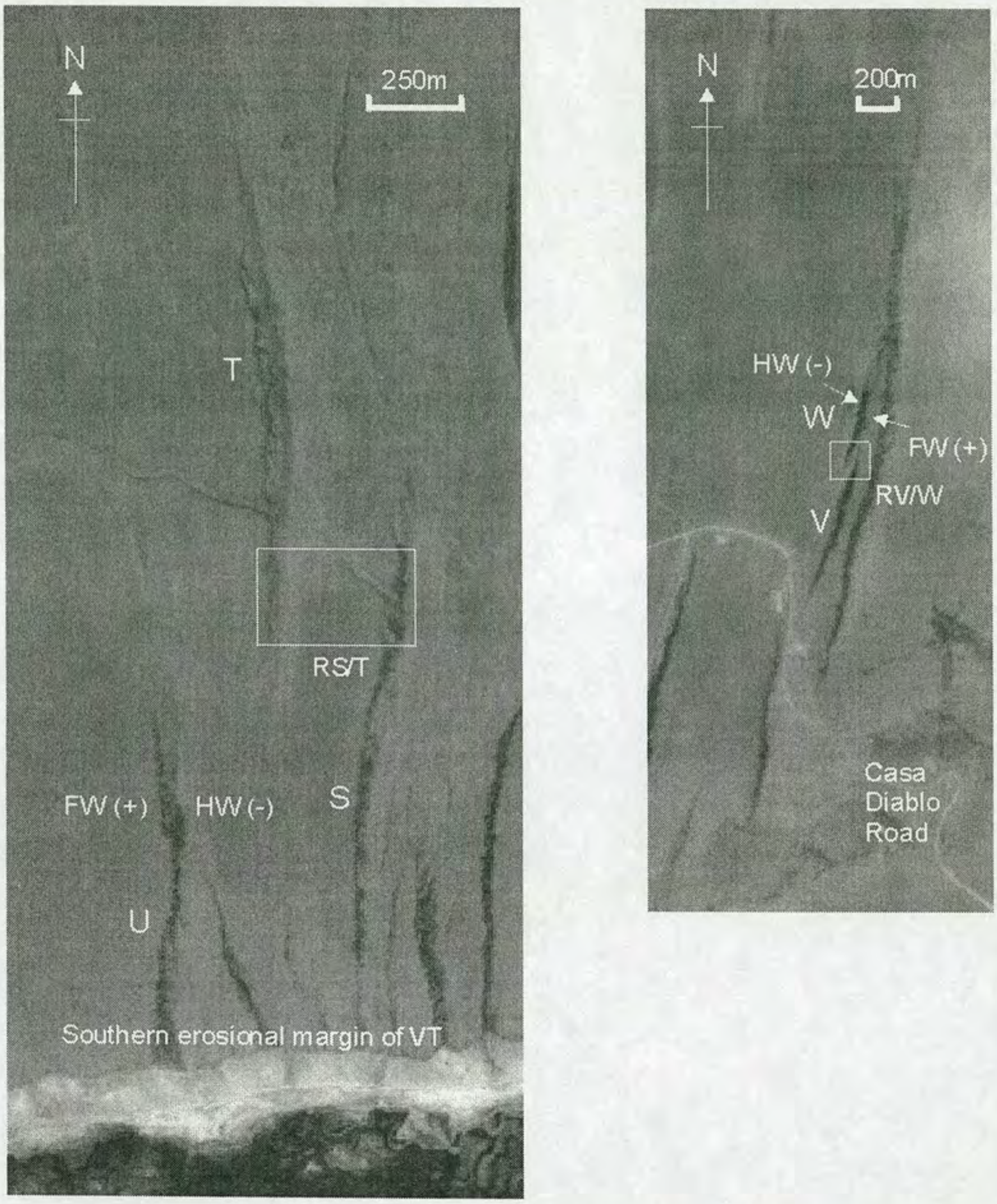

Figure 6.5. Annotated aerial photo showing approximate ramp survey areas from fault pairs S/T and V/W. Note that faults S, T and U have the same sense of throw as that marked for fault U and faults V and W have the same sense of throw as that marked for W.

6.4 Relay ramp data

Ramps were surveyed using a total station laser-theodolite system in the same manner as for some of the fault scarp surveys. The use of the total station surveying system was outlined in section 3.3.1. In order to create a grid of data points for each ramp, surveying is done in successive transects carried out on specific compass bearings. Ramp topography data for each case studied is plotted in 2 dimensions (i.e. maps) and contoured for the third dimension, i.e. height (Figure 6.6). Subsequent ramp descriptions in section 6.5 include simplified versions of the maps in Figure 6.6 highlighting the salient geometrical features, including internal ramp gradients and fault cutoff gradients, for each ramp. The tangents of ramp dip magnitudes at varying points across each ramp are plotted as a proxy for relay ramp strain.

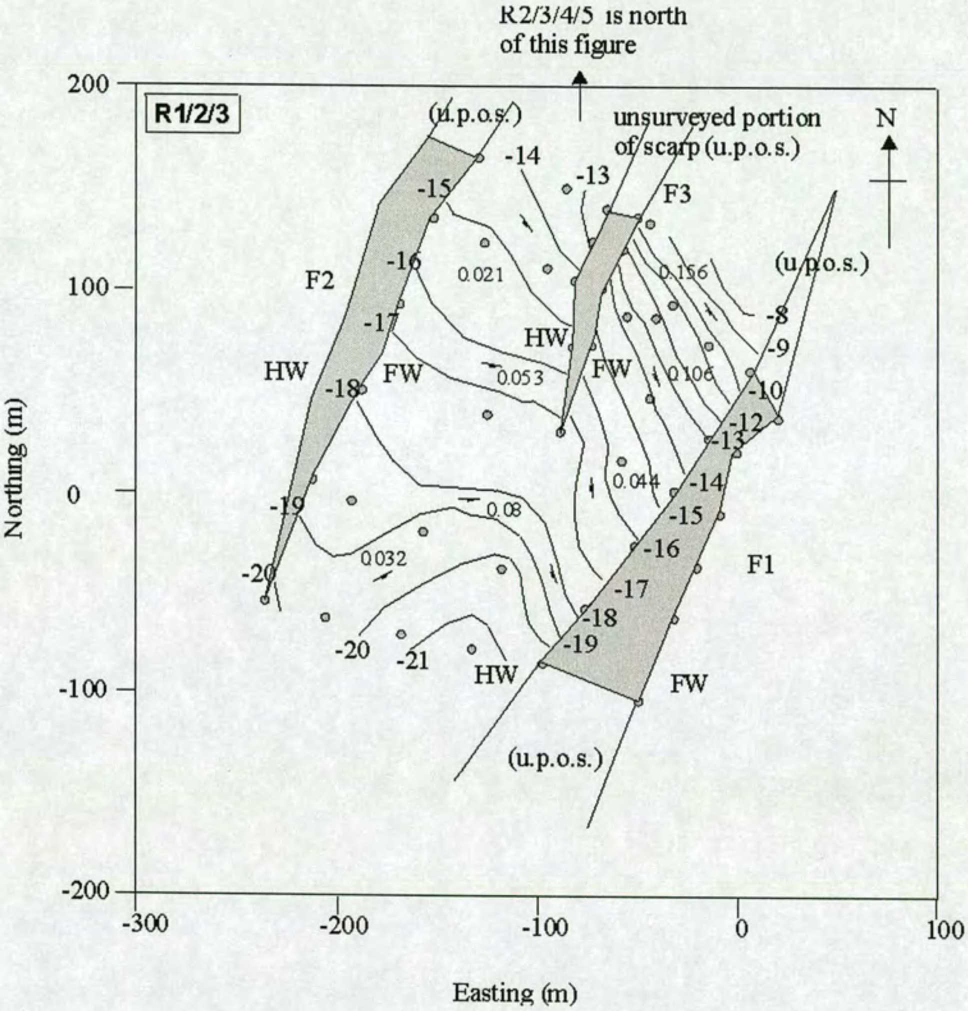

Key			
○	Original survey point	↘	Ramp dip direction
-16	Scarp cutoff heights - relative to a base station location and given in metres	0.105	Tan of ramp dip

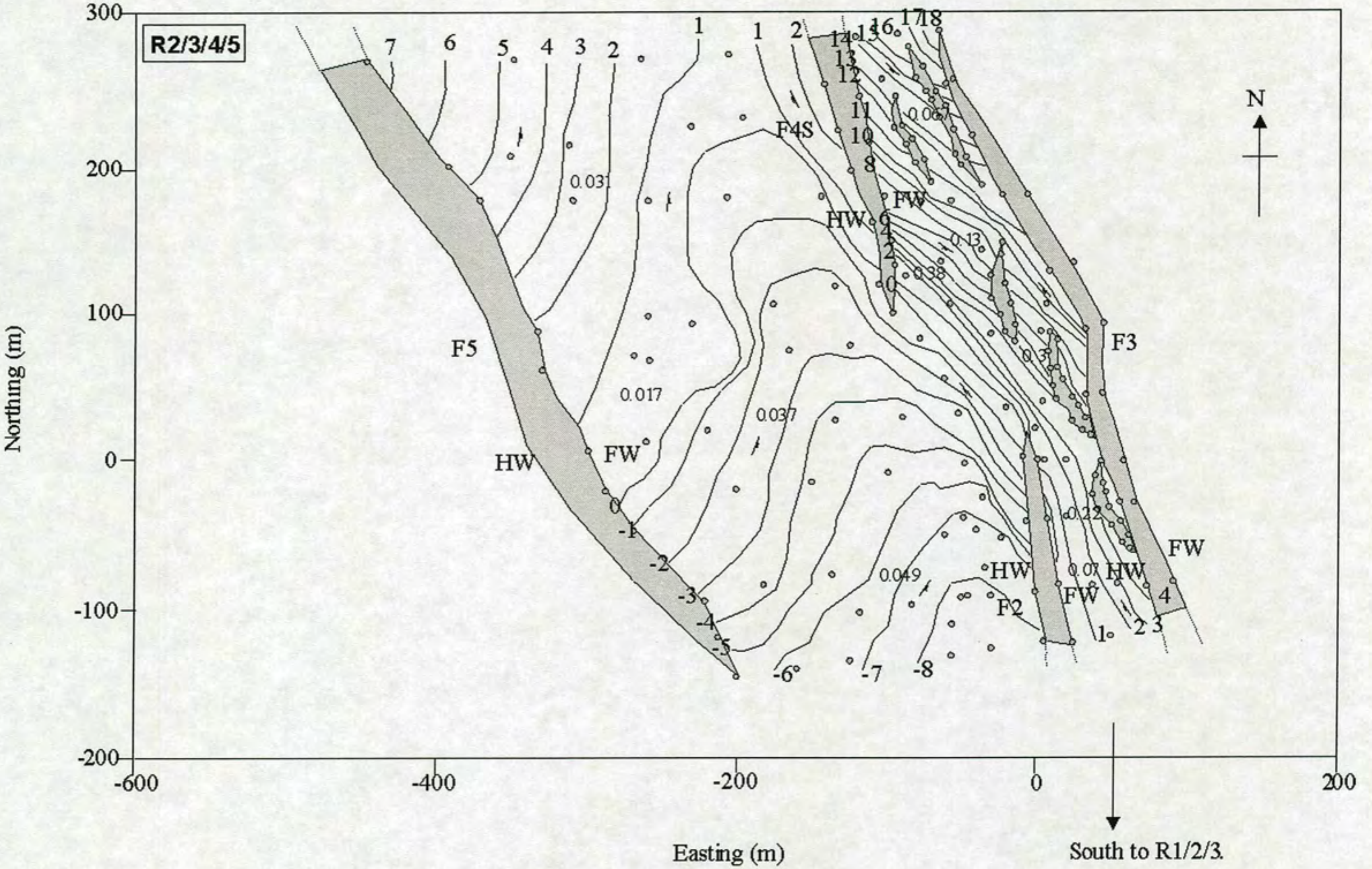
R2/3/4/5
N
F5
F4S
F3
F2
HW
FW
0.031
0.017
0.037
0.067
0.13
0.38
0.3
0.22
0.07
0.049
Northing (m)
Easting (m)
300
200
100
0
-100
-200
-600
-400
-200
0
200
South to R1/2/3.

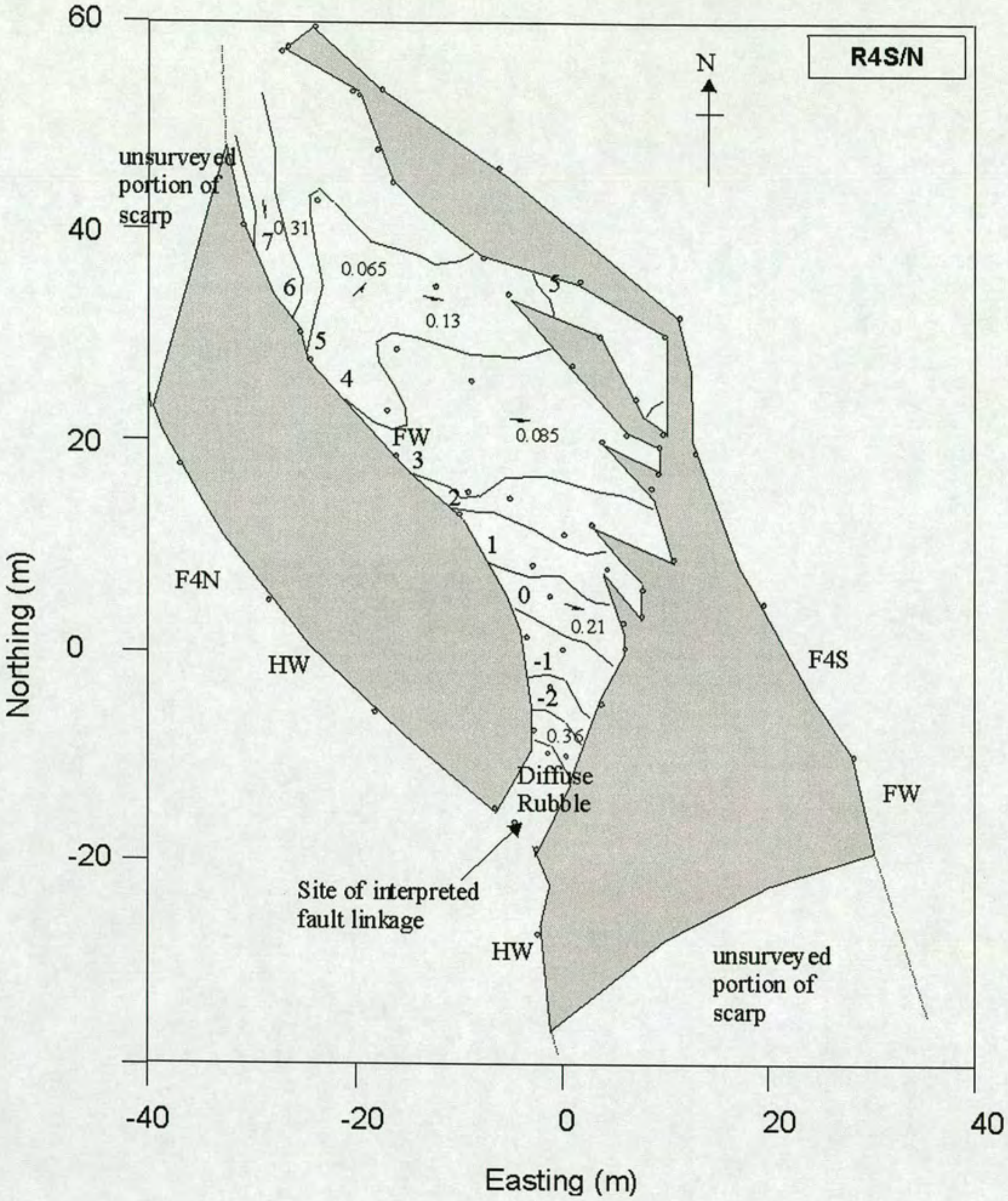
R4S/N
N
unsurveyed portion of scarp
0.31
7
6
0.065
0.13
5
5
4
FW
3
2
1
0.085
0
0.21
F4N
HW
-1
-2
0.36
F4S
Diffuse Rubble
FW
Site of interpreted fault linkage
HW
unsurveyed portion of scarp
Northing (m)
60
40
20
0
-20
Easting (m)
-40
-20
0
20
40

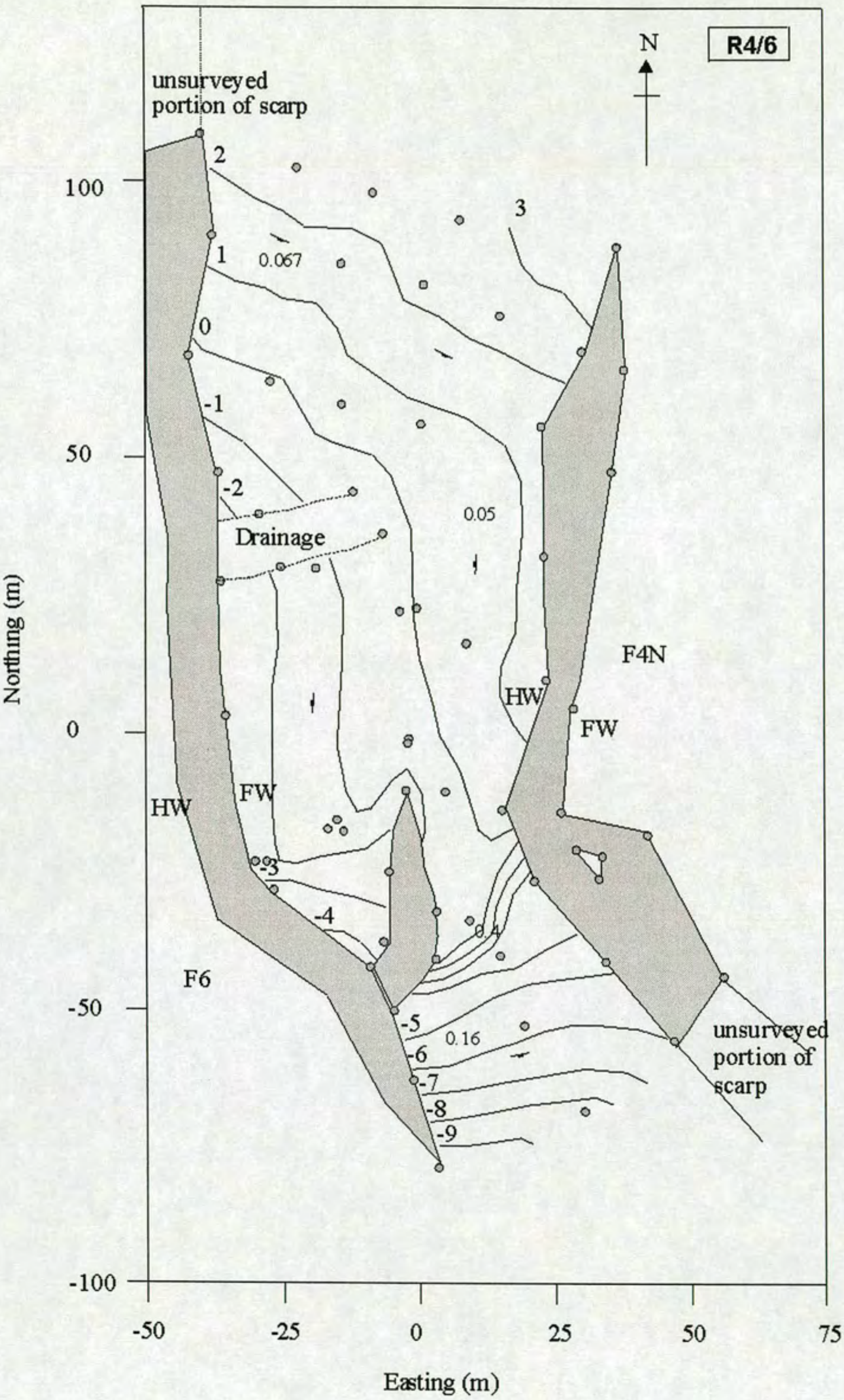
N
R4/6
unsurveyed portion of scarp
2
3
1
0.067
0
-1
-2
Drainage
0.05
F4N
HW
FW
HW
FW
-3
-4
0.4
F6
-5
0.16
-6
-7
-8
-9
unsurveyed portion of scarp
100
50
0
-50
-100
Northing (m)
-50
-25
0
25
50
75
Easting (m)

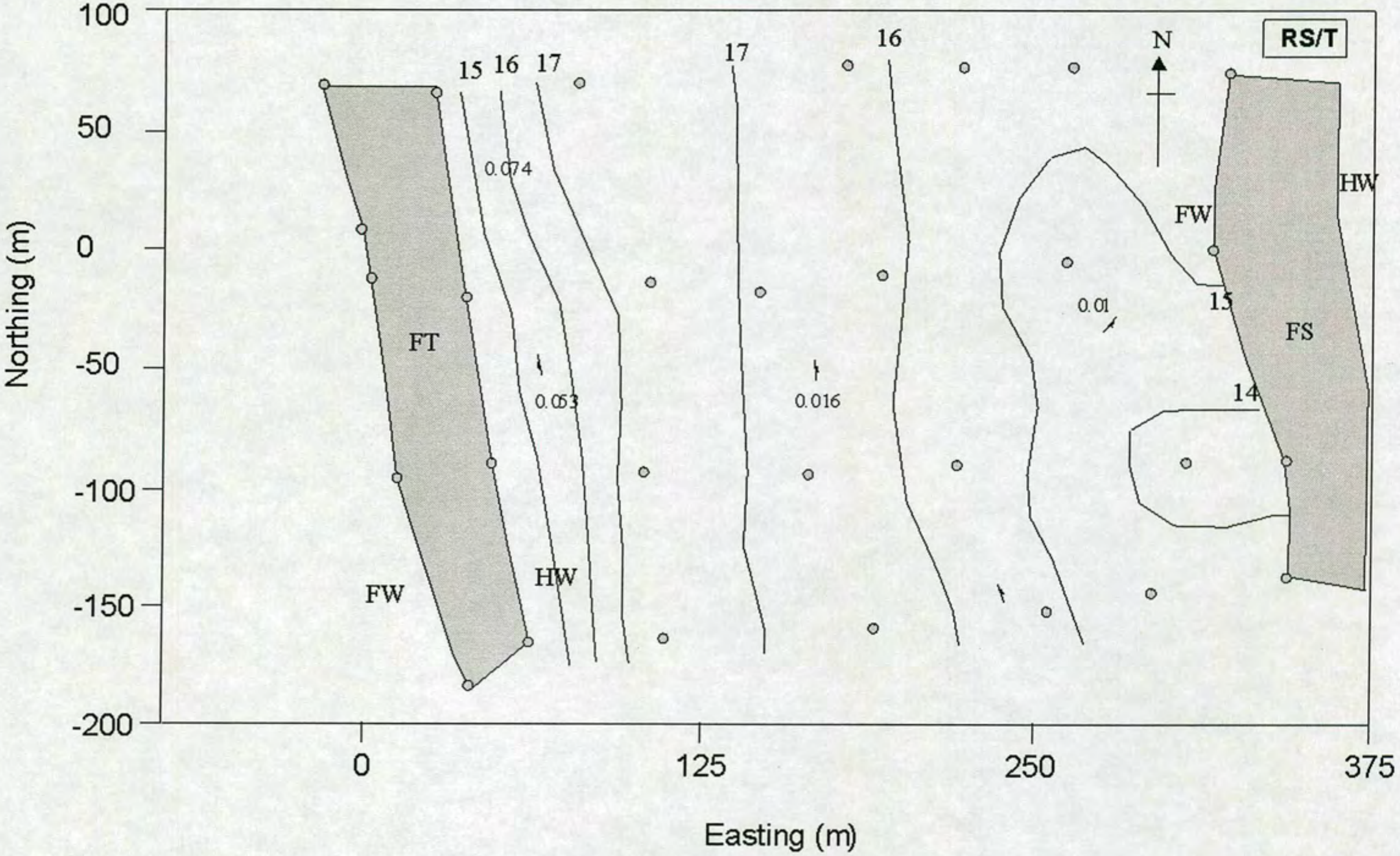
RS/T
N
15
16
17
17
16
0.074
0.053
0.016
0.01
15
14
FT
FS
FW
HW
FW
HW
Northing (m)
100
50
0
-50
-100
-150
-200
Easting (m)
0
125
250
375

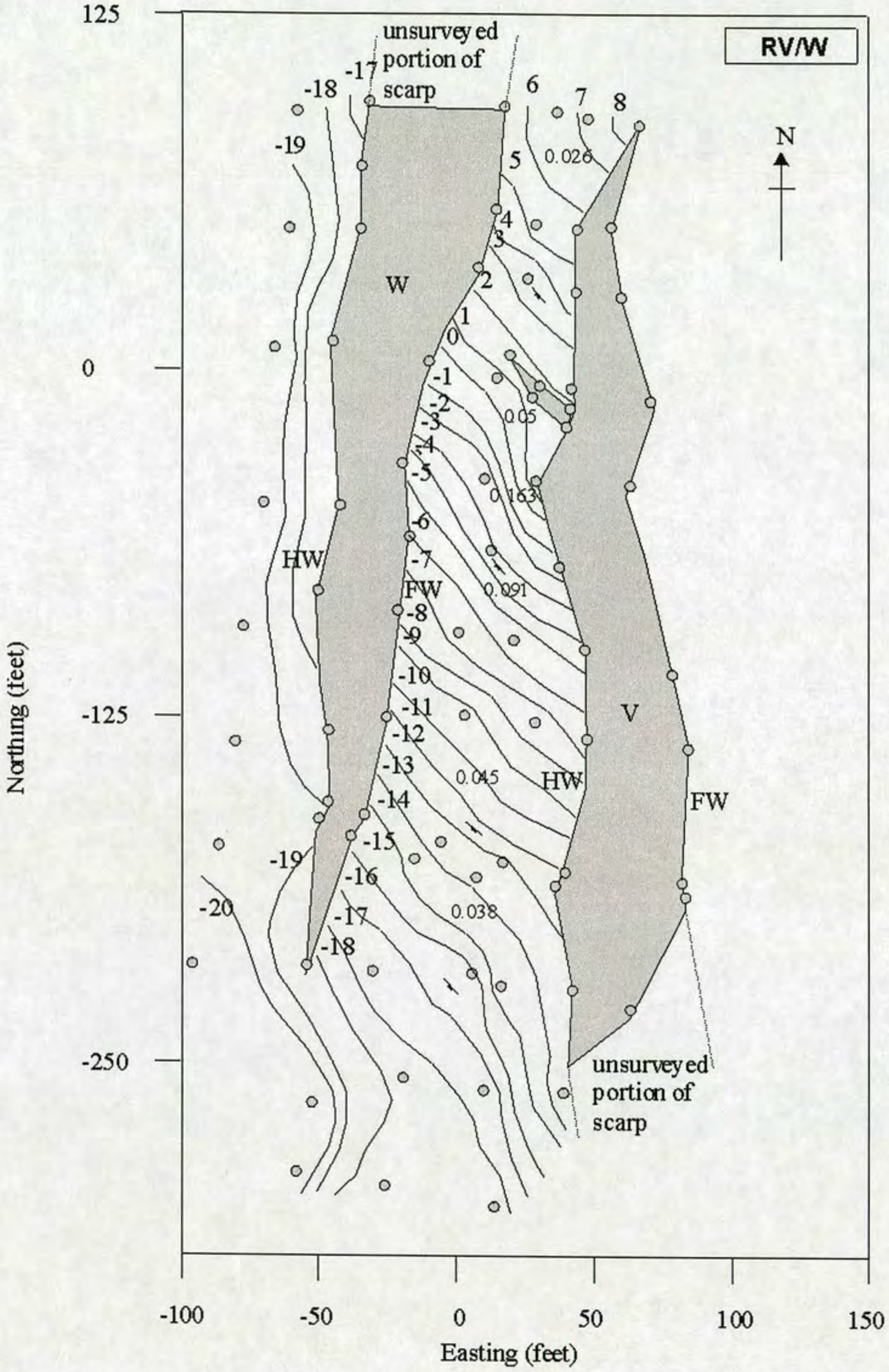

Figure 6.6. Digitised relay ramp survey data, showing 1) original data points as grey circles, 2) fault scarps filled in grey, 3) contour lines constructed from interpolating between the original data, 4) tan of dip magnitudes, including maximum and minimum dip, and dip direction symbols. Note that heights are relative to a base station location and given in metres. R1/2/3, for example, is an abbreviation for the ramp separating faults 1, 2 and 3.

In addition to undertaking detailed total station surveys of various ramps, the general characteristics of numerous other ramps on the Volcanic Tableland were recorded using basic field observations and a compass-clinometer for approximating dip and dip directions. The information obtained from these ramps is included where appropriate in later interpretation sections.

6.5 Ramp topography and bounding fault descriptions

6.5.1 Ramp separating F1 and F2, R1/2/3.

The part of the ramp under consideration here is that south of the southern tip of F3 (Figure 6.7). This area of the ramp is unlinked, with no visible attempts at linkage. The ramp has significantly varying dip directions from obliquely toward the collective footwall, to parallel to the fault strike and finally toward the collective hangingwall. Significant sand accumulations, quantified from pit transects dug in the sand, create a local dip toward the collective hangingwall near the base of F1 and do not reflect the true attitude of the tuff surface. There are no major paleo-drainage routes through the ramp so most of the sediment is thought to be from the adjacent scarp. The scarp of F1 is significantly degraded and thus appears to confirm this hypothesis. Internal ramp gradients, a proxy for minimum ramp strain, vary from 0.02 to 0.08. This is equivalent to a dip range of 1.15 to 5.15°. Cutoff gradients vary from 0.027 to 0.015 on the footwall of F2 and from 0.038 to 0.080 on the hangingwall of F1.

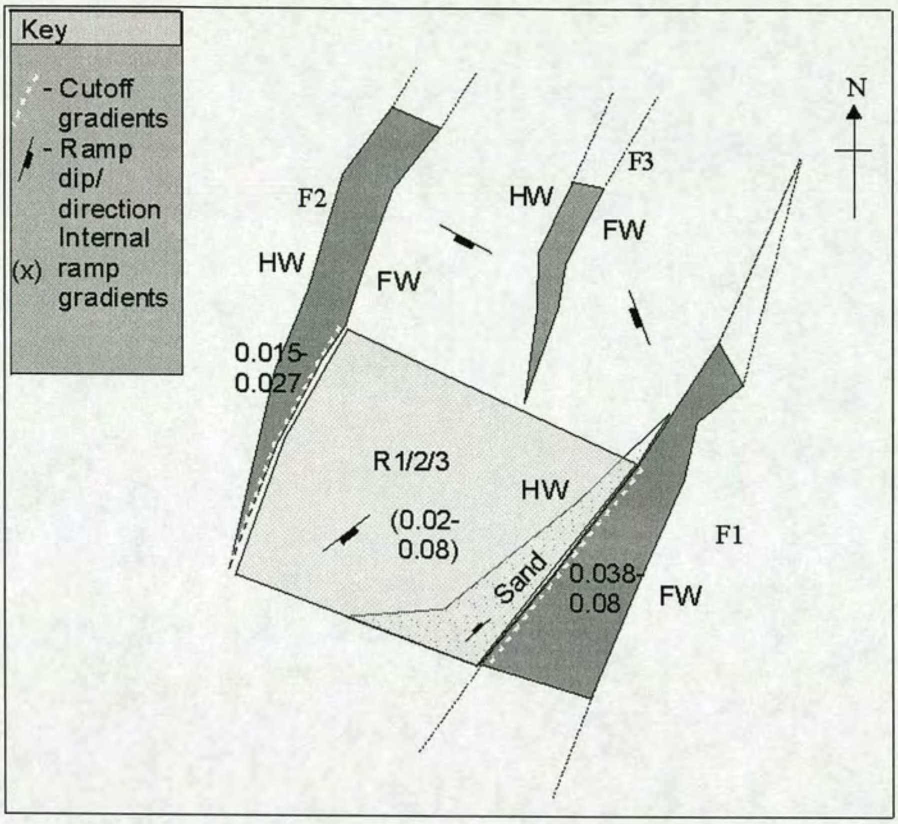

Figure 6.7. Summary of general characteristics of R1/2/3 including broad ramp dip directions, internal ramp gradients and bounding fault cutoff gradients.

6.5.2 Ramp separating F1 and F3, R1/2/3.

This ramp is unlinked, with no visible attempts at linkage (Figure 6.8). The ramp dips consistently toward the collective hangingwall. There is minimum scarp debris beneath the northern tip of F1 and no major paleo-drainage channels. The ramp is thus mostly tuff. Ramp gradients vary from 0.044 to 0.156. This is equivalent to a dip range of 2.51 to 8.87°. Cutoff gradients vary from 0.044 to 0.156 on the footwall of F3 and from 0.048 to 0.106 on the hangingwall of F1.

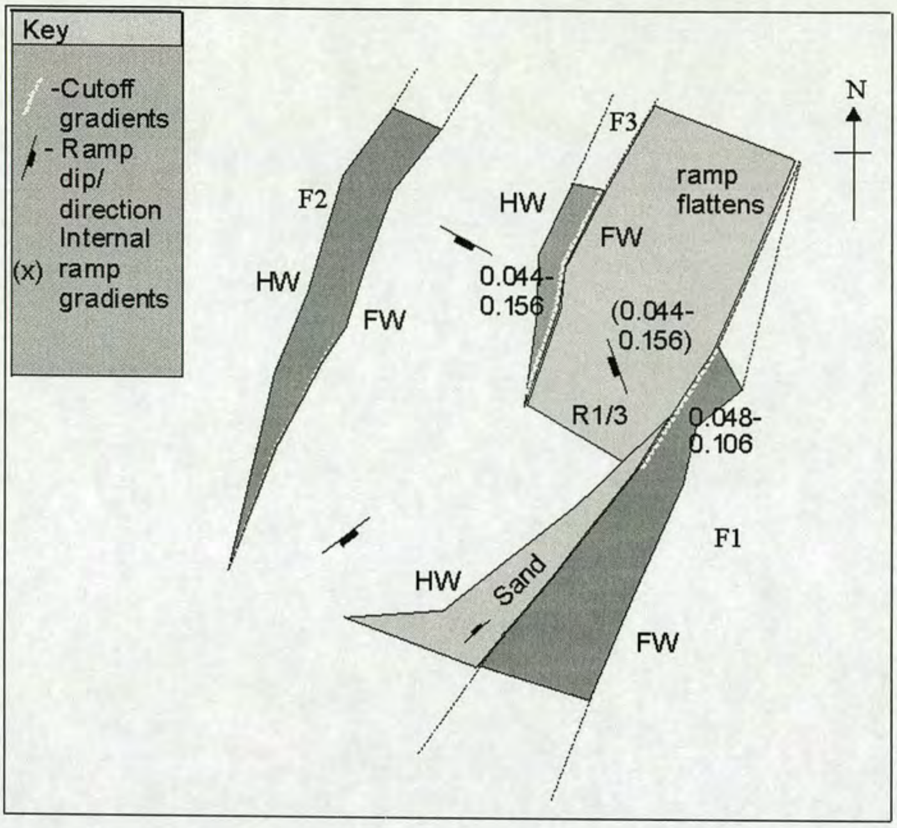

Figure 6.8. Summary of general characteristics of R1/3 including broad dip directions, internal ramp gradients and bounding fault cutoff gradients.

6.5.3 Ramp separating F2 and F3, R2/3/4/5.

This ramp is breached twice by splays off F3 that trend parallel or sub-parallel to the major faults and are perpendicular to the direction of maximum ground surface strain (Figure 6.9). There are moderate amounts of sediment directly beneath F3 in minor basins seldom more than 5 metres wide. Most of this sediment appears to be adjacent scarp debris. A minor paleo-drainage route affects the northern portion of the ramp depositing sand in the major depocentre created by faults 2, 3 and 4. The ramp dips obliquely or directly toward the collective hangingwall. Ramp gradients vary from 0.021 to 0.22. This is equivalent to a dip range of 1.2 to 12.4°. Cutoff gradients vary from 0.021 to 0.087 on the footwall of F2 to between 0.038 and 0.06 on the hangingwall of F3. The maximum cutoff gradient for faults bounding this ramp is thus decidedly less than the maximum ramp gradient.

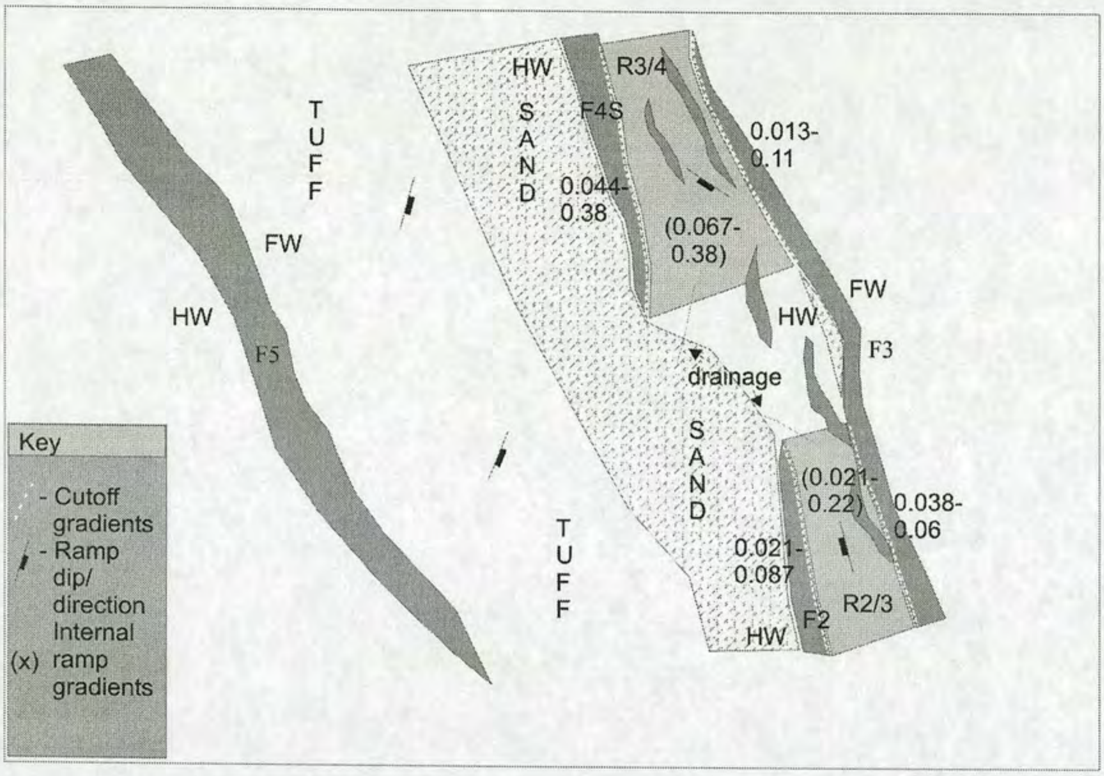

Figure 6.9. Summary of general characteristics of R2/3 and R3/4 including broad dip directions, internal ramp gradients and bounding fault cutoff gradients.

6.5.4 Ramp separating F3 and F4, R3/4.

Numerous breaching splays of varying magnitude affect this ramp (Figure 6.9). Most splays are sub-parallel to the bounding fault trends and oblique to the direction of maximum ground surface strain. There are moderate amounts of sediment directly beneath F3 as described in the previous section. There are significant amounts of sediment beneath F4 brought in by drainage channels from the north. Minor paleo-drainage channels affect the ramp between F3 and F4 and deposit sand in the depocentre beneath F2, 3 and 4. The ramp has a consistent oblique dip toward the collective hangingwall. Ramp gradients vary from 0.067 to 0.38. This is equivalent to a dip range of 3.8 to 16.7°. Cutoff gradients vary from 0.044 to 0.38 on the footwall of F4S and from 0.013 to 0.11 on the hangingwall of F3.

6.5.5 Ramp separating F4S and F4N, R4S/N.

This ramp is fully linked at its base although the linking scarp is now poorly preserved and represented by a steep talus slope (Figure 6.10). The linking splay trends parallel to F4N. A major breaching splay almost fully traverses the ramp at its upper limit. These splays are sub-parallel to the bounding fault trends and oblique to the direction of maximum strain. The ramp dips obliquely toward the collective hangingwall. There are no paleo-drainage routes preserved through this ramp. Ramp gradients vary from 0.085 to 0.36. This is equivalent to a dip range of 3.7 to 19.8°. Cutoff gradients vary from 0.103 to 0.36 on the footwall of F4N and from 0.16 to 0.36 on the hangingwall of F4S.

6.5.6 Ramp separating F4N and F6, R4/6.

This ramp is affected by one breaching splay off F6 trending obliquely to the bounding faults (Figure 6.11). This splay is oblique to the local direction of maximum ground surface strain. The ramp dips toward the collective hangingwall in the north and parallel to the bounding fault trends in the south. A major paleo-drainage channel crosses part of the northern section of the ramp, incising through the scarp of F6 to a depth of over 3 metres. The channel depth decreases on moving east across the ramp and cannot be resolved near the centre of the ramp. Ramp gradients vary from 0.05 to 0.4. This is equivalent to a dip range of 2.9 to 21.8°. Cutoff gradients vary from 0.014 to 0.19 on the footwall of F6 and from 0.049 to 0.4 on the hangingwall of F4N.

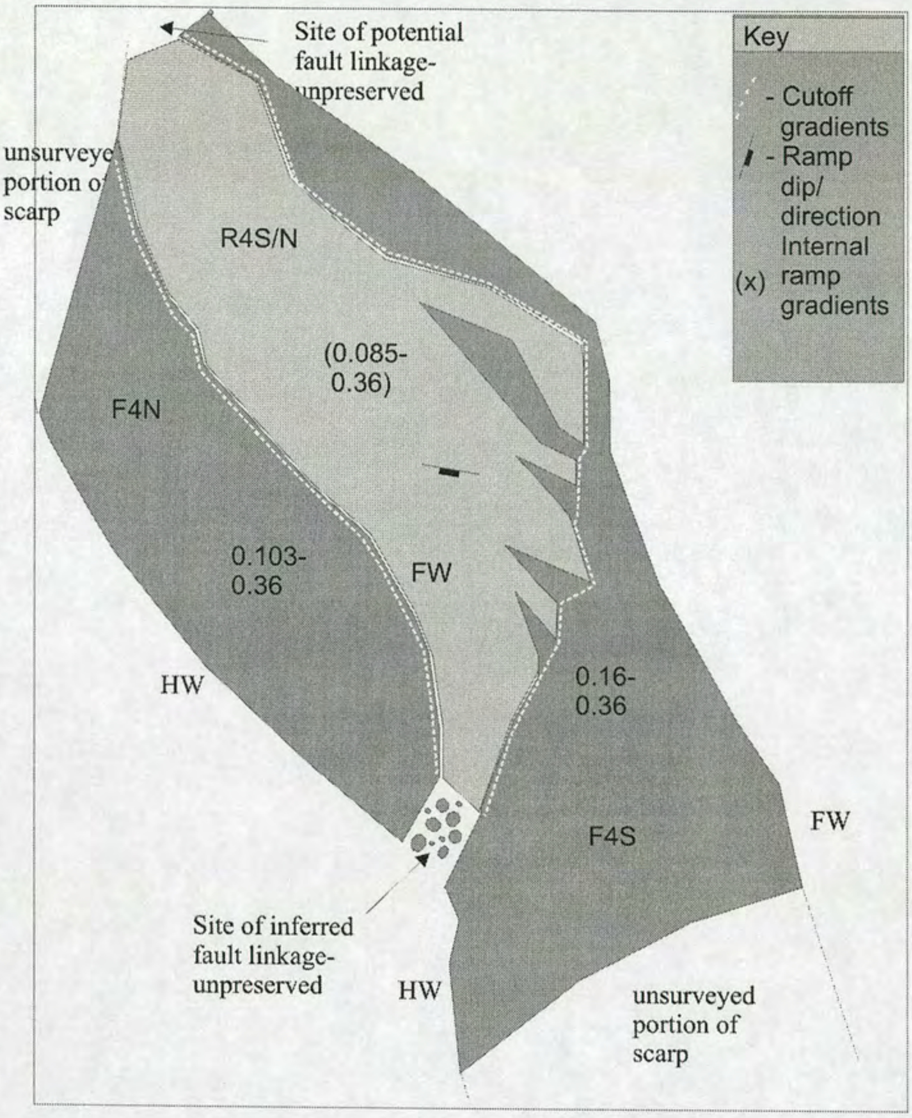

Figure 6.10. Summary of general characteristics of R4S/N including broad dip directions, internal ramp gradients and bounding fault cutoff gradients.

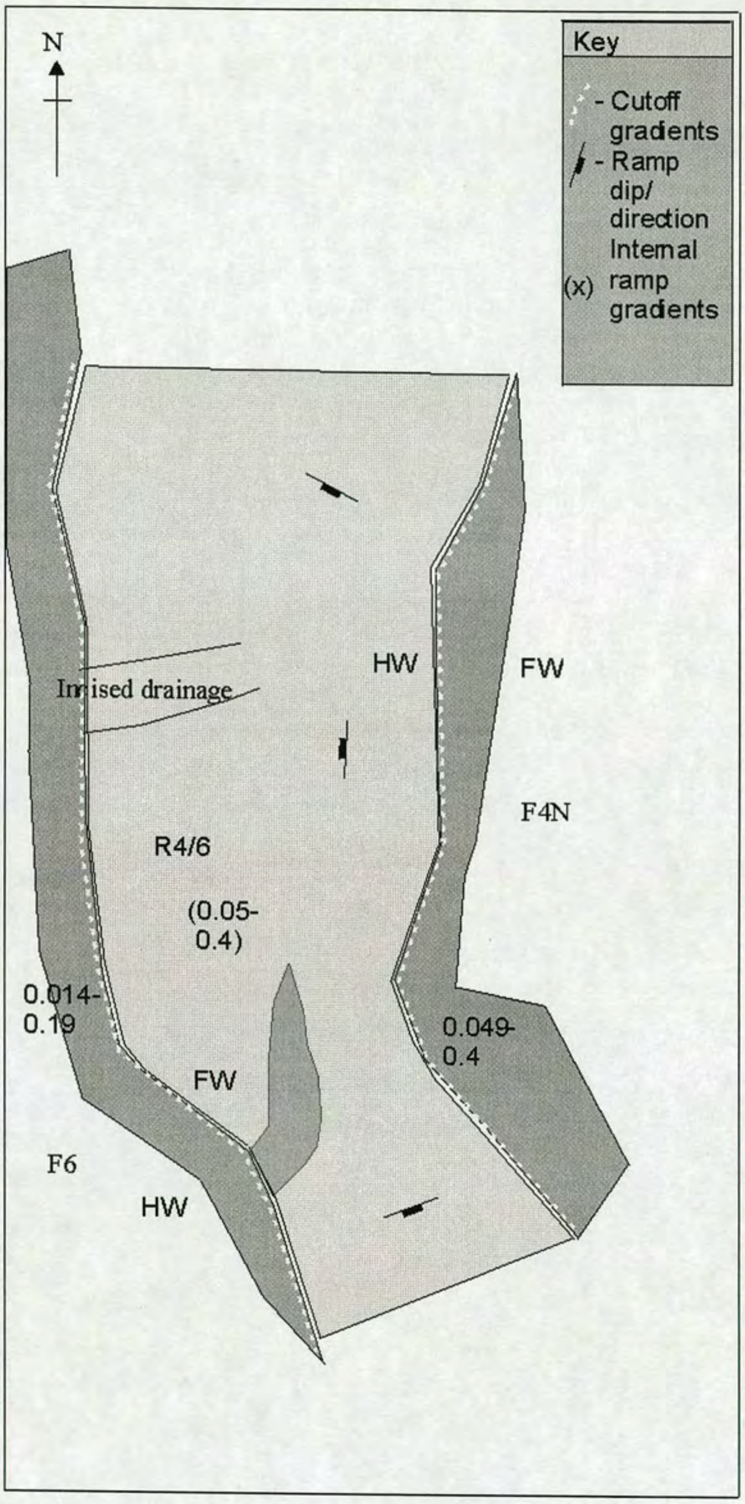

Figure 6.11. Summary of general characteristics of R4/6 including broad dip directions, internal ramp gradients and bounding fault cutoff gradients.

6.5.7 Ramp separating FV and FW, RV/W.

This ramp is affected by one breaching splay off FV that crosses approximately half the width of the ramp and trends obliquely to the bounding faults (Figure 6.12). The splay trends perpendicularly to the current direction of maximum ground surface strain. The ramp dips obliquely toward the collective hangingwall in a consistent fashion. Minimum sediment affects this ramp and no paleo-drainage routes are preserved. The ramp is thus mostly upper tuff surface. Ramp gradients vary from 0.026 to 0.163. This is equivalent to a dip range of 1.5 to 9.3°. Cutoff gradients vary from 0.04 to 0.153 on the footwall of FW and from 0.026 to 0.155 on the hangingwall of FV.

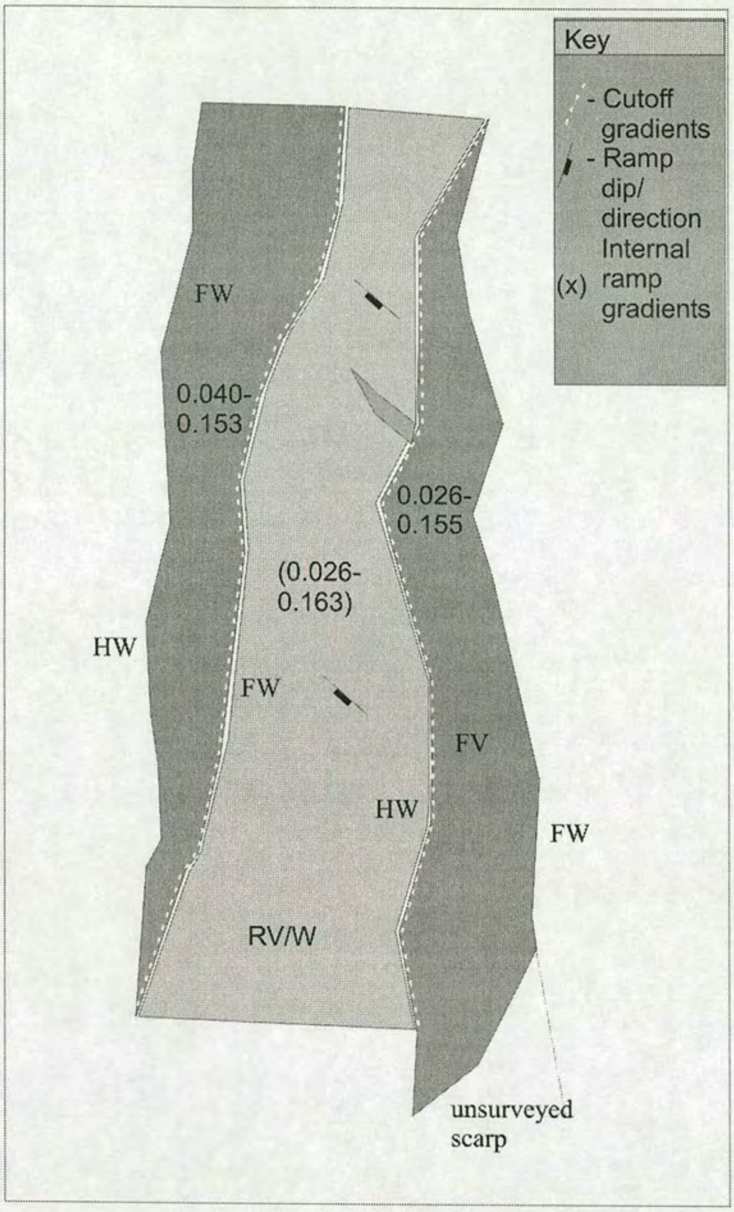

Figure 6.12. Summary of general characteristics of RV/W including broad dip directions, internal ramp gradients and bounding fault cutoff gradients.

6.5.8 Ramp separating FS and FT, RS/T.

This ramp is unlinked with no visible attempts at linkage (Figure 6.13). The ramp dips toward the collective footwall within 70 metres perpendicularly from the scarp of FT and reverses to dip toward FS with increasing proximity to that scarp. A major paleo-drainage route affects this ramp incising through FT and FS. This explains the reversal in dip of the ramp with increasing proximity to FS. Significant amounts of sediment occupy the hangingwall depocentres of both faults. Much of this will have come from localised footwall erosion. Ramp gradients vary from 0.01 to 0.074. This is equivalent to a dip range of 0.57 to 4.2°. Cutoff gradients vary from 0.01 to 0.019 on the footwall of FS to unknown on the hangingwall of FT owing to sand deposits.

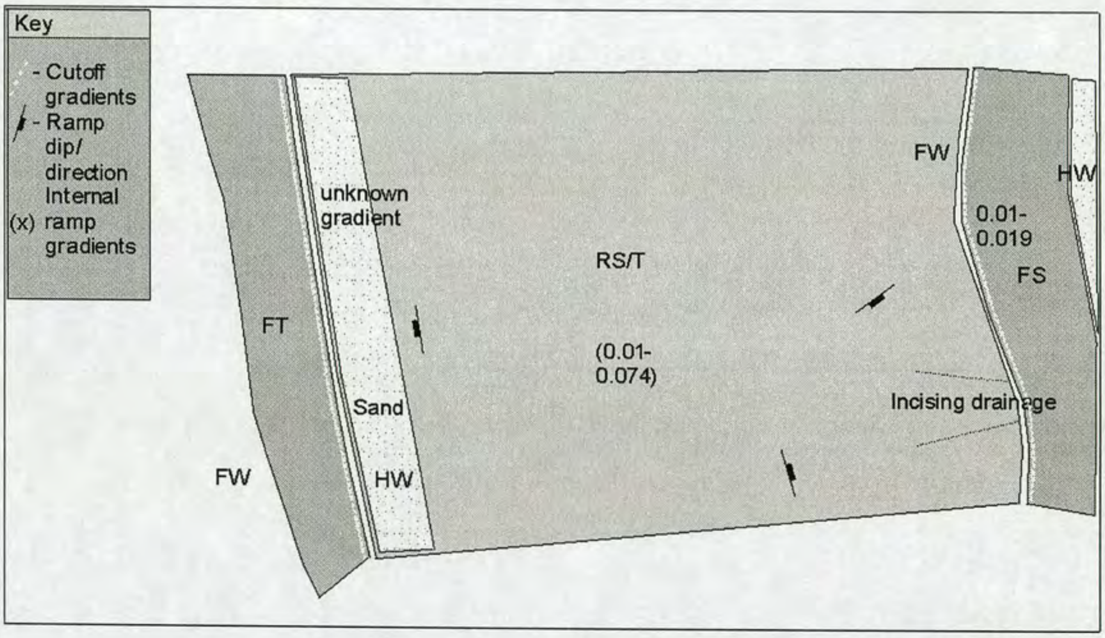

Figure 6.13. Summary of general characteristics of RS/T including broad dip directions, internal ramp gradients and bounding fault cutoff gradients.

6.6 Ramp topography interpretations

The interpretation of relay ramp topography involves an integrated analysis of numerous components, including ramp dip directions, internal ramp gradients, bounding fault cutoff gradients, breaching fault orientations, the state of erosion of ramps and adjacent scarps. The focus of this interpretation section is thus on analysing these parameters in both a quantitative and qualitative fashion. The asymmetry of individual fault displacement profiles and tip gradients, parameters that vary with fault interaction as discussed in previous chapters, are somewhat surprisingly less relevant to the mechanics of relay ramp development. This is so because the state of strain in a ramp must be fundamentally controlled by the cutoff gradients of the ramp bounding faults and fault propagation folding. Fault cutoff gradients are entirely dependent on the manner in which fault growth is partitioned into footwall uplift and hangingwall subsidence. In this study, this phenomenon will be referred to from this point onward as 'growth partitioning'. In a scenario where the back fault in an overlapping and significantly interacting fault pair displays mostly footwall uplift, while the front fault displays mostly hangingwall subsidence, despite both faults possessing exaggerated profile asymmetry and steep tip gradients, they preserve a low strain ramp as most of this strain is not being accommodated within the ramp. (Figure 6.14). By analysing ramp development with respect to cutoff gradients in the ramp area, this study represents a departure from previous ramp studies where ramp development has been analysed in conjunction with overall fault tip gradients (e.g. Cartwright and Mansfield, 1998; Morley and Wonganan, 2000). Fault interaction, as defined in Chapters 4 and 5, can thus to a certain extent be considered separately from relay ramp development while bearing in mind that the driving force for faults to show markedly different styles of growth partitioning may indicate a form of fault interaction in itself.

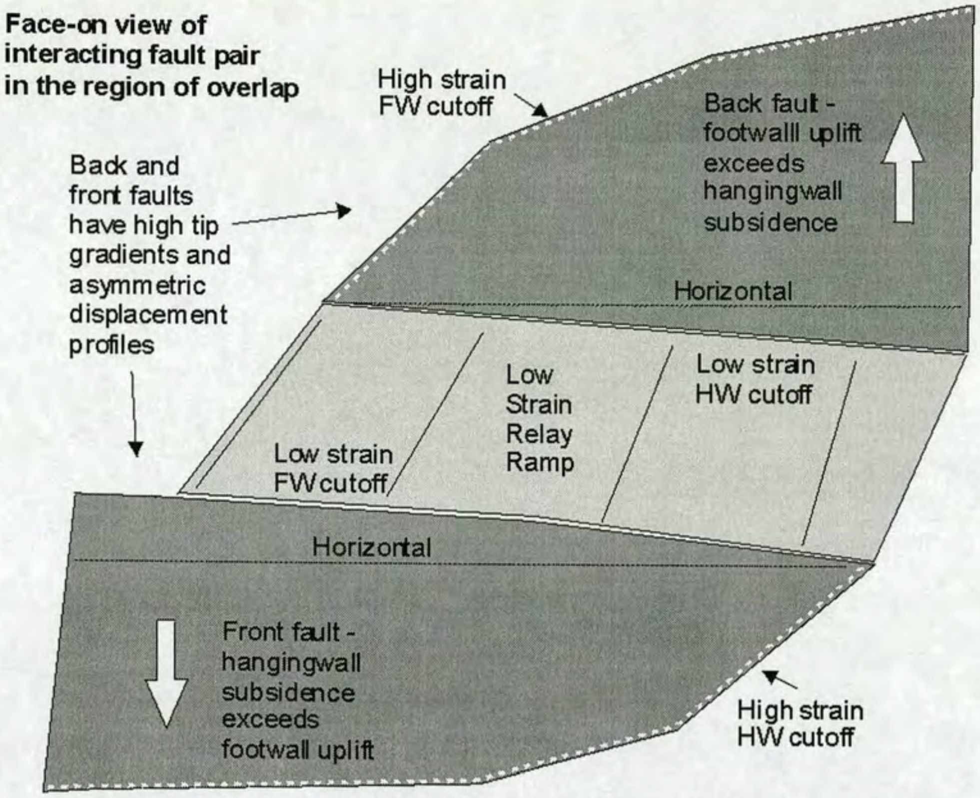

Figure 6.14. Face on view of two significantly interacting overlapping faults that possess exaggerated displacement profile asymmetry and high tip gradients but are separated by a low strain ramp. This scenario results because most of the strain is being accommodated outwith the ramp on the footwall cutoff of the back fault and the hangingwall cutoff of the front fault owing to the partitioning of fault growth.

6.6.1 Ramp dip direction

Most components of relay ramp analysis involve highly variable or poorly quantifiable parameters, such as ramp strain or the degree of erosion of ramps and adjacent scarps, often with much variation confined to very localised areas of particular ramps. Ramp dip direction, however, can take one of two general forms: toward the collective hangingwall or toward the collective footwall. For this reason, ramps are initially put into 2 distinct categories based on their dip direction. It is then of interest to see if ramps in these 2 categories are predictably different in any respect other than their dip direction. This is intended to provide information on whether ramp dip direction results from a particular growth mechanism or is merely a matter of co-incidence. A null hypothesis is proposed that the proximity of faults in an overlapping pair, i.e. the separation distance (S), does not control the ramp dip direction.

Analysis of the data presented in section 6.5 shows that all fault pairs with separations of less than 70 metres, i.e. F1 and 3, 2 and 3, 3 and 4, 4S and 4N, 4 and 6, and V and W, dip toward the collective hangingwall with varying degrees of obliquity to fault strike (Figures 6.7, 6.8, 6.9, 6.10, 6.11, 6.12). Meanwhile, surveyed fault pairs with separations of greater than 140 metres, i.e. F1 and 2, 2 and 5, 4 and 5, and S and T, dip toward the collective footwall with varying degrees of obliquity (Figures 6.7, 6.9, 6.13). Dip direction data was also obtained, using a compass clinometer, for the ramps separating faults 6 and 7, L and M, M and N and T and U. All of these fault pairs have separations of >140m and all the ramps separating them dip toward the collective footwall (Figure 6.15).

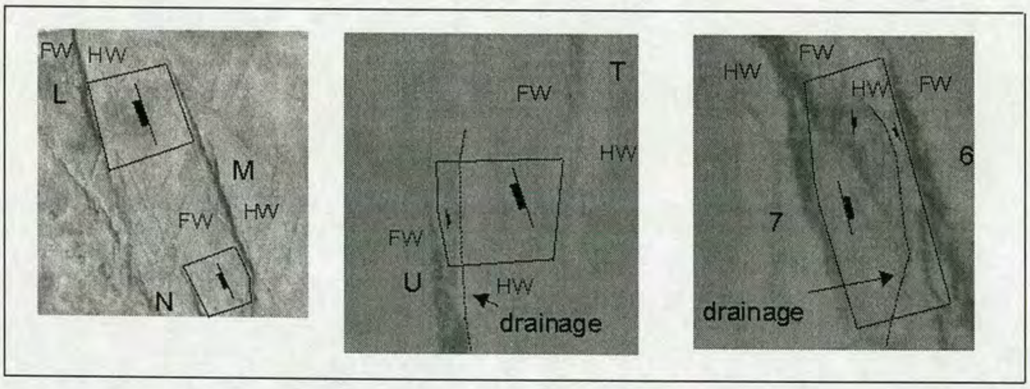

Figure 6.15. Approximate ramp areas between faults L and M, M and N, T and U and 6 and 7 showing the broad dip directions and drainage features as obtained from field reconnaissance with a compass clinometer.

No ramp surveys are available for fault pairs with separations of between 70 and 140 metres so it is not known if this change in dip direction is gradational or abrupt over this distance range. The observations suggest the null hypothesis proposed above, stating that separation distance does not control ramp dip direction, should be rejected for the survey data presented here. It is then proposed that for these ramps, the proximity of overlapping faults, specifically the separation distance, exerts a critical control on the ramp dip direction and thus the mechanisms of relay ramp development. Clearly, subsequent fault propagation folding and hard linkage can radically alter ramp dip and this is discussed later.

6.6.2 Ramp strain

Relay ramp gradients are taken as a proxy for ramp strain. Ramps from section 6.5 are subdivided depending on the gradient magnitudes within the ramp (i.e. ramp dip) (see Figure 6.2 caption), and degree of erosion. Gradient magnitudes are only considered representative when they affect a significant internal area of the ramp and not when only affecting a very localised area. The degree to which erosion can obscure the flexure within a ramp is ultimately a subjective interpretation but based on the presence or absence of through-going paleo-drainage channels and major accumulations of sand in proximal topographic lows.

The ramps separating faults 2 and 3, 3 and 4, 4S and 4N and V and W appear to have suffered little erosion and preserve consistently higher strain than other surveyed ramps, having a consistent dip of 5° or more. None of these ramps are affected by major through-going paleo-drainage channels or contain significant amounts of sediment on the ramp. Significantly, all of these ramps contain breaching structures. The orientations of breaching faults within these ramps are typically perpendicular to the direction of maximum ground surface strain.

The ramps separating faults 1 and 2, 1 and 3, 2 and 5, and S and T appear to have suffered little erosion and preserve lower strain than ramps in the previous paragraph, dipping consistently at less than 5°. Of these ramps, only the ramp separating faults S and T is affected by a major paleo-drainage channel. This feature is significantly incised into the upper tuff surface, limiting the radius of its erosive capability. For this reason erosion is unlikely to have significantly altered the topography of the ramp, other than locally. The ramp separating faults 2 and 5 contains a moderate amount of sediment adjacent to the northern tip of fault 2 although this depocentre is too narrow to hide potential breaching faults affecting the ramp. Significantly, all of the above relay ramps remain entirely unlinked.

The ramp separating faults 6 and 7 was analysed qualitatively and with use of a compass clinometer to record general dip characteristics. The ramp contains a major through-going paleo-drainage channel and has significant sediment on the ramp itself. The ramp thus appears to have undergone significant erosion and preserves correspondingly low ramp gradients. In this case the ramp is almost fully linked by a major breaching fault trending obliquely across the ramp with up to several metres of displacement.

Cutoff gradients and ramp strain

Cutoff gradients refer to the topographic gradient encountered walking along a ramp bounding scarp footwall or hangingwall (see section 6.2). The gradient is measured purely along the footwall or hangingwall side of the fault and thus is not a representation of the overall fault displacement gradient. It is the cutoff gradients that are responsible for the initial strain experienced within a ramp, assuming no pre-existing topography. In order to imply that fault propagation folding has affected a ramp, for example, it would be necessary to identify a zone of high strain on the ramp that exceeds the adjacent fault cutoff gradients. The maximum footwall or hangingwall cutoff gradient for surveyed ramps are plotted here against the tangent of the maximum internal ramp dip, a proxy for maximum internal ramp strain (see Figure 6.2) in Figure 6.16.

As might be expected, a positive correlation exists between maximum ramp cutoff gradients and maximum internal ramp strain as inferred from Figure 6.16, although scatter is introduced to the correlation by one outlier. The significance of this outlier shall be discussed in section 6.7.2.

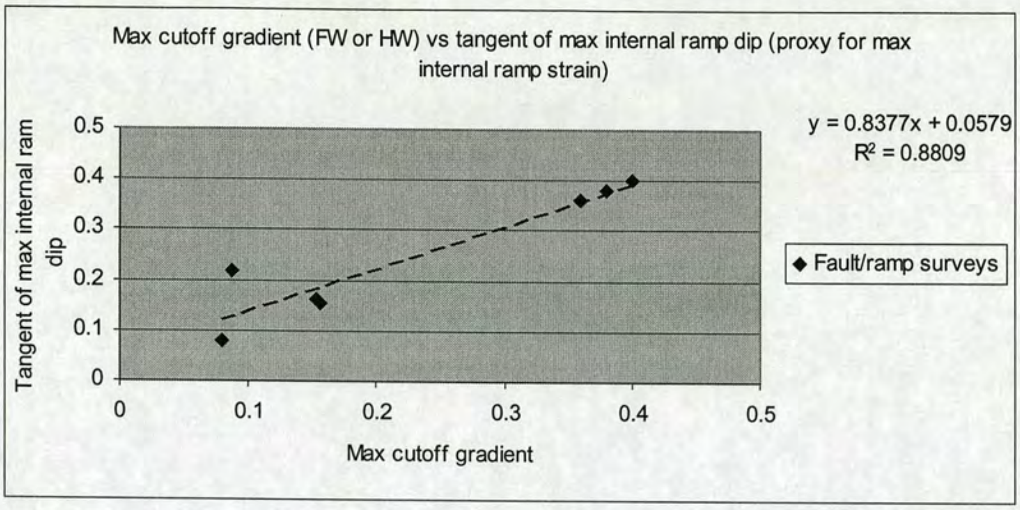

Figure 6.16. Maximum footwall or hangingwall cutoff gradient vs the tangent of the maximum internal ramp dip, a proxy for maximum internal ramp strain.

6.7 Discussion - Ramp topography

6.7.1 Ramp dip direction discussion

The results presented in section 6.6.1 suggest that the separation distance between overlapping faults can exert a fundamental control on the dip direction of the relay ramp. Surveyed ramps with bounding faults separated by less than 70 metres dip toward the collective hangingwall while ramps with bounding faults separated by greater than 140 metres dip toward the collective footwall. In order to assess if this phenomenon is representative of the Volcanic Tableland it is necessary to look at other ramps on the Tableland.

Other relay ramps on the Volcanic Tableland

Two ramps within the array surveyed by Dawers & Anders (1995), which contains three large ramps, provide obvious anomalies to the pattern of ramp dips described in section 6.6.1. The southern-most two ramps in this array have separations of significantly greater than 140 m and both dip toward the collective hangingwall. Both ramps are, however, fully linked unlike most of the ramps with separations of greater than 140m surveyed for this project. The breaching faults affecting both these ramps have accrued significant displacement of up to 11 metres (from Fig 5., Dawers & Anders, 1995). This suggests the entire fault array may be one structure at depth and displacement is currently being taken up on the linking structures. This process has almost re-equilibrated the fault displacement profile back to that expected of a 7 kilometre long single segment fault. It is proposed here that the fault propagation folding which must have preceded hard-linkage of these major structures could have created the ramp dip toward the collective hangingwall which can be seen today. Evidence for this can be seen in the southernmost ramp of Dawers and Anders' (1995) surveyed array where a linking fault seriously affects the dip of the ramp via fault propagation folding beyond the southern limit of its visible ground rupture (Figure 6.17).

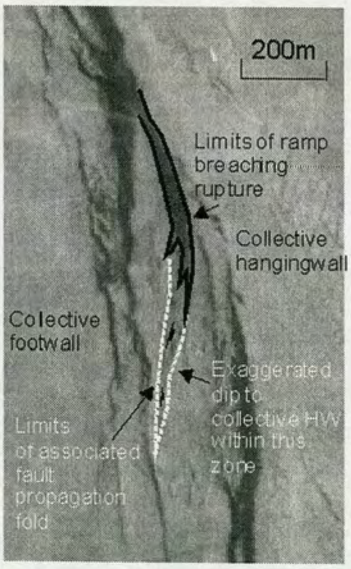

Figure 6.17. Enlarged aerial photo highlighting the fault propagation fold affecting the ramp between the southernmost 2 faults of the array surveyed by Dawers & Anders (1995). The fold is a continuation of the major ramp breaching splay to the north. This particular monoclinal fold has a width of up to 50 metres and an amplitude of several metres, inducing an exaggerated dip toward the collective hangingwall within the ramp.

In the vicinity of this fold a severely exaggerated dip toward the collective hangingwall is induced. Fault propagation folding on such a scale completely alters the overall ramp dip and could be envisaged to do so in similar cases where major breaching faults affect a ramp. The ramp discussed above within the array surveyed by Dawers & Anders (1995) thus highlights the importance of fault propagation folding in controlling ramp dip direction.

Figures 2c and 2d in Ferrill et al. (1999) show relict and unbreached relay ramps on the Fish Slough fault system of the Volcanic Tableland that clearly dip towards the collective footwall. Bounding fault separations in this case are between approximately 400 and 800 metres and thus these ramps conform to the conclusions presented above stating those ramps with widths of greater than 140m dip toward the collective footwall.

In summary on this component of ramp analysis, it appears reasonable to suggest from the data available that separation distance does exert a critical control on ramp dip direction in this setting, excluding ramps whose topography is severely affected by fault propagation folding.

Other controls on ramp dip direction

Aside from generating fault propagation folds as discussed above, ramp breaching faults themselves clearly also affect ramp dip direction. In the case of the surveyed ramp separating faults 3 and 4, the presence of numerous breaching splays within the ramp creates a terracing effect on the ramp topography (Figure 6.18). This enhances the overall dip toward the collective hangingwall via increasing the net elevation change across the ramp.

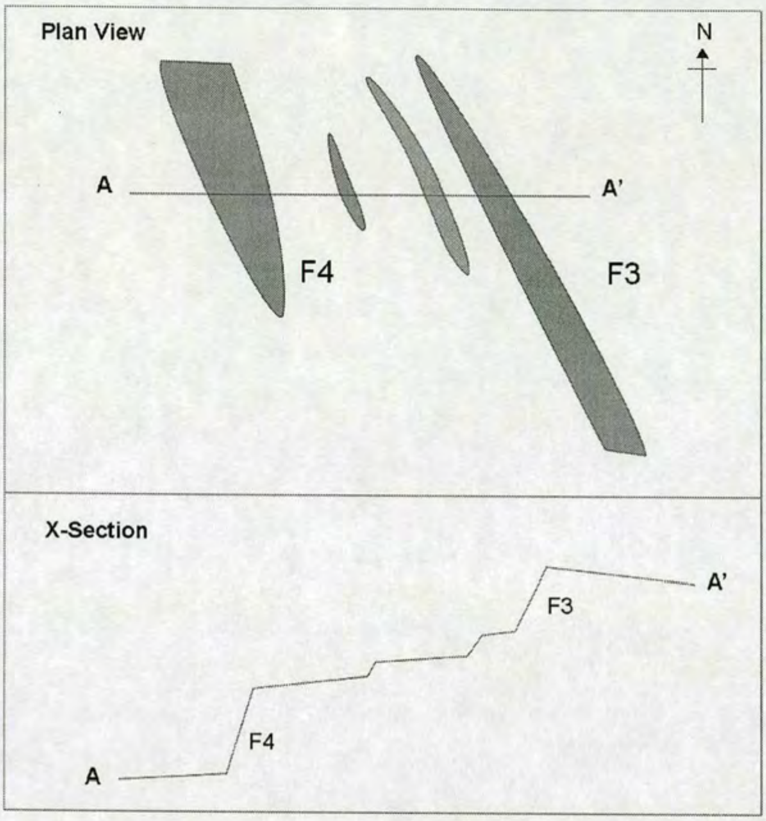

Figure 6.18. Sketch of the ramp separating faults 3 and 4 (see also Figure 6.9). Breaching splays within the ramp create a terracing effect that appears to enhance the overall dip toward the collective hangingwall.

In all other surveyed cases for ramps with separations of less than 70 metres, although breaching splays sometimes enhance the effect, the actual ramp has a clear dip toward the collective hangingwall irrespective of proximity to breaching splays.

Another mechanism for altering ramp topography is via erosion in the form of footwall erosion and corresponding hangingwall deposition. It is not possible to accurately quantify footwall erosion on the Tableland. Estimates can be made by looking at the variation in scarp preservation across the Tableland, the angle of scarp repose and the thickness of associated hangingwall depocentres, be they adjacent to the scarp or remotely connected by a paleo-drainage channel. In the case of numerous faults in this thesis, hole transects were dug in hangingwall depocentres adjacent to major scarps to allow an estimate of the true fault dimensions along strike. The displacement profile surveys were altered to include this sediment thickness. It is never seen to be the case that hangingwall depocentres can completely reverse the topographic slope of a ramp. Slope wash sediment can reverse the topographic slope within 50 metres of the scarp base but this effect is usually obvious and the phenomenon is shown on Figure 6.7 beneath fault 1. The typical scenario is that sand deposits locally disguise the dip of the ramp, as the sand flattens an otherwise dipping ground surface. Hangingwall depocentres are generally of insufficient width to make this effect significant or unable to be accounted for.

In the case of the ramp separating faults V and W, both scarps are well preserved and there appears to be insignificant accumulations of sand in the hangingwall of both faults. The faults currently sit elevated on the footwall high of a major structure and are thus not prone to the collection of sediment from distal regions. This ramp is affected by one minor breaching splay but clearly dips toward the collective hangingwall in a consistent fashion. The consistency of the ramp dip, and general similarity between fault cutoff gradients and adjacent ramp strain, suggest the ramp dip is not being controlled by buried faults warping the ramp via folding. In order to imply fault propagation folding unambiguously it is necessary to identify a zone of high strain on the ramp that exceeds the adjacent fault cutoff gradients. This ramp is therefore taken to be a type case scenario of a ramp that has undergone insignificant erosion, is not fully linked, bounds 2 faults with a low separation distance and has a consistent and real dip towards the collective hangingwall of the fault pair. In conclusion, it is therefore deemed possible that a ramp can be created that dips toward the collective hangingwall without invoking secondary processes such as footwall erosion, breaching faults or fault propagation folding as the cause. This contradicts the results of Crider and Pollard (1998) who numerically model relay ramp development and are unable to produce a ramp that dips toward the collective hangingwall via primary fault growth mechanisms. This is discussed further in section 6.7.3.

The geometry of the particular ramp separating faults V and W provides more crucial information on mechanisms of relay ramp development. It firstly confirms that low separation ramps are not necessarily low strain ramps as this ramp has high strain with respect to other ramps on the Tableland and indeed is partially breached as a result. Low fault pair separation thus does not imply a specific form of fault growth partitioning such as that documented in Figure 6.14. In this case, exactly the opposite situation is encountered. Cutoff gradients are high on both the footwall cutoff of the front fault (W) and the hangingwall cutoff of the back fault (V), both controlling resultant ramp strain. The low separation ramp still dips toward the collective hangingwall. A schematic diagram for ramp development is proposed below (Figure 6.19), once again highlighting the importance of the manner in which fault growth is partitioned in controlling cutoff gradients and thus controlling ramp strain.

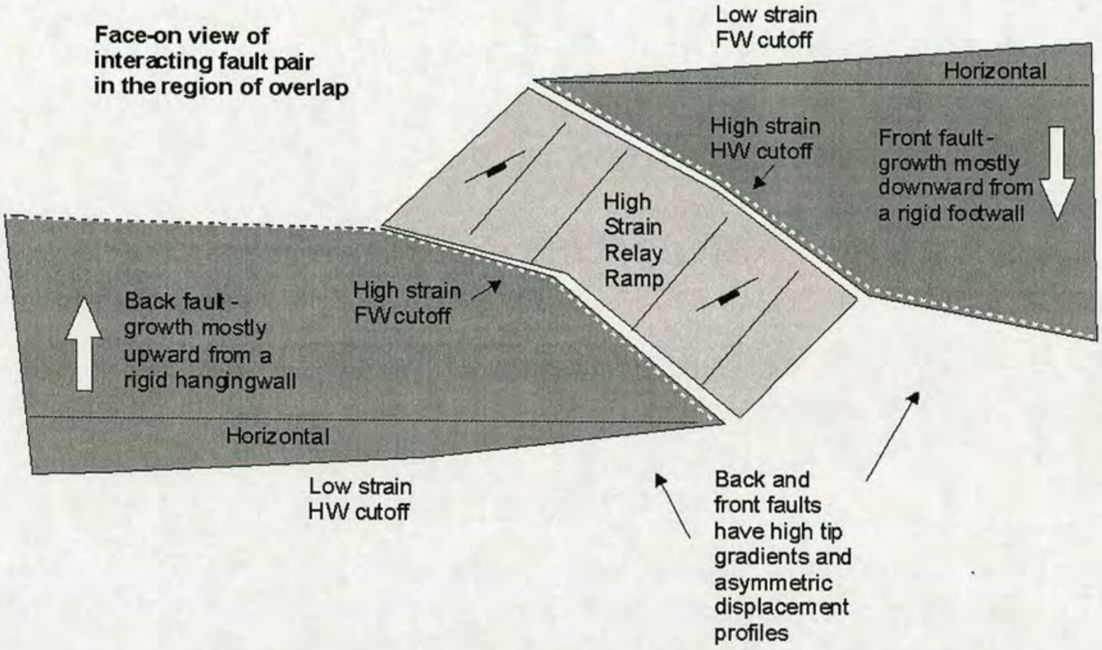

Figure 6.19. Schematic diagram for the development of the ramp between faults V and W. Fault V displays mostly hangingwall subsidence while fault W displays mostly footwall uplift. This still produces a ramp dipping toward the collective hangingwall although with high strain.

It is thus apparent that low separation ramps can develop a dip toward the collective hangingwall from a range of different styles of fault growth partitioning (see definition on p143). In order for low separation ramps to dip toward the collective hangingwall irrespective of the manner in which fault growth is partitioned means the hangingwall cutoff of the back fault must always be higher than the footwall cutoff of the front fault. It is currently unclear, despite detailed analysis of the relevant field data, what controls the manner in which fault growth is partitioned and constrains the relative height of two overlapping faults. This area has significant potential for future work as the predictability of ramp dip directions at low fault pair separations suggest a fundamental mechanical control is in operation.

6.7.2 Ramp strain and linkage discussion

The role of strain in fault linkage

It has been suggested that ramp strain, in the form of "bending, torsion and tension", is the critical factor in controlling subsequent fault linkage (Larsen, 1988; Peacock & Sanderson, 1994). In the transition from elastic to brittle behaviour, a simple correlation between ramp strain and linkage would indeed be expected. This derives from the simple premise that with sufficient strain, an elastic material will fail irrecoverably in the same way that a ruler will snap if bent too far. Ramp breaching would be anticipated to initiate at the site of maximum flexure, or strain, on a ramp, with the breaching splay orientated perpendicular to the axis of maximum strain. Here, ramp strain is examined in tandem with the presence or absence of breaching structures and their orientation.

Strain vs Linkage on the Tableland

Internal relay ramp gradients, i.e. ramp dip, are taken as proxies for strain and as such are compared with the linkage status of surveyed ramps. A link between internal relay ramp strain and ramp linkage is indeed evident for surveyed ramps in this study. In all surveyed cases where ramps preserve consistently high strain with respect to other ramps on the Tableland, with minimal erosion, there are one or more breaching structures affecting the ramp, generally perpendicular to the inferred direction of maximum strain, i.e. in the ramps separating faults 2 and 3, 3 and 4, 4S and 4N and V and W (Figures 6.9, 6.10, 6.12). In all cases where ramps preserve relatively moderate to low strain with respect to other ramps on the Tableland, and minimal erosion, there are no visible breaching structures affecting the ramps, i.e. faults 1 and 2, 1 and 3, 2 and 5, and S and T (Figures 6.7, 6.8, 6.13). This suggests a definite link exists between high strain and fault linkage.

Erosion is clearly capable of altering the topography of a ramp at the ground surface and so anomalies to the link between ramp gradients and linkage inevitably arise. This is seen to be the case for the ramp separating faults 6 and 7. This ramp currently preserves low internal ramp gradients and yet is almost fully linked. Importantly, however, the ramp is significantly eroded with a major paleo-drainage channel running directly through the ramp and significant amounts of sediment covering the ramp itself. In this case, significant ramp erosion explains the apparent anomaly of having a breached low gradient ramp. It is assumed that ramp strain is high enough to generate linkage although is currently disguised at the ground surface by significant sedimentation and erosion. An alternative explanation for the breaching of a ramp which actually has low strain, is to assume that the state of strain in such a ramp is significantly greater below the surface, thus providing the initial impetus for fault linkage. A linking structure may then have propagated vertically to intersect a low strain ramp seen at the ground surface today.

Cutoff gradients and internal relay ramp strain

The cutoff gradients of faults bounding a relay ramp exert a fundamental control on the strain experienced in the ramp. The correlation co-efficient from the regression calculation between these 2 parameters is therefore unsurprisingly high as shown on Figure 6.16. One ramp has a maximum internal ramp strain that differs significantly from the maximum cutoff gradient, specifically the ramp separating the northern tip of fault 2 from fault 3. This results from there being a significant difference in relative elevation, perpendicular to fault strike, between the footwall cutoff of fault 2 and the hangingwall cutoff of fault 3. This creates sufficient bending parallel to fault strike to exceed the strain generated by the cutoff gradients of the bounding faults. Cutoff gradients for ramp bounding faults are, however, generally valuable tools for predicting the state of strain in a relay ramp and consequently the likelihood for fault linkage. This result has applications to the prediction of fault linkage below the limits of seismic resolution assuming the ramp bounding fault cutoff gradients can themselves be resolved.

6.7.3 Numerical modelling of relay ramp development

As stated in the introduction, some motivation for undertaking the detailed ramp studies presented here came from the failure of a numerical fault interaction model by Crider and Pollard (1998) to successfully replicate the ramp dip directions commonly encountered in the field, i.e. toward the collective hangingwall (see section 6.6.1). Crider & Pollard (1998) use a boundary element elastic model to replicate the development of a relay zone and compare it with a real example from south central Oregon. The main difference between the result of their model and the field example proves to be the dip of the ramp. The ramp in their boundary element model dips toward the collective footwall while the ramp in the field dips toward the collective hangingwall (Figure 6.20). Crider and Pollard (1998) propose several possible explanations for this disparity in ramp dip, including the role of erosion and deposition, anticlinal fault propagation folding, material properties, complex subsurface fault geometry and variations in friction. However, section 6.7.1.2 discussed a case study on the Tableland where the relay ramp dips consistently toward the collective hangingwall and it has been shown that many of the processes listed above were unlikely to have been in operation. This importantly suggests that such a ramp dip can result from primary fault growth mechanisms rather than be induced by a secondary process such as erosion, deposition or folding.

Cowie et al. (1993) introduce a numerical rupture model for fault array evolution that includes incremental fault propagation and instantaneous fault zone healing, i.e. the frictional strength of a fault is restored to its original value immediately after rupture. In this model it is possible to produce relay ramps that dip toward the collective hangingwall (see Fig. 4 in Cowie et al., 2000). It could be speculated that modelling fault zones as capable of instantaneous healing, as in the model of Cowie et al. (1993), rather than frictionless elements as in the model of Crider and Pollard (1998), makes it possible to create ramps that dip toward the collective hangingwall via primary fault growth mechanisms as is seen in the survey data presented for this project. This is an area of modelling that contains significant potential for future research in order to improve understanding of the vertical manifestation of fault stress field interactions.

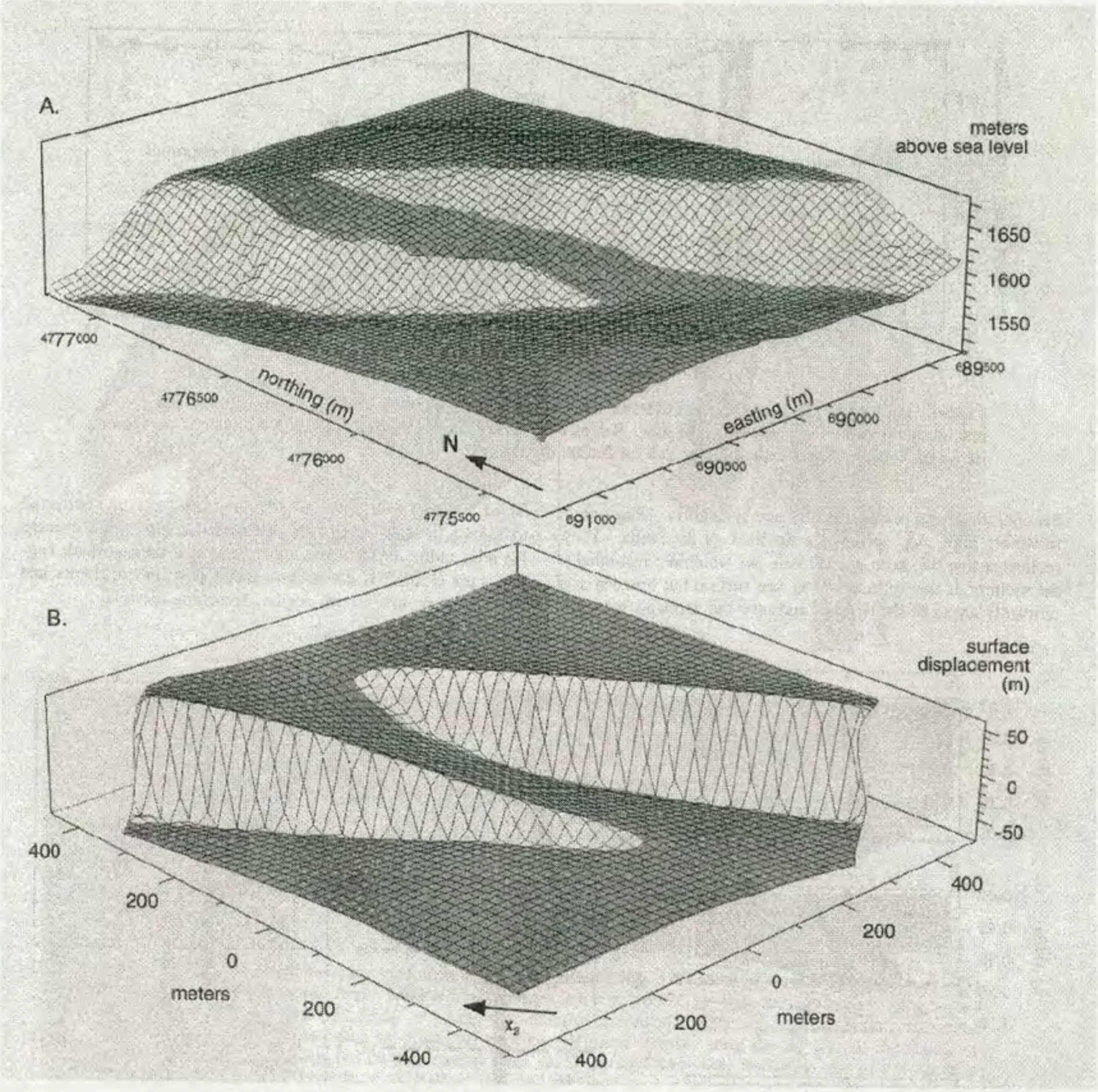

Figure 6.20. Figure 9 from Crider and Pollard (1998) showing the contrast between the ramp dip from their relay ramp survey data (upper picture) and the ramp dip produced in their numerical model (lower picture). The upper picture shows the true ramp dip toward the collective hangingwall and the lower picture shows the ramp dip in the model toward the collective footwall.

6.8 Summary

- Ramps with bounding faults separated by less than 70 metres dip toward the collective hangingwall. This dip direction results from primary fault growth mechanisms although may be enhanced by secondary processes such as erosion, sedimentation and fault propagation folding. Understanding the fault growth mechanisms responsible for inducing this dip direction is an area with significant potential for future research, most probably via numerical modelling.

- The manner in which fault growth is partitioned, i.e. mostly footwall uplift or hangingwall subsidence, controls the strain experienced within a ramp by controlling the cutoff gradients of ramp bounding faults. Low separation ramps can preserve high or low strain. For a low separation fault pair the back fault must by necessity remain higher than the front fault at all times in the growth process to preserve the dip direction toward the collective hangingwall.

- Increasing ramp strain increases the likelihood for fault linkage, consistent with elastic-brittle rheological behaviour of the ramp material. Given that fault cutoff gradients are shown to typically control ramp strain, this makes cutoff gradients a valuable tool for fault linkage prediction. This result has applications for the prediction of fault linkage below the limits of seismic resolution where the cutoff gradients on ramp bounding faults can be resolved.

- Strong fault interaction signals for an overlapping fault pair, i.e. elevated Dmax:L ratios, tip gradients and profile asymmetry, do not imply a specific geometry or strain state for a ramp. Relay ramp development can thus be considered separately from these forms of fault interaction, while acknowledging that the driving force for faults to adopt different styles of growth partitioning may be indicative of a form of fault interaction in its own right.

Chapter 7 – Conclusions and future work

7.1 Re-assessing the definition of an isolated fault

In order to understand the manifestation of fault interactions in a fault displacement profile it is necessary to try and define what a fault would look like had it grown in isolation without the influence of other faults. The most detailed published work on normal fault growth and interaction, by Gupta and Scholz (2000a), assumes a separation distance beyond which two faults will be considered to be growing in isolation based on previous work on strike-slip faults by An (1997) and the numerical modelling of fault interactions by Willemse (1997). This distance has not been verified with evidence from normal faults in the field. A new quantitative process for identifying an isolated fault is developed for this thesis.

D_{max}:L ratios for two faults in a potentially interacting pair, extracted from high resolution fault survey data, are plotted against the separation distance between the faults, normalised by the summed length of the faults under consideration. In this manner, it is possible to monitor how a fault interaction signal varies as the separation distance between a fault pair is increased, for a given fault length. Using this technique, fault growth in isolation on the Volcanic Tableland is quantitatively defined, with the data available, as those faults with separation distances greater than 0.1* the total length of the fault pair in question (i.e. $S/L_t > 0.1$). This is based on changes in D_{max}:L ratios around this threshold, i.e. D_{max}:L ratios increase with decreasing S/Lt ratios of < 0.1 and plateau above S/Lt ratios of 0.1. Independence of D_{max}:L ratios on S/L_t ratios of > 0.1 would suggest that such faults do not affect each other's growth.

D_{max}:L ratios are considered to be a more accurate indicator of fault interaction than profile asymmetry as profile asymmetry is often obscured by fault interaction with rock mass heterogeneities, fault linkage or interactions with neighbouring faults at both tips. This is discussed in more detail below.

7.2 Fault interactions

It is demonstrated that normal faults in overlapping pairs or multi-segment arrays have predictably higher D_{max}:L ratios than faults growing in comparative isolation in the same setting. This observation complements similar discoveries by Dawers and Anders (1995), Peacock and Sanderson (1996), Nicol et al. (1996), Willemse et al. (1996), McFadzean et al. (1999), Gupta and Scholz (2000a) and Poulimenos (2000) on overlapping normal faults of various scales and in various tectonic settings. Few studies have been undertaken to quantitatively assess the controls on different degrees of fault interaction, particularly for faults of the scale encountered on the Volcanic Tableland that have achieved their current dimensions via growth in multiple slip cycles. Recent papers by Gupta and Scholz (2000b) and Poulimenos (2000) document an increase in fault D_{max}:L ratios with increasing regional strain for faults of an order of magnitude larger than those surveyed for this project. This increase in D_{max}:L ratios is assigned to the role of fault interactions in increasingly affecting fault population growth with increasing fault density. These results suggest that fault interaction processes may be scale-independent but do not discuss the controls on the strength of individual fault interactions. With this in mind, the growth parameters of kilometre scale are analysed here on a case by case basis with respect to their spatial relationship to neighbouring structures.

The D_{max}:L ratios of overlapping faults are compared with the separation distance between faults as discussed in section 7.1 and with fault pair O:S ratios. Fault interaction is seen to increase with the increasing spatial proximity of fault segments, i.e. decreasing separation distance, and increasing fault pair overlap for a given separation distance. This latter phenomenon is manifested in rising minimum D_{max}:L ratios and, to a lesser extent, tip gradients with increasing O:S ratio. These results suggest the spatial geometry of faults is indeed linked to the degree of interaction they have experienced during growth over multiple slip cycles.

Given that O:S ratios are shown to exert a control over D_{max}:L ratios, it is of interest to know whether O:S ratios themselves are restricted by the same interaction processes that elevate D_{max}:L ratios. To this end, scale independent O:S plots, with both parameters normalised by fault length, are prepared for all faults on the

Tableland. This test reveals that there are restrictions on attainable plan view fault array geometries, as faults do not overlap beyond a critical distance, related to fault length. This in turn suggests that fault growth in overlapping scenarios may be impaired by the existence of stress shadows that scale with fault length. This has not been directly demonstrated before for normal faults of this scale although is a fundamental assumption of the fault interaction models of Willemse et al. (1996), Crider and Pollard (1998) and Gupta and Scholz (2000a) amongst others. Importantly, this implies that stress shadows from individual slip increments may be able to partially accumulate in the rock mass over multiple slip cycles. The temporal evolution of earthquake induced stress perturbations in the rock mass remains a poorly understood area and results from this project make a contribution to this developing field of research.

7.3 The role of rock mass heterogeneities in affecting fault growth

The upper surface of the Volcanic Tableland is affected by two distinct forms of heterogeneity, namely a pervasive tectonic conjugate joint set and a large number of distributed fumarole mounds, both of whose role in affecting fault growth is analysed. The tectonic origin of the joint set and its relationship to the extensional faulting remains ambiguous while the fumaroles represent sites of degassing as the newly erupted tuff settled into the Owen's valley.

Several cases can be seen where faults clearly deflect into joints. This is often accompanied by a major change in fault strike at the point of deflection. Faults can also be seen to stop or tip out near fumarole mounds. Analysis of displacement profiles where faults interact with joints or fumaroles in this way reveals that such rock mass heterogeneities can predictably affect fault growth. Faults deflecting into or growing along joints develop anomalously low tip gradients in comparison to both interacting and isolated faults in this setting. The portion of the fault growing along the joint consistently accumulates anomalously low displacement for a given length. This process in turn lowers D_{max}:L ratios for the affected faults. This result is consistent with the observations of Wilkins et al. (2001) who analyse the dimensions of faults that have reactivated joints at Split Mountain, Utah. Wilkins et al. (2001) find that such faults have anomalously low D:L ratios for faults of their size in comparison to published fault scaling laws. Faults that tip out at or near fumaroles, by contrast, display anomalously high tip gradients in comparison to interacting and isolated faults in this setting. This process in turn elevates D_{max}:L ratios for the affected faults.

The style of interaction identified between faults and these two forms of heterogeneity suggests that joints and fumaroles act predictably as zones of low and high shear strength respectively within the rock mass. In the case of a fault growing into a joint, the joint length is already established as a discontinuity in the rock mass and thus a fault is required to do less work to use this feature for continued propagation than to rupture intact rock. The tip gradient of a fault, proportional to the shear strength of the surrounding rock (Cowie and Scholz, 1992b), is thus significantly less for a fault deflecting into a pre-established zone of low shear strength. By the same principle, a fault growing toward or past a pre-established zone of high shear strength, such as a fumarole mound, must develop an anomalously high tip gradient to continue to propagate. The signal of a fault's interaction with such a heterogeneity is capable of diluting, enhancing or completely disguising a fault interaction signal. This has important implications for any study of fault interactions, particularly those in the sub-surface where the presence or absence of heterogeneities, their form and density is ultimately unverifiable.

7.4 Relay ramp development

High-resolution field survey data is presented for relay ramps and their bounding faults with a view to assessing the principal controls on ramp dip direction, ramp strain and subsequent fault linkage. Such a field study has not previously been undertaken in the literature.

Survey data shows that relay ramps on the Tableland often dip toward the collective hangingwall of an interacting fault pair, a result that contradicts the results of a numerical model of relay ramp development by Crider and Pollard (1998).

Further analysis reveals that the separation distance between fault pairs exerts a critical control on the dip direction of the ramp, with fault pairs at separations of less than 70m dipping toward the collective hangingwall and fault pairs at separations of greater than 140m dipping toward the collective footwall in this setting. Ramp breaching faults, erosion and fault propagation folding are shown capable of modifying or disguising this dip direction, although crucially it is shown possible to create relay ramps that dip toward the collective hangingwall without invoking such secondary ramp altering processes. The fundamental mechanical controls on ramp dip direction remain poorly understood and represent an area with significant potential for future work. Predicting the dip direction of relay ramps clearly has important implications for the sedimentation history of any evolving extensional terrane given the tendency for drainage routes to utilise ramps for sediment dispersal.

The cutoff gradients of ramp bounding faults refer to the gradients encountered walking along the footwall cutoff of the front fault or hangingwall cutoff of the back fault within a ramp area. The partitioning of fault growth, i.e. into footwall uplift and hangingwall subsidence, controls the cutoff gradients on ramp bounding faults. In this respect, traditional fault interaction indicators such as elevated tip gradients and profile asymmetry can be considered separately from relay ramp development, as cutoff gradients are independent of these parameters. Cutoff gradients in turn are shown to control the strain within a ramp. The probability of fault linkage is directly related to ramp strain with high strain ramps more likely to be linked than their low strain equivalents, consistent with elastic rheological ramp behaviour. This makes cutoff gradients valuable tools for fault linkage prediction and has applications for the prediction of fault linkage below the limits of seismic resolution.

7.5 Future work

The recognition of deformation-free areas in the footwall high of major faults on the Tableland has significant potential for future work. The explanation for this phenomenon may relate to the role of stress shadows in preventing deformation adjacent to an incrementally growing fault (e.g. Ackermann and Schlische, 1997). It may also represent a simpler phenomenon such as footwall uplift leading to localised compression and joint closure such as documented in the Canyonlands graben region by Moore and Schultz (1999). An interesting study would be to analyse changes in fault displacement with respect to changes in the width of the deformation-free zone. This may provide information as to whether the dimensions of the zone are related to stress drop and thus the suppression of fault growth by a stress shadow. Such a study would be important in helping constrain the density of deformation one would expect to find adjacent to major faults, an area of much interest to sub-surface structural geologists.

As discussed in Chapter 6, what causes faults to partition growth differently, from mostly footwall uplift to mostly hangingwall subsidence, remains poorly understood. It is not clearly linked to the processes of fault interaction that lead to changes in fault displacement profiles as modelled by Willemse et al. (1996) and Gupta and Scholz (2000a). This problem requires significantly more field data from different settings. The driving forces for extension on the Volcanic Tableland are thought to be flexural (Pinter, 1995), as opposed to the spreading forces of traditional extensional settings. This might be expected to affect the manner in which faults partition growth, both while they grow in isolation and subsequently interact. In contribution to this problem, it would be an obvious and valuable test to explore whether or not there exists a similar range of separation distances over which a reversal in relay ramp dip direction occurs, such as is evident on the Tableland, in other tectonic settings.

All of the quantitative tests developed and tested here to improve our understanding of fault interactions have unlimited potential for application to other fault populations and indeed fault types. It is anticipated that the local fault interaction affects identified in this thesis will have a generic applicability to the evolution of all fault populations, irrespective of the nature of regional tectonic loading, or the scale of the faults under consideration. This is evidenced here in the similar results obtained from quantitative analysis of cm scale and kilometer scale fault populations from different tectonic settings. However, regional stresses may modify local fault interaction signatures and thus it is clearly valuable to use these quantitative tests on fault data from other tectonic settings. In this manner, the control exerted by different natural variables on fault interactions, such as rock type, tectonic loading conditions and rock mass heterogeneity will gradually become better constrained in their contribution to the growth history of an evolving fault population.

Appendix 1 – Amalgamating total station data sets from different base station locations

Aims

- To rotate co-ordinate axes from different base station surveys so they become aligned with one set of master base station co-ordinate axes.
- To translate or shift data from different base station surveys, after rotation of co-ordinate axes, so that data points are assigned values as if all were recorded from the master base station.

Procedure

- Need **rotation angle** to apply to co-ordinate axes from different base station surveys. To this end, two common points, A and B, are flagged and surveyed from 2 different base station locations, BS1 and BS2:

Point A from BS1 has co-ordinates (x_1,y_1), Point B from BS1 has co-ordinates (x_2, y_2), Point A from BS2 has co-ordinates (x_3, y_3), Point B from BS2 has co-ordinates (x_4, y_4).

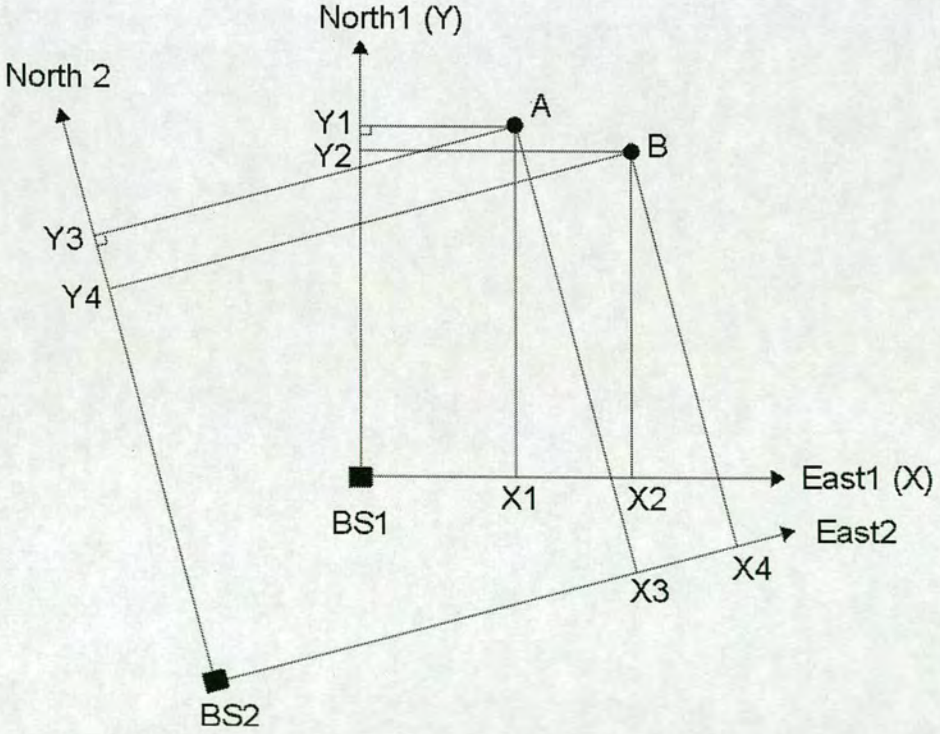

The angle of error between the two northing axes (North1 and North2), as set for the 2 different surveys using a compass, is exaggerated here for ease of visualisation. To acquire the angle between the two different northing lines:

Let point B always be the southernmost of the 2 surveyed points. For the case where point B is further east than point A the diagram below shows the angles we are interested in acquiring:

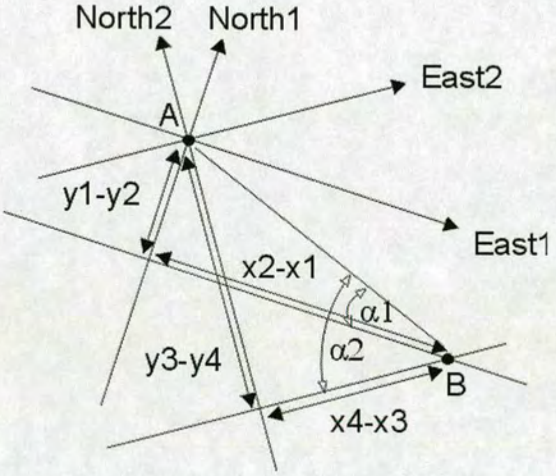

$\alpha 1 = \arctan(y_1 - y_2 / x_2 - x_1)$,

$\alpha 2 = \arctan(y_3 - y_4 / x_4 - x_3)$

Rotation angle to align northing axes = $\alpha 2 - \alpha 1$

For the case where point B is further west than point A the angles we are interested in are shown below:

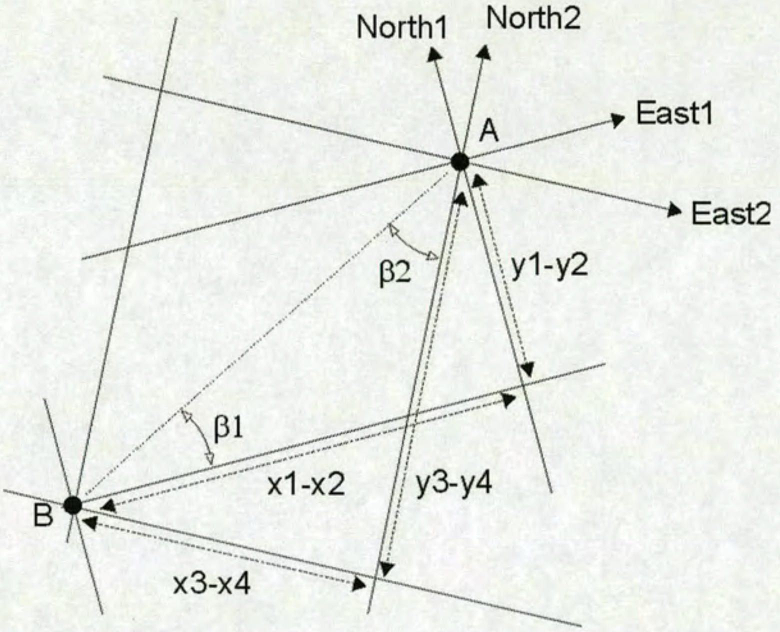

$\beta 1 = \arctan (y1\text{-}y2/x1\text{-}x2)$

$\beta 2 = \arctan (x3\text{-}x4/y3\text{-}y4)$

Rotation angle to align northing axes = $90-(\beta 2+\beta 1)$

The **angles** between surveys should now be known. The data points themselves should not be rotated, rather the rotation angle is used to rotate the co-ordinate axes around the points by the angle specified. The corresponding change in the co-ordinates of a point is demonstrated graphically below:

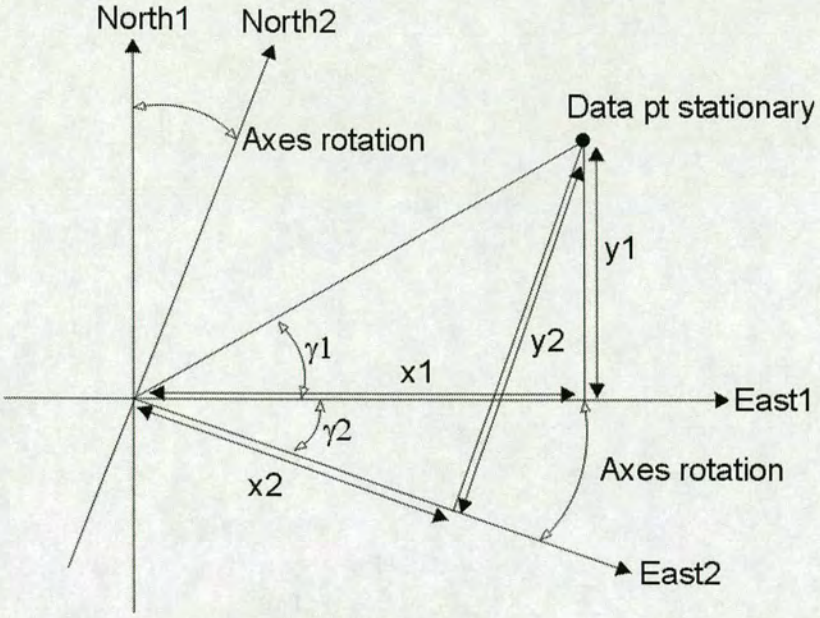

Y1 = rsinγ1

X1 = rcosγ2

Y2 = rsin(γ1+γ2)

X2 = rcos(γ1+γ2)

Y2 = rsinγ1cosγ2 + rcosγ1sinγ2 (1)

X2 = rcosTcosS – rsinTsinS (2)

Substituting Y1 = rsinγ1 and X1 = rcosγ2 into equations (1) and (2) gives:

- Y2 = Y1cosγ2 + X1sinγ2
- X2 = X1cosγ2 – Y1sinγ2

These are the axes rotation solutions.

Finally, it is necessary to **translate** the new rotated data points to give them the co-ordinates they would have if shot from the master base station. This merely involves adding (-a, -b) to all rotated co-ordinates as shown in the diagram below:

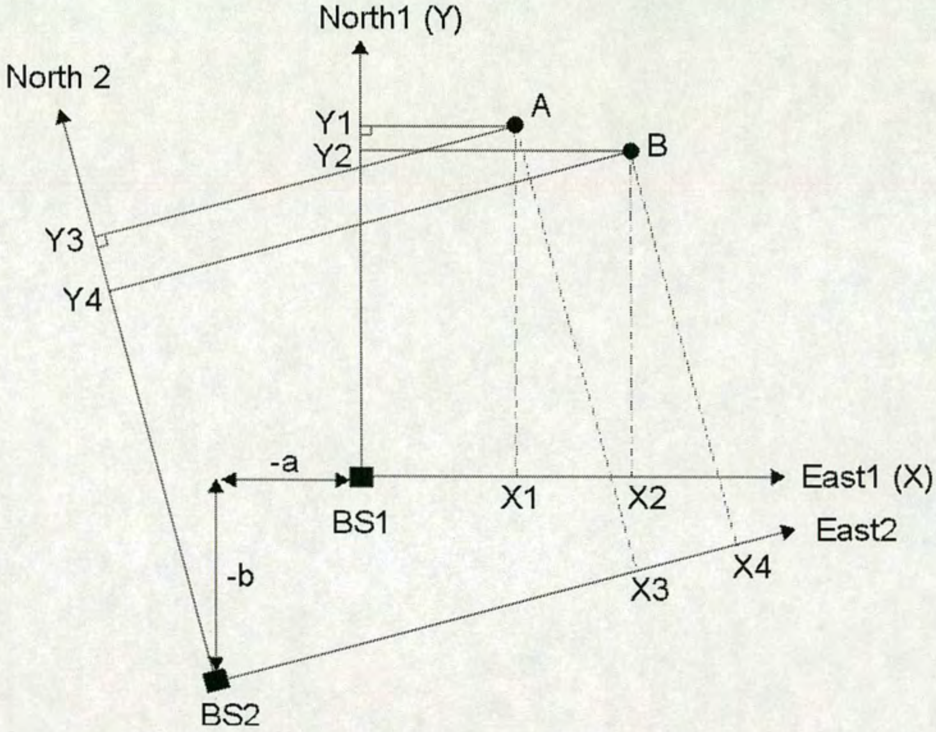

The process described in this appendix allows data from multiple surveys with different base station sites to be accurately converted to read as if all shot from one master base station. In this manner, individual fault surveys can be pieced together into accurate plan view maps showing multi-segment fault arrays.

Appendix 2 – Construction of an average isolated displacement profile

- **Aim**

To construct an average isolated displacement profile from fault survey data on the Volcanic Tableland for comparison with the profiles of faults that are potentially undergoing interaction.

- **Procedure**

Two faults were selected from the data-set of Dawers et al. (1993) which fitted this project's definition of isolated structures (i.e. separated from their nearest neighbour by $>0.1*L_t$). The procedure for creating an average isolated profile from these 2 faults is outlined below:

Firstly, the relevant displacement profiles are normalised by fault length. Using linear interpolation, the distribution of normalised displacement is calculated at 10 regular intervals along strike of these 2 structures. An average value of normalised displacement is then taken from the 2 faults at each regular interval along strike as well as a standard deviation to describe the variation about this mean. The average displacement profile, plus or minus one standard deviation, is plotted below as normalised displacement vs normalised length.

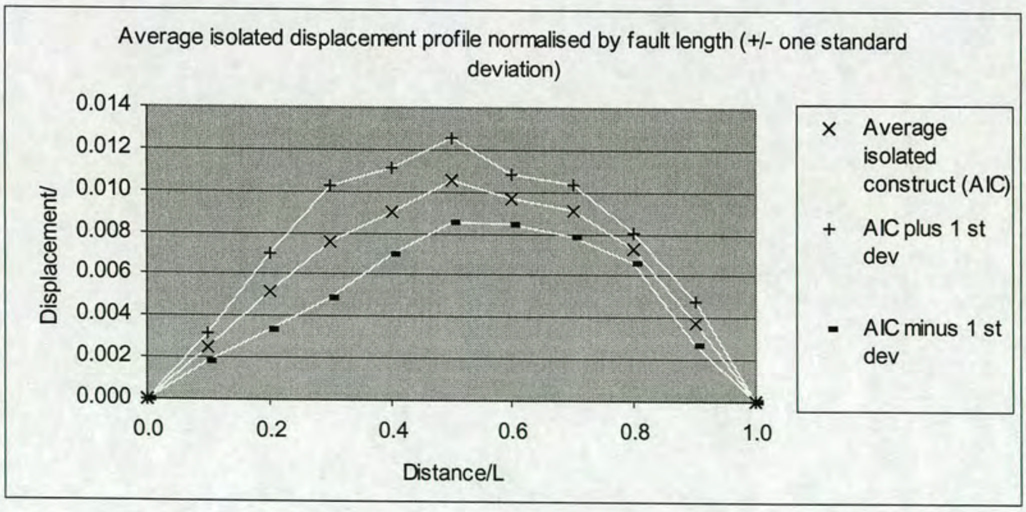

Appendix 3 – Removal of joint controlled tips and construction of hypothetical tips

- **Aim**

To remove the tips of faults that clearly deflect into or grow along joints and construct a new tip based on the displacement gradient immediately prior to the point of deflection or major gradient inflexion.

- **Procedure**

The procedure for removing joint controlled tips is outlined graphically below:

Firstly identify appropriate tips. These can be fault tips that clearly divert into joint trends or faults that follow a joint trend along their entire length as sketched below.

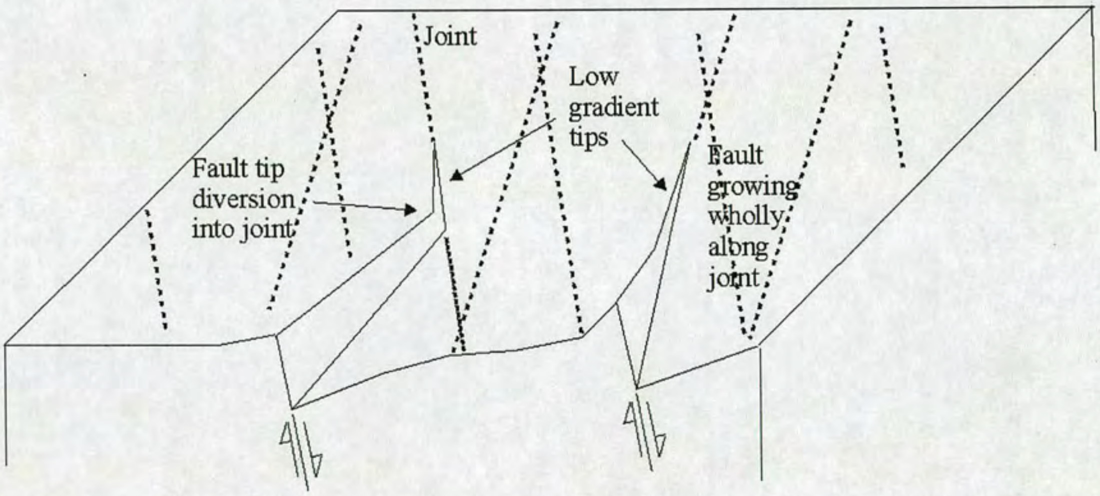

The joint controlled tip is then removed from the displacement profile and replaced with a hypothetical construct based on the gradient encountered immediately prior to the anomalously low tip gradient:

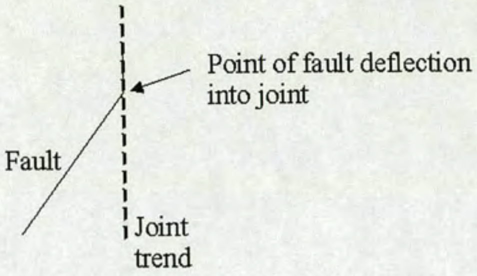

Plan View

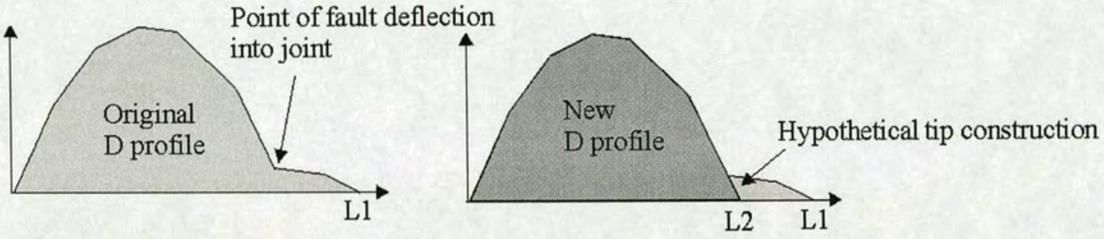

Displacement vs distance plots

The new hypothetical fault has a shorter length and the same D_{max}, thus a higher D_{max}:L ratio, as well as less overlap (O) with neighbouring structures and thus a lower O:S ratio as shown diagrammatically below.

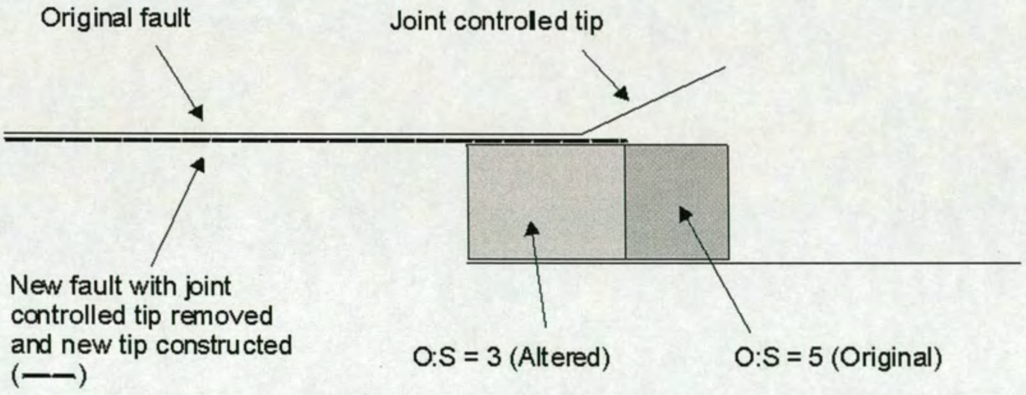
Plan view of overlapping fault pair

Appendix 4 - Tip gradient recording techniques and results

The gradient approaching a fault tip, or the point of zero resolved displacement in the field, is referred to as the tip gradient. This gradient controls the finite stress concentration at the tip of the fault (Cowie and Scholz, 1992b) and thus is intrinsically linked to the processes of fault propagation and interaction. A problem inherent to the recording of tip gradients in the field is defining the horizontal distance over which the gradient is measured. A variety of techniques have been described in the literature although no agreement exists as to whether one technique should be used in preference to others. Cartwright and Mansfield (1998) provide a useful summary of some of the techniques available for use in their analysis of fault tip gradients in the Canyonlands graben district, Utah. These include: i) measuring from the first inflexion point, assuming the inflexion point lies 10% above a smoothed best fit displacement curve, ii) measuring from the point of maximum displacement on the fault, iii) measuring from the first displacement maxima, assuming the displacement maxima point lies 10% above a smoothed best fit displacement curve and iv) measuring from the last point before which there exists a linear gradient to the tip. Methods (i) and (ii) were subsequently rejected by these authors as yielding unrepresentative results for the data set as a whole. The techniques listed above are graphically summarised in Figure A. Cowie and Shipton (1998) employ a different technique in analysing the tip gradients produced by their numerical model of simulated fault growth. Their method involves averaging tip gradients to a distance behind the fault tip that is proportional to the total fault length. The techniques employed for recording tip gradients from the displacement vs distance plots presented in Chapter 3 are outlined here.

Firstly, tip gradients are interpolated from displacement profiles at 50 metre intervals from the tips, up to 200 metres from either tip depending on the length of the fault. If a fault is less than 400 metres long or asymmetric such that the maximum displacement on the fault lies within 200 metres of one tip, recordings stop at 150 metres or less. This technique has the distinction that the distance increments over which tip gradients are being recorded are independent of the scale of the fault under consideration.

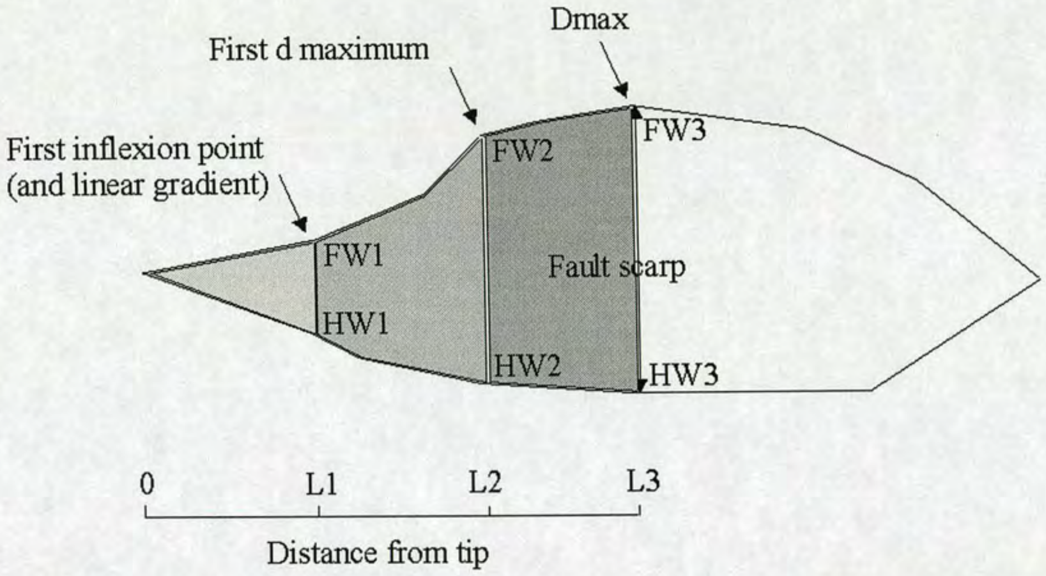

Tip gradient recording method	Tip gradient
Linear tip gradient	(FW1-HW1)/L1
First Inflexion point	(FW1-HW1)/L1
First d maximum	(FW2-HW2)/L2
D max	(FW3-HW3)/L3

Figure A. Various methods for recording tip gradients as outlined by Cartwright and Mansfield (1998). Note that in the figure above the points representing the first inflexion point from the tip and the first linear gradient from the tip are co-incident and thus the tip gradients are equal.

Following on from this technique, an averaging process is used to produce an average tip gradient over the maximum distance of 200 metres from the tip. This technique involves the simple addition of displacement at each distance increment, followed by division by the number of increments, then division by the total distance from the tip.

The next technique involves interpolating tip gradients at distances from the fault tip which are proportional to the total fault length, a method similar to that used by Cowie and Shipton (1998). The distances at which gradients are interpolated are 0.05L, 0.1L, 0.15L and O.2L, with L equal to the total length of the fault in question.

Cowie and Shipton (1998) use an extremely small increment spacing equal to the cell dimensions of their model although such detail is unattainable with more widely spaced field data. Again, an averaging process is subsequently used to obtain the average gradient over 0.2L. This method has the advantage that 4 measures of tip gradient will be taken irrespective of fault length.

The next technique used involves measuring from the first inflexion point or data maxima in the displacement profile, irrespective of the scale of the fault. This technique is not dissimilar to the 'first data point' technique proposed by Cartwright and Mansfield (1998). In their paper they state they have measured their first data point on every fault profile at a point which, by eye, represented the first shift in gradient from a constant linear gradient since the tip. The main differences between their use of this technique and this study's are: (1) the reliance of Cartrwright and Mansfield (1998) on a subjective definition a linear tip taper, i.e. judged by eye rather than from high resolution data as done here, and (2) the data spacing which in their paper can be up to 200 metres, rather than a tenth of this distance as is typical in this study. The data spacing in this study means that inflexion points or data maxima are incurred significantly closer to the tip than would be the case had the linear taper been defined by eye. This may result in the recorded gradients being of less importance in stress transfer to the surrounding rock mass if they are extremely proximal to the tip.

- Comparison of recording technique results

A variety of techniques available for recording tip gradients have been discussed in this appendix and several employed which are deemed appropriate for use on faults on the Tableland. It is necessary to quantitatively compare the results of these different techniques and rate their ability to represent the total data set. This is desirable so that a representative technique or techniques can be chosen in order to use tip gradients in further quantitative analyses, for example with the spatial arrangement of fault segments as is undertaken in Chapter 5. The figures below show cross plots of the various tip gradient recording techniques to compare the results produced.

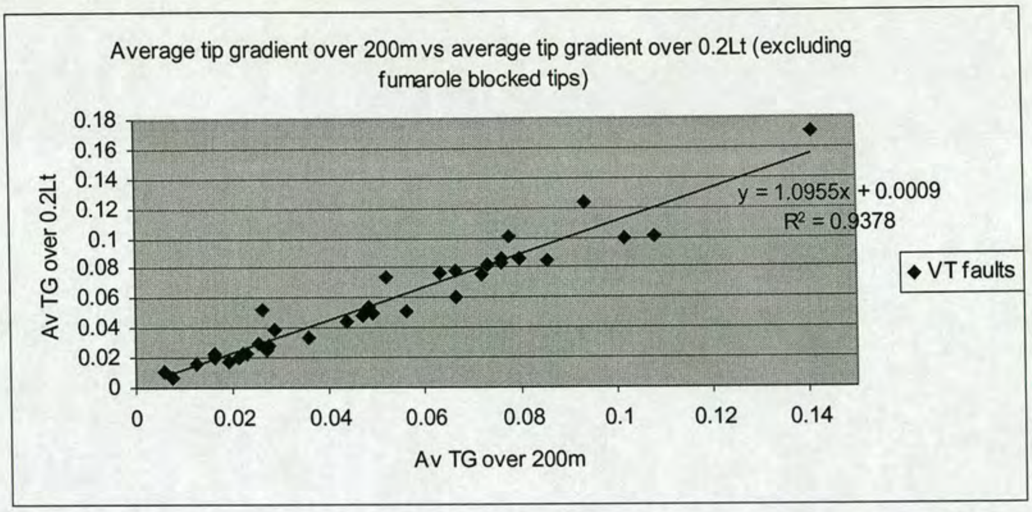

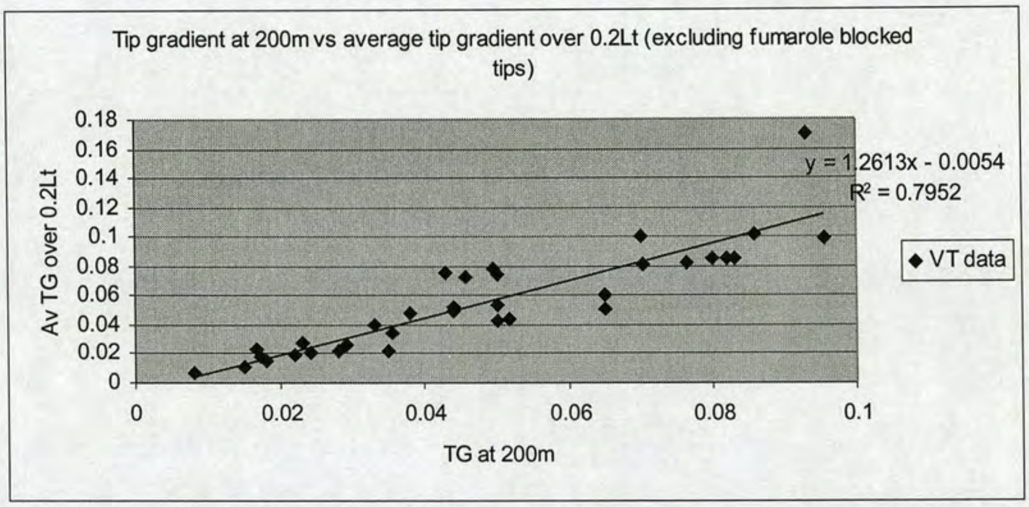

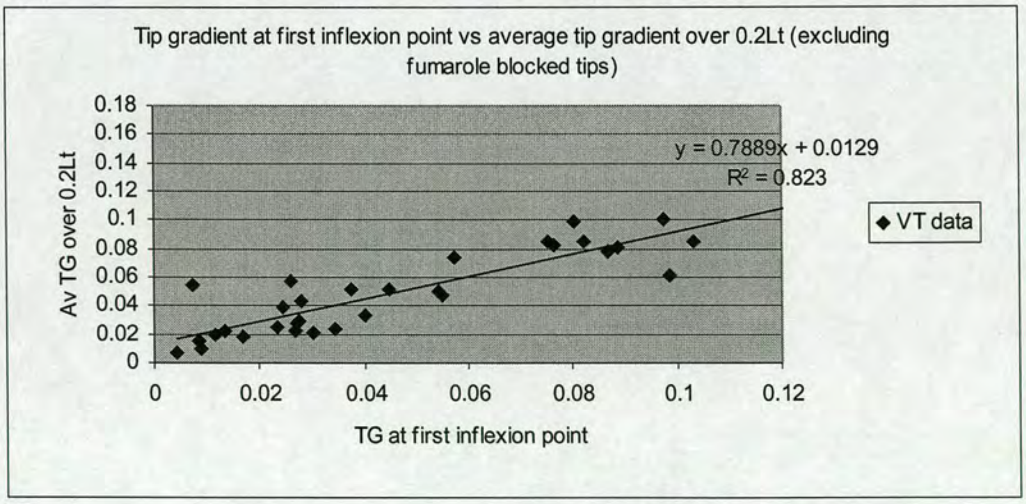

Four techniques are compared above: 1) recording the tip gradient from an arbitrary distance from the tip, in this case 200m or, if this was not possible, from

150/100 or 50m depending on constraints imposed by the fault size or degree of profile asymmetry, 2) recording the tip gradient as the average of the gradients recorded at 50/100/150 and 200m, or as many increments as apply, 3) recording the tip gradient as the average of 4 tip gradients recorded at 0.05/0.1/0.15 and 0.2Lt and 4) recording the tip gradient from the first inflexion point on the profile, be it concave or convex.

The cross-plots shown suggest that the 4 tip gradient recording techniques compared here produce broadly similar results for the fault population under consideration. This is indicated by the fact that Y is approximately equal to X in all cases with generally high linear correlation co-efficients and low Y-axis intercept values. The best match between the output of 2 techniques is for the average gradient over 200m from the tip and the average gradient over $0.2*L_t$ from the tip. A least squares best-fit regression calculation yields the equation $Y=1.09x + 0.0009$, with an R^2 co-efficient of 0.938. Given that these are both averaging techniques, involving measurements at significant distances from the tip, it is suggested that they produce the best representation of tip gradients for this particular set of faults and are used in quantitative analyses with spatial fault array geometries in Chapter 5.

Bibliography

Ackermann, R.V. and Schlische, R.W. (1997) Anticlustering of small normal faults around larger faults. *Geology*, **25**, 1127-1130.

Acocella, V., Gudmundsson, A., Funiciello, R. (2000) Interaction and linkage of extension fractures and normal faults: examples from the rift zone of Iceland. *Journal of Structural Geology*, **22**, 1233-1246.

Adiyaman, O., Chorowicz, J., Kobe, O. (1998) Relationships between volcanic patterns and neotectonics in Eastern Anatolia from analysis of satellite images and DEM. *Journal of Volcanology and Geothermal Research*, **82**, 17-32.

An, L-J. and Sammis, C.G. (1996b) Development of strike-slip faults: shear experiments in granular materials and clay using a new technique. *Journal of Structural Geology*, **18**, 1061-1077.

An, L-J. (1997) Maximum link distance between strike-slip faults: observations and constraints. *Pure and Applied Geophysics*, **150**, 19-36.

Anders, M.H. and Schlische, R.W. (1994) Overlapping faults, intrabasin highs, and the growth of normal faults. *Journal of Geology*, **102**, 165-180.

Aydin, A. and Schultz, R.A. (1990) Effect of mechanical interaction on the development of strike-slip faults with echelon patterns. *Journal of Structural Geology*, **12**, 123-129.

Bachman, S.B. (1978) Pliocene-Pleistocene break-up of the Sierra Nevada-White-Inyo Mountains and formation of Owens Valley. *Geology*, **6**, 461-463.

Bateman, P.C. (1965) Geology and tungsten mineralisation of the Bishop district, California. *U.S. Geological Survey Professional Paper*, **470**, 208p.

Beanland, S. and Clark, M.M. (1994) The Owens Valley fault zone, eastern California, and surface faulting associated with the 1872 earthquake. *U.S. Geological Survey Bulletin*, 29 p.

Bennett, R.A., Davis, J.L., Wernicke, B.P. (1999) Present-day pattern of Cordilleran deformation in the western United States. *Geology*, **27**, 371-374.

Bohnenstiehl, D.R. and Kleinrock, M.C. (2000) Evidence for spreading-rate dependence in the displacement-length ratios of abyssal hill faults at mid-ocean ridges. *Geology*, **28**, 395-398.

Burgmann, R., Pollard, D.D, Martel, S.J. (1994) Slip distributions on faults: effects of stress gradients, inelastic deformation, heterogeneous host-rock stiffness, and fault interaction. *Journal of Structural Geology*, **16**, 1675-1690.

Cartwright, J.A., Trudgill, B.D., Mansfield, C.S. (1995) Fault growth by segment linkage: an explanation for scatter in maximum displacement and trace length data from the Canyonlands Graben of SE Utah. *Journal of Structural Geology*, **17**, 1319-1326.

Cartwright, J.A., Mansfield, C., Trudgill, B. (1996) The growth of normal faults by segment linkage. *Geological Society Special Publication*, **99**, 163-177.

Cartwright, J.A., and Mansfield, C.S. (1998) Lateral displacement variation and lateral tip geometry of normal faults in the Canyonlands National Park, Utah. *Journal of Structural Geology*, **20**, 3-19.

Childs, C., Easton, S.J., Vendeville, B.C., Jackson, M.P.A., Lin, S.T., Walsh, J.J., Watterson, J. (1993) Kinematic analysis of faults in a physical model of growth faulting above a viscous salt analogue. *Tectonophysics*, **228**, 313-329.

Childs, C., Watterson, J. & Walsh, J.J. (1995) Fault overlap zones within developing normal fault systems. *Journal of the Geological Society of London*, **152**, 535-549.

Chinnery, M.A. (1961) The deformation of the ground around fault surfaces. *Bulletin of the Seismological Society of America*, **51**, 355-372.

Cockerhamm, R.S. and Corbett, E.J. (1987) The July 1986 Chalfant valley, California, earthquake sequence: Preliminary results. *Bulletin of the Seismological Society of America*, **77**, 280-289.

Contreras, J. Anders, M.H., Scholz, C.H. (2000) Kinematics of normal fault growth and fault interaction in the central part of Lake Malawi Rift. *Journal of Structural Geology*, **22**, 159-168.

Cowie, P.A. and Scholz, C.H. (1992a) Displacement-length scaling relationship for faults: data synthesis and discussion. *Journal of Structural Geology*, **14**, 1149-1156.

Cowie, P.A. and Scholz, C.H. (1992b) Physical explanation for the displacement-length relationship for faults using a post-yield fracture mechanics model. *Journal of Structural Geology*, **14**, 1133-1148.

Cowie, P.A. and Scholz, C.H. (1992c) Growth of faults by accumulation of seismic slip. *Journal of Geophysical Research*, **97**, 11,085-11,095.

Cowie, P.A., Vanneste, C., Sornette, D. (1993) Statistical physics model for the spatiotemporal evolution of faults. *Journal of Geophysical Research – Solid Earth*, **98**, 21809-21821.

Cowie, P.A., Sornette, D., Vanneste, C. (1995) Multifractal scaling properties of a growing fault population. *Geophysical Journal International*, **122**, 457-469.

Cowie, P.A. and Shipton, Z.K. (1998) Fault tip displacement gradients and process zone dimensions. *Journal of Structural Geology*, **20**, 983-997.

Cowie, P.A., Gupta, S., Dawers, N.H. (2000) Implications of fault array evolution for synrift depocentre development: insights from a numerical fault growth model. *Basin Research*, **12**, 241-261.

Cowie, P.A. and Roberts, G.P. (2001) Constraining slip rates and spacings for active normal faults. *Journal of Structural Geology*, **23**, 1901-1915.

Crider, J.G. and Pollard, D.D. (1998) Fault linkage: Three-dimensional mechanical interaction between echelon normal faults. *Journal of Geophysical Research*, **103**, B10, 24,373-24,391.

Dawers, N.H., Anders, M.H., Scholz, C.H. (1993) Growth of normal faults: displacement-length scaling. *Geology*, **21**, 1107-1110.

Dawers, N.H. and Anders, M.H. (1995) Displacement-length scaling and fault linkage. *Journal of Structural Geology*, **17**, 607-614.

Dawers, N.H. and Underhill, J.R. (2000) The role of fault interaction and linkage in controlling syn-rift stratigraphic sequences: Late Jurassic, Statfjord East area, northern North Sea. *American Association of Petroleum Geologists Bulletin*, **84**, 45-64.

Dawers, N.H., Malinverno, A., Scholz, C.H., and Borgos, H.G. Fault size distributions, linkage and the role of small faults: Observations from the Volcanic Tableland, California. *Journal of Structural Geology*, (in revision).

DePolo, C.M., Clark, D.G., Slemmons, D.B., Ramelli, A.R. (1991) Historical surface faulting in the Basin and Range province, western North America: implications for fault segmentation. *Journal of Structural Geology*, **13**, 123-136.

Dixon, T.H., Robardo, S., Lee, J., Reheis, M.C. (1995) Constraints on present-day Basin and Range deformation from space geodesy. *Tectonics*, **14(4)**, 755-772.

Dixon, T.H., Miller, M., Farina, F., Wang, H.Z., Johnson, D. (2000) Present-day motion of the Sierra Nevada block and some tectonic implications for the Basin and Range province, North American Cordillera. *Tectonics*, **19(1),** 1-24.

Ferrill, D.A., Stamatakos, J.A., Sims, D. (1999) Normal fault corrugation: implications for growth and seismicity of active normal faults. *Journal of Structural Geology*, **21**, 1027-1038.

Ferrill, D.A., Morris, A.P., Stamatakos, J.A., Sims, D.W. (2000) Crossing conjugate normal faults. *American Association of Petroleum Geologists Bulletin*, **84**, 1543-1559.

Ferrill, D.A. and Morris, A.P., (2001) Displacement gradient and deformation in normal fault systems. *Journal of Structural Geology*, **23**, 619-638.

Gawthorpe, R.L. and Hurst, J.M., (1993) Transfer zones in extensional basins: their structural style and influence on drainage development and stratigraphy. *Journal of the Geological Society of London*, **150**, 1137-1152.

Gawthorpe, R.L., Sharp, I., Underhill, J.R., (1997) Linked sequence stratigraphic and structural evolution of propagating normal faults. *Geology*, **25**, 795-798.

Gawthorpe, R.L. and Leeder, M.R. (2000) Tectono-sedimentary evolution of active extensional basins. *Basin Research*, **12**, 195-218.

Gilbert, C.M. (1938) Welded tuff in eastern California. *Geological Society of America Bulletin*, **49**, 1829-1862.

Gillespie, P.A., Walsh, J.J., Watterson, J. (1992) Limitations of dimension and displacement data from single faults and the consequences for data analysis and interpretation. *Journal of Structural Geology*, **14**, 1157-1172.

Gross, M.R, Fischer, M.P., Engelder, T., Greenfield, R.J. (1995) Factors controlling joint spacing in interbedded sedimentary rocks: Integrating numerical models with field observations from the Monterey Formation, USA. *Geological Society of London Special Publication*, **92**, 215-233.

Gupta, A. and Scholz, C. (2000a) A model of normal fault interaction based on observations and theory. *Journal of Structural Geology*, **22**, 865-879.

Gupta, A. and Scholz, C. (2000b) Brittle strain regime transition in the Afar depression: Implications for fault growth and sea-floor spreading. *Geology*, **28**, 1087-1090.

Gupta, S., Cowie, P.A., Dawers, N.H., Underhill, J.R. (1998) A mechanism to explain rift-basin subsidence and stratigraphic patterns through fault-array evolution. *Geology*, **26**, 595-598.

Hardebeck, J.L., Nazareth, J.J., Hauksson, E. (1998) The static stress change triggering model: Constraints from two southern Californian aftershock sequences. *Journal of Geophysical Research*, **103**, B-10, 24,427-24,437.

Hardy, S., McClay, K. (1999) Kinematic modelling of extensional fault-propagation folding. *Journal of Structural Geology*, **21**, 695-702.

Harris, R. and Simpson, R.W. (1992) Changes in static stress on southern California faults after the 1992 Landers earthquake. *Nature*, **360**, 251-254.

Harris, R. (1998) Introduction to special section: Stress triggers, stress shadows, and implications for seismic hazard. *Journal of Geophysical Research,* **103**, B10, 24,347-24,358.

Hearn EH. and Humphreys, ED. (1998) Kinematics of the southern Walker Lane Belt and motion of the Sierra Nevada block, California. *Journal of Geophysical Research – Solid Earth*, **103**, 27033-27049.

Hodgkinson, K.M., Stein, R.S., King, G.C.P. (1996) The 1954 Rainbow Mountain – Fairview Peak – Dixie Valley earthquakes: A triggered normal faulting sequence. *Journal of Geophysical Research*, **101**, 25,459-25,471.

Holt, E.W. and Taylor, H.P. (1998) O-18/O-16 mapping and hydrogeology of a short-lived (approximate to 10 years) fumarolic (> 500 degrees C) meteoric-hydrothermal event in the upper part of the 0.76 Ma Bishop Tuff outflow sheet, California. *Journal of Volcanology and Geothermal Research*, **83**, 115-139.

Hubert-Ferrari A, Barka A, Jacques E, Nalbant SS, Meyer B, Armijo R, Tapponnier P, King GCP. (2000) Seismic hazard in the Marmara Sea region following the 17 August 1999 Izmit earthquake. *Nature*, **404**, 269-273.

Huggins, P., Watterson, J., Walsh, J.J., Childs, C. (1995) Relay zone geometry and displacement transfer between normal faults recorded in coal-mine plans. *Journal of Structural Geology*, **17**, 1741-1755.

Izett, G. A., and Obradovich, J.D. (1994) 40Ar/39Ar age constraints for the Jaramillo normal subchron and the Matuyama-Brunhes geomagnetic boundary. *Journal of Geophysical Research*, **B99**, 2925-2934.

Kattenhorn, S.A. and Pollard, D.D. (2001) Integrating 3-D seismic data, field analogues, and mechanical models in the analysis of segmented normal faults in the

Wytch Farm oil field, southern England, United Kingdom. *American Association of Petroleum Geologists Bulletin*, **85**, 1183-1210.

Kilb, D., Gomberg, J., Bodin, P. (2000) Triggering of earthquake aftershocks by dynamic stresses. *Nature*, **408**, 570-574.

King, G.C.P., Stein, R.S., Rundle, J.B. (1988) The growth of geological structures by repeated earthquakes. 1. Conceptual framework. *Journal of Geophysical Research – Solid Earth*, **93**, 13,307-13,318.

King, G.C.P., Stein, R.S., Jian, L. (1994) Static stress changes and the triggering of earthquakes. *Bulletin of the Seismological Society of America*, **84** (3), 935-953.

Knuepfer, P.L.K. (1989) Implications of the characteristics of end-points of historical surface fault ruptures for the nature of fault segmentation. *U.S. Geological Survey Open File Report* 89-315, 193-228.

Larsen, P.H. (1988) Relay structures in a lower Permian basement-involved extension system, East Greenland. *Journal of Structural Geology*, **10**, 3-8.

Lee, J., Rubin, C.M., Calvert, A. (2001a) Quaternary faulting history along the Deep Springs fault, California. *Geological Society of America Bulletin*, **113**, 855-869.

Lee, J., Spencer, J., Owen, L. (2001b) Holocene slip rates along the Owens Valley Fault, California: Implications for the recent evolution of the Eastern California Shear Zone. *Geology*, **29**, 819-822.

Lienkaemper, J.J., Pezzopane, S.K., Clark, M.M., Rymer, M.J. (1987) Fault fractures formed in association with the 1986 Chalfant valley, California, earthquake sequence: Preliminary report. *Bulletin of the Seismological Society of America*, **77** (1), 297-305.

Liu, M. and Shen, Y. (1998) Crustal collapse, mantle upwelling, and Cenozoic extension in the North American Cordillera. *Tectonics*, **17** (2), 311-321.

Lueddecke S.B., Pinter, N., Gans, P. (1998) Plio-Pleistocene ash falls, sedimentation, and range-front faulting along the White-Inyo Mountains front, California. *Journal of Geology*, **106** (4), 511-522.

Mack, G.H. and Seager, W.R. (1995) Transfer zones in the southern Rio Grande rift. *Journal of the Geological Society of London*, **152**, 551-560.

Macleod, A.E., Dawers, N.H., Underhill, J.R. (2000) The propagation and linkage of normal faults: insights from the Strathspey-Brent-Statfjord fault array, northern North Sea. *Basin Research*, **12**, 263-284.

Marchal, D., Guiraud, M., Rives, T., Van Den Driessche, J. (1998) Space and time propagation processes of normal faults. *Geological Society of London Special Publications*, **147**, 51-70.

Mansfield, C. and Cartwright, J. (1996) High resolution fault displacement mapping from three-dimensional seismic data: Evidence for dip linkage during fault growth. *Journal of Structural Geology*, **18**, 249-263.

Mansfield, C. and Cartwright, J. (2001) Fault growth by linkage: observations and implications from analogue models. *Journal of Structural Geology*, **23**, 745-763.

Marchand, D.E. (1971) Rates and modes of denudation, White Mountains, eastern California. *American Journal of Science*, **270**, 109-135.

Marone, C. (1998) The effect of loading rate on static friction and the rate of fault healing during the earthquake cycle. *Nature*, **391**, 69-72.

Marret, R. and Allmendinger, R.W. (1991) Estimates of strain due to brittle faulting: sampling of fault populations. *Journal of Structural Geology*, **13**, 735-737.

Martel, S.J. (1990) Formation of compound strike-slip fault zones, Mount Abbot quadrangle, California. *Journal of Structural Geology*, **12**, 869-882.

McFadzean, P.J., Dawers, N., Cowie, P., (1999) Field insights to pre-linkage fault interactions. EOS, Transactions of the American Geophysical Union. 1999 Spring Meeting Supplement, **80** (17), S331.

McFadzean, P.J., Dawers, N., Cowie, P., (2000) The role of elastic interactions and rock mass heterogeneity on controlling normal fault array geometries. Proceedings of the Geological Society of America. 2000 Annual Meeting Published Abstract Volume, No. 52306.

Miller, M.M., Johnson, D.J., Dixon, T.H., Dokka, R.K. (2001) Refined kinematics of the Eastern California shear zone from GPS observations, 1993-1998. *Journal of Geophysical Research – Solid Earth*, **106**, 2245-2263.

Moore, J.M. and Schultz, R.A. (1999) Processes of faulting in jointed rocks of Canyonlands National Park, Utah. *Geological Society of America Bulletin*, **111**, 808-822.

Morley, C.K., Nelson, R.A., Patton, T.L., Munn, S.G. (1990) Transfer zones in the East African rift system and their relevance to hydrocarbon exploration in rifts. *The American Association of Petroleum Geologists Bulletin*, **74**, 1234-1253.

Muraoka, H., and Kamata, H. (1983) Displacement distribution along minor fault traces. *Journal of Structural Geology*, **5**, 483-495.

Nicol, A., Watterson, J., Walsh, J.J., Childs, C. (1996) The shapes, major axis orientations and displacement patterns of fault surfaces. *Journal of Structural Geology,* **18**, 235-248.

Pacheco, J., Nabelek, J. (1988) Source mechanisms of three moderate California earthquakes of July 1986. *Bulletin of the Seismological Society of America*, **78** (6), 1907-1929.

Peacock, D.C.P., and Sanderson, D.J. (1991) Displacements, segment linkage and relay ramps in normal fault systems. *Journal of Structural Geology*, **13**, 721-733.

Peacock, D.C.P., and Sanderson D.J. (1994) Geometry and development of relay ramps in normal faults systems. *The American Association of Petroleum Geologists Bulletin*, **78**, 147-165.

Peacock, D.C.P., Price, S.P., Whitham, A.G., Pickles, C.S. (2000) The World's biggest relay ramp: Hold With Hope, NE Greenland. *Journal of Structural Geology*, **22**, 843-850.

Peacock, D.C.P. (2001) The temporal relationship between joints and faults. *Journal of Structural Geology*, **23**, 329-341.

Pinter, N., Keller, E.A., West, R.B. (1994) Relative dating of terraces of the Owens river, northern Owens valley, California, and correlation with moraines of the Sierra Nevada. *Quaternary Research*, **42**, 266-276.

Pinter, N. and Keller, E.A. (1995) Geomorphological analysis of neotectonic deformation, northern Owens valley, California. *Geologische Rundschau*, **84**, 200-212.

Pinter, N. (1995) Faulting on the Volcanic Tableland, Owens Valley, California. *The Journal of Geology*, **103**, 73-83.

Poulimenos, G. (2000) Scaling properties of normal fault populations in the western Corinth graben, Greece: Implications for fault growth in large strain settings. *Journal of Structural Geology*, **22**, 307-322.

Rippon, J.H. (1985) Contoured patterns of the throw and hade of normal faults in the Coal Measures (Westphalian) of northwest Derbyshire. *Proceedings of the Yorkshire Geological Society*, **45**, 147-161.

San'kov, V., Deverchere, J., Gaudemer, Y., Houdry, F., Filippov, A. (2000) Geometry and rate of faulting in the North Baikal Rift, Siberia. *Tectonics*, **19**, 707-722.

Sarna-Wojcicki, A.M., Pringle, M.S., Wijbrans, J. (2000) New ^{40}Ar/^{39}Ar age of the Bishop Tuff from multiple sites and sediment rate calibration for the Mutuyama-Brunhes boundary. *Journal of Geophysical Research*, **105**, No.B9, 21,431-21,443.

Schlische, R.W., Young, S.S., Ackermann, R.V., Gupta, A. (1996) Geometry and scaling relations of a population of very small rift-related normal faults. *Geology*, **24** (8), 683-686.

Scholz, C.H. and Cowie, P.A. (1990) Determination of total strain from faulting using slip measurements. *Nature*, **346**, 837-839.

Scholz, C.H., Dawers, N.H., Yu, J.Z., Anders, M.H. (1993) Fault growth and fault scaling laws – preliminary results. *Journal of Geophysical Research – Solid Earth*, **98**, 21951-21961.

Scholz, C.H. (1998) Earthquakes and friction laws. *Nature*, **391**, 37-42.

Schultz, R.A. (1999) Understanding the process of faulting: selected challenges and opportunities at the edge of the 21st century. *Journal of Structural Geology*, **21**, 985-993.

Schultz, R.A. (2000) Fault-population statistics at the Valles Marineris Extensional Province, Mars: implications for segment linkage, crustal strains, and its geodynamical development. *Tectonophysics*, **316**, 169-193.

Segall, P. and Pollard, D.D. (1980) Mechanics of discontinuous faults. *Journal of Geophysical Research*, **88**, 555-568.

Sharp, I.R., Gawthorpe, R.L., Underhill, J.R., Gupta, S. (2000) Fault-propagation folding in extensional settings: Examples of structural style and synrift sedimentary response from the Suez rift, Sinai, Egypt. *Geological Society of America Bulletin*, **112**, 1877-1899.

Sheridan, M.F. (1970) Fumarolic mounds and ridges of the Bishop tuff, California. *Geological Society of America Bulletin*, **81**, 851-868.

Smith, K.D., Priestley, K.F. (2000) Faulting in the 1986 Chalfant, California, sequence: Local tectonics and earthquake source parameters. *Bulletin of the Seismological Society of America*, **90**, 813-831.

Stein, R.S., King, G.C.P., Rundle, J.B. (1988) The growth of geological structures by repeated earthquakes. 2. Field examples of continental dip-slip faults. *Journal of Geophysical Research – Solid Earth*, **93**, 13,307-13,318.

Stein, R.S., Barka, A.A., Dieterich, J.H. (1997) Progressive failure on the North Anatolian fault since 1939 by earthquake stress triggering. *Geophysical Journal International*, **128**, 594-604.

Stockli, D.F., Farley, K.A., Dumitru, T.A. (2000) Calibration of the apatite (U-Th)/He thermochronometer on an exhumed fault block, White Mountains, California. *Geology*, **28**, 983-986.

Tindall, S.E. and Davis, G.H. (1999) Monocline development by oblique-slip fault-propagation folding: the East Kaibab monocline, Colorado Plateau, Utah. *Journal of Structural Geology*, **21**, 1303-1320.

Trudgill, B. and Cartwright, J. (1994) Relay-ramp forms and normal-fault linkages, Canyonlands National Park, Utah. *Geological Society of America Bulletin*, **106**, 1143-1157.

Tsutsumi, H. and Yeats, R.S. (1999) Tectonic setting of the 1971 Sylmar and 1994 Northridge earthquakes in the San Fernando Valley, California. *Bulletin of the Seismological Society of America*, **85**, 1232-1249.

Twiss, R.J., Moores, E.M. (1992) Structural Geology. W.H. Freeman and company.

Unruh, J.H. (1991) The Uplift of the Sierra Nevada and implications for late Cenozoic epeirogeny in the western Cordillera. *Geological Society of America Bulletin*, **103**, 1395-1404.

Walsh, J.J and Watterson, J. (1987) Distributions of cumulative displacement and seismic slip on a single normal fault surface. *Journal of Structural Geology*, **9**, 1039-1046.

Walsh, J.J. and Watterson, J. (1988) Analysis of the relationship between displacements and dimensions of faults. *Journal of Structural Geology*, **10**, 239-247.

Walsh, J.J and Watterson, J. (1989) Displacement gradients on fault surfaces. *Journal of Structural Geology*, **11**, 307-316.

Walsh, J. and Watterson, J. (1991) Geometric and kinematic coherence and scale effects in normal fault systems. In 'The geometry of normal faults', *Geological Society of London Special Publication*, **56**, 193-206.

Watters, T.R., Robinson, M.S. (1997) Radar and photoclinometric studies of wrinkle ridges on Mars. *Journal of Geophysical Research – Planets*, **102**, 10889-10903.

Watterson, J. (1986) Fault dimensions, displacements and growth. *Pure Applied Geophysics*, **124**, 365-373.

Wilkins, S.J., Gross, M.R., Wacker, M., Eyal, Y., Engelder, T. (2001) Faulted joints: kinematics, displacement-length scaling relations and criteria for their identification. *Journal of Structural Geology*, **23**, 315-327.

Willemse, E.J.M., Pollard, D.D., Aydin, A. (1996) Three-dimensional analyses of slip distributions on normal fault arrays with consequences for fault scaling. *Journal of Structural Geology*, **18**, 295-309.

Willemse, E.J.M. (1997) Segmented normal faults: Correspondence between three-dimensional mechanical models and field data. *Journal of Geophysical Research*, **102**, B-1, 675-692.

Wojtal, S.F. (1996) Changes in fault displacement populations correlated to linkage between faults. *Journal of Structural Geology*, **18**, 265-269.

Wu, H. and Pollard, D.D. (1992) Propagation of a set of opening-mode fractures in layered brittle materials under uniaxial strain cycling. *Journal of Geophysical Research*, **97**, 3381-3396.

Wu, H. and Pollard, D.D. (1995) An experimental study of the relationship between joint spacing and layer thickness. *Journal of Structural Geology*, **17**, 887-905.

Zoback, M.D., Anderson, R.E., Thompson, G.A. (1981) Cenozoic evolution of the state of stress and style of tectonism of the Basin and Ranges Province of the western United States. *Philosophical Transactions of the Royal Society of London Series A*, **300**, 407-434.